Oxydation thermique, comportement à la corrosion induite par intermétallique et traitement de surface de l'alliage Al-Cu-Li

Meicheng Li

PSL UNIVERSITÉ PARIS

THÈSE DE DOCTORAT
DE L'UNIVERSITÉ PSL

Préparée à Chimie ParisTech

Thermal oxidation, intermetallics induced corrosion behaviour and surface treatment of Al-Cu-Li alloy

Soutenue par
Meicheng LI
Le 14 décembre 2020

Ecole doctorale n° 388
Chimie physique et chimie analytique de Paris-centre

Spécialité
Physico-Chimie

Composition du jury :

Mme Christine BLANC Professeur, ENSIACET	*Président*
M Herman TERRYN Professeur, Vrije Universiteit Brussel	*Rapporteur*
M Lionel PEGUET Ingénieur, CONSTELLIUM	*Examinateur*
M Philippe MARCUS Directeur de recherche CNRS, ENSCP	*Co-encadrant*
Mme Jolanta ŚWIATOWSKA Directeur de recherche CNRS, ENSCP	*Directeur de thèse*

Chimie Paris ParisTech | PSL

Acknowledgements

First and foremost, to my Supervisor, Jolanta Światowska, Frédéric Wiame and Philippe Marcus, for supporting so much on the project and for truly understanding what this project is all about. They gave me countless help and comments for not only my academic life but also my daily life and mental health. I cannot fully express my appreciation to their generosity, professional guidance, and goodwill. Thank you especially for Jolanta Światowska who believed in this project and me from the start. My thanks also to Frédéric Wiame who presented what is the professional and faithful attitude for the science and academic research. I would like to express my sincere regards to Philippe Marcus who gave me his firm and powerful support for this project.

For their generous assistance in the research of this project, I would like to acknowledge Sandrine Zanna, Antoine Seyeux, Dimitri Mercier and Zuocheng Wang. They assisted my phD project with their professional and technical ability. I also would like to thank Philippe Vermaut, Fan Sun and Francoise Piller for their help of my TEM and SEM measurement. Furthermore, Thank you, Anne Tang for your kindly assistance for managing my administration issues.

My gratitude also to Eirini-Maria Paschalidou, Shoshan Tamar Abrahami, Martin Weiser and Shova Neupane for sharing your valuable experience and advice from your passed PhD life.

This year is tough and painful, the epidemic really changed a lot and have strong impact on our health and life. But this time will eventually become an unforgettable experience in my life, no matter it is good or bad. I appreciate it.

To all the people above: I appreciate to meet all of you in my life and it is amazing to work with some of you. This end of PhD thesis does not mean the ending of our relation. It is the everlasting.

我们江湖再见

Meicheng

Contents

List of Figures

List of Tables

General Introduction

Development of materials is inseparably interconnected with human society and directly naming the ages of civilisations – the stone, iron and bronze ages – with each new era being brought by a new breakthrough of material. The new material provides more space and possibility for the development of human society while human being uses their intelligence and creativity to explore the possibility and application of material. It is to use an existing material and improve its properties to fulfil the requirement of various application. Taking aluminium alloys as an example, it is a metal with high strength/weight ratio and high corrosion resistance in atmospheric environment. It is widely used in different domains such as the manufacturing industry, for instance in planes, buses, trains and ships. Alloying elements such as Cu, Zn, Mg, Mn *etc*. are introduced into Al to form precipitates and to improve its mechanical properties such as strength and hardness. But these precipitates as chemical heterogeneities in Al alloys, produce galvanic coupling when they are in contact with corrosion environment.

Generally, surface is firstly exposed to the external environment. Therefore, considering the corrosion and breakdown of material, it is always a critical part to be tested and improved for a better stability under various temperatures, chemical environments, *etc*.

In this thesis, AA2050-T8 Al-Cu-Li alloy is studied. AA2050 (Al-Cu-Li) alloy is an advanced alloy with additional Li which has a critical role in improving the mechanical properties of the material. The sample used in this thesis was artificially aged at 155 °C (T8) in order to promote the nucleation of Li containing strengthening precipitates (T1 phase Al_2CuLi) to increase the strength.

The objective of this PhD thesis is to study the chemical surface modifications induced by thermal oxidation, corrosion behaviour and chemical surface protection of AA2050-T8 Al-Cu-Li alloy.

This PhD manuscript is composed of 6 chapters: introduction, experimental part, 3 chaptersof results (3, 4, 5) and conclusions.

In chapter 3, the oxidation mechanism and surface modification of AA2050-T8 aluminium alloy at medium-high temperature (about 200 °C) was studied. Oxidation is a critical factor of metal damage, which can modify the chemical structure and thus the corrosion resistance of the alloy. The study of thermal oxidation has practical meaning for processing and application of Al alloys. Most industrial annealing processes of Al alloys are performed in the range of medium-high temperature for hours such as the one performed on the sample of this thesis: AA2050-T8. The analysis of surface modifications during annealing process can provide information to optimize the following surface treatment. Moreover, thermal oxidation is considered as an inevitable challenge in extreme working environment of aerospace application. The surface modifications may induce structural instability during service time. Our objective of this part is to study the oxidation behaviour and surface modifications of sample at higher temperatures. The surface chemical composition under well-controlled treatments is characterized in situ. The modification of the surface film (the new oxide formed) at high temperature is revealed by 3-dimensional chemical mapping.

In chapter 4, corrosion behaviour and surface modifications of the AA2050-T8 aluminium alloy were studied in aggressive electrolytes: 0.1 M NaCl. A relation between intermetallic particles (IMPs) and the initial corrosion of AA2050-T8 was observed and studied. Larger pits are always related to the presence of larger IMPs (Al-Cu-Fe-Mn). The mechanisms of AA2050-T8 corrosion behaviour and the influence of alloying elements (Cu, Li, Fe) is discussed in details in this thesis. One of the critical points of this part is the behaviour of Li. ToF-SIMS as a high sensitivity technique can detect a small amount of Li (less than 1%) in this alloy. 2-dimensional and 3-dimensional chemical mapping was used to comprehensively present the pitting corrosion initiation in Al-Cu-Li alloy (including the detection of Li).

Chapter 5 focuses on one of corrosion protection of Al alloys: trivalent chromium process (TCP). Today, new chemical surface treatment is developed to replace the Cr^{VI} containing chromium conversion coating, which will be banned from industrial applications by European REACH regulations. The trivalent chromium process (TCP) conversion coatings are regarded as the most promising choices to replace the chromate conversion coatings (CCC). This TCP coatings have higher corro-

sion resistance than the native oxides of bare Al alloys with better adhesion. Before the application of conversion coatings to Al alloys different surface chemical pretreatments such as degreasing and pickling are used. These pretreatments can have a strong influence on the corrosion resistance and morphology of TCP layer. In this work, the composition of the alloy surface, modified by chemical pretreatment (degreasing and pickling) treatments is characterized. Moreover, the effect of pretreatment on TCP coating is discussed.

Different characterization techniques are coupled in order to study chemical, structural and morphological modifications of Al-Cu-Li alloys and their influence on corrosion behaviour. These techniques are X-ray photoelectron spectroscopy (XPS), time-of-flight secondary ion mass spectrometry (ToF-SIMS), scanning electron microscopy (SEM) coupled with electrochemical measurements.

Considering the above, a comprehensive investigation of Al-Cu-Li alloy was performed in this thesis in terms of thermal oxidation, corrosion behaviour and surface treatment for corrosion protection. The studied aspects give an expanded estimation of Al-Cu-Li alloys for its further application and development.

Chapter 1

State-of-the-art and objectives

This chapter presents the state-of-the-art on metallurgy, chemistry, thermal treatment and aging of alloys, and corrosion and corrosion protection. The specific bibliographic studies on thermal treatment, corrosion and surface treatments for corrosion protection related to results is presented in 3 chapters of results: chapter 3, 4, 5 respectively.

1.1 Al alloys and Al-Cu-Li alloys

Aluminium is one of the most commonly used metals in the world. In 2019, the world quantity of primary Al produced was estimated to be 63.7 million tonnes [2]. Its lightness, ductility, thermal conductivity and high corrosion resistance make it applicable in various domains [3]. To fulfil the requirements of each application, alloying elements such as Cu, Mg, Mn, Zn are often added into Al in order to modify and improve the specific properties such as strength, hardness or weldability *etc*.

Series of Al alloys are defined based on their alloying elements and corresponding categories and applications as shown in Table 1.1.

Taking 2xxx Al alloys as an example, Cu and Mg are the main alloying elements in 2xxx Al alloys (Table 1.1). These alloying elements react with aluminium during heat treatment and form finely dispersed precipitates, which can induce lattice distortion and act as obstacles to dislocation motions. This effect is called age hardening and Al alloys, which can be improved after heat treatment, are called heat-treatable alloys [4]. For non heat-treatable Al alloys, their microstructure and mechanical properties can not be well modified by heat treatment.

Table 1.2 presents the chemical specifications of two kinds of 2xxx Al alloys: AA2024 and AA2050 which are two representative Al alloys applied in aircraft industry. AA2024 is one of the best known high-strength Al-Cu-Mg alloys and has been maturely applied in the structural component of aircraft such as wings. Since constant effort was addressed to improve the applied material for a higher strength/weight ratio and a better corrosion resistance, Al-Cu-Li alloy (such as AA2050) is considered as an advanced material for replacing the conventional Al alloys (AA2024). Li is considered to be introduced as part of heat-treatable Al alloy since the 1920s to increase the strength [5]. Then in the 1950s, scientists of Alcoa found that the Li can increase the elastic modulus. For each 1 % of Li added, the elastic modulus can increase of 6 % with 3 % reduction of density [5, 6]. Although the benefit of additional Li is obvious, Li-induced anisotropy and low fracture toughness limits the development of Al-Li alloys [5]. These problems were resolved to some extent by optimizing the alloying additions and thermal mechanical process. AA2050 is an optimized Al-Cu-Li alloy produced since 2004 with good mechanical properties, lightness and high stress corrosion resistance [7, 8]. It is considered by NASA [9] for fabrication of cryogenic propellant

Table 1.1: Al designation system and corresponding applications

Series	Main alloying element	Alloy category	Application
1xxx	–	Commercially pure	Electrical, package
2xxx	Cu, Mg	Heat-treatable	Aircraft
3xxx	Mn	Non Heat-treatable	Cooking utensils
4xxx	Si	Non Heat-treatable	Automotive
5xxx	Mg	Non Heat-treatable	Storage tanks, marine
6xxx	C, Mg, Si	Heat-treatable	Structural, automotive
7xxx	Zn	Heat-treatable	Aircraft
8xxx	Li *etc.*	Non Heat-treatable	automotive

Table 1.2: Specifications of AA2024-T3 and AA2050-T8 alloys (wt%)

Alloy	Cu	Li	Mg	Zn	Mn	Ag	Zr(max)	Fe(max)	Si(max)
2024	3.8–4.9		1.2–1.8	0–0.3	0.3–0.9			0.5	0.5
2050	3.2–3.9	0.7–1.3	0.2–0.6	0–0.25	0.2–0.5	0.2–0.7	0.14	0.1	0.08

tanks to reduce the mass of future heavy-lift launch vehicles or as a promising aerospace material to replace the conventional Al alloys such as AA7050 and AA2024 [7, 8]. As shown in Table 1.2, the difference of chemical composition between AA2050 and AA2024 is not only the addition of Li but also the reduction of Mg. The addition of Li in AA2050 is to adjust the mechanical properties of alloys by forming strengthening precipitates such as T1 phase (Al_2CuLi), δ' phase (Al_3Li), *etc.* The reduction of Mg is to balance the existence of Li. Moreover, other elements such as Zr and Ag in AA2050 are added to optimize the microstructure. Zr prevents the recrystallization by forming Al_3Zr dispersoids and Ag reacts with Mg to form clusters which improve the formation of uniform precipitates [7, 10, 11]. A summary on IMPs present Al-Cu-Li alloy is shown in Table 1.3 with a schematic illustration in Fig. 1.1.

In Table 1.3, T1, T2 and δ' phases are the principal precipitates in the Al-Cu-Li alloys. For alloys with low Li concentration ($\leq$ 0.6 %), the main strengthening precipitate is Al_2Cu θ' (tetragonal). For alloys (AA2050) with medium Li concentration which is the range between 0.6 –1.4 % , the principal strengthening precipitate is T1 phase Al_2CuLi (hexagonal). For the higher Li content ($\geq$ 1.4–1.5 %), Al_3Li δ' (cubic) is the major strengthening precipitate. The strengthening effect of these strengthening precipitates are different. Fig. 1.2 and Fig. 1.3 are the TEM images of T1 phase and δ' phase respectively. T1 phase is a needle shape precipitate while δ' phase is spherical. Csontos *et al.* [12] revealed a inhomogeneous deformation on the Al-Cu-Li alloys due to strain localization

Table 1.3: List of intermetallic particles in Al-Cu-Li alloys [10]

Name and stoichiometry	Size and shape	Role
S′ Al_2CuMg	needle, laths, incoherent 0.1–0.2 µm	hardening precipitates, found in alloys with Li $\geq$ 1.4 %
δ' Al_3Li	spherical, coherent $>$ 0.3 µm	found in alloys with Li $\geq$ 1.4 % metastable precipitates
T1 Al_2CuLi	needle, plate 50–200 nm	major strengthening precipitates found in alloys with medium Li content $\leq$1.4 %
T2 Al_6CuLi_3	plate 0.1–0.2 µm	major strengthening precipitates found in alloys with medium Li content $\leq$1.4 %
β Al_3Zr	spherical 100 nm	dispersoid prevent recrystallization
$Al_2Cu_2Mn_3$	spherical 100 nm	dispersoid prevent recrystallization
θ Al_2Cu	plate	precipitate found in alloys with low Li content $\leq$ 0.6 %
$Al_xCu_yFe_zMn_w$	irregular, normally 1-20 µm	precipitate found in most alloys during casting

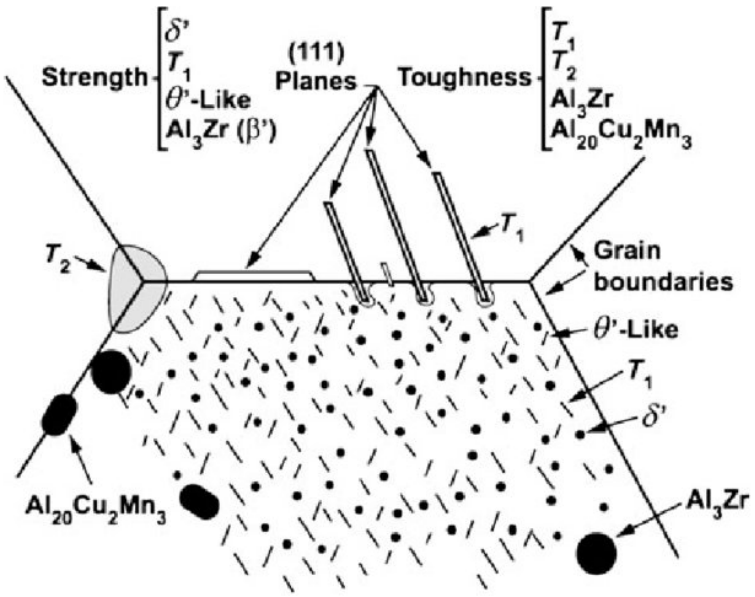

Figure 1.1: Schematic representation of Al-Cu-Li alloy microstructure with different precipitates [1]

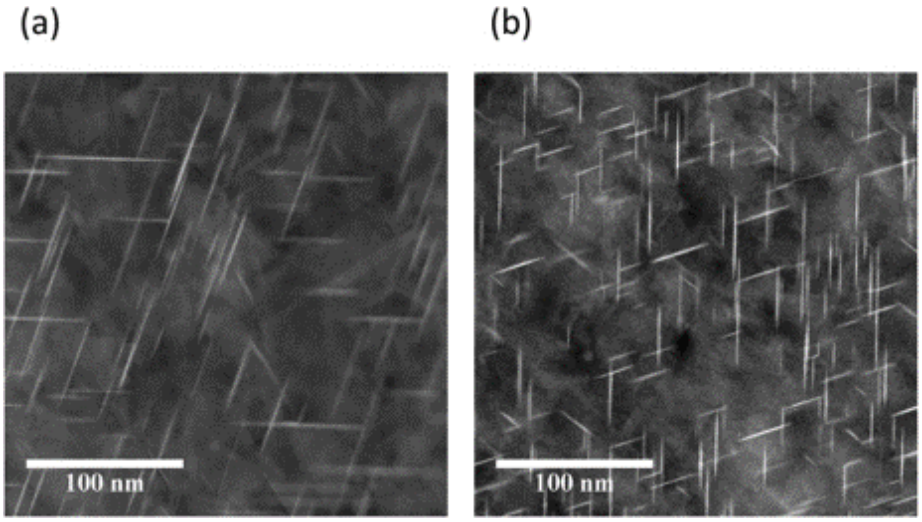

Figure 1.2: Transmission electron microscope of T1 phase [14]

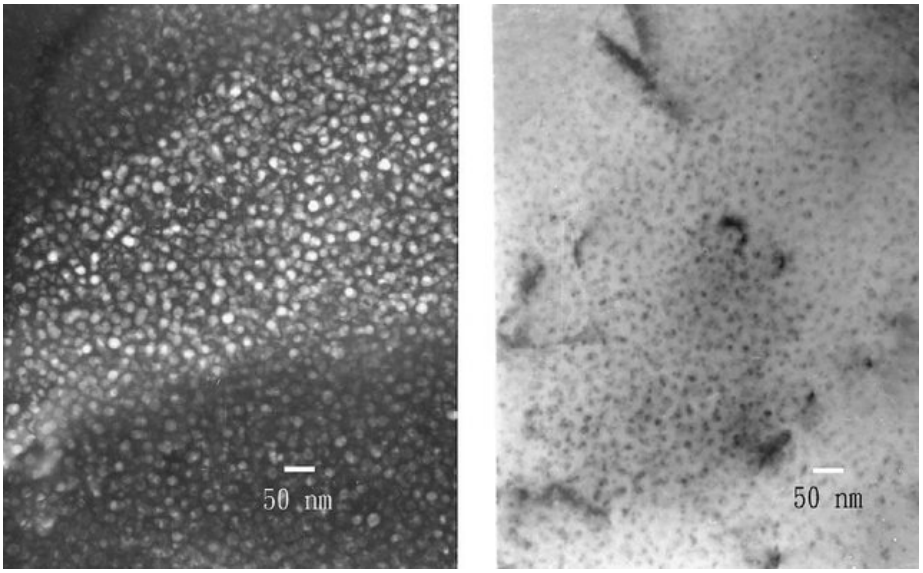

Figure 1.3: Transmission electron microscope of the δ' phase in heat treated Al-9.7 at.% Li alloy [15]

from the shearing of the δ', θ' and T1 strengthening precipitates. Rioja *et al.* [1] indicated that the existence of T1 phase can largely improve the strength as well as the ductility of Al alloys and that spherical δ' phase provides less hardening effect than T1 phase with reduced ductility. Moreover, δ' phase is considered as the origin of localized strain and anisotropic character of Li containing Al alloys [1, 13]. Therefore, the presence of δ' phase into the alloys is undesirable compared to the T1 phase and thus the content of Li has to be restrained to 1.4 % for aerospace industrial Al-Cu-Li alloys.

Besides AA2050, series of optimized Al-Cu-Li alloys such as AA2195, AA2297, AA2198 and

AA2099 are produced for the development of aircraft applications. This type of Al alloys may be considered as an achievement of alloy design. To verify and expand the application of Al-Cu-Li alloys, comprehensive and precise investigation is needed in order to examine their behaviours in various conditions such as heat treatment, oxidation, corrosion and industrial surface treatment, *etc*.

1.2 Effect of thermal treatment on Al-Cu-Li alloys

As introduced in the previous section, microstructure and corresponding mechanical properties of Al alloys can be modified by thermal treatment. The influence of thermal procedures on the mechanical properties of Al alloys can be positive or negative. Therefore, thermal processing should to be designed to improve the mechanical properties of Al-Cu-Li alloys by optimizing the distribution, density and size of strengthening IMPs.

Another effect related to thermal treatment is the segregation of alloying elements. When the temperature increases to some extent, compounds in solid solution tend to accumulate at grain boundaries and free surfaces [16, 17]. Thermal segregation can induce the heterogeneity of surface and decrease the corrosion resistance of Al-Cu-Li alloy. Considering the practical industrial annealing process of Al alloys and extreme working condition of the aircraft, the investigation of the surface composition of Al-Cu-Li alloys under high temperature is essential.

The effect of thermal treatment on both microstructure and surface composition will be introduced in this section.

1.2.1 Microstructure

As introduced in section 1.1, the Li content of most aerospace Al-Cu-Li alloys is restrained below 1.4 % to ensure that T1 phase (Al_2CuLi) is the major strengthening IMPs. Besides the chemical composition, thermal-mechanical process (TMP) can also influence the distribution, density and size of T1 phase. Before annealing, a pre-stretching is applied to increase the number of dislocations, which are preferential sites for the T1 phase nucleation [14, 18]. In the case of AA2050, 3.5–4 % pre-stretching can increase the density of T1 phase efficiently [1, 9]. Alloys are then annealed

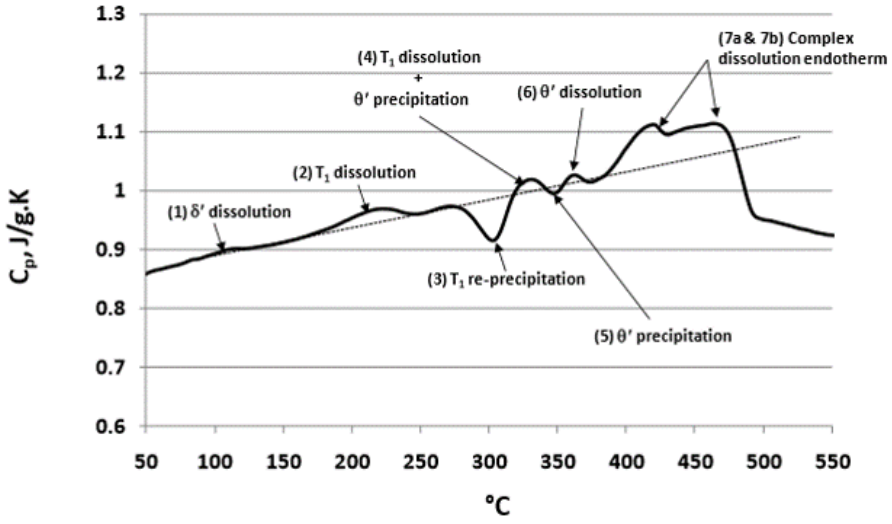

Figure 1.4: Tentative phase identification of thermal events for AA2050-T8 [9]

at specific temperature to induce the nucleation and growth of T1 phase or other strengthening precipitates. Two typical thermal treatments for AA2050, namely T3 and T8 are introduced below [19]:

T3 (pre-stretched & natural-aged): solution heat-treatment (SHT) at 500 °C for 1h, water-quenching followed by 3.5–4.5 % pre-stretching then natural ageing at room temperature,

T8 (pre-stretched & artificial-aged): SHT at 500 °C for 1h, water-quenching followed by 3.5–4.5 % pre-stretching then 155 °C/18 h artificial ageing to peak strength.

In the case of AA2050-T3, only few T1 phase accumulates at grain boundaries, but if the AA2050 is annealed in T8 conditions, a much denser T1 phase is formed, homogeneously distributed both at grain boundaries and inside grains [19].

Fig. 1.4 presents the change of soluble phases in AA2050-T8 along the specific heat capacity curves. According to Fig. 1.4, the T1 phase in AA2050-T8 dissolves when the temperature is higher than 210°C, then a re-deposition behaviour of T1 phase is observed at around 300°C. Therefore, between 200°C and 300°C, strengthening phase starts to coarsen or dissolves accompanied with reduction of tensile strength and hardness. This phenomenon, called overageing, is associated with a strength decreasing behaviour after thermal treatment at higher temperature, and/or for a longer time, than the optimum condition [20, 21]. Therefore, to improve the mechanical properties, an optimized thermal treatment is important.

1.2.2 Segregation of alloying elements

Besides the change of microstructure and corresponding mechanical properties, segregation or re-distribution of alloying elements can also be induced by the heating treatment. A typical case of Al-Cu-Li alloys is the Li surface segregation on the annealed surface. The Li segregation in Al-Li alloys has been proved by several studies under various thermal treatments (120 °C to 600 °C) and the corresponding effect on the surface properties has been investigated [22–25]. First, the hardness of the Li rich surface is found to be lower compared to the original surface. Then, an acceleration of oxidizing process was observed on the Li riched surface. Mg is another active alloying element in Al-Cu-Li alloys which shows a similar segregation behaviour with Li at higher temperature. Lea and Molinari [26] studied the surface segregation of the Mg inside Al alloys at various temperatures by Auger electron spectroscopy (AES). A Mg segregation was observed when temperature increased to 100 °C and this segregation behaviour can develope into evaporation if the temperature is high enough. A linear relation between amount of Mg segregation and the temperature was also found by Saied *et.al* by AES [27]. Moreover, they suggested that presence of oxygen can promote the Mg surface segregation since Mg has high oxygen affinity. Segregation of Mg at grain boundaries was also observed at high temperature (above 150 °C) [28–31]. This phenomenon has an important effect on the intergranular corrosion (IGC), stress corrosion cracking (SCC) and hydrogen embrittlement (HE). Noble alloying elements such as Ag in Al-Cu-Li alloys also segregates under thermal treatments. Hutchinson *et al*. [32] used transmission electron microscopy (TEM) and high-resolution scanning electron microscope (HR-SEM) with energy dispersive X-ray spectroscopy (EDX) to see the Ag atoms segregates to the interfaces between nano-sized IMPs and Al matrix in Al alloys during annealing. Lee *et al*. [33] used AES to study the equilibrium surface composition of a polycrystalline Al–4.2 at.% Ag alloy as a function of temperature(723 K to 848 K at intervals of 25 K) and indicated an segregation behaviour of Ag on the free surface. Wetli *et al*. [34] studied the kinetics of surface segregation of Ag on a (100) surface of Al-3 at.%Ag at 150–250 °C by means of AES and showed that the surface segregation of Ag is controlled by the bulk diffusivity of Ag in Al matrix. However, the surface segregation behaviour of Ag in industrial Al alloys is less studied and the influence of Ag surface segregation on the surface properties such as hardness, corrosion resistance is not clear.

1.3 Corrosion behaviour of Al alloys

Corrosion is a dangerous and costly problem for most industry areas. Therefore, corrosion behaviour of the material is always assessed before use and regularly tested during service life. For example, salt-spray test is a standardized and popular corrosion test method used to check corrosion resistance of Al sheet in aerospace industry [35, 36]. Moreover, the structure of aircraft has to be checked and repaired regularly.

In this section, the corrosion behaviour of Al alloys especially of Al-Cu-Li alloys is introduced. In fact, compared to other metals such as Fe, Al alloys has a high corrosion resistance due to its passive layer which is a compact thin layer of aluminium oxide on the metal surface. This passive layer is stable and acts as corrosion protective layer in the air or the neutral environment [37, 38]. Moreover, the passived layer of Al and Al alloys has been studied in terms of chemical composition, miscrostructure and corrosion mechanism [38–40]. Fig. 1.5 shows the Pourbaix diagram of Al under aqueous medium with various pH. According to Fig. 1.5, corrosion of Al occurs when the pH is higher than 9 or lower than 4.

The reactions of Al corrosion in the alkaline solutions (pH $\geq$ 9) are:

$$2\,Al_2O_3 + OH^- + H_2O = Al(OH)_x \qquad \text{(breakdown of Al oxide layer)} \tag{1.1}$$

$$Al^{3+} + x\,OH^- = Al(OH)_x \qquad \text{(corrosion of Al metal substrate)} \tag{1.2}$$

In the acid environment (pH $\leq$ 4) , the chemical reaction can be described as:

$$Al_2O_3 + 6\,H^+ = Al^{3+} + 3\,H_2O \qquad \text{(breakdown of Al oxide layer)} \tag{1.3}$$

$$2\,Al + 6\,H^+ = 2\,Al^{3+} + 3\,H_2\ (\text{gas}) \qquad \text{(breakdown of Al oxide layer)} \tag{1.4}$$

Besides the above processes, Al alloys also can corrode under neutral electrolytes due to the galvanic coupling of Al with more or less noble elements. The region that provides electrons is the anode and the region collecting electron. When Al alloys is used as cathode, the reactions that happen on the metal surface are:

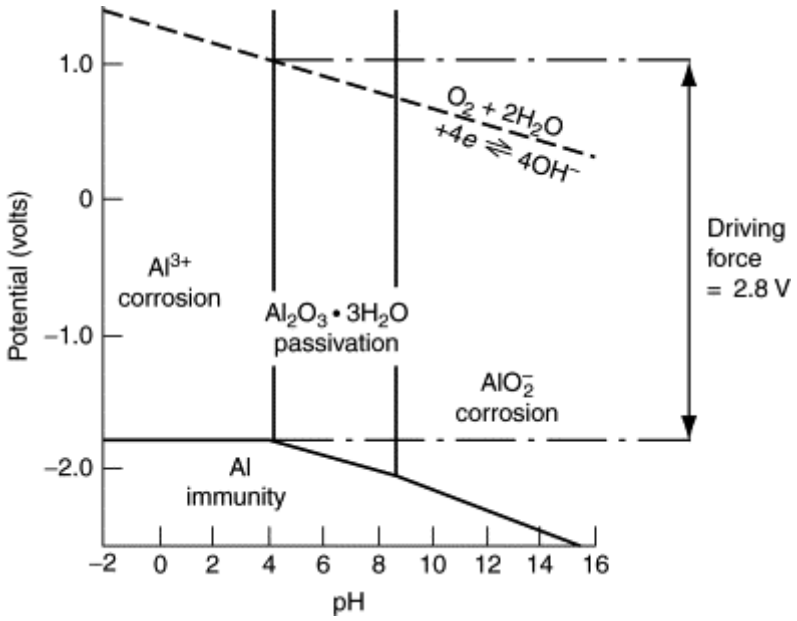

Figure 1.5: Pourbaix diagram for the Al – H_2O system at 25 °C [41]

$$H_2O + O_2 + 4\,e^- = 4\,OH^- \tag{1.5}$$

$$2\,H^+ + 2\,e^- = H_2 \tag{1.6}$$

When Al alloys plays as an anode, the reactions over metal surface are:

$$Al - 3\,e^- = Al^{3+} \tag{1.7}$$

$$Al^{3+} + 3\,H_2O = Al(OH)_3 + 3\,H^+ \tag{1.8}$$

Moreover, in aqueous environment, different corrosion types can be distinguished, such as uniform corrosion, intergranular, galvanic, crevice, pitting and stress corrosion, *etc.* Fig. 1.6 gives an illustration of main corrosion types.

Uniform corrosion is considered as the most common types of corrosion and proceeds uniformly over the entire exposed metal surface. As a consequence, the corroded surface becomes rough in appearance. This kind of corrosion is less dangerous compared to other forms, since it can be evidenced easily and estimated by simple corrosion test.

Intergranular corrosion (IGC) is a form of corrosion that localized attack along the grain boundaries while the bulk of the grains remain almost unaffected. This kind of corrosion occurs when the

boundaries of crystallites are more susceptible to corrosion than their insides. It is assigned to the chemical segregation of alloying elements or specific phases precipitated on the grain boundaries which makes the grain boundaries more anodic and easy to dissolve compared to the grains.

Galvanic corrosion is an electrochemical process induced by presence of two (or more) dissimilar metals which are electrically coupled in conductive electrolyte. As a consequence, the metal with the more anodic potential corrodes faster while the cathodic one is protected and corrodes slower than it would alone.

Crevice corrosion as illustrated in Fig. 1.6, occurs when two components are joined close together to form a crevice. This crevice provides “stagnant” conditions for the electrolyte as well as oxygen. When the oxygen is restricted due to the stagnant environment, the cathodic oxygen reduction reaction cannot be sustained in the crevice area, giving it an anodic character and leading to the creation of an acidic micro-environment, together with a high chloride ion concentration. Therefore, a severe corrosion occurs in the crevice.

Pitting corrosion is one of the most severe problems for Al corrosion and it is addressed in this thesis. It is considered to be more dangerous than the uniform corrosion because pit corrosion is difficult to detect and quantify. It was proved that a small, narrow pit with minimal overall metal loss can lead to the failure of an entire engineering system [42–44]. For Al alloys, the pitting corrosion is always localized at IMPs and enhanced at the IMPs and matrix interface. Fig. 1.7 shows a schematic illustration of pitting corrosion. When the Al alloy surface is placed into the aqueous electrolyte, a potential difference is generated between IMPs and Al matrix due to the chemical heterogeneity. The galvanic coupling between the IMPs and the matrix can be different if the chemical composition of IMPs are distinct. For example, the Cu, Fe-rich IMPs are more cathodic compared to the Al matrix. Therefore, hydrogen and oxygen reduction happens at the IMPs (cathodic sites) and produces OH^- while the matrix adjacent to the IMP dissolves as anode with the generation of H^+ as indicated in equations (1.5–1.8).

A relation called limiting cathodic current is found between the corrosion rate and the amount of cathodic IMPs [47]. This cathodic limiting current model can be used to explain that more IMPs with larger relative areas can induce higher electrochemical activity of Al alloys.

However, not all the IMPs are cathodic compared to the Al matrix. T1 phase, which is the

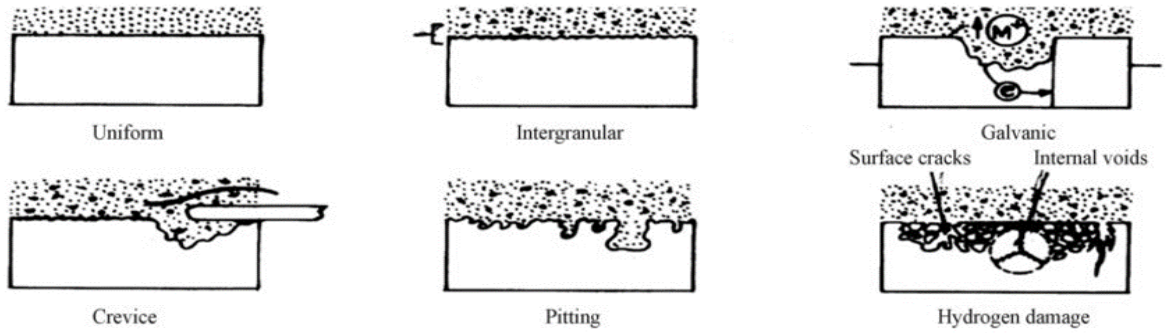

Figure 1.6: Summary of different types of corrosion [45]

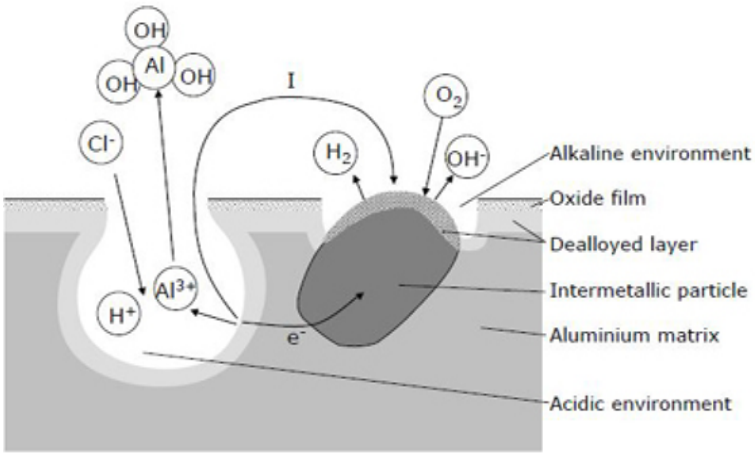

Figure 1.7: Presentation of pitting corrosion mechanism of Al alloys [46]

principal strengthening IMPs in Al-Cu-Li alloy is more anodic compared to the Al matrix and acts as anode during corrosion and dissolve faster compared to the Al matrix [48–51]. The corrosion behaviour of Al-Li alloy is also studied and considered as a more advanced material compared to the convetional Al alloy but the exact effect of Li and its distribution on chemical modifications and corrosion of Al-Li alloys is still under discussion. In this section, two typical localized corrosion behaviours of Al-Cu-Li alloys will be introduced. One is assigned to the dissolution of anodic T1 phase, the other is induced by the local galvanic coupling between the matrix and the cathodic Al-Cu-Fe-Mn constituent IMPs [52].

1.3.1 Pitting corrosion induced by T1 phase

As previously introduced, T1 phase is more anodic to the Al matrix. Severe IGC and transgranular corrosion (TGC) have been observed in Al-Cu-Li alloys and largely depends on the Li dissolution found principally in the nano-sized T1 phase (Al_2CuLi). The presence of Li in T1 phase makes it more anodic than matrix and prone to dissolve during corrosion [48–51, 53]. Li *et al.* [54, 55] used simulated bulk precipitates of T1 and studied the electrochemical behaviours in the NaCl electrolyte. A lower OCP was detected on the bulk T1 phase compared to the aluminium and a preferential dissolution of Li and Al makes the T1 phase to corrode faster than the Al matrix at the beginning. However, due to this dealloying effect of T1 phase, the IMP surface is enriched in a noble element, namely Cu which leads to the increase of the potential. As a result, the corroded T1 phase become cathodic with reference to the alloy which leads to the anodic dissolution of the surrounding alloy. Therefore, the distribution and amount of T1 phase has a critical effect on the corrosion behaviour of Al-Cu-Li alloy. Some previous works [19, 53, 56, 57] focused on the influence of thermal treatment on corrosion mechanisms of Al-Cu-Li alloys such as IGC or TGC as shown in Fig. 1.8.

As mentioned in section 1.2.1, the distribution and amount of T1 phase are different in Al-Cu-Li alloys with different thermal treatment. In the T3 thermal treatment, T1 phase accumulates at grain boundaries. Therefore, alloys with T3 treatment are more susceptible to IGC. While in the case of T8 thermal treatment, T1 phase is fine, homogeneous and dense both inside grains and at grain boundaries, therefore, TGC can be observed [56].

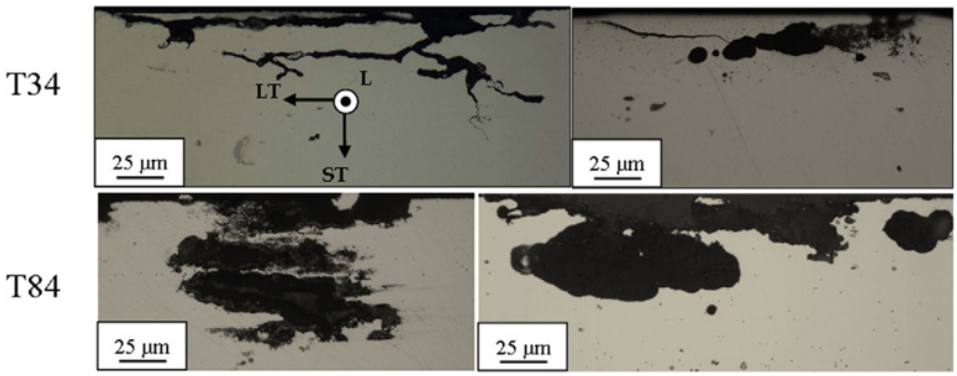

Figure 1.8: Optical microscopy images of the corrosion defects for AA2050-T3 and AA2050-T8 after immersion in 0.7 M NaCl electrolyte after 24 h immersion and after 72 h immersion [56]

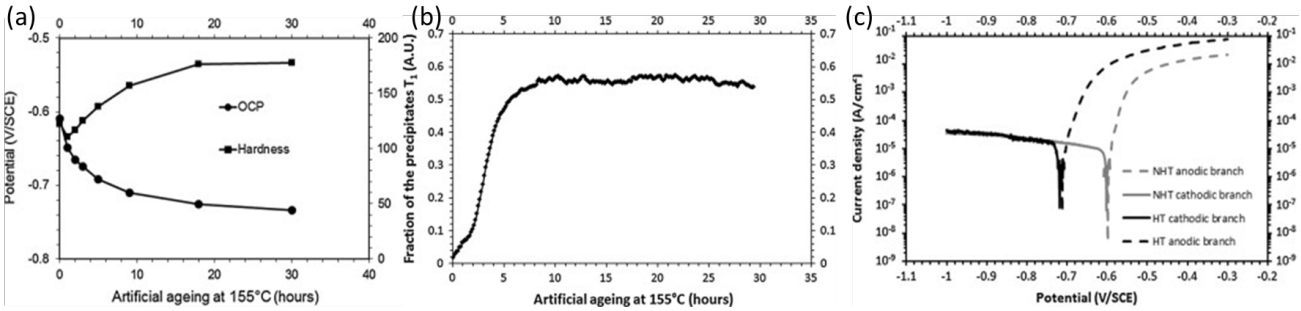

Figure 1.9: (a) Evolution of OCP and hardness of as-received AA2050 alloy at 155 °C artificial ageing. (b) Fraction of T1 phase in AA2050 during 155 °C artificial ageing (c) polarization curve of as-received AA2050 and heat treated AA2050 [53]

Moreover, Proton *et al.* [53] revealed that increasing T1 fraction in AA2050-T8 (artificially aged at 155 °C) results in higher hardness of AA2050 but lower open circuit potential (OCP) in comparison to AA2050-T3 (as received) as shown in Fig. 1.9 (a). In Fig. 1.9(c), the corrosion potential of AA2050-T8 is -0.7 V *vs* saturated calomel electrode (SCE) in 0.7 M NaCl and more negative than the OCP of AA2050-T3 (-0.6 V/SCE). They indicated that this phenomenon is assigned to the increase of T1 phase fraction in AA2050 during ageing and the higher fraction of T1 phase can increase the susceptibility of the corrosion for Al-Cu-Li alloys.

1.3.2 Pitting corrosion induced by Al-Cu-Fe-Mn intermetallic particles

Besides the T1 phase, another kind of IMP with much lager size ($>$ 1 µm) : Al-Cu-Fe-Mn IMPs also plays an important role in the corrosion of Al-Cu-Li alloys. These kinds of IMPs are very common in most industrial Al alloys such as AA2024, AA7075, *etc*. They are formed during casting process and they are randomly distributed in the Al alloys. The cathodic character of Al-Cu-Fe particles

can induce galvanic coupling with the matrix and promote pitting corrosion [19, 58, 59]. The pitting corrosion induced by galvanic coupling was also studied by Zhou *et al*. [60] on AA2024. They found that the propagation of pitting corrosion is involved in the extensive grain boundary attack. They indicated that, when the pitting corrosion occurs and starts to propagate, corrosion developed preferentially along the grain boundary network beneath the alloy surface. Buchheit *et al.* [52] also concluded that the pitting corrosion that occurs close to the Al-Fe-Cu-Mn IMPs is one of the main corrosion behaviours of Al-Cu-Li alloys.

The distribution of Li in Al-Fe-Cu-Mn constituent IMPs and its effect on pitting corrosion is not clear yet. Few studies tried to evidence the distribution of Li in constituent IMPs [61, 62]. A electron energy loss spectroscopy (EELS) of Al-Cu-Fe-Mn particles in Al-Cu-Li alloy is presented in Fig. 1.10. First, they measured the chemical composition of Al-Cu-Fe-Mn IMPs by EDX and divided the IMPs into high-copper-containing particles and low-copper-containing particles. The difference of Cu content is assigned to the diffusion of alloying elements during the sequent thermomechanical processing. They assumed that the lithium in the high-copper-containing particles diffused together with copper into the surrounding alloy matrix. Therefore, the low-copper-containing particles contain much less lithium. Later, they identified two kinds of corrosion behaviours on the Al-Cu-Fe-Mn IMPs with this two kinds of particles as shown in Fig. 1.11. The high-copper-containing particles are more reactive due to the high content of Li. Therefore, more severe corrosion and trenching are observed around these IMPs compared to others with lower Cu and Li contents.

1.4 Surface treatments for corrosion protection of Al alloys

This section is related to surface treatment of metal surfaces and more particularly to the processes and effects of cleaning such surfaces for subsequent treatment. In industry, after being cast or formed into desired shapes, aluminium surfaces are highly deformed and contaminated by the organic industrial lubricants. The native oxide with oil and much defect on the Al alloys can not fulfil the requirements of industrial applications such as strength and corrosion resistance. Therefore, for most aluminium alloys, surface treatments are necessary in order to optimize the surface condition before introducing into service. The surface treatment can be designed for different objectives.

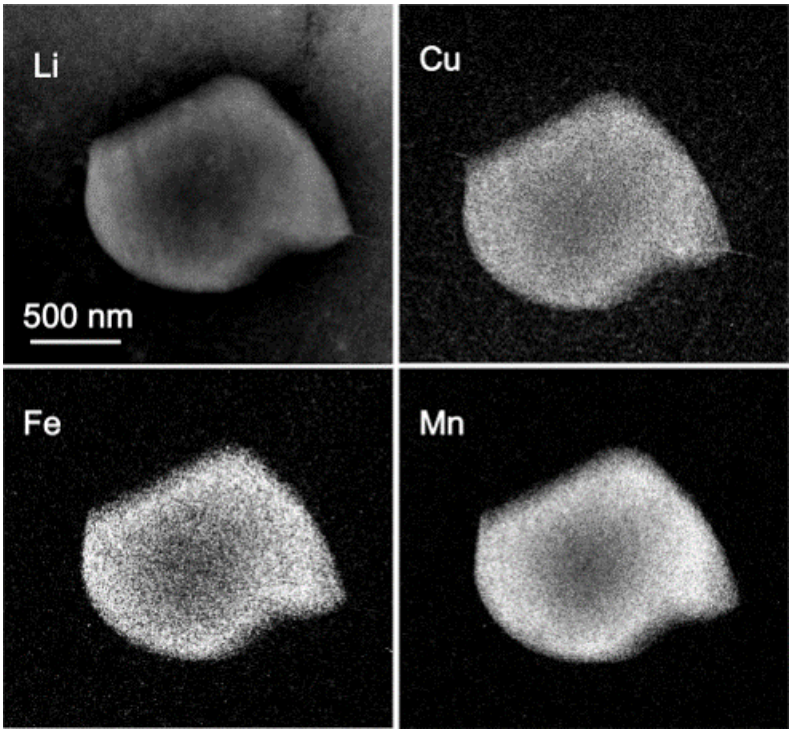

Figure 1.10: EELS imaging of Al-Fe-Cu-Mn particles in AA2099 (Al-Cu-Li alloy) [62]

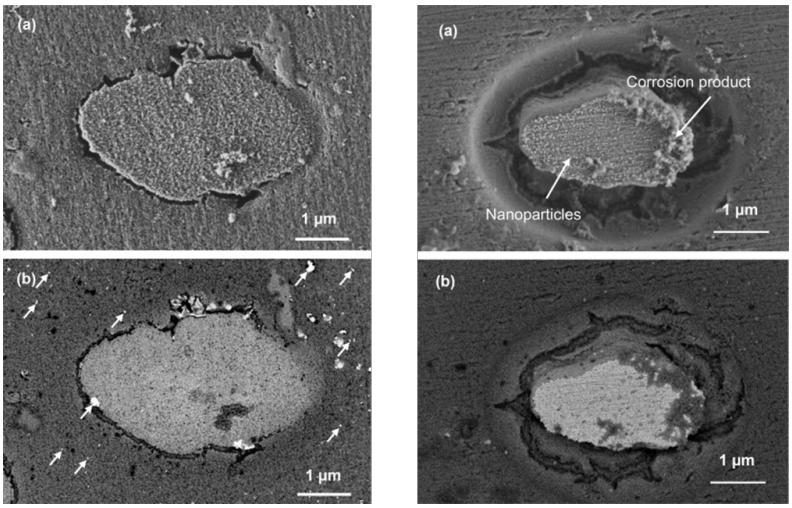

Figure 1.11: SEM images of IMPs with different content of Cu (a) SE image (b) BSE image. Two different corrosion morphologies [62]

Table 1.4: List of surface treatments applied to Al alloys [63, 64]

Type of surface treatments	Cases
Mechanical	blasting, mechanical abrasion, machining, liquid and vapour degreasing, plasma-spray coating, laser
Chemical	alkaline cleaning, acid etching, conversion coating
Electrochemical	electropolishing, DC-anodizing, AC-anodizing

For example, some surface treatments are applied to clean the surface by removing the native oxide layer contamination, some are to improve the adhesion between two phases in a composite material and some surface treatments are for higher corrosion resistance or higher roughness for different application. These treatments are of three types: mechanical, chemical and electrochemical [63]. A list to summarize the surface treatments is shown in Table 1.4. Normally, a mechanical treatment has to be used to give the alloy surface the last finish, for example, by removing minor faults (defects, native oxide, organic contamination) in the metal surface or increase the surface roughness to give a higher contacting surface. Chemical treatment and electrochemical treatment as named are surface modifications by chemical or electrochemical process. These treatments can be combined and designed to achieve the optimum surface with higher corrosion resistance and preferred morphology.

Fig. 1.12 shows a scheme of the Al coating system applied in aerospace industry composed of aluminium substrate, layers of aluminium oxide then primer and paint or topcoat to resist wear or corrosion. As illustrated, the layer in between primer layer and alloy substrate is a treated layer, which is normally an anodized layer or a conversion coating. This treated layer is produced to increase both the corrosion resistance of Al alloys and the adhesion to the primer. In aerospace industry the initial surface treatment consist of immersion in an alkaline degreasing bath followed by acid pickling then anodizing or conversion coating. Normally, alkaline degreasing and the acid pickling are considered as the pretreatment for preparing a morphologically and electrochemically homogeneous surface to improve the performance of the following steps such as conversion coating [65–67].

Chromate conversion coating (CCC) is widely used in industry for the protection of Al alloys against the corrosion. It serves as a barrier layer with high ionic resistivity and inhibits the oxidation-reduction reaction by releasing powerful corrosion inhibitors “on demand” such as hexa-

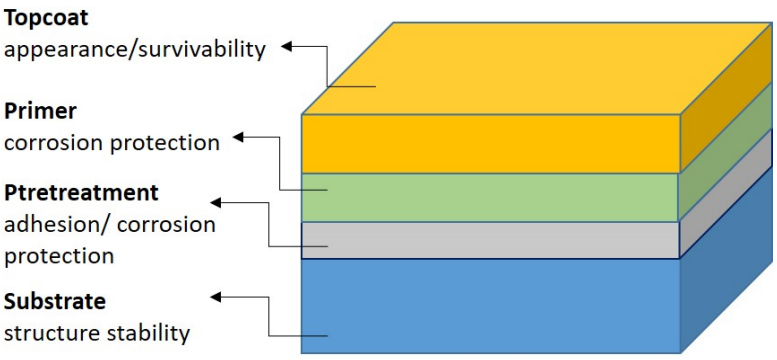

Figure 1.12: Adopted schematic of components of an aircraft coating system [80]

valent chromium Cr^{VI} [68–71]. However, the application of Cr^{VI} will be banned due to the grossly cytotoxicity of Cr^{VI}, which can increase the risk of cancers and penetrate all tissues in the body [72, 73]. In 2007, a law enacted by the European commission was entered into force for regulating chemical substances and their potential impacts on both human health and the environment so-called “European Community regarding the Registration, Evaluation, Authorization and Restriction of Chemicals (REACh)” [74, 75]. It indicated high restriction of the chemical substances containing hexavalent chromium and encourages the efforts made to develop more environmental friendly conversion process. For example, alternative conversion coatings are designed based on solutions containing Cr^{III} and Zr^{IV}, permanganate, phosphates and rare earth elements (REEs) [76]. One of the promising approach to replace the CCC process is trivalent chromium process (TCP) [77–79].

In the following sections, alkaline degreasing, acid pickling and conversion coating (especially TCP), which correspond to complete series of Al alloy surface treatments in aircraft industry is introduced.

1.4.1 Alkaline degreasing and acid pickling

To design a proper cleaning pretreatment for alloys, three points should be considered which determine the reactions required and inheriting relation of cleaning pretreatment:

1. Alloy or grade of aluminium,
2. Surface contaminant,
3. Subsequent processing.

Normally, there are two major steps for the cleaning pretreatments before the conversion or anodizing treatment. Firstly, alkaline cleaning, to remove the thick as-received oxide layer and organic contamination left after manufacturing, also called **"degreasing"** and secondly, acid cleaning, to remove the oxide layer formed during degreasing, the IMPs on the surface and decrease the susceptibility to corrosion, also called **"pickling"**. The objective of pretreatment (degreasing and pickling) is to optimize the surface condition with higher chemical homogeneity and adaptability for the successive chemical/electrochemical surface treatment. They are important processes for the surface treatment and play a critical role in the success or failure of the following procedures [65–67].

Degreasing

Alkaline cleaners for industry are mainly liquid baths containing phosphate, sodium-based carbonates, hydroxide or silicate with some additives such as corrosion inhibitor, *etc*. [81, 82]. During degreasing the native oxide layer with contamination and Al matrix will dissolve, following the formation of a new oxide layer with altered oxide composition and thickness [83–85]. The pH of the alkaline cleaner has an influence on the chemical composition of surface. Joshi *et al.* [83] indicated that if the 7075-T6 was cleaned by a solution with a pH of 9.1 the native oxide is removed and an aluminium-rich oxide layer about 10 nm thick is left. However, if the sample is activated by alkaline solutions with pH over 12, the oxide thickness is about 20–60 nm with different chemical composition. Besides the oxide thickness, the chemical composition will also modified due to the Al dissolution during alkaline degreasing process. Gharbi *et al.* [10] used inductively coupled plasma atomic emission spectrometer (ICP-AES) to measure the dissolution rate of alloying elements in AA2050 Al-Cu-Li alloy during alkaline cleaning and revealed a significant Li and Al dissolution and an enrichment of Cu on the surface. This enrichment is also highly affected by the IMPs in the Al alloys [86]. The Fe and Si containing IMPs dissolve much slower than Al matrix and provide the cathodes for enhancing the anodic dissolution of Al matrix. Therefore, the surface after degreasing needs other treatments since many remnants and IMPs are left on the degreased surface. Therefore, alkaline degreasing is always combined with acid pickling in order to remove the unfavorable remnants and have an optimized surface.

Pickling

As introduced previously, some poorly soluble surface residual smut such as IMPs or metal-oxide precipitates remain on the alkaline cleaned surface and reduce the corrosion resistance. Therefore, acid etching is used to dissolve this smut and re-modify the oxide layer for a better performance. Many acids can be used in the pickling process. The pickling solution can also be a combination of these acids for optimal result. Hughes *et al.* [87] studied the pickling behaviour of AA2024 Al-Cu-Mg alloy with different kinds of acids such as nitric acid, sulphuric acid, phosphoric acid with or without additive HF and made a kinetic model for the acid etching process. The pickling process can be decomposed into 3 stages:

1. The preferential dissolution of the compounds enriched on the alkaline cleaned surface such as Cu, Mg, Zn or Si phase,
2. The pickling of the Al matrix when the surface oxide is completely dissolved, leading to a balance between the dissolution and the formation of an oxide layer as well as the accumulation of alloying elements,
3. The formation of a relatively stable surface in the pickling bath with a modified oxide layer.

Previously, commonly used acid baths were based on Cr-containing formulations, which can clean successfully the smut and the IMPs produced by degreasing. Although they are currently applied in industry, effort was made to replace them by more environmental friendly solutions. Turco® Liquid Smut-Go NC [88] is a non-chromium formulation mainly contains nitric and hydrofluoric acids. It is applied as a standard industrial formulation for the surface treatment with efficient removal of smut [89–91]. Several studies focused on the behaviour of non-Cr acid bath for pretreatments. Toh *et al.* [92] tried to add some rare earth elements into the pickling bath but only first stage was achieved. A bath of HF and HNO_3 with additive Fe^{III} was found most effective in oxide reduction and removal of smut. Hughes *et al.* [93] also proved an efficient pickling of the ferric ion based deoxidizers and an attack of IMPs. Liu *et al.* [94] used TEM and medium energy ions scattering (MEIS) to study the Cu enrichment of AA2024 and AA7075 after treatment with NaOH and HNO_3 solution and indicated that the Cu enrichment of acid treated surface is comparable to that obtained after alkaline cleaning. The enrichment of Cu on the acid pickled surface is also

confirmed by Moffitt *et al.* [84]. The XPS depth profiling performed on the degreased and pickled surface of AA2024 and AA7075 demonstrated that nitric acid can be used to remove Cu oxides but not to reduce the enrichment under the oxide layer.

Only few studies focused on the behaviour of the Al-Cu-Li alloys during pretreatment. Gharbi *et al.* [10] studied the behaviour of alloying elements during surface pretreatment and revealed a preferential Cu, Fe, Mn and Mg dissolution of alkaline cleaned surface in the nitric acid while a slower dissolution rate for Li. However, the distribution of Li on the pretreated surface is still not clear since now.

1.4.2 Chemical conversion coating

After surface pretreatment, a scalloped surface with ridges composed of copper and other non-dissolved impurities is prepared for the later treatment for example conversion coating in order to have higher corrosion resistance and better adhesion. Conversion coatings is normally performed on metals and provides a protective layer through the chemical action between the coating solution and metal. It consists of a thin barrier coating made from aluminium oxide as well as other compounds. There are many forms of conversion coating, the most typical ones are those made with chromate fluorides. As introduced previously, chromate conversion coating (CCC) was commonly used in the aircraft industry before. During this process, Al alloys chemically reacts with hexavalent chromium (Cr^{VI}) species and form a thick complex trivalent chromium (Cr^{III}) oxide layer with high corrosion resistance and self-healing properties [95, 96]. But due to the high toxicity of Cr^{VI}, this method is restricted by the law of European Commission [74] and new environmental friendly approaches are developed in order to replace it.

For example, Ti/Zr based conversion coating [97, 98] has been developed with efficient improvement of corrosion resistance, but this conversion coating can be influenced by the presence of cathodic Fe-containing IMPs, which can induce significantly different thicknesses [99]. Song [100] and Conde [101] investigated the composition and corrosion resistance of other kind of coatings such as cerium conversion films on AA2195 and AA8090 Al-Li alloys. Dabala *et al*. [102] introduced a H_2O_2–cerium conversion coating. This conversion coating is thinner than the traditional one with an obvious improvement of corrosion resistance.

Trivalent Chromium process (TCP)

Trivalent Chromium process (TCP) was developed and known as a promising conversion process to replace the hexavalent chromium species due to its environmental friendly advantage [77–79]. The bath for TCP generally contains ZrF_6^{2-}, Cr^{3+} constituents in an aqueous solution with a pH of 3.8–4.0 at 40 °C. Normally, the thickness of the TCP layer is around 40 nm–120 nm depending on the time of deposition [103]. Efforts were done to study the mechanisms of TCP and the characterization of TCP coatings on the conventional industrial materials. The nucleation and chemical structure of its corresponding oxide layer formed during surface pretreatment and TCP on the conventional Al alloy such as AA2024 and AA7075 have been studied [103–105]. TCP coating is a pH-driven deposition process. It is created by the interface pH induced deposition of Zr^{IV} and Cr^{III} formulations. Verdalet *et al*. [106] used series of XPS, SEM and electrochemical studies to characterize the surface during the TCP coating and proposed a 3-stage model to describe the nucleation and growth of TCP coating.

In step 1, the native oxide dissolves by the activation by fluoride ions and fluoroaluminate is formed on the substrate surface as indicated in the following equations:

$$Al_2O_3 + 2\,x\,F^- + 6\,H^+ = 2\,AlF_x^{(3-x)+} + 3\,H_2O \tag{1.9}$$

$$2\,Al\,(s) + 6\,H_2O = 2\,Al^{3+} + 6\,OH^- + 3\,H_2 \tag{1.10}$$

$$Al^{3+} + 3\,F^- = AlF_3(s) \tag{1.11}$$

Due to the consumption of protons, local pH increases over the surface, promotes the deposition of Cr and Zr species and form a single precursor oxide layer as shown in the following equations:

$$ZrF_6^{2-} + 4\,OH^- = ZrO_2 \cdot (2\,H_2O) + 6\,F^- \tag{1.12}$$

$$Cr^{3+} + 3\,OH^- = Cr(OH)_3 \tag{1.13}$$

In the end of the first stage, a precursor single layer with small amount of F, Cr and Zr is formed over the whole surface. In the second step, the deposition of Cr and Zr continues and a Cr and Zr-

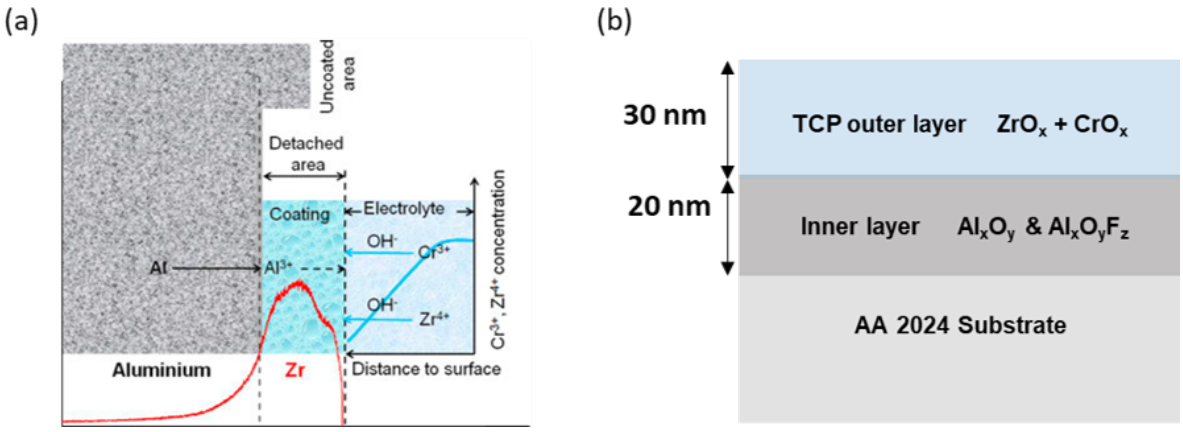

Figure 1.13: (a) schematic diagram of trivalent chromium conversion coating growth on aluminium, (b) simplified view of the TCP layer on the AA2024 [107, 108]

rich outer layer is formed while the precursor layer transforms into the inner conversion layer with high content of fluoroaluminate. Therefore, a double-layered structure developed during second step. In the third step, The Cr and Zr-rich outer layer keep growing until the pH difference between near-surface region and bulk electrolyte is close to zero. Then the growth and dissolution of TCP coating is almost balanced. A schematic diagram of trivalent chromium conversion coating growth and simplified view of the TCP layer on aluminium is presented in Fig. 1.13.

1.5 Objectives and outline of the thesis

The addition of Li improves the mechanical properties of Al-Cu-Li alloys with regards to other conventional Al alloys like 2024. As a relatively new material, the corrosion properties, the chemical and structural modifications induced by thermal or chemical treatments have to be understand and estimated under various conditions in order to guarantee the capability of its applications. It is also necessary to understand the influence of the existing industrial treatments aiming at corrosion improvement of this alloy, such as degreasing, pickling, TCP coating on the Al-Cu-Li alloys, on the surface morphological and chemical modifications and formation of a new type of surface layer and its corrosion stability.

Since the detection of Li in the Al-Cu-Li is challenging since it is light and very active element, the analysis of surface chemical modifications of Al-Cu-Li alloys, especially the corresponding behaviour of Li is limited in terms of analytical methods. The aim of this thesis is to have a better

knowledge on the surface chemistry and morphology of Al-Cu-Li alloys after exposition to thermal treatment, immersion in aggressive chloride solutions or chemical surface treatments. This PhD thesis is composed of three parts:

First, a surface characterization of Al-Cu-Li (AA2050-T8) before and after oxidation at 200 ◦C was carried out by in situ XPS measurement. The objective of this part was to look at surface modifications and kinetics of oxidation process of Al-Cu-Li alloys. Segregation of alloying elements induced by oxidation was evidenced by ToF-SIMS 3-dimentional chemical mapping (chapter 3)..

Second, the intermetallic particle induced pitting corrosion of AA2050-T8 (Al-Cu-Li) in NaCl electrolyte was studied by ToF-SIMS depth profiles, 2-dimentional and 3-dimentional chemical mapping combined with SEM were observed. The objective of this part was to investigate the mechanism of initial pitting corrosion and the surface modification of IMPs during pitting corrosion. The role of Li on pitting corrosion was also discussed (chapter 4).

The third part of this thesis is related to the surface modification of AA2050 (Al-Cu-Li) alloy during surface pretreatment and following TCP under standard industrial conditions. The objective of this part was to study the effect of surface pretreatment on the corrosion behaviour of TCP layer. The TCP conversion layer formed on both polished and pretreated surfaces were compared in order to understand the contribution of pretreatments on the structure of TCP coating. ToF-SIMS, XPS and SEM techniques were used to characterize the surface chemical structure and morphology of converted alloy. The corrosion performance was studied by electrochemical techniques (chapter 5).

Chapter 2

Techniques and sample preparation

This chapter describes the main characterization techniques, their working principle and the data analysis. The main chemical analysis techniques used in this thesis are X-ray photoelectron spectroscopy (XPS) and Time-of-Flight secondary ion mass spectrometry (ToF-SIMS). Surface morphology was investigated by optical microscopy and scanning electron microscopy (SEM). Electrochemical measurements were performed such as open circuit potential and linear sweep polarization. Moreover, the basic surface preparations of samples are also introduced. The experimental details are presented in the following chapters (chapter 3, 4, 5).

2.1 X-ray photoelectron spectroscopy

X-ray photoelectron spectroscopy (XPS) is an important technique for the surface characterization and analysis in terms of its elemental composition, chemical state of the elements, *etc*. It is generally regarded as being a good quantitative, readily interpretable, and informative with regard to chemical properties [109]. In the mid 1960s, Kai Siegbahn and his co-workers developed XPS which was originally called ESCA (Electron Spectroscopy for Chemical Analysis) and got the Nobel Prize in Physics for his contribution to the development of high-resolution electron spectroscopy. The mechanism at the origin of XPS is the photoelectric effect which emits electrons induced by irradiation of a material by electromagnetic radiation. This effect was discovered by Heinrich Hertz in 1883. Later, in 1905, Albert Einstein showed that the energy absorbed by the electron is quantified and that, if the energy is sufficient, the electron is ejected from the atom. Only the electrons emitted from the top 1–10 nm of the surface are detected due to the limited inelastic mean free path in the material which defines the XPS is a surface characterizing technique. A photoemission spectrum is obtained by recording the number of photo-emitted electrons over a range of electron kinetic energies (KE). The peaks appearing in the spectrum are due to atoms emitting electrons of characteristic energies and allow the identification and quantification of surface elements (except hydrogen and helium). A detection limits for most of the elements can be in the parts per thousand range. Moreover, XPS is suitable technique for several material such as organic and inorganic compounds, metal alloys, semiconductors, catalysts, papers, inks, medical implants, bio-materials, coatings except their hydrated forms.

Principle

The XPS analysis is based on the photoelectric effect induced by electromagnetic radiation shining a material. The exciting electromagnetic radiation (X-ray photon) is characterized by its energy calculated by the Planck-Einstein relation [110]:

$$E = h\nu \tag{2.1}$$

where h is the Planck constant (6.63×10^{-34} J s) and ν the frequency of the radiation.

When a material is irradiated by photons of energy $h\nu$, these latter can be absorbed and elec-

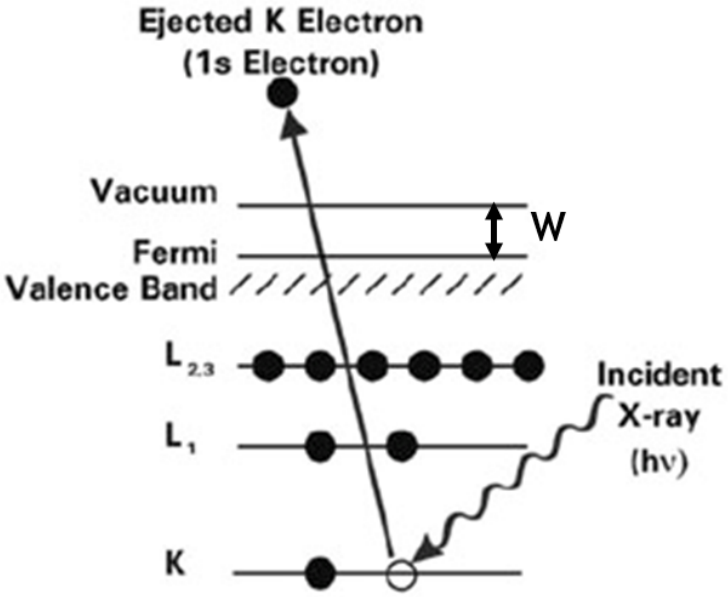

Figure 2.1: The photoemission process involved for XPS surface analysis [111]

trons with binding energy E_b can be ejected with a kinetic energy E_k. This process is called photoemission and the electrons emitted in this manner are called photoelectrons. A schematic representation of this process is shown in Fig. 2.1.

As is shown in Fig. 2.1, the KE of the photoelectron depends on the energy of the X-Ray photon ($h\nu$). If the solid state of material is taken into consideration, a work function (W), corresponding to the minimum energy required to extract the electron from the solid, may be defined as the difference between the vacuum level (E_V) and the Fermi level (E_F) of the material:

$$W = E_V - E_F \tag{2.2}$$

Therefore, the process equation is:

$$E_k = h\nu - E_b - W \tag{2.3}$$

In XPS measurements, if the electron kinetic energy is measured and the work function determined, then the binding energy of electrons in various state such as core and valence electrons can be calculated from KE and work function. Since every element has a unique electronic structure, the associated features in the XPS spectrum are also characteristic.

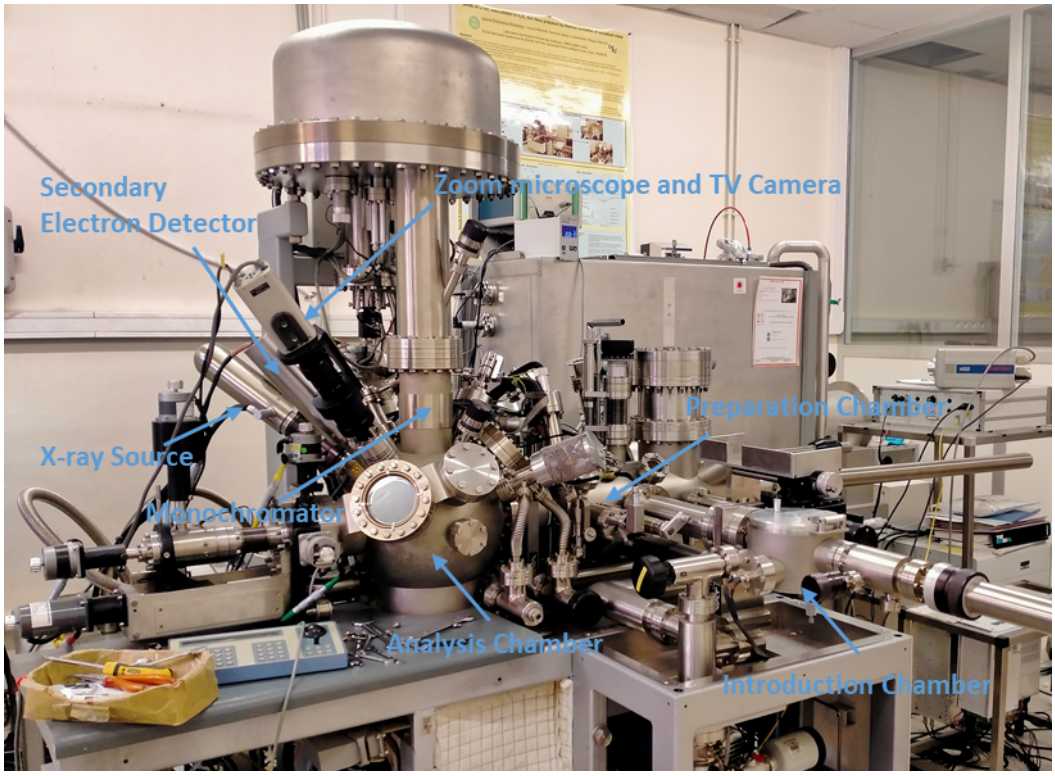

Figure 2.2: Photo of the ESCALAB250 spectrometer employed in this thesis (chapter 5)

Instrumentation

In this thesis, the experiments were carried using two different XPS spectrometers. One is the ESCALAB 250 spectrometer with an Al $K\alpha$ monochromated source ($h\nu = 1486.6$ eV) used for analysis presented in chapter 5. A zoom microscope and a TV camera were used to localize the samples and detection sites. The base pressure in analysis and preparation chambers was controlled at about 10^{-9} mbar. Survey spectra were recorded at a pass energy of 100 eV and a step size of 1 eV while high resolution spectra were recorded at a pass energy of 20 eV with a step size of 0.1 eV. The take-off angle of the analysed photoelectrons was 90°. The XPS spectra were recorded by Thermo Scientific Avantage Software (Version 5.954) and analysed by CasaXPS software (version 2.3.22) [112]. The experiment setup is shown in Fig. 2.2.

The second XPS spectrometer used in this thesis is a new platform which is a Scienta Omicron GmbH multi-chamber UHV system (base pressure $< 10^{-10}$ mbar) including a preparation chamber and two analysis chambers (used for and presented in chapter 3) . The experimental set-up is shown in Fig. 2.3. The preparation chamber is equipped with an Ar^+ cold cathode ion gun for sputtering and a resistive heating filament for thermal treatment. The temperature inside the pre-

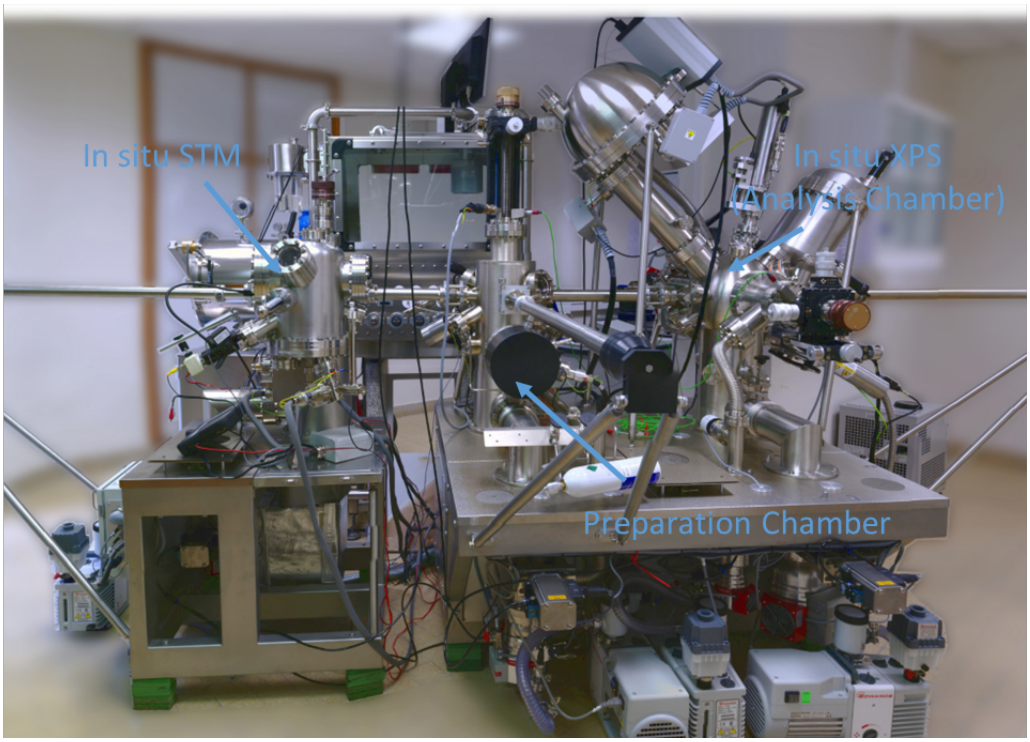

Figure 2.3: Scienta Omicron GmbH XPS set-up employed in this thesis (chapter 3)

paration chamber is controlled by a thermocouple. In-situ XPS measurements are possible with the spectrometer which equipped with 128 channels detector for high resolution and high counting speed. The implemented X-ray source is a monochromatic XM1000 MkII Al K_α (1486.6 eV). The pass energy for survey and high-resolution spectra were 50 eV and 20 eV respectively. The XPS spectra were recorded by Matrix software (Version 3.2) and analysed by CasaXPS software (version 2.3.22) [112]. The experimental details of XPS measurements are presented in chapters 3 and 5.

XPS Spectral Features

The XPS spectra consist of sharp peaks superimposed on the secondary electron background. Each photoemission peak of specific binding energy is corresponding to one electronic state of an element present on the surface [111].

At low energy resolution (survey spectrum), qualitative and quantitative information on the elements present are obtained. To precisely investigate the chemical state and bonding of these elements, high-resolution core-level spectra are measured for each present element. The core-level spectra compared to survey spectrum has improved chemical selectivity with its narrow energy range, lower spectral background and noise. Those spectra provide information like binding en-

ergy, Auger parameter, chemical shift, full width of half maximum (FWHM), *etc.*, which indicate the relative amount of each element and its chemical state.

Each binding energy indicates the unique electronic structure of an element. Therefore, BE database is established to recognize and characterize the specific element. For example, the binding energy of Cu $2p_{3/2}$ in metallic state is 932.6 eV. However, if the Cu is oxidized into Cu^{II}, the peak of Cu 2p shifts to the higher binding energy (around 933.5 eV). This shift of binding energy is induced by the change of local bonding environment of a species which is affected by its formal oxidation state [113]. More coulombic interaction between the photoelectron and the ion core happens. Normally, atoms with higher positive oxidation state have a higher BE.

Besides the core level peaks, another kind of structure namely Auger peak is also present in the XPS spectra. It represents the Auger electrons which are induced by ionization. When a photoelectron is ejected form a core level (K), leaving a vacancy, an electron from a higher energy level (L) may fall into the vacancy, resulting in a release of energy. The released energy can excite an outer shell electron (M) to emission. The ejected electron is called Auger electron and has a characteristic kinetic energy (E_{KLM}) depending on the energies of the three considered levels K, L and M. If the chemical state of an element is difficult to characterize by the core level peak position due to small chemical shift, more insight on the chemical analysis can sometimes be obtained by calculating the modified Auger parameter (α):

$$\alpha' = E_{\mathrm{KLM}} + E_b \tag{2.4}$$

where E_{KLM} is the KE of the Auger electron and E_b is the binding energy of the core level electron.

Taking Cu as an example, the BE of Cu$2p_{3/2}$ in metallic state is 932.6 eV which is very similar to that of Cu^{I}. If the KE of Cu $L_3M_{4,5}M_{4,5}$ is 918.6 eV then α' is 1851.2 eV and the chemical state is metallic. If the KE of Cu $L_3M_{4,5}M_{4,5}$ is 916.7 eV, the calculated α' is about 1849.4 eV and the chemical state is Cu^{I}.

Besides this, other typical peaks are also present on the XPS spectrum such as satellite or plasmons. They also provide information about the electronic structure of elements.

XPS quantitative analysis

XPS chemical analysis is both qualitative and quantitative. The quantitative analysis of XPS

data is based on qualitative spectra combined with a surface model. A layered oxide film model can be assumed to calculate the thickness and composition of the oxide film and the composition of the metal substrate as well. Therefore, fitting of peaks is applied firstly to decompose the peak into metal and oxide. A spectral background, a line shape, and a full width of half maximum (FWHM) have to be considered to fit the peak. The detail parameters will be given in each chapter. When the peak is fitted, the distribution of Al and other alloying elements among the oxide and metal substrate can be calculated from their intensity ratio ($I_{\mathrm{M}}^{\mathrm{M_{ox}}}/I_{\mathrm{M}}^{\mathrm{M_{met}}}$).

For oxide thickness and surface chemical composition, a set of equations based on the quantitative equation of XPS [114, 115] is defined:

$$I_{\mathrm{N}}^{\mathrm{M}} = kA(\beta)FT(E_k)\lambda_{\mathrm{N}}^{\mathrm{M}}\sigma_{\mathrm{N}}D_{\mathrm{N}}^{\mathrm{M}}(z)\int_d^{\infty}\exp\left(\frac{-z}{\lambda_{\mathrm{N}}^{\mathrm{M}}\sin\beta}\right)\,\mathrm{d}z \tag{2.5}$$

where k is the constant dependent of the spectrometer, $A(\beta)$ is the analysed area of the sample dependent of angle β, β is the take-off angle between the surface of the sample and the direction in which the photoelectrons are analysed. Similarly, F is the incident photon flux, $T(E_k)$ is the transmission factor of the analyser which depends on the KE of the analysed electron, $\lambda_{\mathrm{N}}^{\mathrm{M}}$ is the inelastic mean free path of the analysed photoelectrons of element N in matrix M, $D_{\mathrm{N}}^{\mathrm{M}}$ is the density of the element N in matrix M, σ_{N} is the photo-ionization cross section of element N for a given core level and finally d is the thickness of the layer.

For the metal substrate

$$I_{\mathrm{N}}^{\mathrm{M}} = kA(\beta)FT(E_k)\lambda_{\mathrm{N}}^{\mathrm{M}}\sigma_{\mathrm{N}}D_{\mathrm{N}}^{\mathrm{M}}\sin\beta\exp\left(-\frac{d}{\lambda_{\mathrm{N}}^{\mathrm{M}}\sin\beta}\right) \tag{2.6}$$

and for the oxide layer the integral will start from 0 to d, the thickness of the oxide layer:

$$\begin{aligned} I_{\mathrm{N}}^{\mathrm{M_{ox}}} &= kA(\beta)FT(E_k)\lambda_{\mathrm{N}}^{\mathrm{M_{ox}}}\sigma_{\mathrm{N}}D_{\mathrm{N}}^{\mathrm{M_{ox}}}\int_0^{d}\exp(\frac{-z}{\lambda_{\mathrm{N}}^{\mathrm{M}}\sin\beta})\,\mathrm{d}z \\ &= kA(\beta)FT(E_k)\lambda_{\mathrm{N}}^{\mathrm{M_{ox}}}\sigma_{\mathrm{N}}D_{\mathrm{N}}^{\mathrm{M_{ox}}}\sin\beta\left[1-\exp\left(\frac{-d}{\lambda_{\mathrm{N}}^{\mathrm{M}}\sin\beta}\right)\right] \end{aligned} \tag{2.7}$$

The oxide thickness can be determined by $I_{\mathrm{M}}^{\mathrm{M_{ox}}}/I_{\mathrm{M}}^{\mathrm{M_{met}}}$ which is the intensity ratio between the oxide peak and metal peak of the matrix, in our case Al 2s was used (Al 2p is also available).

For the oxide thickness:

$$d = \lambda_{\mathrm{M}}^{\mathrm{M_{ox}}} \cdot \ln\left[1 + \frac{I_{\mathrm{M}}^{\mathrm{M_{ox}}}}{I_{\mathrm{M}}^{\mathrm{M_{met}}}} \cdot \frac{\lambda_{\mathrm{M}}^{\mathrm{M_{met}}}}{\lambda_{\mathrm{M}}^{\mathrm{M_{ox}}}} \cdot \frac{D_{\mathrm{M}}^{\mathrm{M_{met}}}}{D_{\mathrm{M}}^{\mathrm{M_{ox}}}}\right] \tag{2.8}$$

$I_{\mathrm{N}}^{\mathrm{M_{ox}}}$, $I_{\mathrm{N}}^{\mathrm{M}}$ and $\frac{I_{\mathrm{N}}^{\mathrm{M_{ox}}}}{I_{\mathrm{N}}^{\mathrm{M_{met}}}}$ can be obtained by fitting the relevant peaks of M and N, then both oxide thickness and composition of surface can be calculated based on equation 2.6, 2.7 and 2.8.

2.2 Time-of-flight secondary ion mass spectrometry

Time-of-flight secondary ion mass spectrometry (ToF-SIMS) is a high sensitivity (ppb detection range for most elements) surface analytical technique with superior chemical selectivity (M / ΔM $\geq$ 10,000). ToF-SIMS was developed more recently than XPS. It was firstly completed in 1979 by Alfred Benninghoven at the University of Münster. With its imaging capability, ToF-SIMS is useful in various industry and scientific domains especially where both identification of chemicals and corresponding location are required. The lateral resolution of ToF-SIMS can achieve to $\leq$ 100 nm [116]. It is also capable for the depth profiling of organic, inorganic and metallic materials, which allows exploring chemical variability in the depth. However, due to time and cost limit, ToF-SIMS measurement is limited for the shallow surface region.

Principle

ToF-SIMS is an acronym for the combination of the analytical technique secondary ion mass spectrometry and time-of-flight mass analysis. First, a focused primary analyses beam of ions (typically Bi^+) is pulsed on a material surface with a kinetic energy in the magnitude of keV resulting in a collision cascade inside the material and the emission of various secondary particles, such as electrons, neutral species, atoms and molecules present on the surface. The secondary ions species analysed in ToF-SIMS are emitted from the first 2–3 monolayers and are characteristic of the surface composition. Typically, Cs^+ or Ar^+ is used to sputter away the surface layer for measurement. The ToF-SIMS working principle is illustrated in the Fig. 2.4.

When the secondary ions are emitted out of the surface, they are accelerated under an electric field (U) and enter the time-of-flight mass analyser. Based on this principle, the KE of the secondary

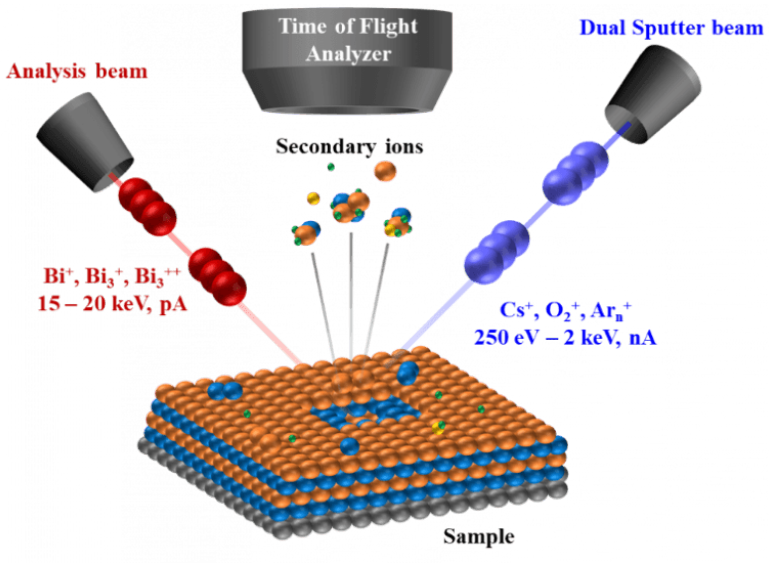

Figure 2.4: Schematic diagram of ToF-SIMS process [117]

ions can be expressed as:

$$E_k = qU = \frac{1}{2}mv^2 = \frac{1}{2}m\frac{L^2}{t^2} \tag{2.9}$$

where q is the charge of the secondary ion, U is the applied potential, m is the mass of the secondary ion and v its speed. The measured time-of-flight (t) is linked to the mass of the ions according to the relation:

$$t = L/v = L \times \sqrt{\frac{m}{2qU}} \tag{2.10}$$

with L the length of flight. Therefore, ions can be sorted by the analyser as a function of their mass/charge ratio. The mass resolution is propotional to the time resolution:

$$R = \frac{m}{\Delta m} = \frac{t}{2\Delta t} \tag{2.11}$$

ToF-SIMS allows different analytical modes. In this work, depth profiling, 2-dimensional (2D) imaging and 3-dimensional (3D) imaging were used for surface analysis. Depth profiles indicates the general chemical structure of surface in depth, 2D imaging provides the lateral distribution of elements and 3D imaging presents both in-depth and lateral distribution of elements in a 3D version.

Instrument

In this work, a ToF-SIMS V spectrometer (ION TOF GmbH-Münster, Germany) presented in

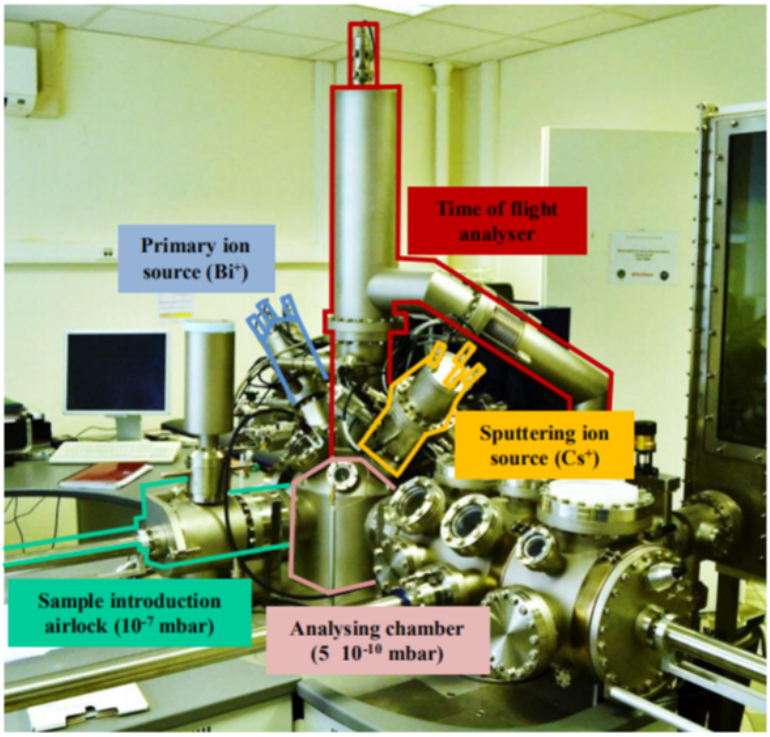

Figure 2.5: Photo of the ToF-SIMS spectrometer used in this thesis

Fig. 2.5. The ToF-SIMS V spectrometer consists of a pulsed primary Bi ion gun, a sputtering Cs ion gun, a highly accurate computer clock, a flight tube and a ToF mass analyser. An Ar gas filled glove box is connected with the transfer chamber of the spectrometer for the sample transfer without exposure to air. The analysis was performed under 10^{-9} mbar ultra high vacuum (UHV) environment. The working conditions such as the energy of primary and sputtering beams are adjusted according to the experiment objectives. The details for all ToF-SIMS analysis performed in this thesis are presented in chapter 3, 4, 5 (experimental parts).

2.3 Microscopic technology

Scanning electron microscopy (SEM), energy dispersive X-Ray spectroscopy (EDX) are commonly used as surface characterization techniques for both morphology and chemical analysis.

During SEM measurement, sample surface is scanned by a focused electron beam. These electrons interact with the material producing various signals which reveal plenty of information including surface morphology, chemical composition and crystalline structure [118]. Usually, the magnification is between 20$\times$ and 30,000$\times$ and the spatial resolution can reach 100 to 50 nm.

For different experiment objectives, different signals were collected and presented in the form of images such as secondary electron image (SEI) and backscattered electrons image (BEI). Both of them are used for the surface analysis. Since secondary electrons have a smaller penetration depth and higher resolution than backscattered electrons, SEI image reflects the topography of surface better than BEI. However, to obtain the information on chemical heterogeneities such as intermetallic particles, BEI is a better choice than SEI.

During EDX measurement, samples are excited by the incident beam resulting in electrons emission from an inner shell of the atoms producing a vacancy. An electron from an outer shell then fills the hole. The difference in energy is released in the form of an X-ray (fluorescence) and measured by an energy-dispersive spectrometer. Since the energies of the X-rays are characteristic of the atomic structure, EDX allows the elemental composition of the specimen to be measured but the detected depth can be 1 µm so the surface sensitivity is low. SEM and EDX measurement presented in this thesis were performed on a digital SEM S440 LEICA with tungsten filament (FEG-SEM).

2.4 Electrochemical methods

Electrochemical measurements such as open circuit potential (OCP) and potentiodynamic polarization using linear scan voltametry were performed on the sample in order to study the corrosion behaviour of samples. 0.1 M NaCl electrolyte prepared with NaCl (VWR, 99.9%) and UP Millipore® water (resistivity $\leq$ 18 MΩ cm) was used as corresponding aggressive chemical environment. The electrochemical measurements were performed by means of a Reference 600 potentiostat (Gamry) using a 3-electrodes electrochemical cell: AA2050-T8 Al-Cu-Li alloy as a working electrode, platinum wire as a counter electrode and a saturated calomel electrode (SCE) as a reference electrode. Detailed experiment procedure for polished surface or chemical treated surfaces is given in the corresponding chapters (chapter 4, chapter 5).

2.5 Sample preparation

The specifications of AA2050-T8 (in wt.%) is presented in Table 1.2. T8 process indicates the corresponding process of alloys manufacturing which includes solution heat treatment (470–530 °C), cold working and artificial ageing (155 °C) for about 17–18 h [19, 119]. The alloy used in this study was provided by Constellium, France [120]. The specimens were cut into 8.0 mm$\times$8.5 mm samples. The sample surface preparation was varied based on the different experimental objectives. In this section, only the fundamental mechanical surface preparation are introduced.

Mechanical surface preparation was performed by polishing with SiC paper from 320 to 4000 grades then by mirror polishing with alumina suspension down to 0.3 µm. After polishing, samples were cleaned by successive ultrasonic baths in iso-propanol, ethanol and finally Millipore water (resistivity $\geq$ 18 M$\Omega\times$cm) for 2 min for each step then dried by filtered compressed air.

The other sample preparations, for example, thermal treatment (chapter 3), electrochemical/corrosion (chapter 4) and the chemical treatment (chapter 5) performed in this thesis are introduced in each chapter.

Chapter 3

Effect of thermal oxidation on surface chemistry and elemental segregation of Al-Cu-Li alloy

This chapter reproduced the accepted version of an article published in Applied Surface Science with the reference:

Li M, Wiame F, Seyeux A, Marcus P, Światowska J. Effect of thermal oxidation on surface chemistry and elemental segregation of Al-Cu-Li alloy. Applied Surface Science.p.147633 (2020), doi: https://doi.org/10.1016/j.apsusc.2020.147633

Abstract

The thermal stability of Al-Cu-Li alloys is critical for the extreme working conditions encountered in the aircraft industry. In this paper, the initial stages of thermal oxidation of an industrial AA 2050-T8 Al-Cu-Li alloy were investigated by in situ XPS and ToF-SIMS.

Annealing of the sample at 200 °C before oxidation leads to a surface enrichment in metallic Li and Ag. When exposed to oxygen at low pressure ($P_{O_2} \leq 10^{-6}$ mbar) a mixed Li-Al oxide layer is formed. Photoemission intensities recorded at emission angles of 45° and 90° relative to the surface are both consistent with the formation of a continuous oxide layer for oxygen exposure from 0 to 5000 langmuirs. Assuming a homogeneous composition of the oxide layer, its thickness was calculated to be 9 $\pm$ 1 Å at 5000 langmuirs. The relative content of Li and Al in the oxide layer evolves from an initial value of 50 % to stabilize at 70 % of Li above 100 langmuirs of oxygen exposure. At the same time, the content of Li at the metal substrate surface is reduced from 10 % to 0 %. Moreover, specific segregation sites are evidenced by ToF-SIMS three-dimensional chemical mapping. For Li, a surface homogenous surface distribution while for Mg the accumulation at the grain boundaries were observed. The segregation of Ag induced by thermal treatment at the oxide/alloy interface was confirmed by ToF-SIMS.

3.1 Introduction

The service life and quality of aircraft is constantly increasing with strong effort to improve materials properties. A balance between advanced mechanical properties and corrosion resistance is always strived. In this context, Al-Cu-Li alloys appear as a promising material for aerospace industry applications. The presence of Li can indeed reduce the weight and improve the mechanical properties to a significant extent [1, 5, 6].

Al-Cu-Li alloys as potential material to replace the conventional Al alloys, were investigated in terms of their thermal stability, corrosion resistance and mechanical properties [7, 121, 122]. The good thermal stability and mechanical properties of different Al alloys including Al-Cu-Li alloys applied in fuselages or wing structures were observed in temperatures between 70 °C and 85 °C and up to 1000 h. The studies focused on the behaviour of Al alloys at higher temperatures (120–

300 °C) revealed that the fracture toughness and the yield strength of Al-Li alloys are comparable to the conventional Al-Cu alloys. Although strength and hardness of Al-Li alloys decreases with higher temperature and longer exposure time, they stay relatively stable up to 200 °C for a relatively short period of time ($<$ 300 h) [20, 123, 124].

Several studies about the thermal stability focused on the variation of microstructure and corresponding mechanical properties [20, 125, 126]. Balducci *et al.* [20] and Liang *et al.* [21] investigated the thermal effect on T1(Al_2CuLi) phase, which is the main strengthening precipitates in AA2099 Al-Cu-Li alloy and model Al-3.5Cu-1.5Li-0.22(Sc+Zr) alloy. It was shown that although T1 phase tends to coarsen under overaging at medium-high temperatures (200 °C) and leads to a decrease of hardness and tensile strength, it still exists up to around 300 °C with the strengthening effect while other strengthening precipitates such as θ and S phase dissolves at the same temperature. Therefore, these authors concluded that T1 phase shows a superior thermal stability and supports the strength and hardness of Al-Cu-Li alloy when exposed to higher temperatures. However, Chen *et al.* [127] demonstrated that T1 phase in AA2189 dissolves when the temperature reaches 300 °C and a dramatic drop in strength occurs at the same time.

Besides the change of microstructure and corresponding mechanical properties the distribution of alloying elements can also be influenced by the heat treatment. For example, surface segregation of Li is a typical phenomenon observed in most of annealed Al-Li alloys. Partridge *et al.* [25] studied the influence of high temperature treatment (530 °C) on the Li distribution and surface microstructure of AA8090 Al-Cu-Li alloy by secondary ion mass spectrometry (SIMS) and scanning electron microscopy (SEM). They showed that a thin Li enriched oxide layer is rapidly formed (in 1 min) leading to a hardness reduction of the near-surface region (up to 800 µm).

Several studies proved the segregation of Li in Al-Li alloys under heating treatment (120 °C to 600 °C) [22–24]. Moreover, Lee *et al.* [23] and Kim *et al.* [24] indicate that a surface reconstruction can be induced by the Li enrichment, resulting in an enhanced oxidation rate of the Al alloys. Mg, as another alloying element in Al-Cu-Li alloys can also segregate on the surface under high temperature treatment. As introduced by Lea *et al.* [26], the Mg inside Al-Mg alloys (AA5657 and AA5252) can segregate at 100 °C and even evaporate over 200 °C. Saied *et al.* [27] found a linear relation between the amount of Mg segregation in 1 % Mg/Al alloy and the temperature and

suggested that the Mg enrichment is chemically promoted by the presence of oxygen due to the high oxygen affinity of Mg. Moreover, Song *et al.* [29–31] evidenced, by in situ scanning Auger microprobe, the Mg segregation along the grain boundaries at 155 °C in AA7175 or AA7075, two typical Al-Zn-Mg alloys. This phenomenon has an important effect on the intergranular corrosion (IGC), stress corrosion cracking (SCC) and hydrogen embrittlement (HE) [28–31]. The evolution of surface chemical structure is especially important considering the aircraft application because surface of Al alloy is responsible for the structure breakdown of aircraft [128–131]. However, according to our knowledge, few studies on the surface chemical analyses of thermal treated Al alloys, especially Al-Cu-Li alloys, have been reported till now. Therefore, to better understand the oxidation process and most particularly the chemical composition of the surface, the oxide layer structure and behaviour of each alloying elements are important for the further development of Al alloys.

In this work, in situ X-ray photoelectron spectroscopy (XPS) and time-of-flight secondary ion mass spectrometry (ToF-SIMS) three-dimensional (3D) imaging were performed in order to study the surface chemical composition of an industrial AA2050-T8 (Al-Cu-Li) alloy under medium-high temperature (200 °C) with controlled oxygen exposure. Firstly, the clean AA2050-T8 surface was prepared by successive sputtering and annealing. Then, the real-time evolution of photoelectron spectrum of oxygen was measured by in situ XPS during oxygen exposure to evidence the oxidation kinetics. Afterwards, high-resolution spectra of O 1s, Al 2s, Cu 2p, Li 1s, Ag 3d and CuLMM were recorded at specific exposures to study the surface chemical modifications. After the final oxidation stage (5000 langmuirs (L), 200 °C), the sample was transferred into a ToF-SIMS spectrometer to study the oxide structure and lateral distribution of alloying elements by 3D analysis. The mechanism of oxidation of the alloy under medium-high temperature and the evolution of oxide were revealed. Different segregation behaviours of alloying elements was in-depth and laterally evidenced.

Table 3.1: Specifications of alloying element (wt% & at%) of the AA2050 alloy

Cu	Li	Mg	Zn	Mn	Ag	Zr(max)	Fe(max)	Si(max)
3.2–3.9	0.7–1.3	0.2–0.6	0–0.25	0.2–0.5	0.2–0.7	0.14	0.1	0.08
1.5–1.6	2.8–4.8	0.2–0.7	0–0.1	0.1–0.2	0.05–0.1	0.04	0.04	0.07

3.2 Experimental

In this study, an industrial AA2050-T8 Al-Cu-Li alloy was used. T8 process includes solution heat treatment (470–530 °C), cold working and artificial ageing (155 °C) for about 17 h [19, 119]. The chemical composition of the AA2050-T8 used in this work is presented in Table 3.1.

Before introduction into ultra-high vacuum (UHV), the sample was mechanically polished with SiC paper to 4000 grades and mirror polished with alumina suspension down to 0.3 µm. The sample was cleaned by successive ultrasonic baths in isopropanol, ethanol and UP Millipore water (resistivity $\geq$ 18 M$\Omega\times$cm) and finally dried by filtered compressed air.

The polished sample was transferred into a multi-chamber UHV system (base pressure: 10^{-10} mbar) including a preparation chamber and an analysis chamber. The preparation chamber is equipped with an Ar^+ cold cathode ion gun for sputtering and a resistive heating filament for thermal treatment. The temperature is controlled by a thermocouple. Cycles of Ar^+ ion sputtering (3 keV, 4 µA, 10 min) and annealing (250 °C, 1 h) were performed on the polished surface to remove the contamination and native oxide at the surface. The prepared surface was transferred into the analysis chamber for in situ XPS measurement. XPS spectra were recorded by an Argus spectrometer with 128 channels for high resolution and counting speed and a monochromatic XM1000 MkII Al Kα X-ray source (1486.6 eV) (Scienta Omicron GmbH).

For oxidation, gaseous O_2 (99.999% pure) was introduced via a leak valve. The oxidation was performed at 200 °C and oxygen pressure was adjusted from 10^{-8} to 10^{-6} mbar in order to ensure the precision and efficiency of the initial oxidation within 100 langmuirs (1 L = 10^{-6} Torr.s) and the later progress to 5000 L. The oxygen pressure was recorded as a function of time to calculate the exact oxygen exposure. In situ XPS real-time measurements were performed at the same time using Snapshot detection mode with 60 eV pass energy (E_{pass}). O 1s spectrum was recorded at 45° take-off angle every 10 s during oxidation in order to follow the variation of oxygen peak intensity.

A series of survey and high-resolution spectra for selected exposures were carried out based on the in situ kinetics results in order to investigate in details the surface evolution. The E_{pass} for survey and high-resolution spectra were 50 eV and 20 eV, respectively. Four oxygen exposures were selected in the initial oxidation range (0 L, 10 L, 50 L, 100 L) and three more at the later oxidation stages (500 L, 1500 L and 5000 L). Survey and high-resolution spectra of Al 2s, Cu 2p, Li 1s, Ag 3d, Cu LMM and O 1s were recorded after each oxygen exposure. Al 2p was not selected due to its superposition with Cu 3p. Both take-off angles at 45° and 90° were recorded in order to determine the distribution of each species in depth. Fermi edge position was measured as a reference energy for all XPS spectra. XPS data analyses were performed using the CasaXPS software (version 2.3.22) [112]. Fitting of Al 2p and Li 1s was performed for each selected oxygen exposure and the accuracy of parameters was ensured by imposing a set of constraints determined from self-consistency of the fitting procedure. Symmetric mixed Gaussian-Lorentzian line shapes were used for fitting oxide species, and Gaussian-convoluted asymmetric Lorentzian line shapes were used for the metallic components. The background was taken into account by a Shirley profile. The errors on peak areas were estimated by varying the fitting parameters within a small range around the constrained values.

After the final stage of thermal oxidation (5000 L, 200 °C) and XPS characterization, the sample was transferred, in an air-tight Ar-filled cell, into a ToF-SIMS spectrometer (Ion-ToF GmbH). Measurements were operated at high vacuum (10^{-9} mbar). The spectrometer was used in dual beam mode, meaning that pulsed Bi^{+} and Cs^{+} beams (primary ion beam and sputtering beam, respectively) are used, to acquire 3D analysis. 3D chemical imaging and ToF-SIMS ion depth profiles retrieved from 3D chemical mapping allowed to study the lateral distribution of the alloying species in the oxide and the in-depth chemical structure of the oxide, respectively. ToF-SIMS 3D imaging was performed in BA-IMAGE mode (lateral resolution $\sim$ 200 nm) by using a 500 eV Cs^{+} beam delivering a 30 nA current at 45° for sputtering and a 25 keV pulsed primary Bi^{+} beam (in which each pulse is splitted into 4 smaller pulses to get sufficiently high mass resolution m/Δm around 6000) delivering 0.2 pA for analyzing. The sputtered area was 300 µm $\times$ 300 µm and the analyzed area was 100 µm $\times$ 100 µm. ToF-SIMS data treatment was performed with Ion-Spec software.

The exact mass values of at least five known species were used for calibration of the data acquired in the negative ion mode which is more sensitive to the oxide species.

3.3 Results

Oxidation kinetics by in situ XPS

After preparation by sputtering and annealing cycles, the surface chemical composition was analyzed by XPS. The atomic percentage of the sputtered surface (before the final annealing) is 94 % Al, 2.9 % Cu and 0.1 % Ag. It is different from that of the bulk material because some Ar (2.5 %) is detected after sputtering and small amount of O (0.3 %) remains on the surface. The amount of Li in bulk material is low as shown in Table. 3.1. However, since the ionization cross section of Li is small, XPS is not sensitive to Li. Therefore, the signal of Li is undetectable in this case.

The sputtered surface of the Al-Cu-Li alloy was then annealed at 200 °C and exposed to oxygen at this temperature. Fig. 3.1 presents the evolution of normalized O 1s intensity as a function of oxygen exposure. Two regions can be distinguished from the kinetic curve. A rapid increase of O 1s was observed at the oxidation initiation (0–500 L). Later, the O 1s intensity increases more slowly, and stabilizes during the further oxidation (500–5000 L). No oxidation saturation was observed till 5000 L exposure.

To investigate these two behaviours, XPS survey and high-resolution spectra were recorded at selected oxygen exposures: 0 L, 10 L, 50 L, 100 L for initial oxidation and 500 L, 1500 L and 5000 L for the further oxidation.

Evolution of surface composition during oxidation by in situ XPS

The surface was re-prepared by the procedure described previously and heated at 200°C during oxidation. Fig. 3.2 shows XPS high-resolution spectra of O 1s, Al 2s, Li 1s, Ag 3d5/2, Cu 2p3/2 and Cu LMM for increasing oxygen exposures. As shown in Fig. 3.2 (a), the area of O 1s peak located at 532.2 $\pm$ 0.2 eV BE with 2.1 $\pm$ 0.1 eV full width at half maximum (FWHM) increases with increasing oxygen exposure. Since O 1s represents to the oxide component therefore less or no conduction electron is available for the shake-up of peak and the O 1s peak is supposed to be

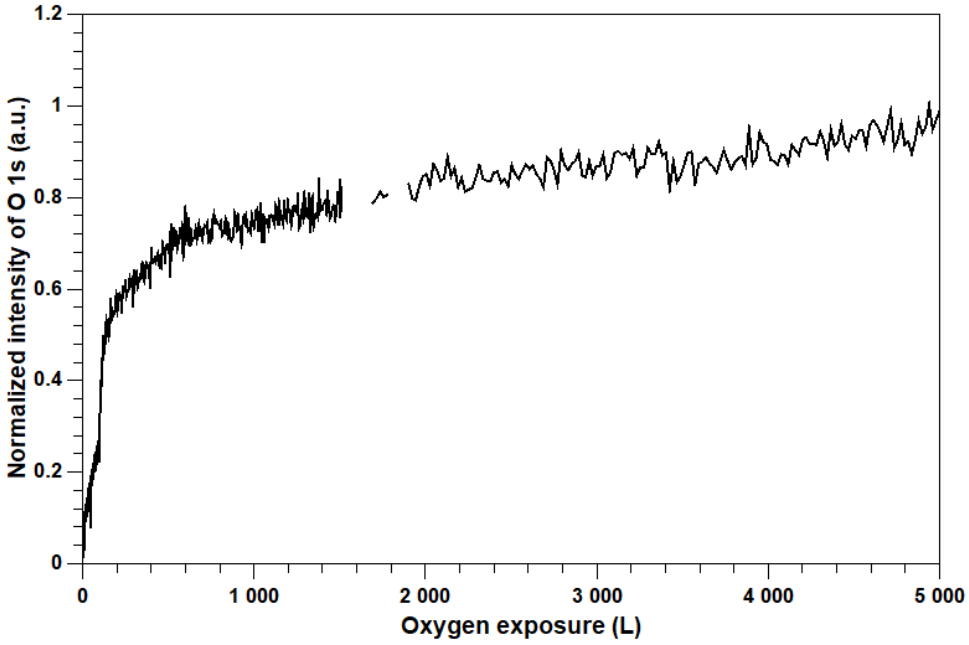

Figure 3.1: Real-time normalized area of O 1s peak as a function of oxygen exposure on AA 2050 Al-Cu-Li alloy at 200 °C

symmetric. However, the line shape of O 1s peak is asymmetric which could indicate that the O 1s peak is composed of different oxide species.

In Fig. 3.2 (b), the Al 2s is decomposed into 2 peaks which are corresponding to Al metal (118.3 $\pm$ 0.1 eV BE, 1.2 $\pm$ 0.02 eV FWHM) and Al oxide (120.1 $\pm$ 0.1 eV BE, 2.3 $\pm$ 0.2 eV FWHM). Cu 3s (122.1 $\pm$ 0.1 eV BE, 2.4 $\pm$ 0.4 eV FWHM) is found at the same region and has been considered in the fitting. The peak area of Cu 3s is consistent with that of the Cu 2p. With increasing oxygen exposure, the Al oxide peak is increasing while the intensity of Al metal peak is significantly reduced obviously after 1500 L.

According to Fig. 3.2 (c), no Li was observed after sputtering. However, after annealing at 200 °C (0 L) a trace of Li was detected at 56.0 $\pm$ 0.1 eV BE (2.4 $\pm$ 0.4 eV FWHM). This indicates that even in absence of oxygen exposure, a surface segregation of Li ($\leq$ 0.5 at%) occurred during annealing at this temperature. The content of oxygen was extremely low on the annealed surface before oxygen exposure. Therefore, the main composition of Li can be considered as metallic. After exposure to oxygen (from 10 L) a second component, assigned to Li oxide, appears at 57.2 $\pm$ 0.1 eV (3.5 $\pm$ 0.5 eV FWHM) and increases with the increasing oxygen exposure. The continuous

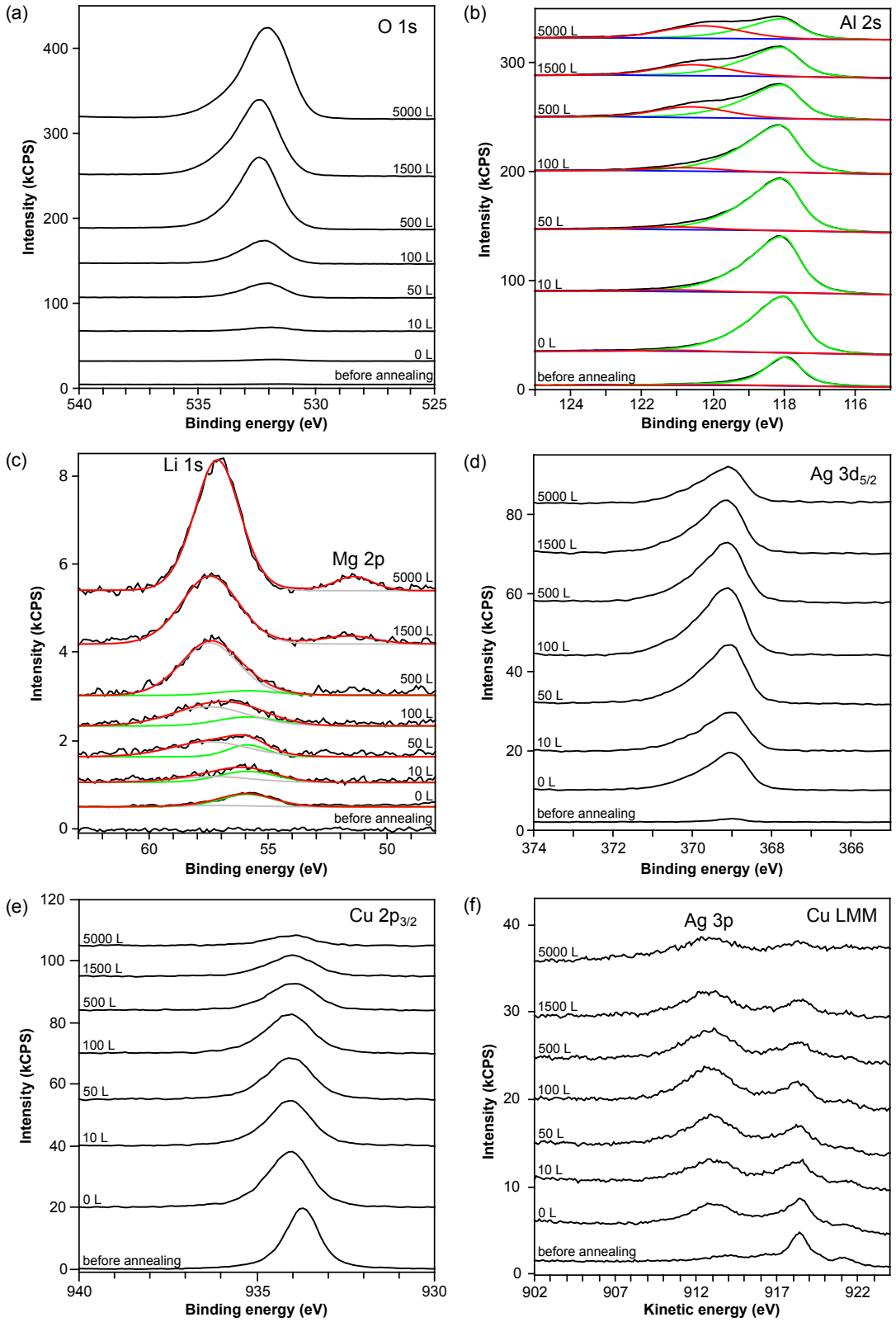

Figure 3.2: Evolution of high-resolution XPS spectra of each element for different oxygen exposure at 200 °C (a) O 1s, (b) Al 2s, (c) Li 1s, (d) Ag $3d_{5/2}$, (e) Cu $2p_{3/2}$, (f) Cu LMM

increase of the Li 1s peak area indicates that Li diffuses to the surface during thermal oxidation. When the oxygen exposure reaches 1500 L, another peak closed to Li 1s shows up at lower BE which is assigned to Mg 2p (51.4 $\pm$ 0.1 eV, 2.2 $\pm$ 0.3 FWHM).his peak indicates that a surface segregation of Mg happens during oxidation at 200 °C ($\leq$ 1%). However, differently to Li, no segregation of Mg was observed on the annealed surface before introducing oxygen. So, oxygen is supposed to play an important role in the surface segregation of Mg, which will be explained here after in the section 3.4.

From the evolution of Ag 3d spectra, presented in Fig. 3.2 (d), a significant signal of Ag $3d_{5/2}$ (369.2 $\pm$ 0.2 eV BE, 1.4 $\pm$ 0.1 eV FWHM) is observed at 0 L. It indicates that a Ag surface segregation occurs during heating at 200 °C similarly to Li. However, the highest intensity of Ag 3d peak is observed at 100 L then it decreases with increasing oxygen exposure till 5000 L. Moreover, the line shape, width and position of Ag 3d during the oxidation are the same as before oxidation indicating that the chemical state of Ag does not change and remains in the metallic state during the whole process of thermal treatment.

As observed in Fig. 3.2 (e), the area of Cu $2p_{3/2}$ peak (934.0 $\pm$ 0.1 eV, 1.6 $\pm$ 0.1 eV FWHM) is decreasing during oxygen exposure and the FWHM increases from 1.5 eV to 1.7 eV. The broadening of the peak could indicate oxidation of Cu. However, it is difficult to decompose the spectrum into two components corresponding to the oxide and metallic copper since their very close BE. Usually, Cu LMM is used to identify the chemical states of Cu.

As shown in Fig. 3.2 (f), the Auger feature located at 918.0 $\pm$ 0.2 eV kinetic energy (KE) is attributed to metallic Cu. However, after heating at 200 °C, a new peak at 574.1 eV $\pm$ 0.4 eV BE (912.5 $\pm$ 0.4 eV KE) corresponding to Ag $3p_{3/2}$ shows up. Although Ag $3p_{3/2}$ partially overlaps Cu Auger peaks, the metallic signature of Cu is still observed till 5000 L. This indicates that Cu remains metallic during oxidation even the Cu 2p shows a BE shift. This displacement of Cu 2p peak position indicates the change of chemical environment of Cu atoms, which can be due to the surface modification by Ag and Li segregation. However, we cannot fully exclude the presence of some Cu oxide partially hidden by the Ag $3p_{3/2}$. The intensity of metallic Auger feature (Fig. 3.2 (f)) decreases during oxidation in agreement with the Cu 2p decrease, which could be explained by the presence of some oxides leading to attenuation of Auger and Cu 2p signals.

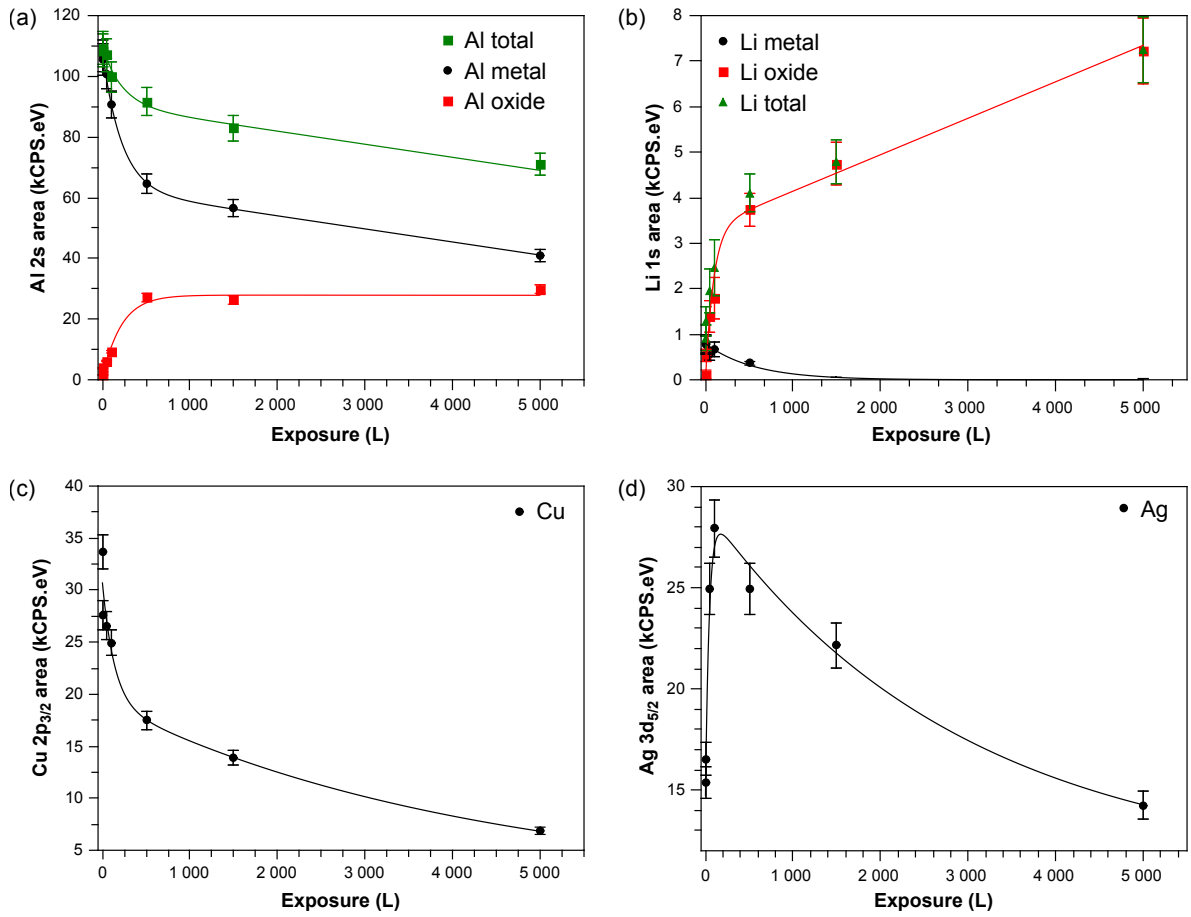

Figure 3.3: Intensity evolution of XPS components as a function of oxygen exposure at 200 °C: (a) Al 2s, (b) Li 1s, (c) Cu $2p_3/2$ (d) Ag $3d_{5/2}$

Fig. 3.3 presents the intensity evolution of the components in Al 2s and Li 1s and of Ag $3d_{5/2}$ and Cu $2p_{3/2}$ peaks as a function of oxygen exposure. The evolution of Al 2s components is presented in Fig. 3.3 (a). The total intensity of Al decreases with oxygen exposure. Al metal is continuously decreasing during oxidation while the area of Al oxide increases continuously from 0 to 500 L then stabilizes at about 27 kCPS.eV.

As presented in Fig. 3.3 (b), the intensity of metallic Li decreases from 0.8 kCPS.eV at 0 L to 0.4 kCPS.eV at 500 L. When the exposure reaches 1500 L, the metallic Li component drops to almost zero. The intensity of Li oxide is initially much lower (close to 0) compared to metallic Li but increases rapidly once oxygen is introduced. The evolution of the total Li and of Li oxide are similar with the oxygen uptake curve (Fig. 3.1). A continuous increase of Li 1s can be observed from 0.9 kCPS.eV to 7.2 kCPS.eV during oxidation which indicates that the segregation of Li is going on during oxidation at 200 °C.

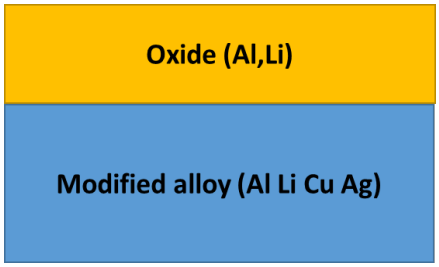

Figure 3.4: Layered model for composition calculation

According to Fig. 3.3 (c), a converse evolution was observed in the intensity of Cu. A rapid decrease occurred during initial oxidation (0–500 L) from 34 kCPS.eV to 25 kCPS.eV followed by a slower decrease till 7 kCPS.eV at 5000 L.

Intensities of most elements are monotonically increasing or decreasing during oxidation but a different behaviour is observed for Ag 3d spectra as shown in Fig. 3.3 (d). Initially, the intensity of Ag $3d_{5/2}$ increases from 0 L (15 kCPS.eV) to 100 L (28 kCPS.eV), then it starts to decrease with increasing exposure till 5000 L (14 kCPS.eV). The increase of intensity is assigned to the segregation of metallic Ag to the alloy surface as mentioned previously while the decrease after 100 L indicates that besides the effect of segregation, other competing processes influence the Ag intensity. One of these could be the attenuation of the Ag signal by a layer growing above. Indeed, the comparison of the spectra recorded at 45° and 90° emission angle confirms the fact that the metallic Ag is located below the surface.

The fast decrease of the metallic components associated with the fast increase of the oxide components between 0 L and 500 L is consistent with a model of continuous mixed Al and Li oxide layer growing on top of a modified alloy as shown in Fig. 3.4. Based on this model, a quantitative analysis of the layer thickness and surface composition [114, 132]. The oxide thickness is estimated from the intensity ratio between the attenuated Al 2s metallic component and the increasing oxide component. The chemical composition of oxide and modified alloy are calculated from the intensity of oxide peak (Al, Li) and metal peak (Al, Li, Cu, Ag) respectively. The calculated oxide thickness is presented in Fig. 3.5 (a) and the composition is shown in Fig. 3.5 (b–d).

From Fig. 3.5 (a), two regions can be distinguished from the thickness evolution of oxide layer: from 0 L to 500 L, the oxide equivalent thickness increased from 0.20 $\pm$ 0.05 Å to 5.5 $\pm$ 0.6 Å at

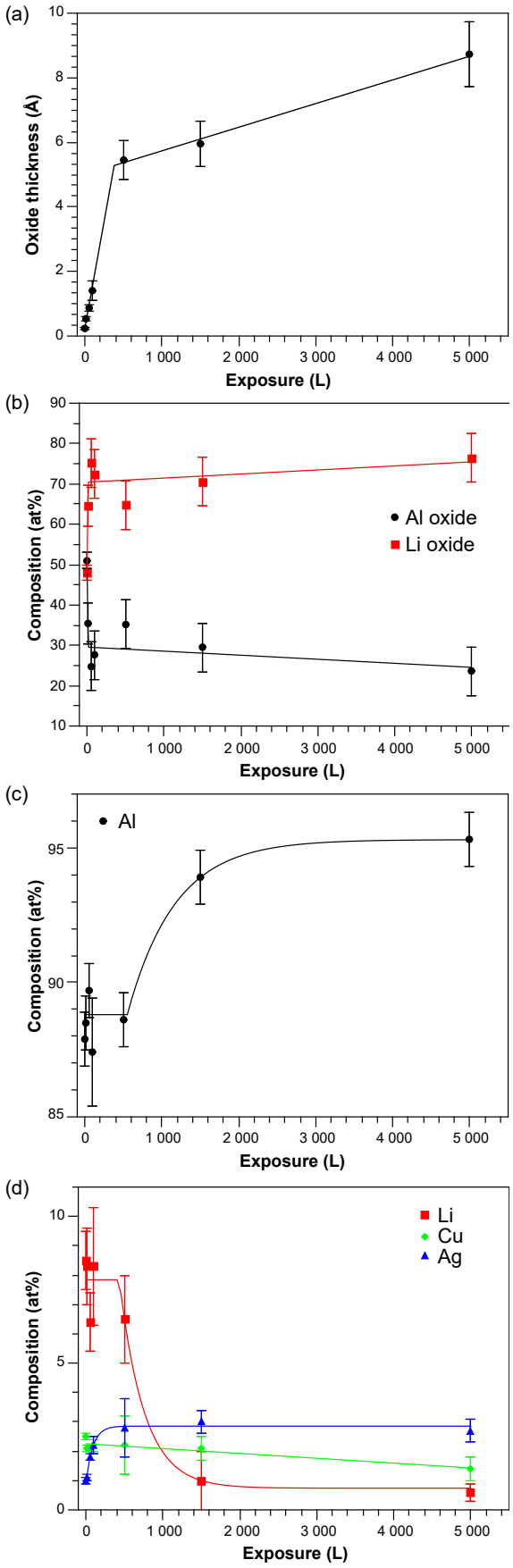

Figure 3.5: (a) calculated oxide thickness based on the layered model, (b) variation of the relative concentrations of compounds in the oxide phase as a function of O_2 exposure, (c) variation of the relative concentrations of Al in metal substrate as a function of O_2 exposure, (d) variation of the relative concentrations of alloying elements in metal substrate as a function of O_2 exposure

about 0.01 Å/L and from 500 L to 5000 L, the oxide thickness increased from 5.5 $\pm$ 0.6 Å to 9 $\pm$ 1 Å at a growth speed of about 0.0008 Å/L which is 100 times slower than that of initial oxidation.

Fig. Fig. 3.5 (b) shows the evolution of the atomic composition of the oxide layer. Once the oxygen was introduced, the ratio of oxidized Li increased from 50 at% to 65 at% at 10 L. Then, the composition of the oxide stayed relatively stable and the ratio of Li to Al atoms is 30 at% Al versus 70 at% Li. As shown in Fig. 2 (c), Mg 2p presents at 1500 L and increases during oxidation. The Mg oxide is not taken into account the oxide composition due to its very low content compared to Li oxide and Al oxide (about 0.2 % at 5000 L).

Fig. 3.5 (c) shows the atomic content of Al in the modified alloy. From 0 L to 500 L, the composition of metallic Al is relatively stable at 88 $\pm$ 2 at%. But after 500 L exposure, the composition of metallic Al increases to about 94 $\pm$ 1 at% and stays stable till 5000 L. This difference in Al composition is induced by the decrease of metallic Li during oxidation. As observed in Fig. 3.5 (d), an obvious decrease of concentration of metallic Li is found between 500 L to 1500 L from 7.5 $\pm$ 2.5 at% to 1 $\pm$ 1 at%. Therefore, a certain proportion (about 7.5 $\pm$ 2.0 at%) of metallic Li in the modified alloy is replaced by other elements such as Al after longer exposure.

The evolution of Ag and Cu composition in the modified alloy is also presented in Fig. 3.5 (d). An increase of Ag concentration can be observed form 0 L ($\sim$ 1 at%) till 100 L ($\sim$ 2 at%) then become relatively stable after 500 L exposure ($\sim$ 3 at%). The concentration of Cu in the modified alloy is relatively stable at about 2 at% until 1500 L, then it slowly decreases to 1.4 $\pm$ 0.1 at% at 5000 L.

The oxide thickness and the composition obtained at 90° take-off angle (Figs. B.1, B.2 and B.3) are in agreement with the results obtained at 45°. Similar results obtained at different take-off angles are confirming the validity of the model used. Moreover, the in-depth distribution of species can be evidenced comparing the intensity of peaks under 90° and 45° angles where a higher intensity of Li 1s is observed under 45° while a lower intensity of Al 2s is observed at the same take off angle (45°). This indicates that Li oxide is mainly located at the surface of the oxide layer. The in-depth and lateral distribution of each component is revealed by ToF-SIMS 3D analyses (chemical mapping and in-depth ions profiling) and discussed in the next section.

In-depth and lateral chemical distributions of elements after thermal oxidation by ToF-SIMS

To investigate the lateral distribution of alloying elements and the in-depth composition of the oxide formed on the AA2050 surface by thermal oxidation (5000 L oxygen exposure at 200 °C), ToF-SIMS depth profiles and 3D imaging have been carried out. Ions depth profiles reconstructed from Tof-SIMS 3D chemical mapping are presented in Fig. 3.6 (a) and (b). As already showed in the literature [133, 134] the Al_2^- (53.970 atomic mass unit -u) and AlO_2^- (58.970 u) ions are characteristic of the metallic Al and Al oxide, respectively. $^{18}O^-$ (17.999 u) was selected as characteristic of the oxygen (and thus the oxide scale) since the $^{16}O^-$ (15.994 u) saturates the detector. Other alloying elements and their oxides are represented by their corresponding ions such as Li^- (7.016 u), LiO^- (39.006 u), Cu^- (62.929 u), CuO^- (78.927 u), Ag^- (106.909 u) and AgO^- (122.905 u). MgO^- (39.979 u) was selected to represent magnesium since the mass of Mg^- (23.986 u) is overlapped with C_2^- (24.001 u). For reasons of clarity, all these profiles were presented in two separate figures: oxide and substrate region characteristic profiles in Fig. 3.6 (a) and interface characteristic profiles in Fig. 3.6 (b). As a function of the shape of ion depth profiles and the intensities of signals, three regions can be identified: oxide layer region (0 to $\sim$60 s), interface ($\sim$60 s to $\sim$150 s) and metal substrate region (over 150 s). These regions are delimited by vertical, dashed lines in Fig. 3.6.

The oxide layer is characterized by the maximum intensity of Li^-, LiO^- and MgO^- and increasing intensity of AlO_2^- signal (Fig. 3.6a). Li^- signal has a higher intensity but a very similar shape as LiO^- signal so it can be concluded that it is also characteristic of the Li oxidized species. These results are consistent with the XPS result when comparing the intensity of Li 1s at 45° and 90° take-off angles after the final stage of oxidation, showing the enrichment of the surface aluminium oxide layer in the lithium and magnesium oxides (Fig. 3.2). In the oxide region, low intensities of aluminium (Al_2^-), copper (Cu^-, CuO^-) and silver (Ag^-, AgO^-) signals (Fig. 3.6 (a) and (b)), corresponding to metallic aluminium, metallic or oxidized copper and silver, respectively, are observed, indicating that the extreme surface of the oxide layer is impoverished in metallic and oxidized copper and silver species. These results corroborate the XPS data (Figs. 3.2 and 3.3) where both metallic Ag and Cu are enriched in the metal/oxide interface and covered by the oxide grown during the oxidation as confirmed by the intensity decrease of Cu 2p and Ag 3d.

The important interval sputtering time of interface layer (from around 60 to 150 s of sputtering)

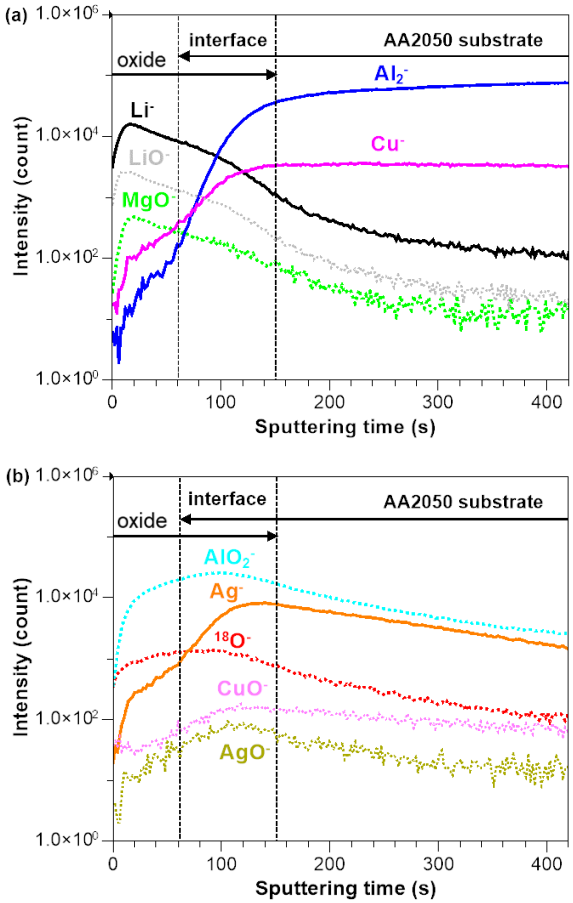

Figure 3.6: ToF-SIMS depth profiles extracted from 3D ToF-SIMS images obtained for AA2050 after 5000 L oxygen exposure at 200 °C: a) Li^-, LiO^-, MgO^-, Al_2^- and Cu^- ion depth profiles, b) AlO_2^-, Ag^-, CuO^-, $^{18}O^-$, and AgO^-. Oxygen (O) and oxides corresponding ion profiles (XO) are presented as dashed lines

can be related to the roughness of the analyzed sample submitted to the subsequent sputtering and oxidation processes. The interface region shows a step and continuous increase of the intensity of the aluminium and copper metallic signals (Al_2^- and Cu^-, respectively) in Fig. 3.6 (a), that stabilize in the substrate region. Slightly different behaviour can be observed for Ag^- signal, which reaches a maximum intensity in the interface zone (after around 120 s of sputtering) and slightly reduces to reach a plateau in the substrate zone. This behavior indicates a metallic Ag enrichment at the oxide/metal interface (Fig. 3.6 (b)). The silver interface enrichment is consistent with the intensity evolution of Ag $3d_{5/2}$ measured by XPS (Figs. 3.2 and 3.3).

CuO^- and AgO^- signals exhibit a similar shape as Cu^- and Ag^- profiles, respectively, showing a slight enrichment in the copper and silver species at the oxide/substrate interface. It should be noted that CuO^- and AgO^- signals have very low intensities, which means that presence of silver and copper oxides traces cannot be completely ruled out. The interface region is also characterized by relatively high intensities of AlO_2^- and $^{18}O^-$ signals from around 60 to 100 s of sputtering time, which decrease in the second part of the interface region (from around 100 s of sputtering time). As already observed by XPS (Fig. 3.3 (a) and (b)) this can be explained by a fast aluminium and lithium oxide growth in the first stages of thermal treatment and then and subsequent decrease of aluminium oxide growth and enrichment in the lithium and magnesium oxides as discussed above.

The last region (over 150 s of sputtering) corresponding to the AA 2050 substrate shows a quasi-stable intensity of (Al_2^- and Cu^- signals (Fig. 3.6 (a)) and declining depth profiles for other oxide signals presented in Fig. 3.6 (b).

ToF-SIMS 3D images, showing only selected ions: AlO_2^-, Al_2^-, MgO^-, Li^-, Cu^- and Ag^-, corresponding to the ion depth profiles discussed above, are presented in Fig. 3.7 (a–f). A relatively homogeneous distribution of Al oxide (AlO_2^-) is observed over the surface as shown in Fig. 3.7 (a). Slight differences in the signal intensity can be the effect of the surface morphology and of the increased surface roughness resulting from the surface preparation and thermal treatment during in situ XPS experiment. Moreover, Cs^+ sputtering beam used in 3D ToF-SIMS depths can have different sputtering yields depending on grain orientation [135–137] leading to different roughness and morphology and as a consequence to strongly corrugated surface. The effect of the grain orientation is particularly observed in the case of the Al_2^- image (Fig. 3.7 (b)). A thorough analysis of

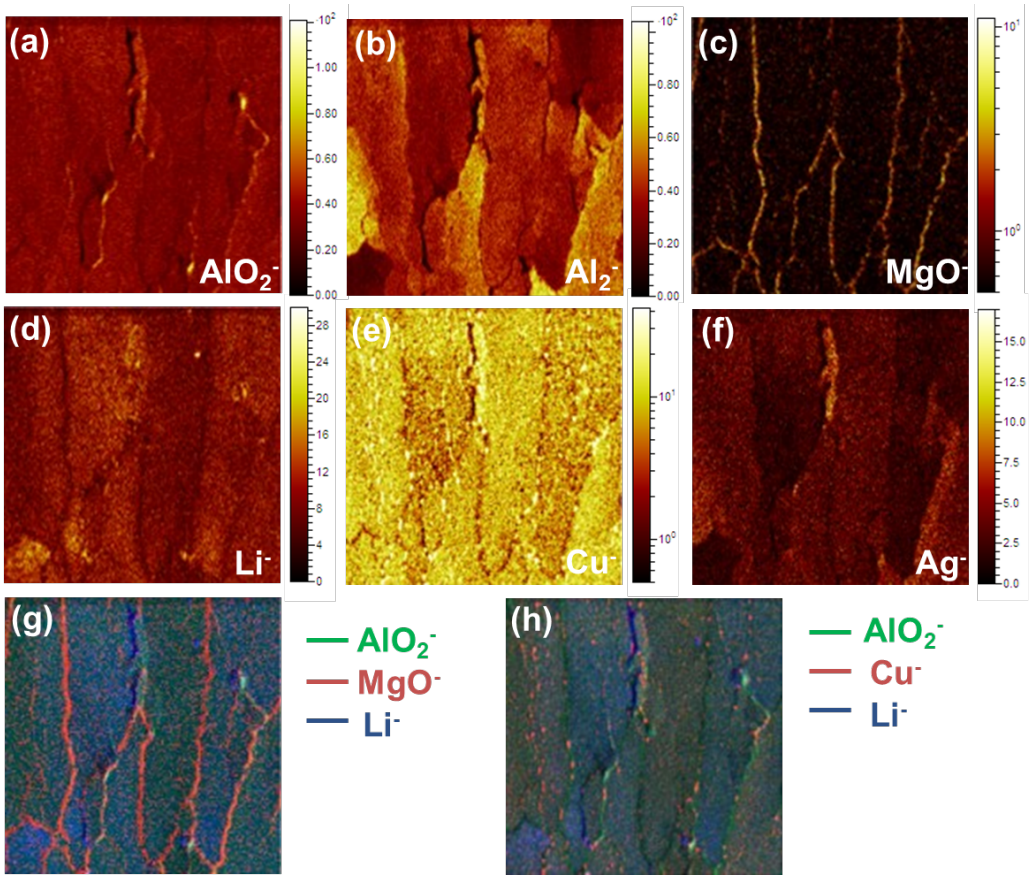

Figure 3.7: ToF-SIMS 3D chemical mapping (100 µm × 100 µm) acquired from different depths corresponding to 460 s of sputtering time showing (a) AlO_2^-, (b) Al_2^-, (c) MgO^-, (d) Li^-, (e) Cu^- and (f) Ag^-, and (g) overlay of AlO_2^- (green), MgO^-(red), Li^-(blue), (h) overlay of AlO_2^- (green), Cu^-(red), Li^-(blue)

the Al_2^- signal (characteristic of the Al metallic substrate) shows that the intensity varies with different grain orientations. The same effect was already observed in our previous studies on aluminium alloys (AA 2024) on which 3D ToF-SIMS chemical images were performed (not published).

From Fig. 3.7 (c), the MgO^- signal shows an obvious segregation of Mg along the identified grain boundaries of the Al substrate (from the Al_2^- map in Fig. 3.7 (b)). The overlayered signals of MgO^-, Li^- and $AlO2^-$ (Fig. 3.7 (g)) evidence very nicely the significant intensity of red MgO^- signal (in red) along the grain boundaries. The Mg segregation has been observed for many Mg containing Al alloys after the thermal treatments [28–30, 138, 139]. For example, Paine *et al.* [138] used scanning transmission electron microscopy (STEM) with EDX to analyze the composition of grain boundaries of Al-6.5 wt% Mg. Here, from combination of ion-depth profiles (MgO^- signal in Fig. 3.6 (a)) and 3D chemical mapping (Fig. 3.7 (c) and (h)) it can be concluded that despite the magnesium is enriched in the oxide it is segregated at location corresponding to grain boundaries of the Al substrate.

According to Fig. 3.7 (d–f), a relatively homogenous intensity of Li^-, Cu^- and Ag^- is observed over the grains. Slight intensity changes of these ions over the grains can be related to differences in sputtering yield of grains with various orientations as already observed for Al_2^- signal and discussed above. Thus, it can be concluded that these results are in agreement with literature showing that under the thermal treatment conditions applied here, close to the T8 industrial thermal treatment, the distribution of T1 phase (Al_2CuLi) in the alloy is homogeneous in the grains and no enrichment is observed in the grain boundaries [57]. However, some slight Cu enrichment can be observed in certain surface hollows and grain boundaries. These local grain boundaries enrichment is more visible in the Fig. 3.7 (h) where the AlO_2^-, Li^- and Cu^- signals are overlayered.

For the sake of clarity, and to have a better view of the lateral and in-depth distribution of different species, three different ions were selected each time and represented as 3 D images as shown in Fig. 3.8 (a) and (b) (for (a): $Al_2{}^-$ orange, MgO^- black and Li^- green, and for (b): $AlO_2{}^-$ red, Ag^- green and Cu^- blue). The metallic aluminium and copper represented by ($Al_2{}^-$ orange in Fig. 3.8 (a)) and Cu^- signals (blue in Fig. 3.8 (b)), respectively, are observed in the alloy substrate. As it can be observed in the right image in the Fig. 3.8 (b), the border between the green (Li^-) and the orange ($Al_2{}^-$) signals (corresponding to the oxide/metal interface) is not sharp, and these two

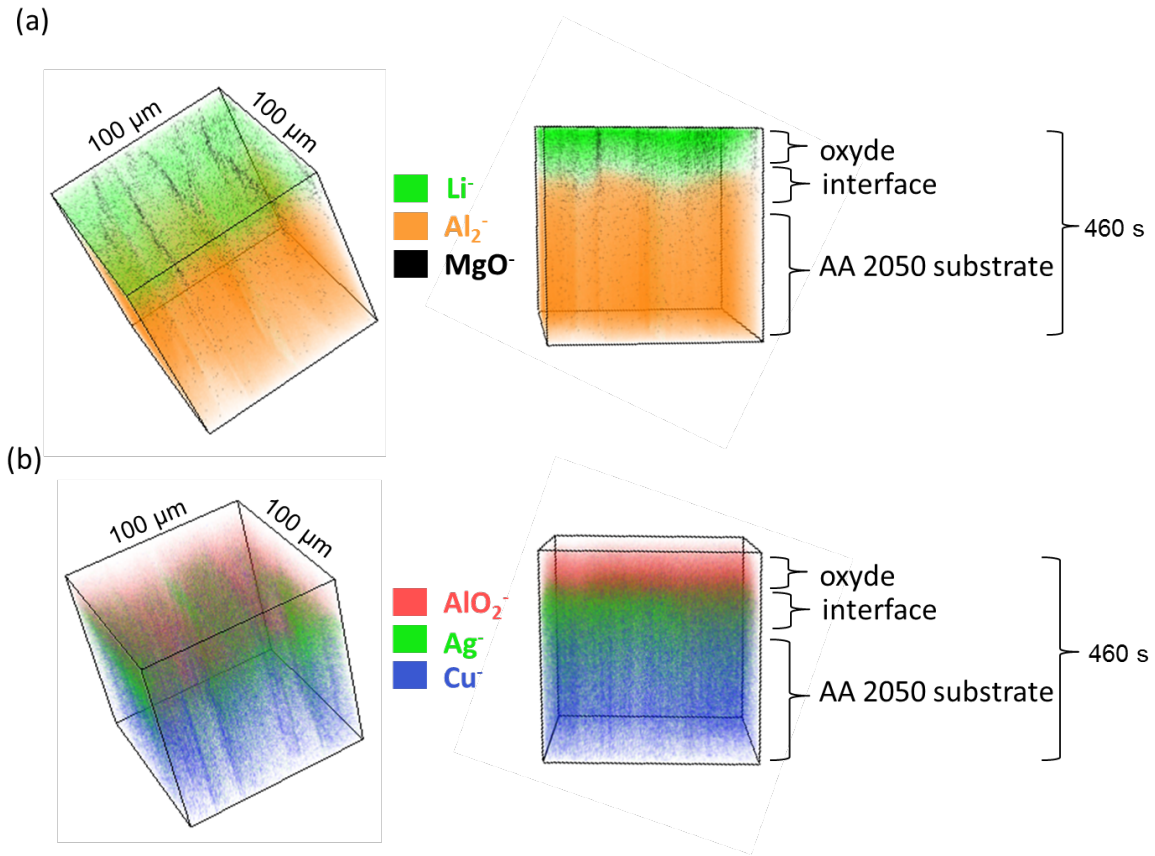

Figure 3.8: ToF-SIMS 3 D chemical images (100 µm × 100 µm × 460 s) obtained for the AA2050 after 5000 L oxygen exposure at 200 °C (a) overlay of Al_2^- (orange), MgO^- (black) and Li^- (green), and (b) overlay of AlO_2^- (red) Ag^- (green) and Cu^-(blue)

regions cannot be delimited by a straight line, indicating important roughness of the alloy as already mentioned above. The extreme surface shows the homogeneous distribution of Li^- (in green) and a localized incorporation of Mg (in black) (Fig. 3.8 (a)), previously evidenced as the grain boundary segregation (Fig. 3.7). Slightly below the Li-rich layer (defined above as the Li oxide layer), the aluminium oxide layer (AlO_2^-) is clearly visible (Fig.3.8 (b)). The enriched metal/oxide interface in silver (Ag^- in green) is also visible in Fig. 3.8 (b). This in-depth distribution of different species was already discussed in details in the ion depth profiles presented in Fig. 3.6.

3.4 Discussion

As shown in previous sections, thermal treatment induces in-depth and/or lateral segregation of alloying elements, homogeneously distributed in the surface oxide and in the oxide/metal interface

in the case of Li and Ag, respectively. In the case of Mg, a localized distribution in the oxide part over the grain boundaries of the Al alloy substrate was observed. This accumulation of some alloying elements at defect sites, in particular at grain boundaries or free surfaces, is common during thermal treatment, and it is govern by reduction of the system energy [140, 141]. Several aspects such as the solid solubility of alloying elements, heating temperature, interaction energy between atoms can influence the segregation process which could explain the different segregation behaviours of alloying elements [16, 17]. The surface segregation of Li and Mg in Al alloys at high temperature has been introduced and studied in the literature [22, 23, 142, 143]. Therefore, it is not surprising to find both Li and Mg segregating to the surface in our study. However, some differences in segregation behaviour can be observed between Li and Mg. As shown by XPS in Fig. 3.2 (c), the surface segregation of Li was evidenced during annealing before oxidation (0 L) but a delayed Mg surface segregation was observed and it was induced by exposition to oxygen (after 1500 L exposure). It indicates that Li is more prone to segregate on the surface compared to Mg and that oxygen play an important role in this behaviour. Several studies indicated that oxygen can chemically promote the surface segregation of Li and Mg due to their high oxygen affinity [22–24, 27]. The oxygen affinity of Li is even higher than that of Mg [144]. Therefore, Li is more easily oxidized on the surface compared to Mg. Another difference between Li and Mg segregation is their location, which has been discussed in section 3.3 and shown that most of Mg is accumulated in the oxide, over the grain boundaries of the substrate while Li homogeneously distributes over the grains. This can be explained by the superior thermal stability of Li containing T1 phase, which is relatively stable till 300 °C where other strengthening precipitates dissolve [20, 126], as discussed in the introduction. The oxygen affinity is not the only factor that can influence the segregation behaviour, atomic radius, diffusion coefficient, concentration, heating temperature, *etc.* also play roles [140, 141, 145] on it but were not studied here.

A surface segregation of metallic Ag at the oxide/metal interface was observed on the annealed sample before oxidation and during the longer oxygen exposure. According to XPS results, both Ag and Li segregate on the surface before oxidation, but Li oxidizes when is exposed to low oxygen pressure while Ag stays in a metallic state. The oxidation process is mainly controlled by the free enthalpy change for the oxidation of each metal. The standard enthalpy of formation of lithium

oxide and Mg are -1 42.9 kcal/mol [146] and -143.8 kcal/mol [147], respectively, and of Ag oxide is -7.4 kcal/mol [148] which explains the preferential oxidation tendency of Li and Mg to Ag.

The elemental segregations described above are not desired in real applications for aircraft structure since both surface and grain boundary segregation increase the chemical heterogeneity and induce corrosion problems. Mg segregation along the grain boundaries can induce the intergranular corrosion, stress corrosion cracking and hydrogen embrittlement [28–31]. The surface segregation of reactive elements such as Li can change the surface structure and properties, which can also induce corrosion problems [25]. As far as we know, there is no literature about the effect of Ag surface segregation in Al alloys. However, a segregation of Ag was observed at the interface of a Cu-Al_2O_3 based composite fabricated by internal oxidation after annealing between 169 °C and 189 °C [149]. Before annealing, Ag was homogeneously distributed in the Cu matrix then started to diffuse to the interface of Cu-Al_2O_3 at higher temperatures. This behaviour is similar to that of Ag in our study. Moreover, an increased electrical conductivity (EC) of the Cu-Al_2O_3 composite was observed when 0.92 at.% Ag was introduced, which indicates that Ag promotes the EC sufficiently [149]. It should be noted that the higher EC is unfavourable to corrosion resistance because higher EC can improve the transport of electrons and therefore promote the corrosion.

3.5 Conclusions

Thermal oxidation at 200°C of AA2050-T8 Al-Cu-Li alloy was studied by *in situ* XPS in a range of 0-5000 L oxygen exposure. The final surface state of alloy was also analyzed by 3D ToF-SIMS chemical mapping and ion depth profiles. These studies allowed to draw the following conclusions:

- Before oxidation, Li and Ag segregates on the annealed surface. During exposure to oxygen, Li oxidized rapidly while Ag stays in a metallic state at the oxide /metal interface.
- Initial stages of thermal oxidation at 200°C of AA2050-T8 Al-Cu-Li alloy, reveal the formation of a continuous mixed Al-Li oxide layer with a thickness of 9 $\pm$ 1 Å after 5000 L oxygen exposure.
- Two regimes of oxide growth are evidenced with a fast oxidation below 500 L and a slower growth rate during further oxidation up to 5000 L.

- Atomic ratio of Li in the oxide increases form 50% to 70% during 10 L–100 L exposure and becomes stable at further stages of oxidation (till 5000 L). A Mg enrichment is observed at the surface.
- The segregation is confirmed by ToF-SIMS 3D map. Relatively homogeneous distribution of Li, Cu and Ag is observed in the grains while a significant accumulation of Mg is observed above the grain boundaries of the Al substrate.

Chapter 4

Intermetallic particles induced corrosion behaviour of Al-Cu-Li alloys

This chapter reproduces the accepted version of an article published in Corrosion Science with the reference:

Li M, Seyeux A, Wiame F, Marcus P, Światowska J. Insights on the Al-Cu-Fe-Mn intermetallic particles induced pitting corrosion of Al-Cu-Li alloy. Corrosion Science.

A second paper to-be-submitted for publication in Journal of the Electrochemical Society with a reference:

Li M, Seyeux A, Wiame F, Marcus P, Światowska J. Phase-dependent surface modifications evidenced by ToF-SIMS 3D chemical mapping. Journal of the Electrochemical Society (to be submitted).

4.1 Insights on the Al-Cu-Fe-Mn intermetallic particles induced pitting corrosion of AA2050-T8 Al-Cu-Li alloy

Abstract

The pitting corrosion and surface modifications of aluminium alloy AA2050-T8 (Al-Cu-Li) resulting from immersion in 0.1M NaCl at open circuit potential were studied by time-of-flight secondary ion mass spectrometry (ToF-SIMS). ToF-SIMS chemical mapping showed a local distribution of chlorides and hydroxides in the pits enriched in Cu and Fe. Preferential sites of corrosion initiation were evidenced in the alloy matrix close to Al-Fe-Cu-Mn intermetallic particle. A formation of an oxide-hydroxide layer with different composition and/or higher thickness was evidenced over IMP than the alloy matrix. Li oxide dissolved from the oxide layer but metallic lithium was still present in the matrix.

4.1.1 Introduction

Al-Li alloys have been developed since 1958 as advanced materials for aircraft manufacturing [1]. The presence of Li in the Al alloy allows to decrease the alloy density and improves its mechanical properties. Indeed, the addition of 1 wt% Li results in a significant reduction of weight (3 %) and a considerable increase in elastic modulus (6 %). When the content of Li is over 1.3 wt%, the tensile strength and thermal stability of Al-Li alloy decrease. Moreover, the material may show higher anisotropy of mechanical properties [7]. A development of one of the first generations of Al-Li alloys was focused on the lightweight but their low mechanical properties limited the applications of these alloys. In order to optimize the Al-Li alloy properties (i.e. density, mechanical properties and thermal stability), the content of Cu in Al-Li alloy was increased and Li was limited to 1.3wt% [5–7]. AA2050 is such an Al-Cu-Li alloy, produced by Alcan since 2004. AA2050 has better mechanical properties, higher corrosion resistance and lower density compared to conventional Al alloys such as AA2024 and AA7075 used for aircraft and heavy lift launch vehicles [8, 150–152]. Al-Cu-Li alloy has been used on the Boeing 777 as an advanced material for reducing weight [153]. Several studies have shown that Al-Cu-Li alloys have better corrosion resistance compared to other conventional Al alloys [5, 7, 154]. However, the corrosion behavior of Al-Cu-Li alloy is still an open subject as Li is

considered as one of the possible factors of the alloy instability and leads to a complex corrosion behavior [121, 155]. Severe intergranular (IGC) and transgranular corrosion (TGC) observed in Al-Cu-Li alloys, largely depend on the Li dissolution principally observed in the nano-sized T1 phase (Al_2CuLi). The presence of Li in T1 phase makes it more anodic than the matrix and prone to dissolution. The T1 phase is preferentially located in the regions with high density of dislocations or high level of misorientation [48–51]. It can also be significantly influenced by thermal treatments during alloy processing. Therefore, some studies focused on the relation between the distribution of T1 phase induced by thermal treatment and corrosion behavior of Al-Cu-Li alloys [52, 53, 156].

Pitting corrosion is another main type of corrosion. Al-Fe-Cu-Mn IMPs (dimension $\leq$ 1 µm) in Al alloys are considered as one of the preferential sites of pitting corrosion [58, 59, 157]. Birbilis *et al.* [58] evidenced the cathodic behaviour of Al7Cu2Fe particles in AA7075-T651 (Al-Zn-Mg-Cu) alloy leading to the pitting corrosion between matrix and IMPs. Boag *et al.* [59] studied the pitting corrosion of AA2024 Al-Cu-Mg alloy in NaCl electrolytes and also found a preferential corrosion at the interface of Al-Cu-Fe-Mn particle and matrix. The pit propagation induced by Al-Cu-Fe-Mn IMPs was studied by Zhou and Glenn [60, 158] on AA2024 who found that they had a significant influence on extensive grain boundary attack. In the case of Al-Cu-Li alloy (AA2090), Buchheit *et al*. [52] concluded that there are two corrosion mechanisms. One is the dissolution of anodic T1 phase located at grain boundaries. The other is the pitting corrosion that occurs close to the Al-Fe-Cu-Mn IMPs. However, the distribution of Li in Al-Fe-Cu-Mn IMPs and its effect on pitting corrosion is not clear yet. Few studies tried to evidence the distribution of Li in IMPs. MacRae *et al.* [61] studied the composition of coarse IMPs and found the existence of Li inside the IMPs by using soft X-Ray emission spectroscopy. Ma *et al.* [62] investigated the pitting corrosion of Al-Cu-Li alloy (AA2099) and evidenced two kinds of corrosion morphology on the Fe containing IMPs with different Cu contents. They showed that IMPs with higher Cu content containing more Li (evidenced by electron energy loss spectroscopy) are more reactive. The IMPs with lower Cu content showed trenching and the IMPs with higher Cu content showed dissolution of Al and Li over the IMPs. However, as described in Ma's study, pitting in both cases was superficial. Some researchers claimed that the presence of Li in the Al alloy increases corrosion resistance [6, 159]. The corrosion can be inhibited by the higher concentration of OH^- which produced by the reaction

of metallic Li with water. This OH^- which can neutralize the acidic pitting region and make the pits more superficial [160, 161]. Ghanbari and Lei [160, 161] applied various electron microscopy and electrochemistry techniques and point defect model method to investigate the localized corrosion of Al-Li alloys in order to prove the effect of Li. In their study, the formation of more superficial pits and better corrosion resistance was confirmed in the Al-Li alloy with highest content of Li.

Although, the effect of T1 phase on the corrosion of the Al-Li alloys has already been studied by electrochemical and microscopic techniques, the exact effect of Li and its distribution on chemical modifications and corrosion of Al-Li alloys is still unclear [162]. Li is difficult to characterize, particularly at such low concentration (around 1 % in the alloy), due to the low detection limits of different techniques (e.g. energy dispersive x-ray spectroscopy (EDS)) and high reactivity of Li, which is prone to dissolve once exposed to electrolyte. Time-of-flight secondary ion mass spectrometry (ToF-SIMS) is a highly sensitive surface technique and is able to detect a low amount of Li. Thus, in this study, ToF-SIMS ion depth profiling and chemical mapping were combined with scanning electron microscopy (SEM) to analyse the sample before and after corrosion and to better understand the corrosion behaviour of AA2050-T8 (Al-Cu-Li) alloy and its Al-Fe-Cu-Mn IMPs in 0.1 M NaCl electrolyte. Series of ToF-SIMS imaging were performed on a pitted region to get information about the chemical composition of pitted areas and chemical modifications of the alloy matrix and Al-Fe-Cu-Mn IMPs. The in-depth distribution of Li and other alloying elements (Cu, Mg, Fe) were also analyzed before and after corrosion.

4.1.2 Experiment

Samples

The specification of AA2050-T8 (Al-Cu-Li) alloy used in this study is presented in Table 4.1. The samples were provided by Constellium, France. The specimens were cut into 8.0 mm $\times$ 8.5 mm pieces (about 3 mm thickness). Surface preparation was performed by mechanical polishing with SiC paper from 320 to 4000 grades then by mirror polishing with alumina suspension down to 0.3 µm . After polishing, samples were cleaned by successive ultrasonic baths in iso-propanol, ethanol and finally Ultra-pure (UP) Millipore® water (resistivity $\geq$ 18 M$\Omega\times$cm) then dried by filtered

Table 4.1: Specifications of alloying element (wt% & at%) of the AA2050 alloy

Cu	Li	Mg	Zn	Mn	Ag	Zr(max)	Fe(max)	Si(max)
3.2–3.9	0.7–1.3	0.2–0.6	0–0.25	0.2–0.5	0.2–0.7	0.14	0.1	0.08
1.5–1.6	2.8–4.8	0.2–0.7	0–0.1	0.1–0.2	0.05–0.1	0.04	0.04	0.07

compressed air.

Immersion tests

The polished AA2050-T8 samples were immersed in 0.1 M NaCl electrolyte prepared with NaCl (VWR, 99.9%) and UP Millipore® water (resistivity $\leq$ 18 MΩ cm) for 45 minutes at the open circuit potential (OCP). The potential was controlled by a Reference 600 potentiostat (Gamry). A classical 3-electrode electrochemical cell with a platinum wire and a saturated calomel electrode (SCE) were used as counter and reference electrodes, respectively, and a polished AA2050-T8 sample as a working electrode. The corroded AA2050-T8 samples were then rinsed with UP water, dried and transferred to analysis by ToF-SIMS, optical microscopy and SEM/EDS.

Surface characterization

ToF-SIMS measurements were carried out using a ToF-SIMS spectrometer(ION TOF GmbH, Munster, Germany) operating at high vacuum (10^{-9} mbar). The first series of analysis (the in-depth profiles and ToF-SIMS images) were performed on AA2050-T8 sample before and after immersion in NaCl, then the second series of analysis (ToF-SIMS images) was done on the sample AA2050-T8 on which the region of interest with the IMP was first identified then the same region was analysed after immersion. To do so, before measurements, the surface sample was marked by etching the number “1” using the Cs^+ sputtering beam of the Ion-ToF spectrometer in order to easily identify the same analysed area called here the region of interest. ToF-SIMS ion-depth profiles were performed by using a 2 keV Cs^+ beam delivering a 100 nA current for sputtering and a pulsed 25 keV primary Bi^+ delivering a 1.2 pA current (in high current bunched mode) for analyzing. In the high current bunch mode a lateral resolution was around 5 µm and a mass resolution M/ΔM around 7000. The sputtered area was 1000 µm $\times$ 1000 µm and the analyzed area was 100 µm $\times$ 100 µm.

ToF-SIMS imaging (chemical mapping) was performed over the area of 100 µm $\times$ 100 µm in-

cluding the selected Al-Fe-Cu-Mn IMP (region of interest) before and after corrosion. ToF-SIMS images were performed at different depths corresponding to different sputtering times: 60 s (attributed to the oxide part) and 150 s (attributed to the oxide/metal interface). A 1 keV Cs^+ beam delivering a 38 nA current was applied for sputtering (500 µm $\times$ 500 µm) and 25 keV primary Bi^+ beam was set in burst alignment mode with a primary current adjusted to 0.3 pA over the total area (100 µm $\times$ 100 µm). in order to get a high lateral resolution ans a good mass resolution the long primary pulses are split into four small pulses. In this mode a lateral resolution was around 200 nm and a mass resolution M/ΔM around 7000, pixel array was 256$\times$256. Data treatment and post processing of ToF-SIMS measurements were performed with Ion-Spec software (version 6.8).

Microscopy characterization

The AA2050-T8 morphology (comprising the ROI) before and after corrosion was also analyzed by a digital VHX-5000 Keyence optical microscopy. SEM using Zeiss Ultra55 microscope with high-resolution Schottky thermal field emission gun (Schottky SEM-FEG) was used to select the resion of interest with an Al-Fe-Cu-Mn IMP close to the ToF-SIMS formerly identified region with mark "1" made by Cs-ion beam.

4.1.3 Results

Morphological characterization of AA2050-T8 after corrosion

During immersion in the 0.1 M NaCl electrolyte, the OCP of AA2050-T8 decreased approximately from -0.5 ($\pm$ 0.1) V to -0.68 ($\pm$ 0.03) V *vs* SCE. This final potential is close to the pitting potential (around -0.70 ($\pm$ 0.03) V *vs* SCE) of Al-Cu-Li alloys in 3.5 wt. % ($\sim$ 0.6 M) NaCl electrolyte as observed previously on AA2198, AA2524, AA1460 Al-Cu-Li alloys and AA7050 Al-Cu-Mg alloy [159, 162]. The immersion leads to formation of numerous corrosion pits as observed by optical microscopy (Fig. 4.1) and ToF-SIMS chemical mapping (see Fig. 4.3 on AlO_2^- ion map). Similar modifications with significant pitting were observed before on AA3003 and AA7075 in 0.1 M NaCl by Liu [163] and Birbilis [58], respectively.

Chemical surface and in-depth analysis of AA2050-T8 before and after corrosion

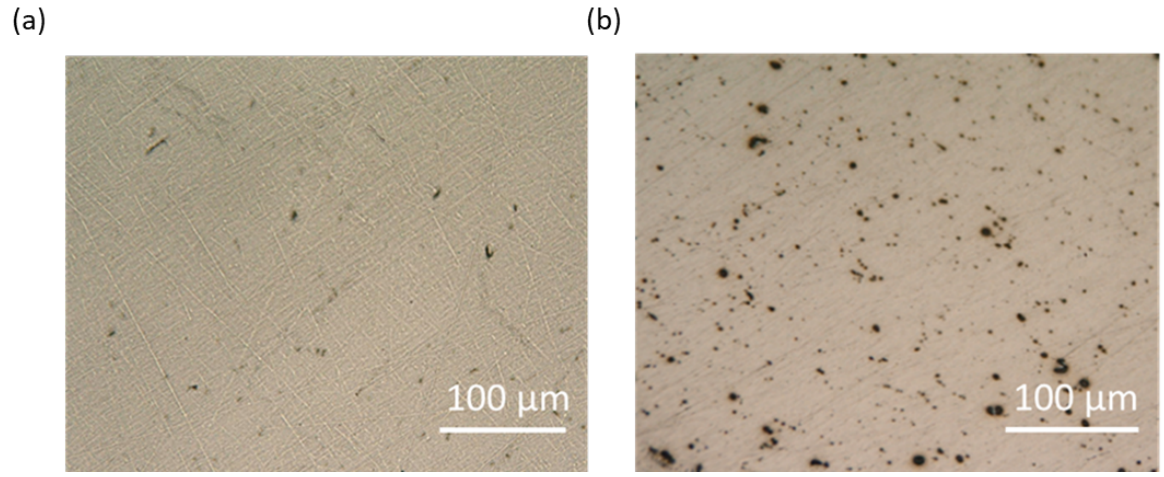

Figure 4.1: Optical microscopy of AA2050-T8 polished surface (a) before immersion (b) after 45 min immersion in 0.1M NaCl

In order to get more information about surface chemical modifications of AA2050-T8 induced by immersion in chloride electrolyte (0.1 M NaCl in 45 min), ToF-SIMS ion depth profiles were performed and compared to polished sample (Fig. 4.2).

The ion intensities are plotted versus Cs^+ sputtering time in logarithmic scale in order to enhance the low signal intensities. Al_2^- (m = 53.9634 u), AlO_2^- (m = 58.9728 u) and AlO_2H^- (m = 59.9812 u) signals represent Al metal, Al oxide and hydroxide, respectively. $^{18}O^-$ isotope ion was chosen to represent oxygen since $^{16}O^-$ saturates the detector. Cl^- (m = 34.9696 u) was recorded to observe the corrosion products and the presence of some chloride residues. Cu^- (m = 62.9268 u), Li^- (m = 7.0168 u) and MgO^- (m = 39.9797 u) ion profiles were also plotted to observe the alloying elements. The identification of Zn and Zn compounds (Zn^- (m = 63.9413 u), ZnO^- (m = 79.9355 u)) was not possible due to the overlap with Cu (CuH^- (m = 63.9268 u), $CuOH^-$ (m = 79.9354 u), respectively) and difficultly in detection of other Zn isotopes. Three regions can be identified in ToF-SIMS depth profiles, thanks to the intensity modifications of the ions corresponding to oxide and substrate species (Fig. 4.2):

1. the oxide layer (up to about 70 s of sputtering time),

2. the interface layer (from about 70-80 to about 150-160 s of sputtering),

3. the metal substrate (from about 150-160 s of sputtering where the intensity of Al_2^-- and Cu^- signals reaches a plateau).

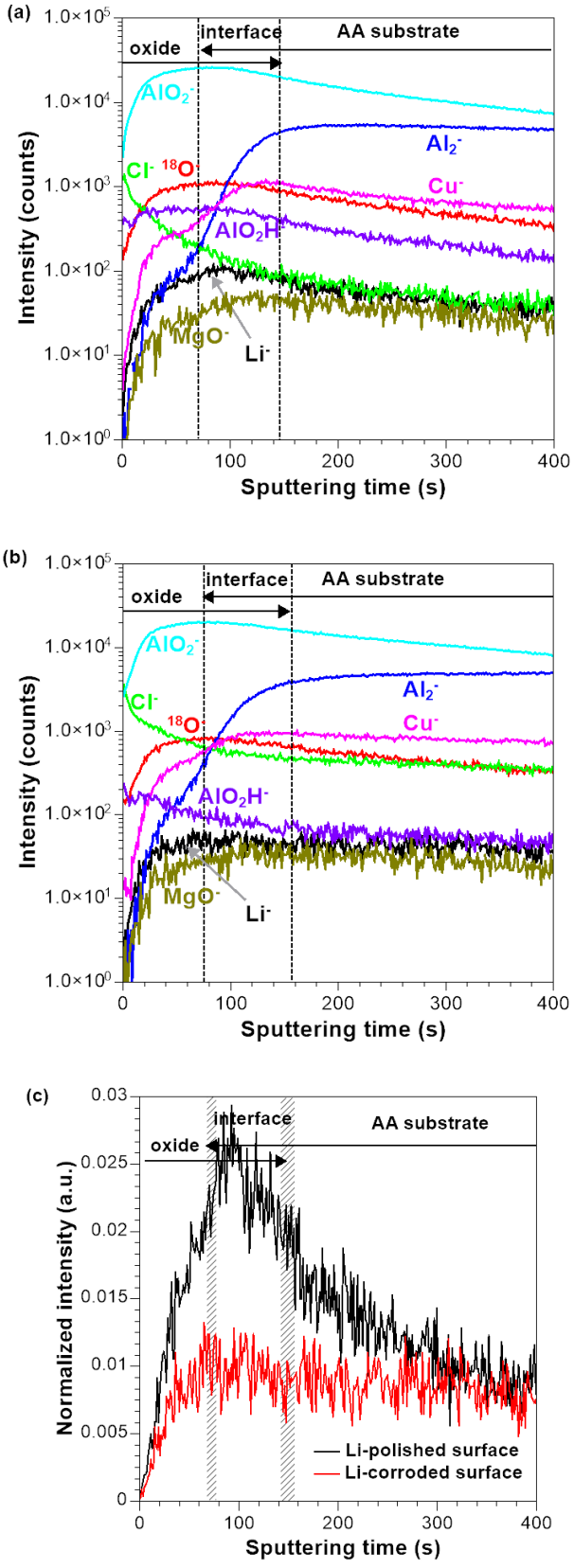

Figure 4.2: ToF-SIMS negative ion depth profiles for AA2050-T8 polished (a) pristine sample before immersion and (b) sample after 45 min immersion in 0.1M NaCl, c) Li signal before immersion (black curve) and after immersion (red curve). The oxide, interface and the substrate regions are delimited by the hatched wide areas corresponding to dashed lines shown in figures a) and c). The hashed areas cover the difference in sputtering time for polished and corroded samples

At very first seconds of sputtering rapid signal intensity changes are observed, which then tend to stabilize with increasing sputtering time. The oxide layer extends up to the position where the AlO_2^- and $^{18}O^-$ signals reach the maximum intensity (i.e. about 70 s of sputtering time). This region can also be delimited from the high intensity of AlO_2H^- signal (for pristine surface), indicating the formation of an aluminium oxide-hydroxide layer covering the metallic substrate. After corrosion the intensity of AlO_2H^- decreases slightly compared to the pristine sample indicating chemical modifications of the oxide layer.

A Li^- ion intensity increase is observed in this region up to the interface region for the pristine sample. Less abrupt intensity increase of Li^- can be observed for the corroded sample (see also normalized Li^- ion profiles in linear scale for pristine and corroded sample in Fig. 4.2(c)). It can be then concluded that Li enrichment is observed in the oxide layer of pristine sample then it undergoes dissolution in the chloride solution. A Li enrichment in the oxide layer was also found by means of Glow-discharge optical emission spectroscopy elemental depth profiles by Gharbi *et al.* [10] for a AA2050-T3 alloy after pretreatment and anodically polarized alloy in the neutral NaCl electrolyte. The Li enrichment can be explained by easier Li oxidation at the surface compared to other elements such as Mg as observed in our previous work [164]. No significant modifications are observed for the MgO^- profile for the pristine and corroded samples.

Relatively high Cl^- signal intensity is observed on the pristine surface, which can be explained by sample exposition to the ambient atmosphere, some pollutions due to the sample cleaning/rinsing. It should be emphasized that due to the high sensitivity of ToF-SIMS technique even a very low quantity of certain elements can be easily detected (which is the case of chloride ions in negative polarity). However, significant increased intensity of Cl^- signal (few orders of magnitude) is observed for the corroded sample in the oxide region. The signal intensity progressively decreases with sputtering time. An intersection point of Cl^- and $^{18}O^-$ signals is observed at the beginning of the depth profile (at about 20 s of sputtering) for the pristine sample. For the corroded sample this intersection is shifted to longer times of sputtering (about 60 s). Moreover, for the corroded sample, the Cl^- signal is relatively high and almost overlapped with the $^{18}O^-$ signal during the whole time of sputtering indicating the enrichment in chlorides.

The interface region is the intermediate region between the oxide and the metallic substrate

region and the width of this region depends on the sample roughness. A step increase of the Al_2^- signal (comprised between the first plateau characteristic of the oxide region and the second plateau characteristic of the substrate region) can be observed here.

Similarly, to Al_2^- signal, the Cu^- ion profile shows a significant intensity increase in this region. However, the Cu- signal shows a maximum intensity when reaching the substrate region, which indicates a metallic copper enrichment in the alloy at the metal/oxide interface. The ion profiles corresponding to the oxides and hydroxides (AlO_2^-, $^{18}O^-$, AlO_2H^-) show a decrease of intensity with increasing sputtering time. The substrate region (from about 140 s) can be characterized by almost stable intensity of Al_2^- and Cu^- profiles.

Chemical mapping of AA2050-T8 after corrosion

As aforementioned, the ion depth profiles represent the average chemical distribution over the analyzed surface (100 µm $\times$ 100 µm). However, the aluminium alloys show important surface chemical heterogeneities, due to the presence of different IMPs [165, 166]. Thus, the ToF-SIMS chemical mapping was performed on the AA2050-T8 after immersion in 0.1 M NaCl electrolyte in the oxide region (Fig. 4.3(a) after sputtering to 65 s) and at the metal/oxide interface (Fig.4.3 (b) after sputtering to 150 s). Fig. 4.4 presents the corresponding overlay of AlO_2^- and Cl^- ions.

The surface is not homogenous and this is particularly reflected by variation in the signal intensity in O^-, OH^-, Cl^-, AlO_2^- two-dimensional (2D) mapping in the oxide (Fig. 4.3 (a) and (b)) and at the interface and, additionally, from Al_2^- mapping performed in the interface region (Fig. 4.3 (b)). Locally higher Cu^- and FeO^- intensity signals are also observed in the interface region (Fig. 4.3(b)). Several points with higher intensity signal can be observed in the Cl^- ion mapping. The higher intensity of Cl^- overlaps with a lower signal intensity of AlO_2^- (Figs. 4.3 and 4.4) and Al_2^- in the substrate region (Fig. 4.3(b)) indicating pitting corrosion after immersion in 0.1 M NaCl for 45 min. Some larger pits show higher intensity of other ions such as OH^- in the oxide region (Fig. 4.3(a)). In the metal/oxide interface region (Fig. 4.3b) the OH^- intensity is even higher and some additional pits with OH^- enrichment can be observed with respect to the oxide layer (Fig. 4.3(a)), indicating, that the corrosion products (OH^-) are buried under the oxide layer. The high intensity of OH^- and Cl^- ion signals at pit locations corresponds also the higher intensity of Cu^- and FeO^-

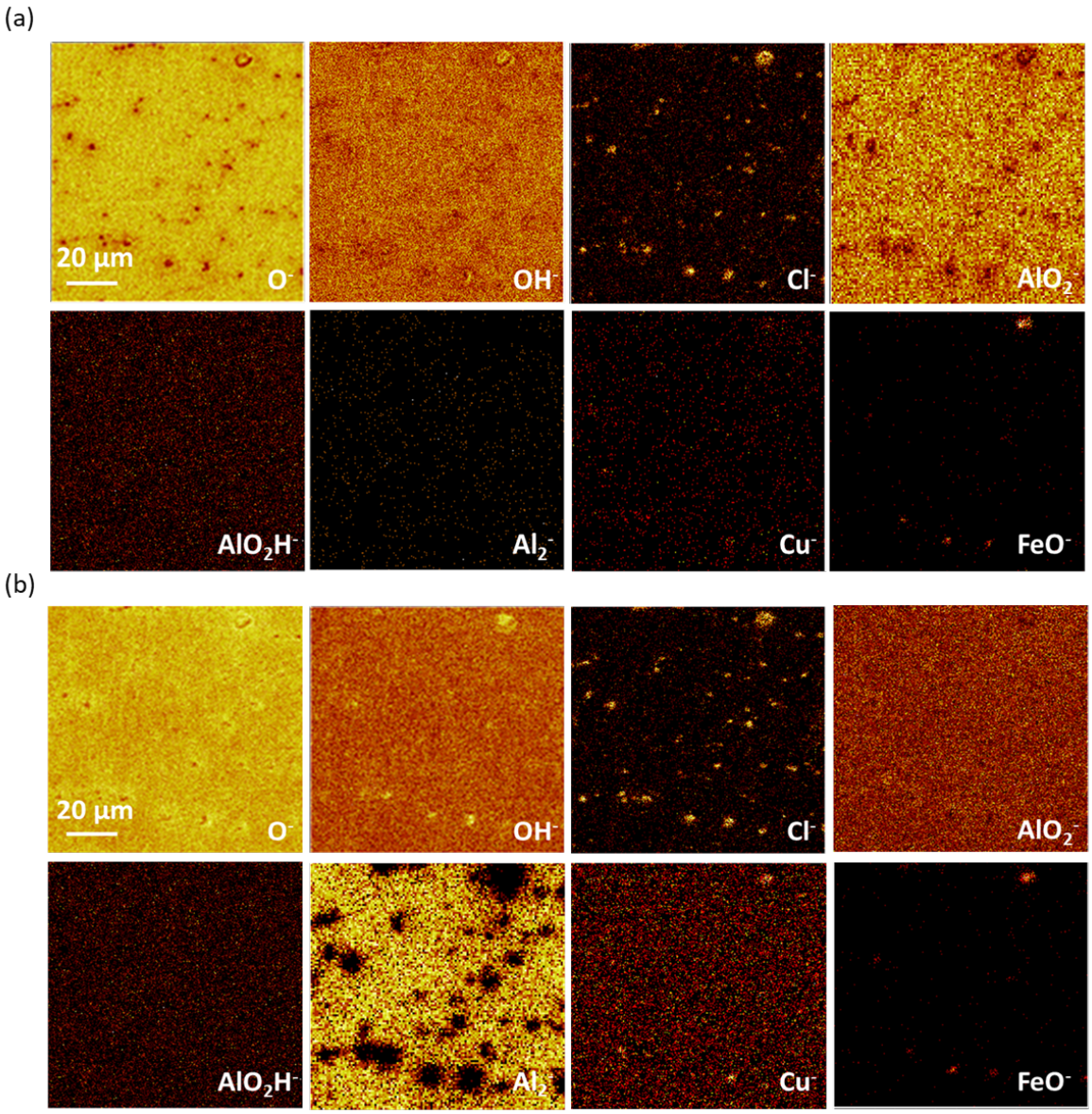

Figure 4.3: ToF-SIMS chemical mapping (100 µm × 100 µm) for AA2050-T8 after immersion in 0.1M NaCl for 45 min (a) in the oxide (sputtered to 65 s) and (b) at the metal / oxide interface (sputtered to 150 s)

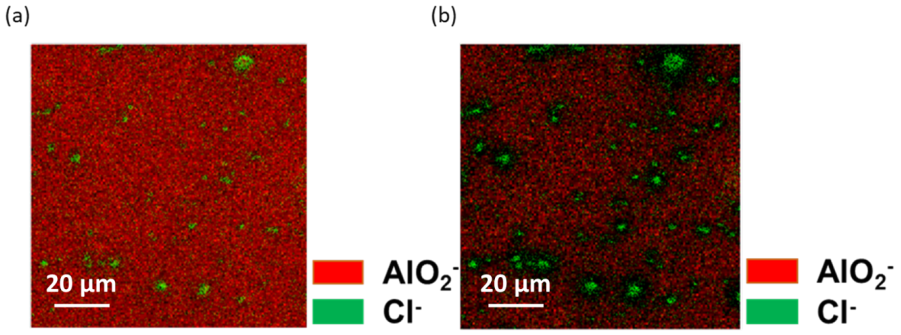

Figure 4.4: Overlay of AlO_2^- (red) and Cl^- (green) signals obtained from ToF-SIMS chemical images (100 µm × 100 µm) for AA2050-T8 after immersion in 0.1M NaCl for 45 min (a) in the oxide (sputtered to 65 s) and (b) at the metal / oxide interface (sputtered to 150 s)

at the metal/oxide interface (Fig. 4.3 (b)) indicating that the corrosion is induced by the presence of Cu and Fe-rich intermetallic particles, assigned to the Al-Fe-Cu-Mn IMPs. These types of IMPs are sensitive sites for pitting corrosion, and corrosion initiation [52, 167]. Moreover, the presence of OH^- and Cu^- in some pits (usually bigger in size) corroborates with a trace of $CuOH^-$ species as shown in appendix B (Fig. B.5). As discussed above due to the ZnO^- (m = 79.9355 u) overlapping with $CuOH^-$ (m = 79.9354 u), the analysis of OH related species is difficult. However, the presence of ZnO^- can be discarded since the OH^-, Cu^- and $CuOH^-$ signals are observed in the same pitting spots.

Chemical mapping in the area of Al-Fe-Cu-Mn IMP before and after corrosion of AA2050-T8

A local surface characterization of the AA 2050-T8 sample before and after corrosion was performed using ToF-SIMS chemical mapping combined with morphological and chemical characterization by SEM. First of all, on the pristine AA 2050-T8 sample before corrosion, a ROI with a typical Al-Fe-Cu-Mn IMP (with a size of around 30 µm) was selected by means of SEM (Fig. 4.4 (a)). The chemical composition of the selected IMP was characterized by ToF-SIMS chemical mapping in positive mode, performed on the AA 2024-T8 sample after removing the whole oxide film to reach the metallic substrate (Fig. 4.6(a)). The positive mode has a better sensitivity to metallic species. The high signal intensity of Fe, Cu, Mn elements in the IMP indicates that this IMP corresponds to the Al-Fe-Cu-Mn IMP. It should be noted that ToF-SIMS is not a quantitative technique and does not allow us to calculate the exact stoichiometry of this IMP. Li ion mapping shows that Li is principally observed in the Al matrix. The lateral resolution of ToF-SIMS chemical images (around 200 nm) and the size of the ToF-SIMS chemical images (100 µm $\times$ 100 µm) do not allow us to observe the presence of Li in the nano-sized T1 phase in the alloy matrix. Thus, T1 phase is considered as part of “matrix” where the Li signal shows a rather homogenous intensity. The homogenous distribution of T1 phase in the matrix of AA2050-T8 alloy was confirmed by the TEM analysis shown in the supplemental information in Fig. B.6. ToF-SIMS (Fig. 4.6) shows also a low intensity and inhomogeneous Li signal inside the IMP. Li inside the IMPs was also previously observed by Ma *et al*. [62] who concluded that the localized distribution of Li in the IMPs was as-

sociated to presence of Cu. However, no correlation between Cu and Li distribution was observed in our study.

Immersion in NaCl electrolyte did not remove the selected IMP as shown by SEM in Fig. 4.5 (b). The surface morphology of the aluminium alloy matrix and intermetallic particle is modified and shows a formation and deposition of corrosion products. As discussed in the literature, a dissolution of the surrounding aluminium matrix leading to protrusion of the cathodic IMPs is a typical corrosion mechanism [168, 169], however here the SEM image does not allow us to directly conclude about it. The zoom on the IMP presented in the inset of Fig. 4.5 (b) shows the formation of a pit of $\sim$1 µm in diameter close to the IMP.

A set of ToF-SIMS images were performed in the positive and negative modes in the same region of interest to better understand the chemical modifications of IMP and surrounding matrix induced by corrosion. The chemical mapping in negative mode used for better sensitivity to the oxidized species was performed at two different sputtering depths of 65 s and 150 s corresponding to the oxide layer (Fig. 4.7(a)) and oxide/metal substrate interface (Fig. 4.7(b)), respectively. The sputtering times (at which the images were performed) were chosen based on the ion depth profiles shown in Fig. 4.2.

ToF-SIMS chemical mapping performed in the oxide region (at 65 s of sputtering in Fig. 4.7(a)) shows a relatively high and stable intensity of AlO_2H^- and O^-, AlO_2^- signals, which indicate the formation of a thick and dense homogeneous oxide-hydroxide layer over the whole alloy surface exposed to NaCl electrolyte. However, a slightly higher OH^- signal intensity and a lack of the Al_2^- signal over the IMP than the matrix can be observed (Fig. 4.7(a)). A stronger contrast of the OH^- signal between the IMP and matrix can be observed in the images taken deeper (at 150 s of sputtering depth, Fig. 4.7(b)) corresponding to the oxide/metal substrate interface. Here at this depth, much higher intensity over the IMP can be also observed for O^-. These results can indicate the formation of a highly hydrated oxide-hydroxide (corrosion) layer with a different composition over the IMP than over the matrix. A different composition of this layer formed over the IMP than over the alloy matrix can lead to differences in sputtering rate in the IMP and matrix regions. However, assuming a similar sputtering rate over the whole analyzed area (IMP and matrix), the formation of the thicker oxide-hydroxide layer over the IMP than the matrix is suggested.

This hypothesis can be also supported by the lack of Al_2^- signal over the IMP and the presence in the matrix region in the image of Al_2^- signal (in Fig. 4.7(b)) after 150 s of sputtering.

Summarizing, these results (high O^- and OH^- and low Al_2^- signals) indicate the formation of an oxide-hydroxide layer with a different composition and/or thickness over the IMP than over the matrix. These chemical variations induced at the surface by corrosion and strongly influenced by the alloy composition and presence of IMP will be discussed in the next section.

It should be also noticed that the intensity of O^- signals is not the same over the IMP region, and a higher intensity can be observed at the IMP periphery (Fig. 4.7(b) and O^- chemical mapping after image treatment in Fig. B.8) as also demonstrated previosuly [170, 171].

In Fig. 4.7 (a) and (b), a highlighted point (pit) in the Cl^- ion mapping close to IMP is observed. Combined with the SEM presented in Figs. 4.5 (b), it can be concluded that the enrichment in Cl^- species is associated to pitting corrosion. The chloride species enrichment in the pits is in agreement with the results discussed above and presented in Fig. 4.3 and 4.4.

To have a better insight into the lateral distribution of alloying elements such as Cu, Li, Fe and Mn corresponding to the Al-Fe-Cu-Mn IMP, the chemical mapping was also performed in positive mode at the oxide/metallic substrate interface (150 s sputtering time) (as shown in Fig. 4.6(b). The comparison of the chemical maps recorded after corrosion (Fig. 4.6(b)) with maps obtained before corrosion (Fig. 4.6(a)) shows clearly the inverse signal intensity in the matrix and IMP for Cu^+ and Mn^+. After corrosion the enrichment of Cu and Mn was not observed anymore in the IMP region but in the matrix. Only slightly higher intensity in the area of IMP was observed for Fe^+ indicating the presence of IMP. As aforementioned, the ToF-SIMS chemical maps were obtained at the oxide/metal substrate interface, however the lack of Cu, Mn corresponding to the IMP indicates that after 150 s of sputtering the oxide/metal interface was reached at the matrix region but not for IMP region. This confirms the hypothesis of a thicker layer or a layer with different composition (different nature) formed over the IMP than over the matrix.

A higher intensity of Cu adjacent to IMP was also observed in the positive mode image (Cu^+ in Fig. 4.6 (b)). The analysis of the same area by SEM, allowed to conclude that this Cu enrichment is located at the area of small pit where the presence of Cl was also observed (Cl^- in Fig. 4.7).

The higher Li^+ intensity in the matrix than in the IMP was observed after corrosion (Fig. 6(a))

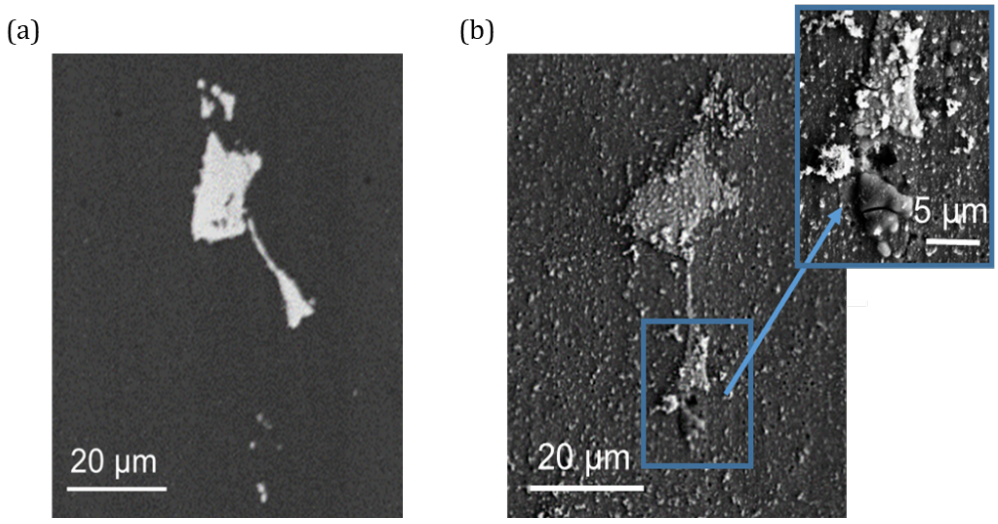

Figure 4.5: Scanning electron microscopy performed on the AA 2050-T8 sample in the region of interest comprising Al-Fe-Cu-Mn IMP (a) before and (b) after immersion in 0.1M NaCl for 45 min

and this lateral distribution of Li is similar to the pristine sample (Fig. 4.6(b)). The presence of Li in the alloy matrix indicates that Li is probably in a metallic state. The presence of other possible Li-related negative secondary ions (such as LiO^-, $LiOH^-$) were carefully checked and they were not detected after corrosion confirming the dissolution of Li from the oxide layer (as also discussed for the negative ion depth profile presented in Fig. 4.3(b)).

4.1.4 Discussion

Combined SEM and ToF-SIMS analyses were applied to study the pitting corrosion behavior of AA 2050-T8 and the surface chemical modifications of the alloy induced by immersion in 0.1 M NaCl. Optical microscopy images indicated a significant pitting corrosion of AA2050-T8 occurring in NaCl electrolyte. The surface attack by chlorides was also observed by ToF-SIMS chemical mapping, with the presence of high Cl^- signal intensity in the pits. The thorough analysis of ToF-SIMS mass spectra was unsuccessful in observing the metallic cation, associated to Cl, which could correspond to the formation of MeCl species. It was also demonstrated by Grilli *et al.* [172] that, even in the presence of Cl, no Al-Cl species were detected due to high solubility of $AlCl_3$ during sample rinsing. Also, the insoluble CuCl, $CuCl_2$ and their complexes can be washed away from the surface, and only some possible residual quantities can be present in the sample cavities like pits and pores.

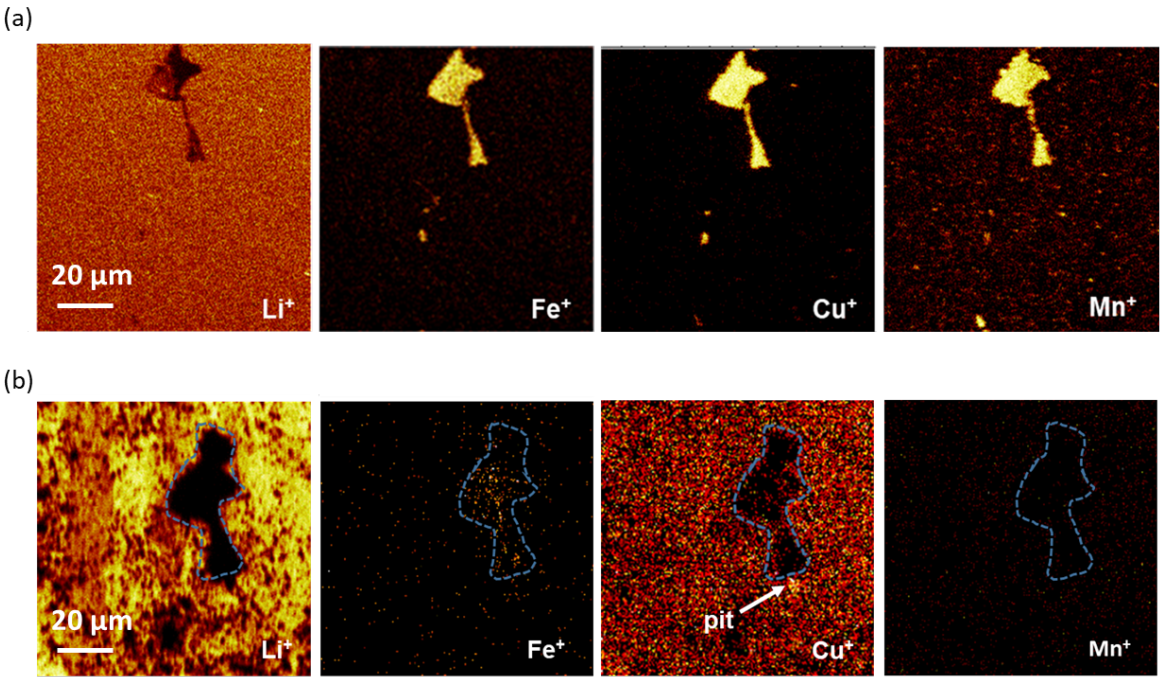

Figure 4.6: Positive (Li^+, Fe^+, Cu^+ and Mn^+) ToF-SIMS chemical mapping (100 µm $\times$ 100 µm) of AA2050-T8 sample in a region of interest comprising a selected Al-Fe-Cu-Mn IMP (a) before corrosion at the metallic substrate, (b) after immersion in 0.1M NaCl for 45 min performed at the metal / oxide interface (sputtered to 150 s)

A higher intensity of Cu^- and FeO^- observed in the area of larger pits indicates a relation of pits formation and presence of IMPs (Fig. 4.3). This conclusion was also confirmed by the local characterization of well identified Al-Fe-Cu-Mn IMP before and after corrosion (Fig. 4.5, 4.6 and 4.7). The analysis showed that pitting corrosion occurred in the area adjacent to the IMPs with a significant surface chemical modifications over IMPs.

However, the formation of pits, widely reported in literature [50, 58–60], is not the only evidence of the AA2050-T8 corrosion in NaCl electrolyte. Some important surface modifications occur over the matrix and over the IMPs during alloy exposure to chloride-containing electrolyte as demonstrated in our results. ToF-SIMS images performed in the oxide (65 s of sputtering) showed that the surface after corrosion is covered by a continuous Al oxide and hydroxide layer including both matrix and IMP (similar intensities of AlO_2^- and AlO_2H^- shown in Fig. 4.7 (a)). ToF-SIMS images performed after longer sputtering time (150 s) corresponding to the oxide/metal substrate interface showed differences in lateral distribution of Al oxide (AlO_2^-) and hydroxide (OH^-) indicating a more important thickness and highly hydrated oxide layer over the IMP (Fig. 4.7(b)). The difference in the layer thickness and/or composition over the IMP compared to the matrix can be related to

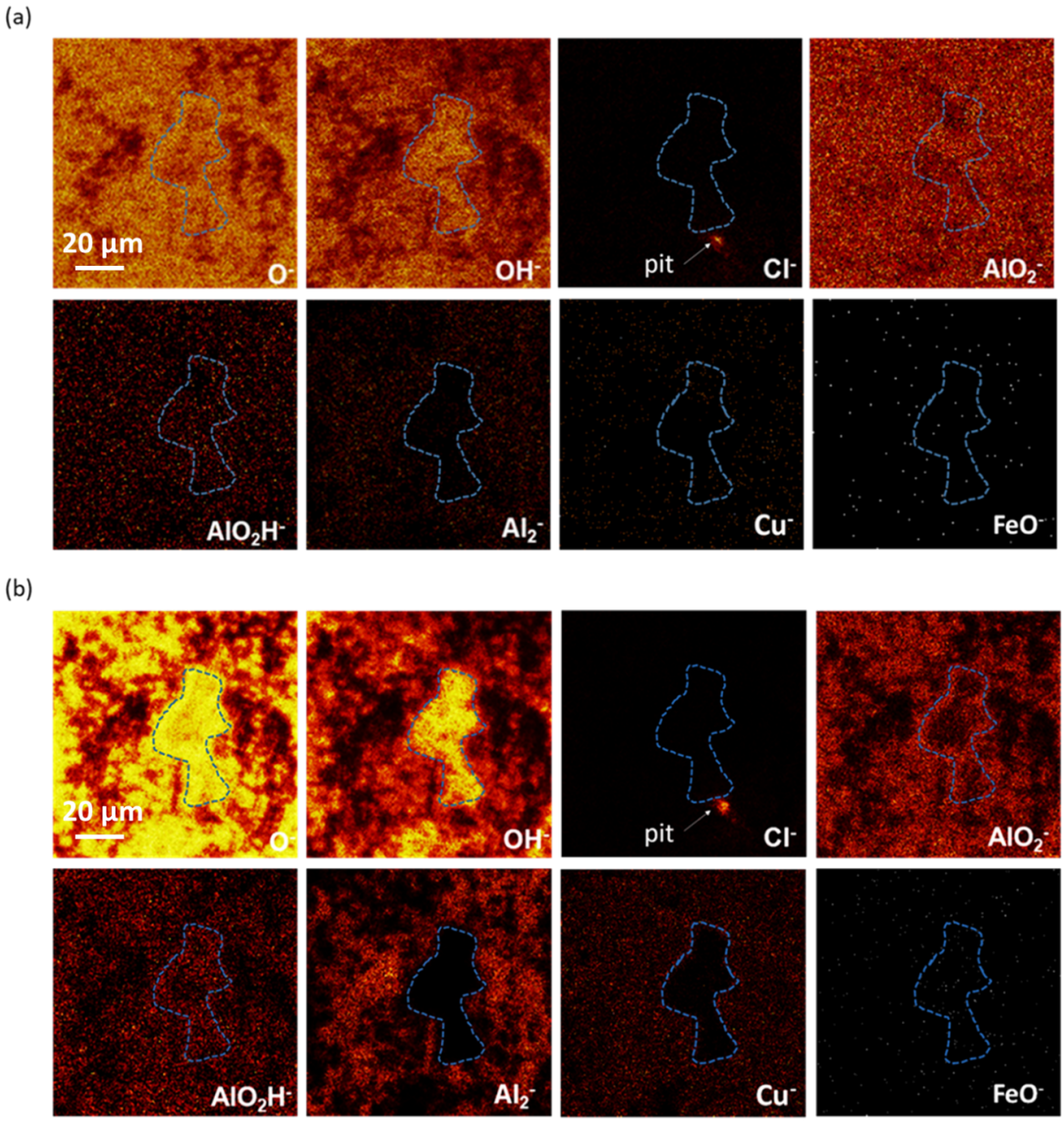

Figure 4.7: ToF-SIMS image chemical mapping (100 µm $\times$ 100 µm) of AA2050-T8 in the region of interest comprising a selected Al-Fe-Cu-Mn IMP after immersion in 0.1M NaCl for 45 min (a) in the oxide (sputtered to 65 s) and (b) at the metal / oxide interface (sputtered to 150 s)

different behaviors during the immersion in chloride solutions. This different activity of IMPs is related to the cathodic character of IMPs as previously evidenced for Fe-Cu-Mn-containing IMPs [41, 58, 169, 173–175]. Over the IMP a cathodic reaction of oxygen reduction (ORR) or hydrogen evolution (HER) occur [173]. Both cathodic reactions lead to the local pH change in the region adjacent to the IMP and dissolution of Al alloy. As a consequence, corrosion products (O and OH-rich) form a layer of deposit over the IMPs [44, 121, 175**?**]. Due to the high difference of the corrosion potential between the more cathodic (more noble) Cu-rich IMP and a more anodic Al alloy, Al matrix dissolution is enhanced. Moreover, a more severe corrosion at the interface of IMPs and matrix and initiation of pitting corrosion can be observed here (Figs. 4.5, 4.6 and 4.7). A similar behavior was demonstrated in previous works. Büchler [170, 171] using fluorescence microscopy to trace the distribution of corrosion products and reporting fluorescent rings around the IMPs, which indicated the stronger reaction at the IMP periphery. It was concluded that aluminium oxidation occurs at the border of matrix and cathodic IMPs while the oxygen reduction takes place over the IMPs. Grilli *et al.* [172] used Auger electron spectroscopy and scanning Auger microscopy to study the role of IMPs in pitting corrosion. Looking at corrosion products (rich in aluminium and oxygen), they also demonstrated the corrosion initiation at the boundary between IMPs and matrix which was similar to our results (Figs. 4.5, 4.6 and 4.7). Then, they also evidenced the corrosion propagation into the IMPs with a progressive accumulation of corrosion products over IMPs. Our results, most particularly pitting corrosion adjacent to the IMPs and increase of oxygen signal (corresponding to the corrosion products) at the IMP periphery (Fig. 4.7(b) and B.8), indicate the enhanced reactivity at the interface between IMP and Al matrix [169–171, 176].

Some important findings on the distribution of alloying elements can be highlighted. After corrosion, the ToF-SIMS images allowed us to conclude that the Cu enrichment can be observed in some pits corresponding to Al-Cu-Fe-Mn IMPs (Fig. 4.3) and also in pits formed close to the IMP (Fig. 4.6 and 4.7). An enrichment of more noble elements like Cu over the pitting area was already observed in the literature due to the preferential dissolution of more active elements like Al [166, 177]. It should be noted that the surface enrichment in noble elements (such as Cu) is not enough to shift the OCP to higher values [54].

Even more interesting is the distribution of Li. According to ToF-SIMS ion depth profiles (Fig.

4.2), the shape of Li profile showing a maximum intensity in the oxide and interface region indicates a Li enrichment inside the oxide layer on pristine AA2050-T8 surface. After corrosion, the Li profile shows more flattened shape over the oxide, interface and substrate regions indicating a preferential dissolution of Li as already observed before [121, 155] and the modification of the oxide layer composition. The similar intensity of the Li signal in the substrate region for the corroded sample as for the pristine sample indicates no changes of Li distribution in the alloy substrate. ToF-SIMS images performed at the oxide/metal substrate interface (Fig. 4.6) confirmed that Li is well present in the alloy substrate. In contrast with previous studies [121, 155], our results show that in the experimental conditions applied here (immersion at OCP in 0.1M Na Cl) there is no formation of stabilizing Li-containing layer, which could inhibit the corrosion of AA2050 as discussed by Gui and Devine [178] or Gharbi *et al.* [10]. The fact that Li is still present in the alloy matrix (including T1 phases) is important for the mechanical properties of the alloy but also for the corrosion behavior of the alloy. The presence of Li can have an influence on the pit formation in the matrix. It was demonstrated previously that in the alloys containing Li the pits are more superficial due to formation of locally more alkaline pH neutralizing the acid pitting areas and stopping the dissolution of Al matrix [6, 159–161].

4.1.5 Conclusions

In this study, ToF-SIMS ion depth profiles and chemical mapping were used to characterize the surface modifications of AA2050-T8 Al-Cu-Li alloy induced by pitting corrosion. A well-defined area including Al-Fe-Cu-Mn constituent IMP was characterized before and after corrosion in order to understand the influence of IMPs on the corrosion initiation and surface modifications of Al-Cu-Li alloy. The main findings are the following:

1. ToF-SIMS negative ion depth profiles show that the native oxide formed on the pristine AA2050-T8 surface is enriched in Li, but it undergoes dissolution once the sample is immersed in NaCl electrolyte. However, ToF-SIMS chemical mapping shows the presence of metallic Li in the matrix (including T1 phase),

2. Corrosion pits observed in the alloy show enrichment in chlorides and hydroxides, corroborat-

ing also with the presence of the trace of Cu and Fe as demonstrated by ToF-SIMS chemical mapping,

3. A thorough SEM and ToF-SIMS analysis of the alloy with a well-defined area of Al-Fe-Cu-Mn IMP showed that the vicinity of the IMP was a preferential site of pitting corrosion initiation due to the galvanic coupling between the more anodic character of the matrix and the more cathodic character of IMP,

4. A different oxide-hydroxide layer composition and/or thicker layer over Al-Fe-Cu-Mn constituent IMP formed due to the cathodic reactions and enhanced anodic dissolution of surrounding Al matrix leading to formation of deposit layer rich in O and OH on the surface of IMP.

4.2 Phase-dependent surface modifications evidenced by ToF-SIMS 3D chemical mapping

Abstract

The three-dimensional (3D) chemical mapping by means of time-of-flight secondary ion mass spectrometry (ToF-SIMS) represents a promising tool in imaging of pitting corrosion occurring on aluminium alloys in the presence of intermetallic phases as kink sites of corrosion initiation. In this paper, Tof-SIMS 3D chemical mapping combined with scanning electron microscopy (SEM) was performed to study the localized corrosion behaviour of Al-Cu-Li alloy (AA2050-T8) in a region of Al-Cu-Fe-Mn intermetallic particle (IMP). Initiation of corrosion was locally observed within the IMPs and between IMP and matrix substrate. Moreover, a modified oxide/hydroxide layer was observed over IMPs compared to matrix. This new layer is enriched with chlorides as well as hydroxides, namely Cu hydroxides. Distribution of Li on the corroded surface was revealed by ToF-SIMS 3D mapping. Some Li was detected over the alloy matrix, while no Li was present in the area of the IMP region where pitting corrosion occurred.

4.2.1 Introduction

Pitting corrosion of Al alloys is known to be the most frequent cause of failure of high-strength aluminium alloys [44, 179]. It is also considered as a precursor of stress corrosion cracking (SCC) and a potential origin for fatigue cracks [180–183]. Therefore, pitting corrosion is not only a lateral local breakdown of surface oxide but also can lead to in-depth oxide modifications. The localized corrosion is generally related to the chemical heterogeneities such as intermetallic particles (IMPs) on the surface. It has been shown that the Al-Cu-Fe-Mn IMPs are the preferential sites of pitting corrosion initiation in Al alloys [180–183]. Birbilis *et al.* [58] revealed the role of Al-Cu-Fe particles on the pitting corrosion of AA7075-T651 (Al-Zn-Mg-Cu) alloy and indicated that the cathodic behaviour of Al-Cu-Fe IMPs leads to the evolution of localized corrosion between matrix and IMPs. Boag *et al.* [59] have also shown that a preferential corrosion in NaCl electrolyte is associated with the presence of Al-Cu-Fe-Mn particles in the AA2024 Al-Cu-Mg alloy. This IMP-induced pitting corrosion has been usually investigated by conventional techniques such as scanning electron mi-

croscopy (SEM), energy-dispersive X-ray spectroscopy (EDX) [184, 185]. Some local techniques such as atomic force microscopy (AFM) [186], scanning Auger spectroscopy [187], and scanning Kelvin probe force microscopy (SKPFM) [188], can focus more precisely on local morphological or chemical surface modifications to reveal the influence of IMPs on the corrosion behavior of Al alloys. However, application of new techniques and development of new methods for detailed surface characterization of corroded areas including pits, oxides or corrosion products is necessary in order to be able to detect the traces of elements and to get information on their lateral and in-depth distribution. Therefore, three-dimensional (3D) chemical mapping with a high surface sensitivity is essential to better understand the corrosion mechanisms of heterogeneous materials such as aluminium alloys with intermetallic phases [189–191].

Based on the current state of the art, several 3D imaging techniques can be highlighted such as scanning transmission electron microscopy (STEM), X-ray computed tomography (XCT), *etc* [192–195]. In EM tomography (EMT), a series of EM images from the same sample can be collected though a range of angles and depth from which a 3D image can be reconstructed. It has been applied as an advanced technique to study the corrosion behaviour of different alloys [196–199]. Mingo *et al.*[197] and Laleh *et al.* [198] performed the EMT and X-ray CT characterization, which clearly revealed the 3D spatial structure of localized corrosion on the cast aluminium alloy A356 and 316L stainless steel, respectively. More advanced approaches do not only provide the 3D morphology but also the 3D chemical image. Synchrotron X-ray tomography is a well-established non-destructive technique down to the micrometer scale or even less [200]. It is non-destructive and allows for superior resolution (usually $\sim$ 1 µm) [201]. However, the chemical sensitivity of this kind of techniques is limited for the elements with lower atomic mass like Li, especially in low amount. Another 3D imaging technique, which is applied here in this work to study localized corrosion is time-of-flight secondary-ion mass spectrometry (ToF-SIMS). It is known to be an extremely sensitive surface technique, which is applicable to many types of solids by a dual-beam mode allowing the detection of spatial and lateral distributions of elements in 3D even in an extremely low amount [202]. This technique has been used in many domains such as biology, medical and other fields relevant to the chemistry [203–207]. Niehuis *et al.*[208] performed series of in situ TOF-SIMS/scanning force microscopy (SFM) measurements on both inorganic and organic solid sur-

faces, showing the potential of this technique for a wide range of applications. ToF-SIMS imaging was also applied to study the corrosion behaviour and surface treatment of materials. Mercier *et al.* [209] and Esmaily *et al.* [210] used 3D ToF-SIMS imaging to study the localized corrosion behaviour of Mg (99%) and Mg alloy, respectively, by revealing the spatial chemical structure of corroded surface. Stoica *et al.* [211] used ToF-SIMS 3D imaging to study the structure of trivalent chromium protection (TCP) coating on the AA2024 Al alloys and revealed different chemical structures of TCP coating over IMP and Al matrix. ToF-SIMS has high detection limits in depth and spatial resolution and is widely applied for analysis of Li in the Li-containing alloys or Li in electrode materials used in Li-ion batteries [212–215]. Therefore, based on the high sensitivity to low-atomic-mass element like Li and the applicability of spatial detection, ToF-SIMS chemical imaging is considered as a promising technique for the study of Al-Cu-Li alloys.

In this paper, ToF-SIMS 3D imaging combined with SEM/EDX characterization was used to study the localized corrosion of AA2050-T8 (Al–Cu–Li) alloy. A region of interest including an Al-Cu-Fe-Mn intermetallic particle (IMP) was selected and characterized before and after immersion in 0.1M NaCl. This paper aims to, not only, reveal the localized corrosion of Al-Cu-Li alloys with regards to the IMP, but also inspire the applicability of ToF-SIMS 3D imaging in the detection of localized chemical modifications of surface especially when low-atomic-mass species are involved.

4.2.2 Experiment

Samples

AA2050-T8 (Al-Cu-Li) alloy provided by Constellium, France was used in this study. The sample specification is presented in table 4.1. The size of specimens was 8.0 mm $\times$ 8.5 mm and the surface were prepared by mechanical polishing with SiC paper to 4000 grades then by alumina suspension down to 0.3 µm to mirror finishing. Then, the samples were successively sonicated in iso-propanol, ethanol and finally Ultrapure (UP) Millipore water and dried by filtered compressed air. The polished AA2050-T8 samples were immersed in 0.1 M NaCl electrolyte (VWR, 99.9% & UP Millipore water, resistivity $\geq$ 18 M$\Omega\times$cm) for 45 minutes and rinsed with UP Millipore water, dried and transferred for analysis by ToF-SIMS and/or SEM.

Surface characterization

Time-of-flight secondary ion mass spectrometry (ToF-SIMS) measurements were performed with an IONTOF ToFSIMS5 spectrometer (IONTOF GmbH, Munster, Germany) operating under high vacuum (10^{-9} mbar). A region of interest with Al-Cu-Fe-Mn IMP was first identified then the same region was first analyzed by 2D ToF-SIMS (corresponding to the surface characterization) before the immersion test and then by 3D ToF-SIMS imaging (surface and in-depth characterization) after immersion test. The identification of the sample surface was performed by marking the sample with the Cs^+ ion beam of the Ion-ToF spectrometer. The region of interest including the Al-Cu-Fe-Mn IMP was selected nearby the mark made with the Cs^+ ion beam and characterized by SEM and EDX. Then, ToF-SIMS chemical mapping was performed over the same area including the region of interest before and after corrosion. A dual beam mode with pulsed Bi^+ and Cs^+ beams (primary ion beam and sputtering beam, respectively) under BA–IMAGE mode was used to acquire 2D and 3D images. This mode allows us to get a very good lateral resolution of $\sim$ 200 nm. To also get a very good mass resolution, the initially wide primary Bi beam was splitted into 4 small pulses (Burst mode) providing a high mass resolution, M/ΔM $\sim$ 6000 (measured on the Si peak). The polished surface was slightly sputtered by a 45° 2 keV Cs^+ beam delivering a 100 nA current to remove the native oxide layer in order to perform 2D imaging of the metallic substrate in positive polarity using a 25 keV pulsed primary Bi^+ beam delivering 0.1 pA. Then, after corrosion, 3D imaging was performed by using the same Cs^+ sputtering beam and a 25 keV primary Bi^+ beam delivering 0.3 pA for analyzing. For both measurements, the sputtered area was 1000 µm $\times$ 1000 µm and the analyzed area was 50 µm $\times$ 50 µm. ToF-SIMS data treatment was performed with Ion-Spec software (version 6.8) and represented in 50 µm $\times$ 50 µm $\times$ 300 s. A schematic presentation of the principle of 3D ToF-SIMS chemical mapping based on the 2D successive maps recorded after sputtering at different depths of sample is presented in Fig. 4.8. 2D chemical maps were performed in total and the sputtering time between each 2D image was 4 s. The final 3D chemical map represents a stack of 2D images performed at different depths.

Microscopy characterization

SEM and EDX measurement by Zeiss Ultra55 microscope with high-resolution field emission gun (Schottky SEM-FEG) were performed to select the region of interest with an Al-Fe-Cu-Mn IMPs and study the corresponding corrosion morphology.

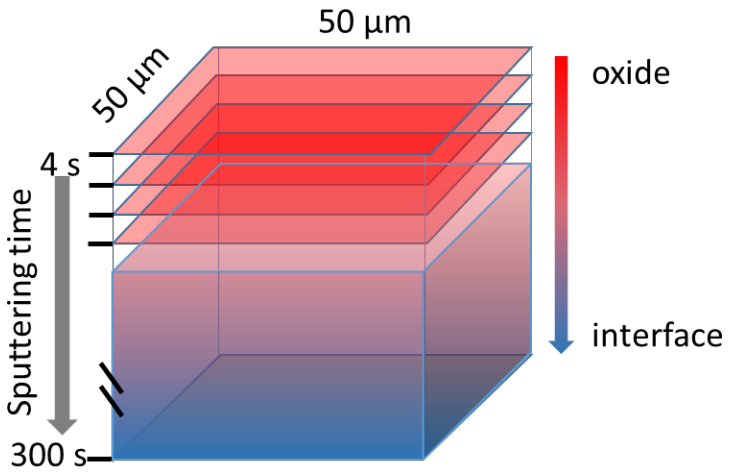

Figure 4.8: Schematic representation of 3D ToF-SIMS chemical mapping principle performed by successive acquisition of 2D chemical maps (50 µm × 50 µm) each 4 s (in total 76 images) from the extreme surface through the oxide down to the interface corresponding to 300 s of in-depth sputtering.

4.2.3 Results and discussion

The SEM images with the same area of Al-Cu-Fe-Mn IMPs before and after corrosion are presented in Fig. 4.9 (a) and (b). According to the SEM (BSEs) image, the IMPs is heterogeneous and the periphery of the IMPs appears brighter indicating higher molar weight and some differences in the chemical composition within the IMP. This compositional heterogeneity was already observed previously on AA3003, an Al–Mn alloy [216, 217]. EDX analysis in the center of IMPs shows that the chemical composition of detected region of IMP was 71.7 at% Al, 13.3 at% Cu, 7.5 at% Fe and 7.5 at% Mn. The same sample region but slightly enlarged with reference to the SEM micrograph comprising the same IMPs (marked in a blue rectangle in Fig. 4.9) was analyzed by ToF-SIMS 2D chemical mapping using a positive mode, which is more sensitive to metallic species [189, 209]. Before analysis the native oxide layer present on the surface of AA2050 was removed by sputtering. ToF-SIMS 2D chemical mapping shows a high intensity of Cu^+, Fe^+, Mn^+ signals, and lower intensity of Al^+ in the area of IMP indicating that the selected IMP was a typical Al-Cu-Fe-Mn phase. According to literature, and our previous TEM results [164], Li in AA2050-T8 is principally observed in the T1 phase (Al_2CuLi), which is homogeneously distributed in the matrix [164, 218]. However, the lateral resolution of ToF-SIMS mapping, which is around 200 nm, is not sufficient to observe the nanometer-sized precipitates in the alloy matrix. Thus, it can be concluded that at

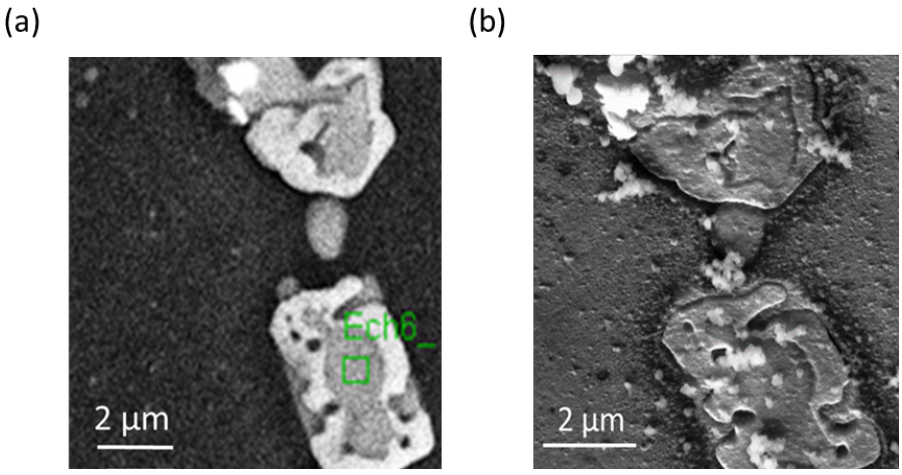

Figure 4.9: Scanning electron microscopy performed in the same region of the AA 2050-T8 sample comprising Al-Fe-Cu-Mn IMP (a) before immersion (backscattered electrons (BSEs)) and (b) after immersion (secondary electrons (SEs)) in 0.1M NaCl for 45 min

the micrometric scale a homogeneous distribution of Li over the whole surface of the matrix can be observed. Slightly lower intensity of Li signal was observed in Al-Fe-Cu-Mn IMPs compared to the alloy matrix as shown in Fig. 4.10. Similarly to these results, the presence of Li was previously observed in the Al-Fe-Cu-Mn by Ma *et al*.[62] and MacRae MacRae *et al*. [61] by Electron energy-loss spectroscopy (EEELS) and soft X-Ray emission spectroscopy, respectively.

After immersion of AA2050-T8 sample in 0.1M NaCl electrolyte for 45 min first signs of corrosion appeared in the selected area around and over the Al-Cu-Fe-Mn IMPs as shown in Fig. 4.9 (b). Most particularly trenching is visible around IMPs. As discussed in the literature, an enhanced dissolution of Al matrix occurs close to the Al-Cu-Fe-Mn IMPs, which is induced by the galvanic coupling between the cathodic IMPs and more anodic alloy matrix [47, 167]. However, it should be noticed, that the compositional heterogeneity mentioned above, (Fig. 4.9 (a)) can result in localized corrosion attack inside the IMP as observed in SEM in Fig. 4.9 (b) and as also discussed in the literature [216, 219].

ToF-SIM 3D chemical images were recorded in the same area on the sample surface after corrosion (Fig. 4.11). As explained in the experimental part and presented in Fig. 1, the sequence of 2D successive chemical images was used to reconstruct a 3D chemical image (50 µm $\times$ 50 µm $\times$ 300 s). Fig. 4.11(a) (b) and (c) present the 3D maps of AlO_2^- (m = 58.9728 u), AlO_2H^- (m=59.9812 u) and $Al_2{}^-$ (m = 53.9634 u) signals. These signals are characteristic of Al oxide, Al hydroxide and Al metal, respectively. According to Fig. 4.11(a) and (b), the 3D image of AlO_2^- and

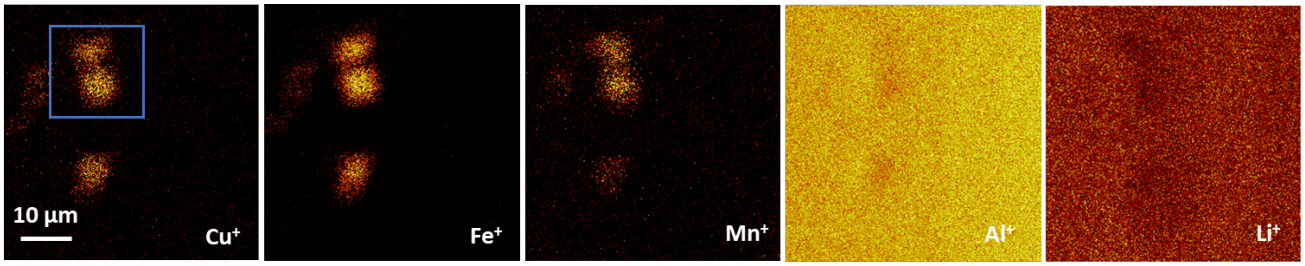

Figure 4.10: ToF-SIMS 2D chemical images (50 µm × 50 µm) of Cu^+, Fe^+, Mn^+, Al^+, Li^+positive ions on the pristine AA2050-T8 sample comprising a selected Al-Fe-Cu-Mn IMP before immersion. A blue rectangle marked in the Cu^+ image corresponds to the region of SEM micrograph presented in Fig. Fig. 4.9

AlO_2H^- show a relatively homogeneous and high intensity of Al oxide/hydroxide signal over the whole analyzed volume. The slightly lower intensity of AlO_2^- signal over IMPs region presented in the plan view of 3D image can correspond to the morphology effect of corroded surface and/or the oxide breakdown over this area. In Fig. 4.11(c) the increased intensity of Al_2^- in the bottom of the cube of matrix region (at the oxide/metal interface after 300 s of sputtering) can be observed but not over the IMPs region. The difference of Al_2^- intensity means that within the sputtering depths (300 s), the oxide/substrate interface in the area of IMP has not been reached but the oxide/substrate interface was reached in the matrix region. It should be noticed also that the lower Al_2^- signal intensity over the IMPs after 300s of sputtering can be also influenced by a lower quantity of Al in the IMPs than in the alloy matrix and/or preferential dissolution of Al induced by pitting corrosion. The differences in the intensity of Al_2^- in the area of IMPs and matrix will be discussed hereafter.

Cl^- (m = 34.9696 u) and OH^- (m = 17.0048 u) depth profiles were recorded to observe the corrosion products and the presence of some residues of NaCl. The data for these ions are presented in Fig. 4.11(d) and (e), respectively. Cl^- is present on the top of the surface and then is found locally over the IMPs region within the oxide layer. This higher intensity of Cl^- over the IMPs can be clearly observed in the plane view map of Cl^-. The presence of Cl^- confirms the localized corrosion occurring over this area, which was followed by the oxide breakdown over IMPs. Moreover, a slightly higher intensity of OH^- is also observed through the oxide in the IMPs region. Different to the distribution of Cl^-, some OH^- signal is also observed in the matrix region. The presence of OH^- in the matrix over the whole depth of the oxide corroborates with the high intensity of AlO_2H^-. The chlorides and hydroxides as the pitting corrosion products has been reported previously[172, 189, 220].

Cu^- (m = 62.9268 u), $CuOH^-$ (m = 79.9354 u) and Li^- (m = 7.0168 u) signals were also plotted to represent the distribution of the principle alloying elements. Cu^- and $CuOH^-$ ion signals (Fig. 4.11(f) and (g), respectively) show also higher intensities over IMP region through the oxide layer, similar to the Cl^- and OH^- signals. This enrichment with more noble elements such as Cu over the corroded area was already observed in the literature and explained by the preferential corrosion sites in case of aluminium alloys with Cu-rich IMPs [43, 221–224]. The origin of this enrichment can be the preferential dissolution of Al induced by local submicron sized compositional heterogeneities within the IMP. As shown in Fig. 4.11(g), $CuOH^-$ signal in the matrix region is lower than in the intermetallic particle region, and is similar to the distribution of OH^-, indicating that copper hydroxide is one of the corrosion products. The Cu^- ion signal over matrix region is more intense at the oxide/metal interface indicating that the Cu^- mainly corresponds to the metallic state of copper, which can be found in the alloy substrate.

Fig. 4.11(h) shows a homogenous distribution of Li through the oxide layer in the 3D image of Li^- signal (m = 7.0168 u). However, the plane view clearly shows that no or a very low Li signal is observed over the IMPs, indicating a local Li dissolution. These results are in agreement with our previous findings where no Li was observed in the area of corrosion [189]. However, the lower signal intensity over the IMP can also be a result of sputtering time not sufficient to reach the oxide /metal interface over this region or preferential dissolution of Al and other light elements like Li in the pitting corrosion zone comprising the IMPs. Hereafter, the ion depth profiles retrieved from the area of IMP and alloy matrix regions are shown and discussed in details.

In order to better visualize the distribution of species, the most characteristic ions of localized corrosion are overlayed in Fig. 4.12: AlO_2^- in blue, Cl^- in green and Cu^- in orange. In this figure, the intensity of the AlO_2^- signal was slightly attenuated with respect to Fig. 4.11 (b) to make all 3 signals clearly visible. As discussed above (Fig. 4.11 (b)), the AlO_2^- is observed in the whole analyzed volume. Discontinuity of signals in depth, which appears here in Fig. 4.12, is a measurement artifact related to the ion current variation during the measurements. As observed here a significant difference in chemical composition can be observed between IMP and matrix region. The Cl^- signal shows a high intensity over the first seconds of sputtering corresponding to the top surface of the alloy and then an increasing intensity is observed above Cu-rich intermetallic particle as ob-

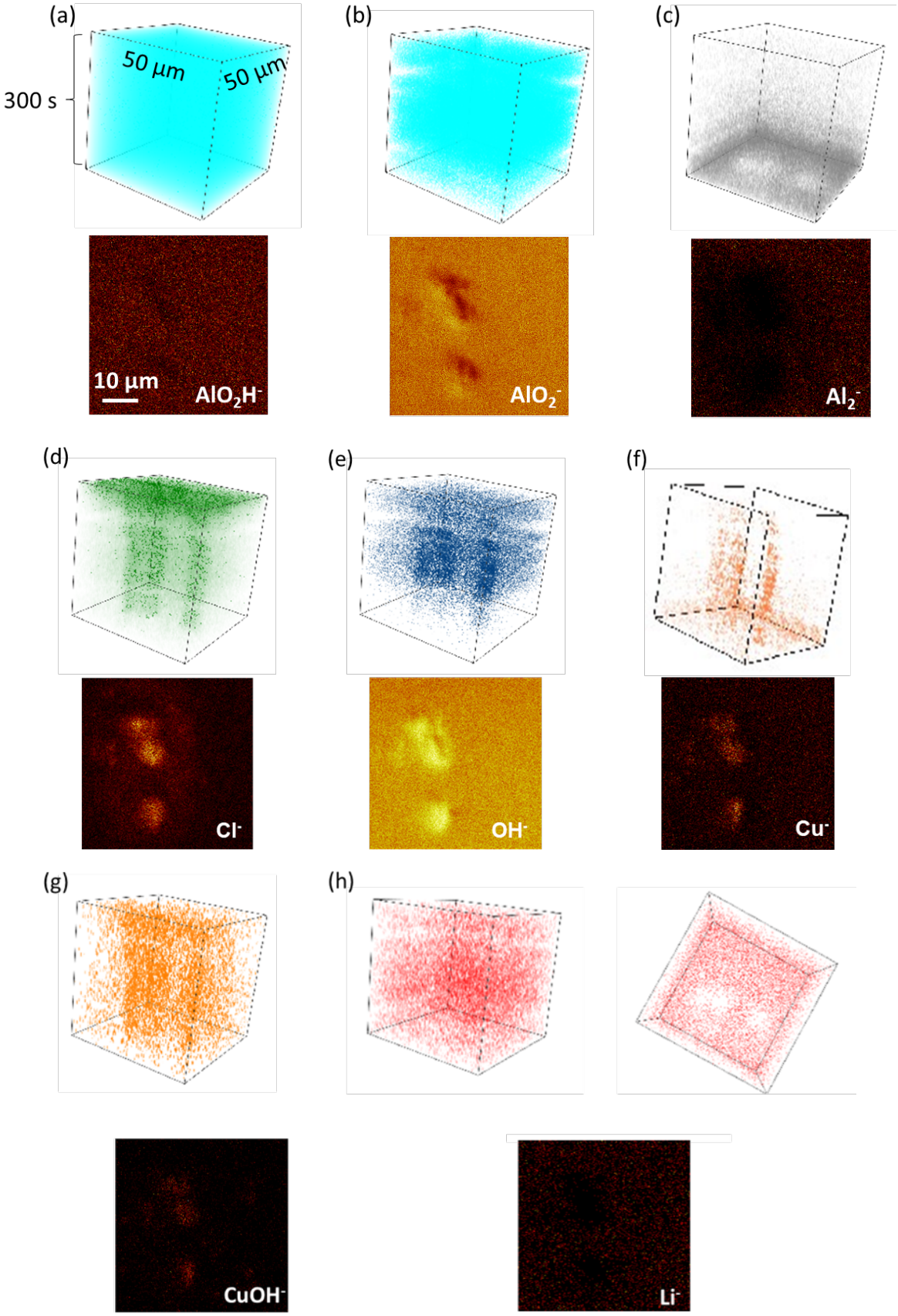

Figure 4.11: ToF-SIMS 3D chemical images (50 µm × 50 µm × 300 s) and corresponding plan views (obtained by summing stacks of 2D images at different depths) for (a) AlO_2H^-, (b)AlO_2^-, (c) Al_2^-, (d) Cl^-, (e) OH^-, (f) Cu^-, (g) $CuOH^-$, (h) Li^- (additional 3D top view image) obtained on the corroded surface (after immersion in 0.1 M NaCl) comprising a selected Al-Fe-Cu-Mn IMP

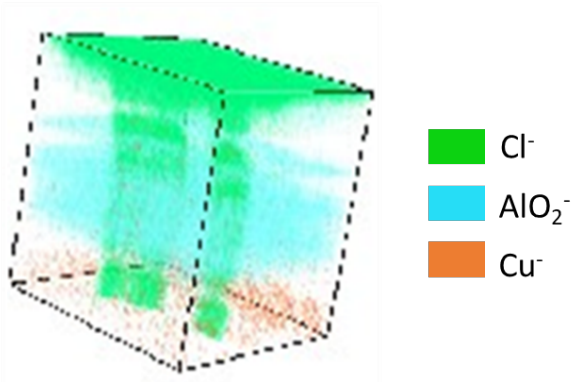

Figure 4.12: ToF-SIMS 3D map (50 µm × 50 µm) showing the overlay of AlO_2^- (blue), Cl^- (green) and Cu^- (orange) obtained on the corroded surface (after immersion in 0.1 M NaCl) comprising a selected Al-Fe-Cu-Mn IMP

served previously for Al_2Cu IMPs in Al-Cu model alloy [190]. At the oxide/alloy substrate interface Cu enrichment is also observed over the matrix region.

To gain more insight into the differences between IMPs (corroded) region and matrix after corrosion, distinct ion depth profiles (for IMP and matric region) were reconstructed from 3D maps. As shown schematically in Fig. 4.13 (a), three regions can be distinguished: the blue IMP region corresponding to $\sim$ 2% of the total surface, the green matrix region corresponding to $\sim$ 78% of surface, and the rest, grey area, considered as the boundary between IMPs and matrix. The ion depth profiles corresponding to matrix and IMP regions are plotted separately to see in details the in-depth distribution of the different species. The grey region was excluded as a transitory region between the matrix and the IMPs regions. In order to easier compare the intensity of different ions for IMP and matrix regions, the intensity of depth profiles was normalized by the analyzed area and presented in Fig. 4.13 (b) and (c), respectively.

The signal intensity variations as a function of sputtering time is observed for the matrix region and IMPs region in Fig. 4.13 (b) and (c), respectively. It reflects the modifications of the chemical composition and the in-depth structure of the analyzed oxide.

As shown in Fig. 4.13(b) and (c), OH^- and AlO_2^- and AlO_2H^- ion depth profiles for both IMPs and matrix for the sample after corrosion immersion test have similar intensity and shape, which can indicate a similar chemical structure of the aluminium oxide/hydroxide layer over both regions.

The low Al_2^- signal intensity in the area of IMPs (in Fig. 4.13 (c)) over the whole sputtering time (300 s) indicates a low quantity of metallic aluminium in the IMPs region induced by preferential dis-

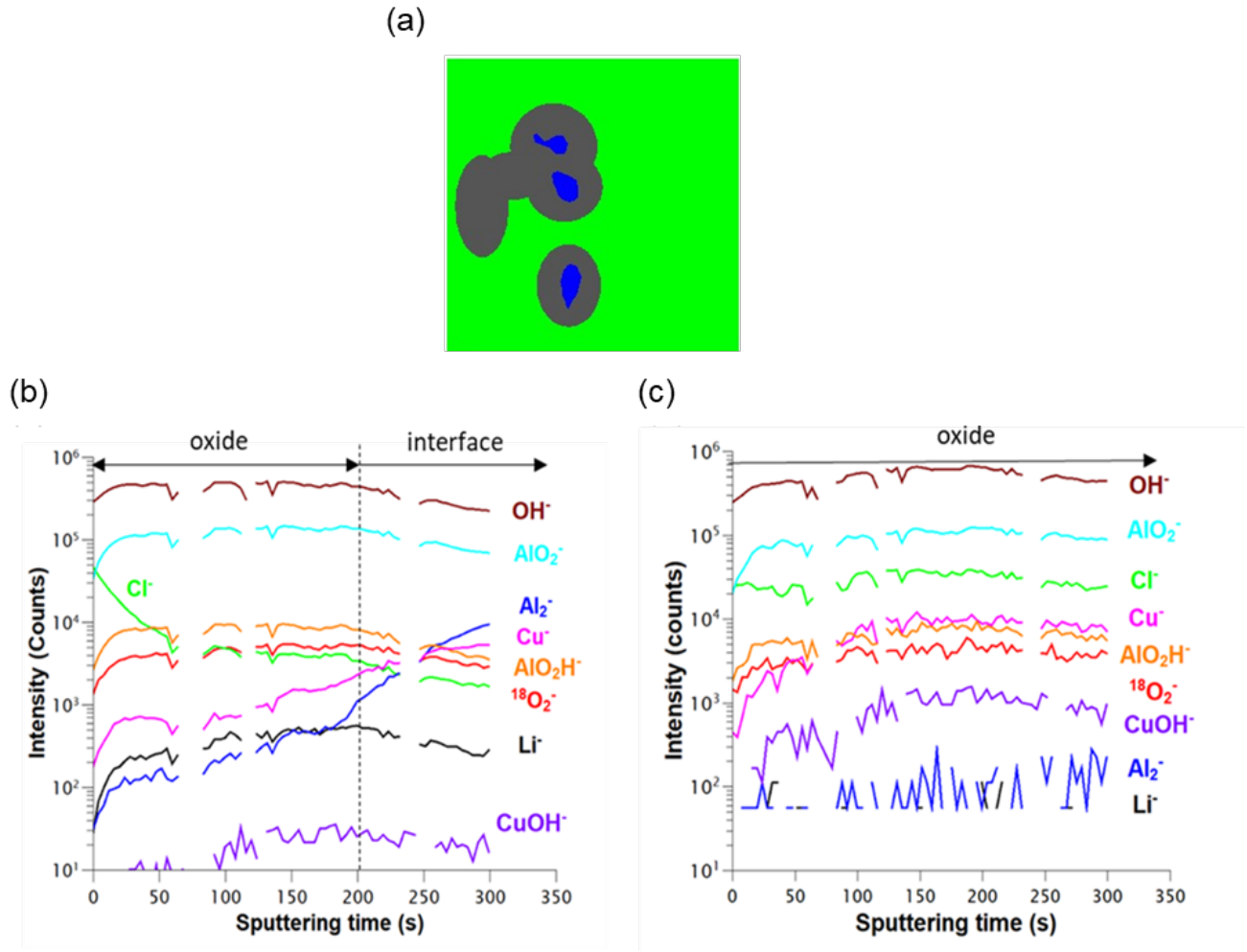

Figure 4.13: (a) ToF-SIMS 3D image reconstruction for the region of interest after corrosion with selected IMP showing three regions corresponding to IMPs (blue), matrix (green) and boundary between IMPs and matrix (grey) for reconstruction of the separated ion depth profiles; (b) ToF-SIMS ion depth profiles of matrix region corresponding to the green area; (c) ToF-SIMS ion depth profiles of IMPs region corresponding to the blue area. The intensity was normalized by the analyzed area

solution of Al within the IMPs and/or that the oxide/metal substrate interface has not been reached after 300 s sputtering. In the case of the matrix region, a step intensity increase of Al_2^- signal from 10^2 to 10^4 is already observed from 200 s of sputtering indicating the interface with substrate region (Fig. 4.13 (b)). The longer sputtering time necessary to reach the oxide/metal interface for the IMPs can be related to the formation of a thicker and/or with a different composition layer like previously demonstrated [189]. Using the same approach (3D ToF-SIMS chemical mapping) it was demonstrated that on the polished model Al-Cu alloy, the native oxide layer is thinner over the Cu-rich IMPs compared to Al matrix [190]. However, after immersion in NaCl electrolyte, the large difference in corrosion potentials of more noble Cu-rich IMP and less noble Al-based matrix as well as local micrometric chemical heterogeneities within the IMPs (as shown in Fig. 4.9) induce localized cathodic and anodic reactions, respectively. This leads to the dissolution of the Al alloy in the region adjacent to the IMP and also to the preferential dissolution of Al inside the IMPs leaving Cu remnant above IMPs. The Al dealloying can conduct to the particle etching out [167]. The possible initially thinner oxide layer over the Cu-rich IMPs compared to Al matrix [190] can lead to locally higher cathodic reactivity within the IMP and increase the rate of oxygen reduction reaction, as shown by DFT calculations [225]. This implies the corrosion initiation in the areas enriched with noble elements like Cu (over IMP) and then corrosion propagation with dissolution of Al matrix leading to particles trenching as observed by time depended SKPFM studies on Al-Cu-Fe-Mn particles in AA7075-T6 [167]. In the further stages, both continuous cathodic and anodic reactions will enhance locally the formation of a new layer enriched with the corrosion products over IMP and/or near IMP. In our previous studies by ToF-SIMS 2D images, we focused on the reactivity of matrix vs that of the IMPs and demonstrated the formation of thicker and/or modified in terms of composition oxy-/hydroxy layer over Al-Cu-Fe-Mn IMPs in comparison to the matrix [189]. The corrosion mechanism discussed here is consisted with our previous studies, showing here a formation of modified oxide/hydroxide layer over IMPs. The chemical modifications of this layer, can be confirmed by a higher Cl^-, Cu^- and $CuOH^-$ signal intensities in the IMPs region with reference to the matrix region as demonstrated by the in-depth ion profiles in Fig. 4.13 (b) and (c). The enrichment of the Cl^- through the oxide layer above IMPs while a rapid decrease of the Cl^- signal in the Al matrix from the top of surface to the interface is observed. Similar distribution of Cu^- and $CuOH^-$

signals is observed in the IMPs depth profiles with higher intensity through the oxide layer. This result confirmed that the corrosion product is located over the IMPs and the chemical structure of oxide through the depth is homogenous since the intensity of each element is relatively stable at different sputtering time.

Contrary to the IMPs, a very low signal of $CuOH^-$ is observed in the Al matrix region and the corresponding Cu^- signal keeps increasing from oxide to the interface, reflecting a metallic state. A marked difference between the depth profile of Li in the IMPs and in the matrix is observed. Some Li is detected in the oxide layer on the matrix while no trace of Li was found in the IMP region. The presence of Li in the oxide over the matrix can be explained by a high stability of the oxide and no corrosion occurring in this area. The lack of Li signal over the IMPs can be principally explained by the absence of Li in the Al-Cu-Fe-Mn IMPs. As shown in Fig. 4.11(h) and Fig. 4.13, ToF-SIMS provides a spatial detection of Li in Al-Cu-Li alloy before and after corrosion, even in a low amount ($\leq$ 1 wt%). This is a significant advantage for the characterization of Al-Cu-Li alloys (after various surface treatments) since many experimental techniques are less sensitive to the species with low atomic mass and low initial concentration in the bulk sample.

It should be noted that these differences in the intensities of Cl^- and Cu^-, $CuOH^-$ and Li^- signals over the IMPs and matrix indicate some variations in the composition of layers formed in the both regions. Although, the significant intensity increase of Cl^- and Cu^-, $CuOH^-$ and Li^- can be observed, the principal compounds of the layers are oxide (AlO_2^-, O_2^-) and hydroxide (OH^-) (Fig. 4.13). Since the sputtering time of the oxide above IMP is at least 1.5 times longer than that of the matrix a thicker oxy-/hydroxy layer can also be proposed. The formation of thicker oxide layer over the IMPs was proposed previously. Davoodi *et al.*[188] used AFM/SECM to study the topography of corroded Al alloy and a greater height was observed on the IMPs, but this protrusion of the IMP was explained by their slower dissolution kinetics of the oxide layer over IMPs and the attack of IMPs. However, due to the limitation of analysis techniques, it was difficult to identify if the local protrusion was induced by the higher oxide thickness and/or the difference in the topography of metal substrate. With other techniques like TEM or FIM-SEM, it is also difficult to detect the fragile oxide layer after corrosion especially if a particular and laborious sample handling and surface preparation are necessary. Cu enrichment and the enhanced oxide coverage was observed along

the attacked Al-Cu-Fe-Mn particle/matrix interface region by SKPFM and AFM studies of AA7075-T6 corrosion [167]. Similarly to this study, it can be concluded that here it was observed that the primary corrosion attack started on Al-Cu-Fe-Mn IMPs. This preferential attack of IMPs in the first stages of corrosion is associated with the higher quantity of noble elements in the particles. It is followed by surface modifications with formation of locally thicker layer with different composition. The dissolution of surrounding matrix can occur in further stages of corrosion. The combined different modes of ToF-SIMS characterization (3D chemical imaging and ion-depth profiling) allowed to have more insights into the mechanisms of phase-dependent surface modifications in AA2050-T8 alloy induced by corrosion and most particularly to structure, thickness and chemical composition of the modified layer over the attacked area.

4.2.4 Conclusions

In this paper, ToF-SIMS 3D chemical mapping was performed on a corroded region of interest of AA2050 Al-Cu-Li alloy including Al-Cu-Fe-Mn IMPs. A high sensitivity and high detection limit of ToF-SIMS using 3D chemical mapping mode allowed us to visualize a distribution of low atomic mass species like Li. The trace of Li was clearly detected by 3D mapping after corrosion. No Li was observed in the oxide over the IMPs while trace of Li was detected in the oxide over the matrix. The ToF-SIMS 3D images and ion depth profiles which can be retrieved from the images can provide a better view on the lateral or in-depth distribution of different species. According to the ToF-SIMS results, a modified layer was observed over the corroded IMPs with Cl, OH and Cu enrichment. Moreover, a formation of locally modified layer thickness on the attacked area corresponding to the IMPs is proposed based on the significantly longer sputtering time according to ToF-SIMS depth profiles.

4.3 General conclusion

In this chapter, the corrosion behaviour of AA2050-T8 Al-Cu-Li alloy in aggressive electrolytes was discussed. Large Al-Cu-Fe-Mn IMPs whose diameter are over 1 µm is considered as the initial site for the pitting corrosion. The corrosion morphology and mechanism of Al-Cu-Fe-Mn IMPs

in AA2050-T8 (Al-Cu-Li alloy) in 0.1 M NaCl electrolyte are studied. ToF-SIMS depth profiles, 2D imaging, 3D imaging combined with SEM were performed on the corroded surface in order to study the surface modifications induced by corrosion.

Two randomly selected Al-Cu-Fe-Mn IMPs were measured before and after corrosion by ToF-SIMS 2D and 3D chemical mapping. Preferential sites of corrosion initiation were evidenced in the alloy matrix close to or over the Al-Fe-Cu-Mn IMPs. A local distribution of chlorides and hydroxides in the pits, enriched in Cu and Fe. Cu hydroxides was proven to be one of the corrosion product in the pit area. A formation of an oxide-hydroxide layer with different composition and/or higher thickness over the IMPs than over the alloy matrix was evidenced. Distribution of Li on the corroded surface was revealed by ToF-SIMS 3D mapping. Some Li was detected over the alloy matrix, while no Li was present in the area of the IMP region where pitting corrosion occurred. Metallic lithium was still present in the matrix.

An advanced performance of ToF-SIMS on the 3D detection of pitting corrosion was illustrated particularly regarding with high sensitivity to low atomic mass species like Li. The ToF-SIMS 3D maps can also be retrieved as plan view images and separated depth profiles for a better review on the lateral and in-depth observation. Moreover, the trace of Li was clearly detected in 3D maps after corrosion. No Li was observed over the oxide over the IMPs while trace of Li was detected in the oxide over the matrix indicating that the Li in the oxide dissolved after pitting corrosion.

Chapter 5

Surface modifications induced by pretreatments and effects on the chemical structure of TCP conversion coating on Al-Cu-Li alloy (AA2050)

This chapter reproduces a to-be-submitted version of paper for publication in Surface and Coatings Technology with a reference:

Li M, Zanna S, Seyeux A, Wiame F, Marcus P, Światowska J. Surface modifications induced by pretreatments and effects on the chemical structure of TCP conversion coating on Al-Cu-Li alloy (AA2050). Journal of the Surface and Coatings Technology.

Abstract

Trivalent Chromium process (TCP) was developed as a promising conversion process aiming at enhancement of corrosion properties and adhesion of aluminium alloys. A set of surface pretreatments such as alkaline etching and acid pickling is usually applied on aluminium alloys before TCP deposition in order to optimize their properties. In this work, the surface modifications of an Al-Cu-Li alloy (AA2050) at different steps of pretreatment (alkaline degreasing and acid pickling) and subsequent trivalent chromium process (TCP) are investigated by X-Ray photoelectron spectroscopy (XPS), time-of-flight secondary ion mass spectrometry (ToF-SIMS) and scanning electron microscopy (SEM). A significant influence of the pretreatment on the subsequent TCP treatment is evidenced by comparing the TCP layers formed on polished and pretreated samples. A thicker TCP conversion coating (outer oxide) with less cracks is formed on the pretreated surface compared to the polished one. Moreover, a Cu enrichment is evidenced in the TCP layer of the pretreated sample. Linear sweep voltammetry confirms that TCP coating plays a beneficial role on corrosion resistance with a decrease of cathodic current for the TCP coated polished samples. However, a higher (10 times) cathodic current is observed on the TCP layer of pretreated samples and the related influence of Cu enrichment on the TCP coating is discussed.

5.1 Introduction

Most industrial alloys, after being cast or formed into desired shapes, are highly deformed and contaminated by organic industrial lubricant. The native oxide on the alloy surface with contamination and defects is not good enough to fulfil the requirements of industrial applications. Therefore surface treatments are necessary in order to optimize the surface properties before going into service. In the aerospace industry, a typical surface treatment for Al alloys consists of alkaline degreasing, acid pickling then anodizing and /or conversion coating. The alkaline degreasing and acid pickling aim at preparing a more morphologically and chemically homogeneous surface for next treatments like conversion coating [65–67]. During degreasing, preferential dissolution of organic contaminations, native oxide layer and Al substrate occurs and a new oxide layer with modified composition and thickness is formed [83–85]. Hughes textit*et al.* [226] found that insoluble remnants, enriched

with Mg, Zn, Si, and Fe, developed during alkaline cleaning on the surface of AA2024 due to the preferential dissolution of Al. Lunder *et al.* [227] found a more severe pitting corrosion on the alkaline cleaned surface due to the remaining Fe-containing IMPs. Therefore, the degreasing is not efficient enough since many remnants and IMPs are can still be present on the surface. The role of acid pickling is to remove these remnants, IMPs and the oxide after degreasing and provide a better surface finishing for the subsequent treatments [92, 93].

Conversion coatings are normally performed after degreasing and pickling for a higher corrosion resistance and better adhesion for primer. It consists of a thin barrier coating made of chromium fluorides , oxides and aluminium oxide as well as other chemical compounds. The chromate conversion coatings (CCC) are one of the most commonly used coatings in the aircraft industry. During the CCC process, Al alloys chemically react with hexavalent chromium (Cr^{VI}) species and form a thick complex trivalent chromium (Cr^{III}) oxide layer with high corrosion resistance and self-healing properties [95, 96]. However, due to the high toxicity of (Cr^{VI}), the CCC is restricted by the regulation of the European commission - REACH [74]. Therefore, new environmental friendly approaches are developed and trivalent chromium process (TCP) is considered as a promising solution [77–79]. TCP coating is a pH-driven deposition process based on Zr^{IV} and Cr^{III} formulations [103–105]. When a sample is placed into the TCP bath, the surface is first activated by F^- ions resulting in the dissolution of aluminium oxide and metal substrate. Due to the consumption of protons (cathodic reactions), the local pH increases over the surface and promotes the deposition of Cr and Zr species and results in the formation of a multilayer structure of hydrated metal oxide coating consisting of an outer layer composed of hydrated zirconia ($ZrO_2 \cdot n\,H_2O$) and chromium hydroxide ($Cr(OH)_3$) and inner fluoroaluminate layer (e.g. O_xAlF^{3+x}) [228]. The thickness of TCP layers is around 40 nm—120 nm depending on the deposition conditions [103]. Qi *et al.* [229–231] used Rutherford backscattering spectrometry (RBS), SEM, AES and XPS to characterize the TCP coating on the AA2024 Al alloy and indicated a similar corrosion resistance compared to other chromate conversion treatment. They also found improved performances resulting from reduced number of intermetallic particles when the surface is pretreated by alkaline and de-oxidizer [230]. The effect of pretreatment (degreasing and pickling) on the TCP coating of AA2024 was also stud-

ied by Viroulaud *et al.* [133] who indicated a significant influence of surface pretreatments on the TCP coating homogeneity and coverage.

Most research works relevant to the surface pretreatment and conversion coating are performed on the conventional Al alloys such as AA2024 or AA7075 and few studies focused on more advanced Al-Cu-Li alloys. Gharbi *et al.* [10] used inductively coupled plasma atomic emission spectrometry (ICP-AES) to measure the dissolution rate of alloying elements in AA2050 Al-Cu-Li alloy during alkaline and acid cleaning. They revealed a significant Li and Al dissolution and enrichment of Cu on the surface after alkaline cleaning. When the surface is placed into nitric acid bath, remnants, comprising Cu, Fe, Mn and Mg, dissolve. A development of advanced materials such as on Al-Cu-Li alloys and adaptation of surface (pre)treatments are necessary to improve their properties. Therefore, in this paper, the surface modifications of Al-Cu-Li (AA2050-T8) alloy during alkaline degreasing, acid pickling and TCP coating is studied. Moreover, the effect of pretreatment on the TCP coating is discussed.

5.2 Experiment

Sample preparation

The Al-Cu-Li alloy studied in this paper is an industrial AA2050 alloy under T8 ageing process provided by Constellium France. The specifications of alloying elements in AA2050-T8 is presented in Table 5.1. The specimens were cut into 8.0 mm $\times$ 8.5 mm samples. Surface preparation was performed by mechanical polishing with SiC paper from 320 down to 4000 grades then mirror polishing by alumina suspension down to 0.3 µm.

After polishing, samples were cleaned by successive ultrasonic baths in iso-propanol, ethanol and finally Ultra-pure (UP) Millipore® water (resistivity $>$ 18 MΩ cm), dried by filtered compressed air, then exposed to different baths for surface treatment as presented in Fig. 5.1. As shown in Fig. 5.1, each bath has constrained temperature, agitation rate and pH. Firstly, the polished sample was degreased in a sodium tripoliphosphate (40 g/L) and borax (40 g/L) solution (pH $\sim$ 9) with Turco 4205 additive (5 mL/L) at 60 $\pm$ 5 $^{\circ}$C for 20 min. Then the sample was immersed in SOCOSURF A1858 (40 %) and A1806 (10 %) aqueous solution (containing HNO_3, H_2SO_4 and Fe(III), pH $\leq$ 1)

Table 5.1: Specifications of alloying element (wt% & at%) of the AA2050 alloy

Cu	Li	Mg	Zn	Mn	Ag	Zr(max)	Fe(max)	Si(max)
3.2–3.9	0.7–1.3	0.2–0.6	0–0.25	0.2–0.5	0.2–0.7	0.14	0.1	0.08
1.5–1.6	2.8–4.8	0.2–0.7	0–0.1	0.1–0.2	0.05–0.1	0.04	0.04	0.07

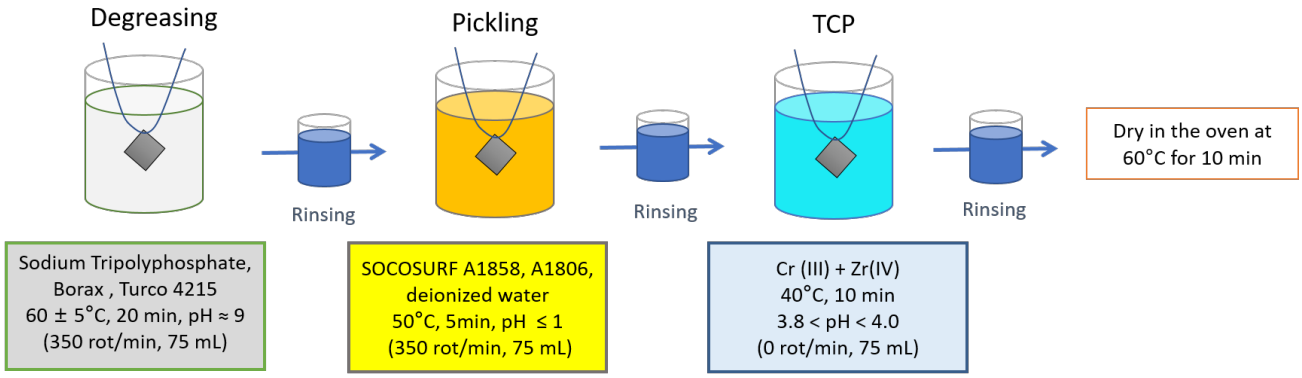

Figure 5.1: Procedure of surface degreasing, pickling and trivalent chromium process (TCP) applied in this paper

at 50 ◦C for 5 min. Next, the sample was treated with the SOCOSURF TCS (Trivalent Conversion and Sealing) solution denoted here as a Trivalent Conversion Process (TCP). TCP bath contained Zr^{IV} and Cr^{III} salts ($3.8 \leq$ pH ≤ 4.0) and TCP deposition was performed at 40 °C, for 10 min without agitation.

All the experiments were performed in 100 mL beakers for 75 mL solution and all baths were used no more than 3 times. The pH of all baths was adjusted with diluted NH_4OH (5 %) or diluted HNO_3 (5 %). Samples were rinsed in deionized water for 1 min between each treatment. After the TCP treatment, the samples were cleaned by deionized water and then dried in the oven at 60 °C for 10 min.

Surface characterization

The surface characterization was performed by XPS, ToF-SIMS and SEM. XPS measurements were performed in a XPS Thermo Electron Escalab 250 spectrometer under high vacuum (10^{-9} mbar) with an Al Kα monochromatised X-ray source. A 90° take-off angle is used. Survey spectrum and high resolution core level spectra including Al 2s, Cu 2p, Ag 3d were recorded with a pass energy of 100 eV and 20 eV, respectively. Spectrum were not corrected for charging effect with reference to C 1s hydrocarbon at 285.0 eV. Cu Auger LMM lines were also recorded. Peak fitting was performed with CasaXPS software (version 2.3.22). ToF-SIMS measurements were carried

out using an Ion-ToF ToF-SIMS spectrometer (Munster, Germany) operated under ultra–high vacuum (10^{-9} mbar). The in–depth profiles were performed with a pulsed 25 keV Bi^{+} primary beam ion source as analysis beam delivering 1.2 pA current within an area of 100 µm $\times$ 100 µm and a 2 keV Cs^{+} ion beam as the sputtering beam delivering a 100 nA current within an area of 1000 µm $\times$ 1000 µm (for pretreated sample) or 300 µm $\times$ 300 µm (for TCP coated sample) depending on the thickness of the oxide layer. Data processing was performed using Ion-Spec software (version 6.9). Surface morphology was studied by ZEISS Ultra–55 field emission scanning electron microscope.

Electrochemical measurements

A classical 3-electrode electrochemical setup connected with Reference 600 potentiostat (Gamry) was used to perform electrochemical measurements. Platinum wire and a saturated calomel electrode (SCE) were used as counter and reference electrodes, respectively. AA2050-T8 with surface treatments (polished, degreased, degreased and pickled and TCP coated) were used as working electrode. First, the open circuit potential (OCP) of samples in 0.1M NaCl electrolytes was measured for 45 min, followed by linear sweep voltammetry (LSV). The cathodic and anodic polarizations were performed separately after potential stabilization at OCP starting from the OCP to the anodic or cathodic direction (for around plus or minus 0.6 V, respectively) with the scanning rate of 1 mV/s. The reproducibility was confirmed by analyzing three samples under the same conditions.

5.3 Results

Surface modification during pretreatment

In order to observe the topography and chemical modification of the surface during each step of pretreatment, SEM, XPS and ToF-SIMS depth profiles were performed on the degreased and the surface after degreasing & pickling treatments.

Fig. 5.2 (a) and (b) present the morphology of degreased surface. It is clearly observed that most of IMPs in the alloy remain on the degreased sample. However, when the degreased surface is treated with pickling bath, most of the IMPs dissolve, leaving holes and revealing also the grain

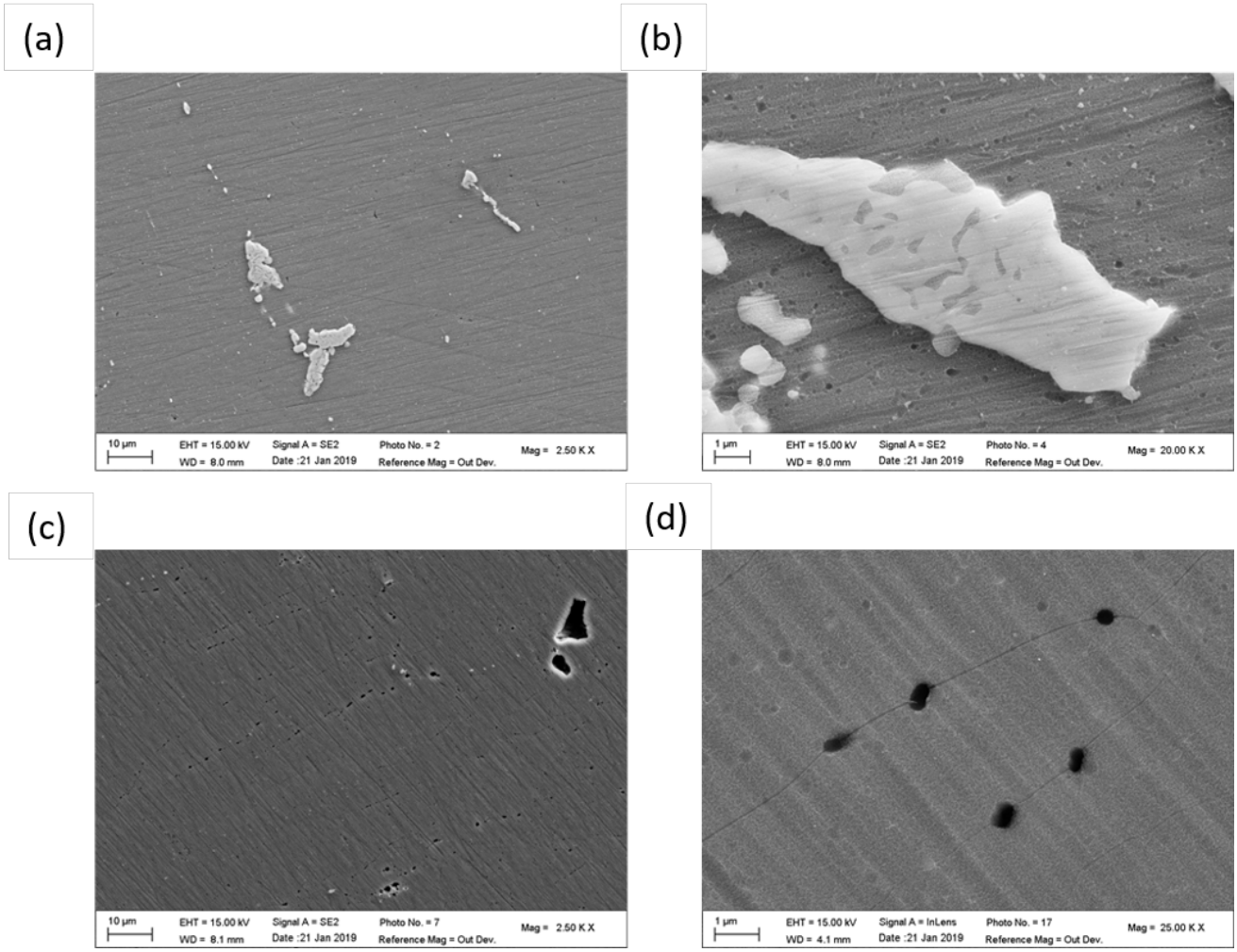

Figure 5.2: SEM images of AA2050-T8: (a and b) degreased surface, (c and b) degreased and pickled surface performed and lower and higher magnifications

boundaries (Fig. 5.2 (c) and (d)). This morphology observation is in very good agreement with previous studies [89–91, 133].

Fig. 5.3 shows the ToF-SIMS depth profiles for polished, degreased surface and degreased & pickled surface of AA2050-T8. Each depth profile is normalized by its Al_2^- intensity in the metal substrate assuming the metal substrate is not modified by the pretreatments. Three regions are defined as a function of intensity changes of different signals with sputtering time: the surface oxide layer, the metal substrate and the interface between oxide and metal substrate as already described in details in our previous paper [189]. The oxide layer is defined from the beginning of the sputtering time to the time where the maximum intensity of AlO_2^- signal is observed. The metal/oxide interface region can be characterized by a steep increase of the Al_2^- signal and the decrease of AlO_2^- signal. The substrate region is defined by a stable intensity of Al_2^- signal.

The oxide layer thickness for the polished sample corresponds to a sputtering time of around 75 s. After the degreasing treatment, no significant modification of the oxide layer thickness is observed (around 80 s), whereas it increases up to 250 s after the degreasing and pickling treatments. The interface region for the polished sample is from 75 s to 150 s, which means a range of only 75 s. Significantly longer sputtering times are observed for the interface region on degreased and degreased & pickled surface. On these samples, the interface region spreads from 80 s to 300 s (i.e. 220 s range) and 250 s to 1100 s (i.e. 850 s range), respectively. Moreover, according to Fig. 5.2, the surface morphology is significantly modified during degreasing and pickling, which leads to the change of the roughness. The roughness increase can also have an influence on the shape of depth profiles especially in the interface region leading to the longer sputtering times observed.

In order to observe the influence of pretreatments on the alloying elements, the Li^-, Cu^- and Ag^- signals are also presented in 5.3. The shape of the Li signal is similar for all samples but slightly lower intensity is observed on the sample after degreasing and pickling, whereas the intensity of Ag and Cu for degreased and degreased & pickled surfaces is about 10 times higher than that of polished surface in the interfacial region indicating a significant enrichment in Cu and Ag species. However, it is difficult to distinguish the chemical state of Cu or Ag species using only ToF-SIMS, thus to clarify their chemical states XPS analysis will be presented hereafter.

Fig.5.4 presents the XPS spectra of Al 2s, Cu $2p_{3/2}$ and Ag $3d_{5/2}$ for all samples and the fitting

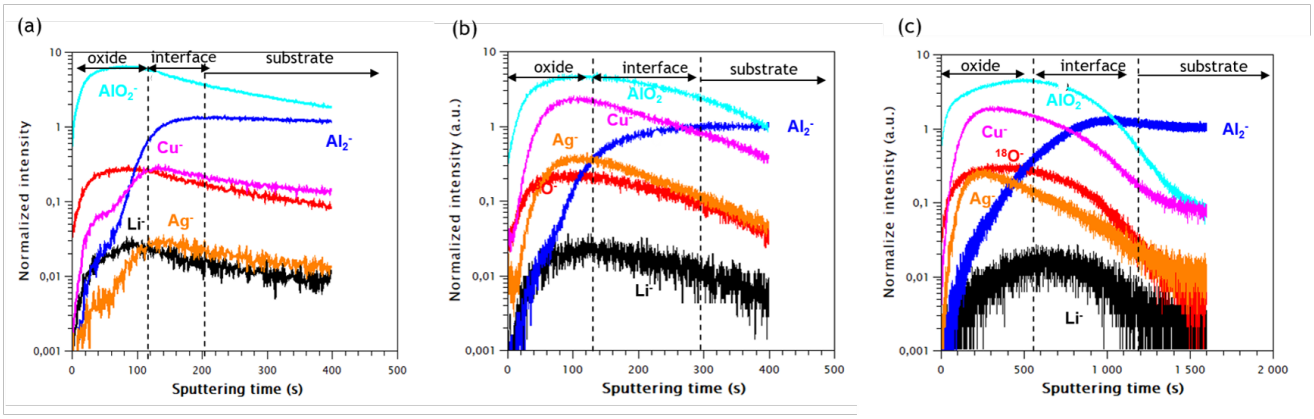

Figure 5.3: ToF-SIMS ion depth profiles for: (a) polished , (b) degreased and (c) degreased and pickled samples of AA2050-T8

Table 5.2: Fitting parameters (binding energy and full-width-at-half-maximum) for Al 2s, Cu $2p_{3/2}$ and Ag $3d_{5/2}$ XPS spectra presented in Fig. 5.4

Al 2s	**metallic peak**	**oxide peak**	**Cu 2s peak**
position(eV)	118.0 $\pm$ 0.12	120.5 $\pm$ 0.2 (121.3 for pretreated sample)	122.5 $\pm$ 0.2
FWHM (eV)	1.2 $\pm$ 0.2	2.3 $\pm$ 0.2	2.5 $\pm$ 0.5
Ag $3d_{5/2}$	**metallic peak**	**oxide peak**	**other peak**
position(eV)	368.1 $\pm$ 0.1	369.2 $\pm$ 0.2	370.2 $\pm$ 0.1
FWHM (eV)	0.6 $\pm$ 0.1	2.3 $\pm$ 0.1	2.4 $\pm$ 0.1
Cu $2p_{3/2}$	**metallic peak**	**oxide peak**	**hydroxide peak**
position(eV)	932.5 $\pm$ 0.1	933.8 $\pm$ 0.1	336.5 $\pm$ 0.1
FWHM (eV)	1.0 $\pm$ 0.1	2.4 $\pm$ 0.4	3.0 $\pm$ 0.1

parameters, peak position and full width at half maximum (FWHM)are depicted in Table 5.2. Li is not detectable by XPS due to its low amount and small cross section of Li 1s. Al 2s spectra obtained for all 3 samples shows that the Al 2s can be decomposed into 2 peaks corresponding to Al metal (118.0 $\pm$ 0.2 eV BE, 1.2 $\pm$ 0.2 eV FWHM) and Al oxide (120.5 $\pm$ 0.2 eV BE, 2.3 $\pm$ 0.2 eV FWHM).

However, the BE for Al oxide of degreased & picked sample is 0.8 eV higher than the polished and degreased surface due to the charging effect arised from the thicker oxide layer. As shown in Fig. 5.4(a), different intensity ratios between Al oxide peak and Al metal peak are observed. A higher $I_{\mathrm{Al}}^{\mathrm{Al_{ox}}}/I_{\mathrm{Al}}^{\mathrm{Al_{met}}}$ value observed for degrease and degreased & pickled surfaces indicates an increased thickness of Al oxide layer. Cu 3s (122.0 $\pm$ 0.5 eV BE, 2.5 $\pm$ 0.5 eV FWHM) is found at the same region and has been considered in the fitting. The peak area of Cu 3s is consistent with that of the Cu 2p. A significant increase of Cu 3s peak intensity is also observed for degreased and degreased & pickled surfaces compared to the polished sample indicating higher Cu content

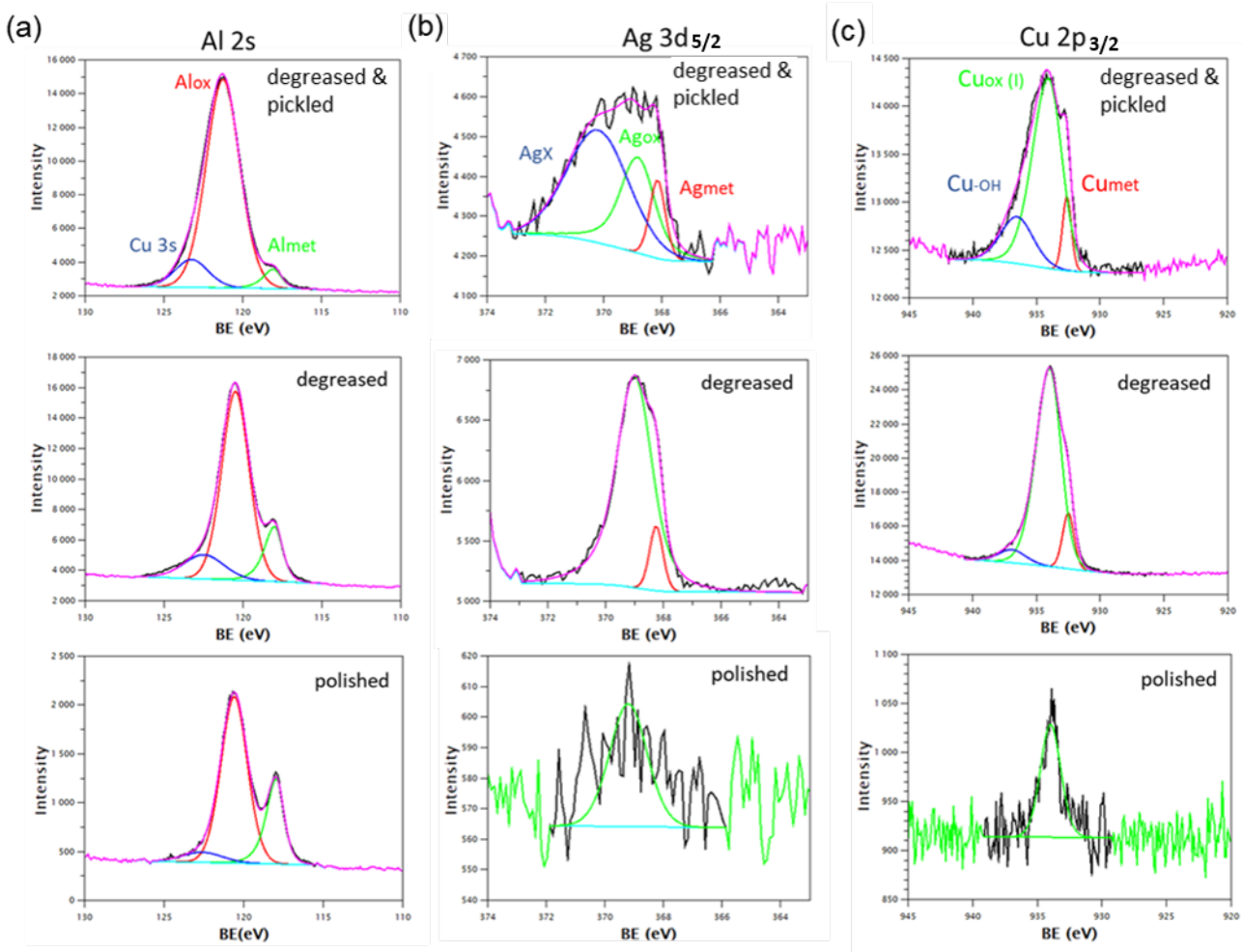

Figure 5.4: High-resolution XPS spectra of (a) Al 2s, (b) Ag $3d_{5/2}$, (c) Cu $2p_{3/2}$ on and degreased & pickled samples of AA2050-T8

Table 5.3: Calculated composition of the oxide and undermined AA2050-T8 substrate and oxide layer thickness for the polished, degreased and polished & degreased surfaces

	Elements	Polished sample	Degreased sample	Degreased & pickled sample
Oxide film thickness (nm)		3.5 ± 0.4	4.3 ± 0.4	7.2 ± 0.7
Oxide film composition (at%)	Al	99.6 ± 0.4	95 ± 1	98 ± 1
	Cu	0.30 ± 0.05	4.7 ± 0.5	1.0 ± 0.1
	Ag	0.15 ± 0.05	0.50 ± 0.05	0.20 ± 0.05
Modified surface composition (at%)	Al	100 ± 1	90 ± 1	87 ± 1
	Cu	$\leq$ 0.05	10 ± 1	13 ± 1
	Ag	$\leq$ 0.05	0.15 ± 0.05	0.20 ± 0.05

on the corresponding surfaces. This observation is confirmed by the significant increase of the Cu $2p_{3/2}$ peak intensity on the samples after both pretreatments as shown in Fig. 5.4(c). Cu $2p_{3/2}$ can be decomposed in 3 peaks corresponding to metallic Cu (932.5 ± 0.1 eV BE, 1.0 ± 0.1 eV FWHM), Cu (I) oxide (933.8 ± 0.1 eV BE, 2.4 ± 0.4 eV FWHM) and hydroxide peak (936.5 ± 0.1 eV BE, 3.0 ± 0.1 eV FWHM). For Cu oxide, the chemical state is confirmed by the characterized Auger parameter, which is calculated to be 1849.4 eV indicating a Cu^I oxide state as shown in supplementary materials B.9.

Besides Cu enrichment, higher intensity of Ag is also observed on the degreased and degreased & picked surfaces as shown in Fig. 5.4 (b). The Ag $3d_{5/2}$ spectrum can be decomposed into 3 peaks: metal peak (368.1 ± 0.1 eV BE, 0.6 ± 0.1 eV FWHM), oxide peak (369.2 ± 0.2 eV BE, 2.3 ± 0.1 eV FWHM) with higher BE and larger FWHM. After pickling, a strong and broad peak appears at higher BE (370.2 ± 0.1 eV BE, 2.4 ± 0.1 eV FWHM) which can corresponding to Ag_2SO_4 originating from one of the component of pickling solution. It should be noticed that the shift of binding energy of the Al oxide peak is observed in the Al 2s spectra for degreased & pickled surface but no shift is observed for the Cu 2p and Ag 3d spectrum. It can be explained by a redeposition of principally metallic Cu and Ag on the degreased & pickled surface. Only a small amount of Cu and Ag are in oxidized form. Some of these species can segregate at the oxide/metal interface. Therefore, it can be explained that the modification of Al oxide layer will not influence the binding energy of Cu oxide and Ag oxide significantly. The quantitative XPS data for the oxide thickness and the surface chemical composition of the oxide and interface (modified surface) are presented in Table 5.3.

A flat and homogenous oxide layer was assumed to be formed over the alloy substrate for the calculation [114, 132]. A 10% error of intensity was accounted for the measurements and/or data treatment. The significant increase of oxide thickness during degreasing and pickling is confirmed. The estimated oxide thickness on the degreased & pickled surface is about 7 nm, which is twice thicker than the oxide layer on the polished surface. However, the amount of Cu and Ag oxides reduce significantly after pickling. High amounts of Cu and Ag exist in both oxide layer and interface after degreasing and pickling evidenced by both ToF-SIMS depth profiles and XPS spectrum. XPS results reveal that Cu and Ag enrichment on the degreased and degreased & pickled surface consists of oxide and metallic species . Moreover, after pickling, the amount of Cu and Ag oxide on the surface is significantly decreased while the composition of metallic Cu an Ag remains stable. The metallic Cu and Ag is mainly accumulated at the interface region according to the ToF-SIMS depth profiles.

TCP coating on the degreased & pickled sample and polished sample

As previously introduced, pretreatments can significantly influence the behavior and properties of following treatment such as TCP coating. To investigate this effect, both polished (without pretreatment) and degreased & pickled samples were TCP coated and the surfaces were characterized by SEM, ToF-SIMS, XPS and electrochemical measurements.

Fig. 5.5 (a) and (b) present the SEM images of TCP coated surface of polished and degreased & pickled samples, respectively. On the polished sample, there are many cracks homogeneously distributed over the surface. IMPs can still be observed on the TCP layer of the polished sample as shown in Fig. 5.5 (a) but there is no evidence that IMPs are the preferential sites of TCP cracking. A relatively smooth and complete TCP coating is observed on the degreased & pickled sample. The morphology of the TCP coating for degreased & pickled sample (Fig. 5.5 (b)) is strongly influenced by the substrate morphology (presence of holes and revealed grain boundaries (Fig. 5.2 (c) and (d)).

The normalized (same way as Fig. 5.3) ToF-SIMS depth profiles of TCP layers deposited on polished and degreased & pickled samples are presented in Fig. 5.6 (a) and (b). A typical multilayer TCP structure showing three regions can be defined with an outer Cr and Zr oxide/hydroxide-rich layer (TCP), an inner layer composed of aluminium oxyfluorides (Al-O-F), , which can be also

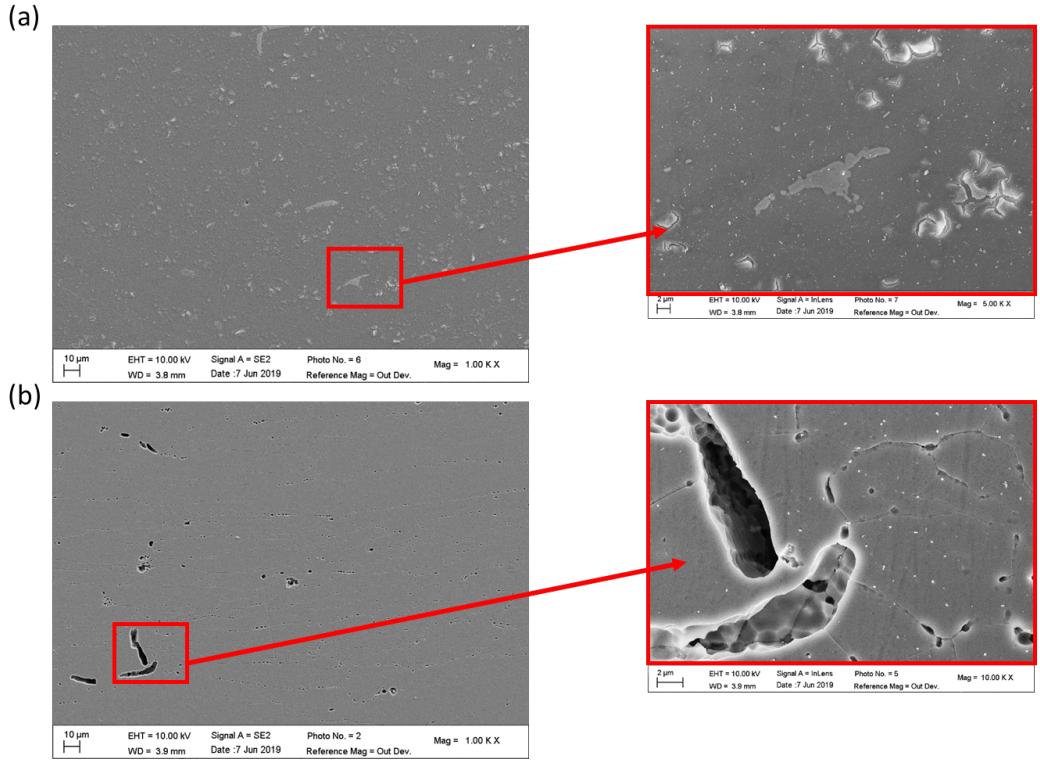

Figure 5.5: SEM images and corresponding zoom of TCP layer of (a) polished AA2050-T8 sample, (b) sample after degreasing & pickling.

defined as an interfacial TCP layer/metallic substrate, and the metallic substrate, in agreement with previous works [133, 232]. In the TCP layer, high content of Cr and Zr oxide/hydroxide is observed with a low intensity of oxidized Al and oxy-fluoro Al (i.e AlO_2^- and $AlOF^-$). In the Al-O-F-rich inner layer, the Al oxide (AlO_2^-) and Al-O-F ($AlOF^-$) signals reach the maximum intensities and the Al_2^- signal, representative of the metallic Al, continues to increase while the intensity of Cr and Zr species decreases. Then, the metal substrate can be defined where the signal of Al_2^- increases and shows a plateau. Concomitantly, Al oxide species decrease towards lower values. As shown in Fig. 5.6, the sputtering time for the TCP layer of the polished sample is 80 s while that of degreased & pickled sample is much longer (150 s). The sputtering time of the inner Al-O-F layer on the polished and degreased & pickled sample are similar (about 120 s). Therefore, the TCP layer for degreased & pickled sample is much thicker than that for the polished sample. Besides the difference in thickness, the chemical composition of the TCP coating is also different between polished and degreased & pickled surfaces and could influence the sputtering rate also. First, a higher intensity of Cu^- and Ag^- signals in the outer part of the TCP layer deposited on the degreased & pickled sample (Fig. 5.6 (b)) evidences the Cu and Ag enrichment. It should be

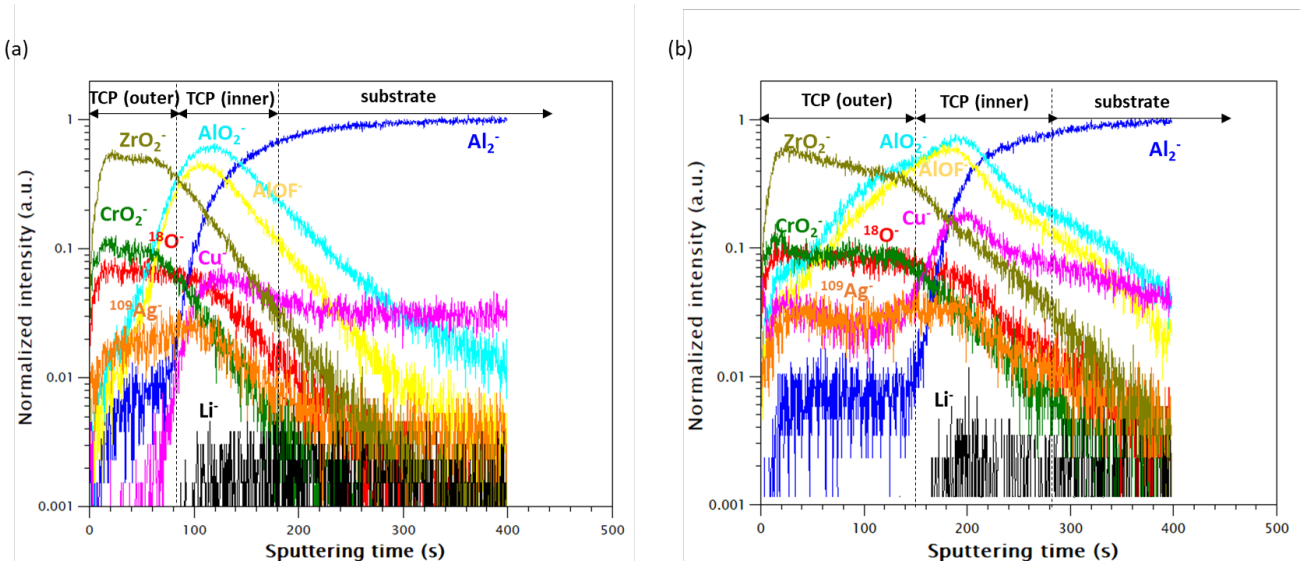

Figure 5.6: ToF-SIMS ion depth profiles for the TCP coatings (a) on polished AA2050-T8 without surface pretreatment (b) on sample with surface pretreatment (degreasing & pickling)

noted that no trace of Cu and a lower quantity of Ag are observed in the TCP layer on the polished surface. A similar behavior can be observed in the case of Li^- signal for polished and degreased & pickled samples showing a slight enrichment in the TCP inner layer.

Electrochemical behaviour of pretreated surface and TCP layers

The OCP measured before anodic polarization was similar for all the samples (about -0.65 ± 0.03 V *vs* SCE). A lower anodic current compared to the bare or pretreated surface (of two orders of magnitude in the potential range from -0.6 to -0.45 V) is observed for the TCP coated sample, indicating a higher corrosion resistance after TCP coating deposition. The anodic polarization curves for TCP coated samples are also different. Slightly lower current is observed for the TCP layer on the polished sample than for the TCP on the degreased and pickled sample (in the range between -0.65 ± 0.03 V to -0.40 ± 0.05 V). However, when the surface is polarized to a potential of 0.4 V or higher, the anodic current for TCP coated polished sample increases fast, which indicates a surface oxide breakdown and initiation of pitting corrosion. The breakdown potential for TCP layer of the degreased & pickled sample is similar with the polished sample. Different to the TCP coated samples, the surface breakdown and pitting of polished, degreased and degreased & pickled surface occurred immediately at about -0.6 V. This indicates that the effect of pretreatment is not visible in the electrochemical behaviour of samples during anodic polarization and the thick, Cu-rich oxide layer over degreased and pickled surface is not corrosion resistant.

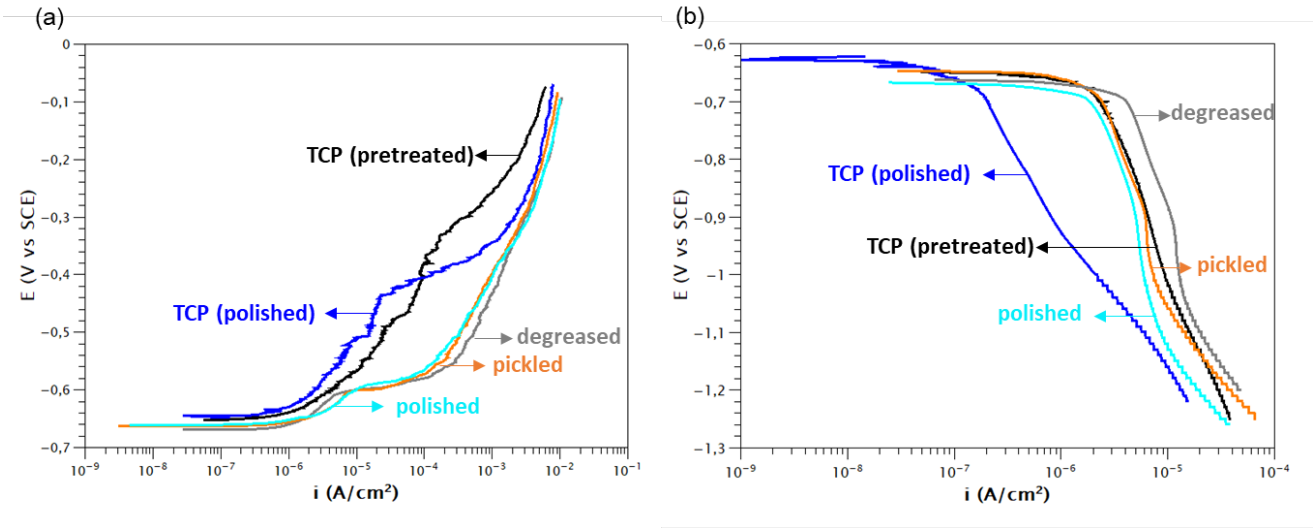

Figure 5.7: LSV curves performed separately in anodic (+ 0.6 V from OCP) and cathodic directions (-0.6 V from OCP) in 0.1 M NaCl solution with a scan rate of 1 mV/s: (a) anodic polarization curve, (b) cathodic polarization for polished, degreased, pickled (degreased & pickled) and TCP coated samples (polished and degreased & pickled)

The cathodic polarization curves (Fig. 5.7 (b)) show that the cathodic current of the TCP coated polished sample is one order of magnitude lower than other samples (in the potential range from -0.7 to -1 V). Therefore, the TCP layer of the polished sample show the lowest cathodic activity among samples. The cathodic current of TCP coated degreased & pickled sample is similar to that of the degreased & pickled sample or even slightly higher than the polished sample. This indicates that the cathodic activity of degreased & pickled sample stays relatively high after TCP coating and the effect of TCP coating on cathodic polarization is lower on the pretreated sample.

5.4 Discussion

The effect of the AA2050-T8 alloy pretreatment (degreasing and degreasing & pickling) on the surface chemical and morphological modifications of the alloy and the formation of TCP coating was studied. From the ToF-SIMS depth profiles (Fig. 5.3) and XPS results (Fig. 5.4), a significant enrichment in Cu and Ag-species was confirmed in the oxide and interface region after degreasing. However, Cu and Ag enrichment in the oxide layer is reduced after degreasing & pickling step and most of enriched Cu as well as Ag are in the metallic state and accumulates at the oxide/metal interface. Besides the chemical modification, IMPs and grain boundaries are also revealed after

pickling leaving holes and defects on the surface. Later, comparison of the TCP coating deposited on the degreased & pickled sample and polished sample by SEM (Fig. 5.5) and ToF-SIMS depth profiles (Fig. 5.6) indicated that, the TCP layer on the degreased & pickled sample is thicker than that on the polished sample. Moreover, the cracks in the TCP layer on the pretreated surface are less significant than on the polished sample (Fig. 5.5). Besides the thickness, the chemical structure of the TCP layers is also different according to Fig. 5.6. The enrichment of Cu and Ag is observed in the TCP layer of the degreased & pickled sample while no trace of Cu and a lower Ag signal intensity is detected in the TCP layer on the polished sample. Moreover, a more significant enrichment of Cu is evidenced in the inner TCP layer on the degreased & pickled sample compared to the polished sample. This difference in the amount of Cu present in the TCP layers is assigned to the alloy pretreatment. As introduced before, after pickling, some Cu accumulates in the oxide and in the metallic substrate. The initiation of the TCP coating is the dissolution of the passivating aluminium oxide layer present on Al alloy substrate (driven by the F^- ions). During this dissolution, Cu and Ag, present in the oxide layer and substrate, also dissolve. Due to the consumption of protons, local pH increases over the surface and promotes the deposition of Cr and Zr species. It is highly possible that the Cu and Ag accumulated in the TCP layer on the degreased & pickled sample is from the dissolved Cu and Ag-species of degreased & pickles surface, which are reduced and redeposited in a metallic state. The effect of Cu on the TCP coating properties is not clear. George textitet al. [233] studied the growth rate of Zr coating on different Al-Cu alloys with different Cu contents and concluded that the growth rate decreased with increasing Cu/Al ratio. They suggested that this decrease is due to the copper species present in the coating impeding the cation transport to the coating base. However, Viroulaud *et al*. [133] reported that Cu enrichment on the surface did not have a decisive effect on the growth of TCP layer. Our results are consistent with that of Cerezo *et al*. [234]. These authors modified the Zr-based conversion coating solution by adding a small amount of copper salts (30–50 ppm). The copper components formed copper and/or copper oxide agglomerates on the substrate, which created local alkalinity that catalyzed the coating formation. Moreover, they found that the coating thickness increased on the multi-metal substrate (AA6014, cold rolled steel and hot dip galvanized steel). Qi *et al*. [235] also investigated the effect of copper by adding small amount of Cu salt into the TCP bath

and indicated that the copper-rich deposits were preferred cathodic sites for oxygen reduction. Deposition of Zr oxide is an electrochemically driven process and the existence of cathodic sites on the surface is the driving force for the formation of the conversion layer [236]. Therefore, the behaviour of Cu on the degreased & pickles surface can be interpreted as a similar effect of Cu in the TCP bath that promotes the cathodic oxygen reduction then increases thickness of TCP conversion coating. The effect of Cu on the TCP coating is complex. According to the results of electrochemical measurement (Fig. 5.7), the TCP layer on the polished sample shows a lower current during anodic (no more than +0.2 V vs OCP) and cathodic polarization, especially during the cathodic polarization. The enrichment of Cu can not only increase the cathodic activity during the TCP process, but also increase the cathodic activity of TCP layer. Although the TCP coating is considered as the critical step for improving the corrosion resistance, the cathodic current of the TCP layer of the degreased & pickles sample is similar to that of the polished or pickled surfaces.

5.5 Conclusions

In this work, the surface modifications of AA2050 (Al-Cu-Li) alloy during surface pretreatments and following TCP deposition have been studied. The pretreatments (alkaline etching and acid pickling) led to formation of a thicker aluminium oxide layer with significant enrichment of Cu and Ag at the oxide/metal interface. Most intermetallic particles were removed, leaving defects on the surface. TCP coating applied on polished and degreased & pickled samples showed a bilayer structure with an outer part composed of Cr and Zr oxides and an inner oxide part with aluminium oxyfluorides. The significant Cu and slight Ag enrichments were observed in the outer and inner (interfacial) TCP layer deposited on the degreased & pickled sample. A thicker TCP coating (outer oxide) with less cracks was also observed on the degreased & pickled sample than on the polished sample. According to the linear sweep voltammetry measurements a lower anodic current was observed for both TCP coated samples indicated the beneficial role of TCP layer on the corrosion resistance. However, a significant difference is observed for the cathodic currents between the TCP coated samples showing a decreased cathodic current for TCP coated polished sample with reference to the TCP coating on degreased & pickled sample. The difference between cathodic

activity of polished and degreased &pickled samples as well as thickness of TCP coated samples is assigned to the Cu enrichment on the degreased & pickled sample. During the initial stages of TCP coating formation, the metallic Cu is responsible for the cathodic reactions (oxygen and/or hydrogen reduction). In a similar way, Cu can also promotes the cathodic reactions during the formation of conversion layer. Some Cu dissolved with the oxide layer can be redeposited with Zr and Cr species and become an outer part of TCP layer.

Chapter 6

Conclusions and perspectives

6.1 Conclusions

The objective of this PhD project was to perform the in-depth surface characterization and corrosion properties of Al-Cu-Li alloy (AA2050-T8). The work consists of three parts, which are thermal oxidation, corrosion behaviour in aggressive aqueous environment and chemical treatments for corrosion protection.

First, the initial stages of thermal oxidation (at 200℃) of Al-Cu-Li alloy was studied by *in situ* XPS and ToF-SIMS 3D mapping. Formation of a continuous mixed Al-Li oxide layer was revealed with a thickness of 9 ± 1 Å after exposure to 5000 L of oxygen. Besides the oxide thickness, the chemical composition of oxide layer and metal substrate was also analyzed in details. First, a segregation behaviour of Li and Ag was observed on the annealed alloy surface before oxidation. During exposure to oxygen, Li oxidized rapidly while Ag stayed in a metallic state and enriched at the oxide /metal interface. The study of the oxidation kinetics by *in situ* XPS showed that two regimes of oxide growth can be distinguished: one with a fast oxidation below 500 L and the second one with a slower kinetics during further oxidation up to 5000 L. The increase of atomic ratio of Li was observed form 50 % to 70 % during 10 L–100 L exposure. During further stages of oxidation (till 5000 L) the Li quantity stabilized and it was accompanied by Mg enrichment. Segregation phenomena of alloys compounds after thermal oxidation was confirmed by ToF-SIMS 3D map. Relatively homogeneous distribution of Li, Cu and Ag was observed in the grains while a

significant accumulation of Mg was observed above the grain boundaries of the Al substrate. The second part of the work consists of corrosion behavior of bare Al-Cu-Li alloys (AA2050–T8) in aggressive (chloride-based electrolytes). Before and after the electrochemical tests the surface was characterized by microscopic (SEM, optical microscopy) and surface techniques (XPS, ToF-SIMS). The mechanism of pitting corrosion of Al-Cu-Li alloy and the role of Li is discussed in this part. First, pitting corrosion was observed on the sample after immersing in aggressive media for 45 min by optical microscopy. Then, ToF-SIMS chemical mapping indicated enrichment of Cu, Fe and Cl in the pits. This enrichment indicates the relation between Cu and Fe-containing intermetallic particles (Al-Cu-Fe-Mn) and pitting corrosion. Both ToF-SIMS 2D and 3D imaging were performed for localized study the corrosion behaviour of Al-Cu-Fe-Mn IMPs. The corrosion attack was observed around and over the IMPs. Pits and trenching was observed at the boundary of IMPs and matrix. High intensity of OH^- observed over IMPs indicated that a highly hydrated surface over IMPs was formed. This hydration was induced by the cathodic nature of the IMPs: a galvanic coupling between IMPs and matrix and cathodic reaction (oxygen reduction) occurring over the IMPs producing the OH^- . Some local micrometric chemical heterogeneities within the IMPs in the case of 3D ToF-SIMS chemical mapping demonstrated also to be detrimental for corrosion. The local pH changes and increase concentration of OH^- led to reaction with the dissolved Al species and deposition over the IMPs. Moreover, high Cl^- , OH^- and $CuOH^-$ signal observed in the pitting area indicated the enrichment of corrosion products with Cl and OH, Cu hydroxide. The behaviour of Li was also analyzed by Tof-SIMS depth profiles. Before corrosion, the existence of Li was clearly presented in the oxide layer but after corrosion, the Li in the oxide layer decreased a lot indicating a dissolution of Li occurred during corrosion process. The third part of the work was focused on the chemical surface treatments for corrosion protection of AA 2050-T8 alloy. A complete surface treatment applied in industry (degreasing based on sodium tripoliphosphate, borax and Turco 4205 additive then pickling using SOCOSURF A1858 and A1806 solution and conversion bath using SOCOSURF TCS) was performed including alkaline degreasing, acid pickling and TCP conversion coating. Alkaline degreasing and acid pickling are considered as surface pretreatment for the followed TCP process. Besides the removal of IMPs, both XPS and ToF-SIMS depth profiles revealed a thicker oxide layer with enrichment of Cu and Ag after degreasing and pick-

ling. Moreover, it was shown that the surface pretreatment influences the TCP layer regarding both morphology and chemical surface structure. The TCP layer formed on the degreased and pickled surface was thicker with less cracks compared to that formed on the polished surface. Moreover, Cu enrichment was observed over the TCP layer of degreased & pickled sample. The electrochemical measurements showed a lower anodic current for both TCP coated samples in comparison to non-coated sample indicated the critical role of TCP layer on the corrosion resistance. Significant difference was observed in the cathodic cathodic current between the TCP coated samples. The difference between cathodic acitivity as well as higher TCP thickness was assigned to the Cu enrichment on the degreased & pickled sample. It was concluded, that the presence of Cu has an important effect on the cathodic activity of the sample (increase oxygen reduction reaction) during TCP growth and enhanced growth of TCP coating.

6.2 Perspectives

Based on this work several perspectives can be proposed.

Thermal oxidation

In this work, we focused on the initial stages of the thermal oxidation of Al-Cu-Li alloys, which we think are essential to understand the mechanisms that can occur in more real conditions. During thermal treatment of alloy or at the high working temperatures, material is always exposed to the atmospheric environment with different ambient pressure compared to our testing condition (low pressure). Moreover, the exposition to different types of gases, humidity and temperatures can have an important influence on the chemical and morphological modifications of the alloy. It will be also very interesting to look at electrochemical behavior of modified alloy. Thus, the electrochemical and corrosion performance of the thermally treated alloy could be one of the important aspect in future studies in order to look at the influence of chemical/morphological modifications of the alloy on its corrosion behavior.

Corrosion behaviour

Another important point would be to better understanding the pitting corrosion behaviour related to IMPs. Based on our exploratory data presented in Appendix A, after 2 h immersion in 0.1

M NaCl electrolyte, small nano-sized pits around larger Al-Cu-Fe-Mn IMPs are observed on the AA2050 Al-Cu-Li alloy which significantly increase the total corroded area. It would be interesting to understand which kind of IMPs induced this small pits and study the corrosion mechanism of this pitting behaviour. Moreover, these small pits are not observed and reported for the AA2024 Al-Cu-Mg alloys as far as we know. It could be one of typical characters for the corrosion behaviour of Al-Cu-Li alloys. As indicated in Chapter 4, different corrosion behaviors of Al-Cu-Fe-Mn IMPs were revealed. More sever corrosion was observed on an individual Al-Cu-Fe-Mn IMPs with compositional heterogeneity where complex galvanic effect within IMP was proposed. A more detailed analysis of different types of IMPs and the chemical and structural heterogeneities within each IMP will be essential. It would be also very interesting to look in details on kinetics of corrosion and influence of chloride concentration in electrolyte. The chemical surface characterization, formation of pits and surface layer formation (corrosion layer) could be analyzed in details by XPS, ToF-SIMS and also by Nano Auger. Nano Auger is a local characterization technique, which can be very powerful in characterization of different IMPs and matrix.

Surface treatment

Based on our present data, surface pretreatment are critical in the formation and properties of TCP coating which in further stages can have influence on corrosion properties of the TCP coated alloy. It is important to have a deeper understanding of the effect of Cu during the TCP coating formation and coating properties. Three kinds of Cu species should be considered and studied: the Cu in the alloy, Cu in the TCP bath and Cu on the pretreated surface. In this thesis project, the Cu accumulated on the pretreated surface is studied and a dissolusion–redeposition process is proposed. Inductively coupled plasma atomic emission spectrometer (ICP-AES) could be used to detect the behaviour of Cu in the TCP bath. A more fundamental studies could be also performed using the model intermetallic particles. Also the local *ex situ* and *in situ* characterization techniques could be employed on the industrial alloys (with different IMPs) after different types of pretreatments to have a better insight into the deposition mechanisms of the conversion coating and corrosion behavior over IMPs and matrix.

Bibliography

[1] R. J. Rioja and J. Liu, The evolution of Al-Li base products for aerospace and space applications, *Metallurgical and Materials Transactions A*, 43(9), 3325–3337 (2012).

[2] I. A. Institute, http://www.world-aluminium.org.

[3] C. Vargel, *Corrosion of aluminium*, Elsevier (2004).

[4] A. E. Hughes, G. E. Thompson, J. M. Mol, N. Birbilis, S. J. Garcia and X. Zhou, *High strength Al-alloys: microstructure, corrosion and principles of protection*, INTECH Open Access Publisher (2011).

[5] E. Starke, T. Sanders and I. Palmer, New approaches to alloy development in the Al-Li system, *JOM*, 33(8), 24–33 (1981).

[6] T. Dursun and C. Soutis, Recent developments in advanced aircraft aluminium alloys, *Materials & Design (1980-2015)*, 56, 862–871 (2014).

[7] P. Lequeu, K. Smith and A. Daniélou, Aluminum-copper-lithium alloy 2050 developed for medium to thick plate, *Journal of materials engineering and performance*, 19(6), 841–847 (2010).

[8] R. Wanhill, Aerospace applications of aluminum–lithium alloys, in *Aluminum-lithium Alloys*, pp. 503–535, Elsevier (2014).

[9] R. A. Hafley, M. S. Domack, S. J. Hales and R. N. Shenoy, Evaluation of aluminum alloy 2050-T84 microstructure and mechanical properties at ambient and cryogenic temperatures, Tech. rep., NASA (2011).

[10] O. Gharbi, N. Birbilis and K. Ogle, Li reactivity during the surface pretreatment of Al-Li alloy AA2050-T3, *Electrochimica Acta*, 243, 207–219 (2017).

[11] N. Sukiman, X. Zhou, N. Birbilis, A. Hughes, J. Mol, S. Garcia and G. Thompson, Durability and corrosion of aluminium and its alloys: overview, property space, techniques and developments, in *Aluminium Alloys-New Trends in Fabrication and Applications*, Intech (2012).

[12] A. A. Csontos and E. A. Starke, The effect of inhomogeneous plastic deformation on the ductility and fracture behavior of age hardenable aluminum alloys, *International Journal of Plasticity*, 21(6), 1097–1118 (2005).

[13] A. Deschamps, B. Decreus, F. De Geuser, T. Dorin and M. Weyland, The influence of precipitation on plastic deformation of Al–Cu–Li alloys, *Acta materialia*, 61(11), 4010–4021 (2013).

[14] B. Rodgers and P. Prangnell, Quantification of the influence of increased pre-stretching on microstructure-strength relationships in the Al–Cu–Li alloy AA2195, *Acta Materialia*, 108, 55–67 (2016).

[15] C.-S. Tsao, C.-Y. Chen, T.-Y. Kuo, T.-L. Lin and M.-S. Yu, Size distribution and coarsening kinetics of δ' precipitates in Al–Li alloys considering temperature and concentration dependence, *Materials Science and Engineering: A*, 363(1-2), 228–233 (2003).

[16] M. Seah and E. Hondros, Grain boundary segregation, *Proceedings of the Royal Society of London. A. Mathematical and Physical Sciences*, 335(1601), 191–212 (1973).

[17] V. Leroy and H. Viefhaus, Segregation on the surface of steels in heat treatment and oxidation, *ISIJ international*, 35(2), 95–113 (1995).

[18] K. Kumar, S. Brown and J. R. Pickens, Effect of a prior stretch on the aging response of an Al-Cu-Li-Ag-Mg-Zr alloy, Tech. rep., NASA (1991).

[19] C. Luo, S. P. Albu, X. Zhou, Z. Sun, X. Zhang, Z. Tang and G. E. Thompson, Continuous and discontinuous localized corrosion of a 2xxx aluminium-copper-lithium alloy in sodium chloride solution, *Journal of Alloys and Compounds*, 658, 61–70 (2016).

[20] E. Balducci, L. Ceschini, S. Messieri, S. Wenner and R. Holmestad, Thermal stability of the lightweight 2099 Al-Cu-Li alloy: Tensile tests and microstructural investigations after over-aging, *Materials & Design*, 119, 54–64 (2017).

[21] W. Liang, P. Qinglin, H. Yunbin, L. Yunchun, Z. Yingchun and L. Congge, Effect of aging on the mechanical properties and corrosion susceptibility of an Al-Cu-Li-Zr alloy containing Sc, *Rare Metals*, 27(2), 146–152 (2008).

[22] C.-S. Zhang, F. Esposto, B. Flinn, P. Norton and R. Timsit, The influence of Li surface segregation on the initial oxidation of an Al Li alloy at room temperature, *Surface Science*, 290(1-2), 103–112 (1993).

[23] D. Lee, H. Lee, C. Hwang, J. Maeng, S. Kim, K.-J. Kim and B. Kim, Photoemission studies of oxygen adsorbed on a LiAl (110) alloy surface: Role of Li segregation, *Applied Surface Science*, 252(14), 5116–5123 (2006).

[24] J. W. Kim, Y. K. Kim and S. Kim, Segregation induced reconstructions of Li Al (110) alloy surface, *Surface Science*, 375(2-3), L392–L396 (1997).

[25] P. Partridge, Oxidation of aluminium-lithium alloys in the solid and liquid states, *International Materials Reviews*, 35(1), 37–58 (1990).

[26] C. Lea and C. Molinari, Magnesium diffusion, surface segregation and oxidation in Al-Mg alloys, *Journal of Materials Science*, 19(7), 2336–2352 (1984).

[27] S. Saied and J. Sullivan, A study of thermally induced segregation of magnesium in aluminium-magnesium alloys by means of AES, *Journal of Physics: Condensed Matter*, 5(33A), A165 (1993).

[28] G. Scamans, N. Holroyd and C. Tuck, The role of magnesium segregation in the intergranular stress corrosion cracking of aluminium alloys, *Corrosion Science*, 27(4), 329–347 (1987).

[29] R. Song, W. Dietzel, B. Zhang, W. Liu, M. Tseng and A. Atrens, Stress corrosion cracking and hydrogen embrittlement of an Al-Zn-Mg-Cu alloy, *Acta Materialia*, 52(16), 4727–4743 (2004).

[30] R. Song, M. Tseng, B. Zhang, J. Liu, Z. Jin and K. Shin, Grain boundary segregation and hydrogen-induced fracture in 7050 aluminium alloy, *Acta Materialia*, 44(8), 3241–3248 (1996).

[31] X. Sun, B. Zhang, H. Lin, Y. Zhou, L. Sun, J. Wang, E.-H. Han and W. Ke, Correlations between stress corrosion cracking susceptibility and grain boundary microstructures for an Al-Zn-Mg alloy, *Corrosion Science*, 77, 103–112 (2013).

[32] C. R. Hutchinson, X. Fan, S. J. Pennycook and G. J. Shiflet, On the origin of the high coarsening resistance of ω plates in Al-Cu-Mg-Ag alloys, *Acta Materialia*, 49(14), 2827–2841 (2001).

[33] H. Lee, R. Hyland Jr, H. Aaronson and P. Wynblatt, Surface segregation in an al–4.2 at% ag alloy, *Surface science*, 408(1-3), 288–299 (1998).

[34] E. Wetli, M. Erbudak and G. Kostorz, Segregation kinetics of ag on a (100) surface of al-3at% ag, *Applied surface science*, 64(2), 111–113 (1993).

[35] K. Baldwin and C. Smith, Accelerated corrosion tests for aerospace materials: current limitations and future trends, *Aircraft Engineering and Aerospace Technology* (1999).

[36] J. Li, M. Li and Z. Sun, Development of an artificial climatic complex accelerated corrosion tester and investigation of complex accelerated corrosion test methods, *Corrosion*, 55(5), 498–502 (1999).

[37] Y. Liu, Z. Wang and W. Ke, Study on influence of native oxide and corrosion products on atmospheric corrosion of pure al, *Corrosion Science*, 80, 169–176 (2014).

[38] J. Ryl, J. Wysocka, M. Jarzynka, A. Zielinski, J. Orlikowski and K. Darowicki, Effect of native air-formed oxidation on the corrosion behavior of aa 7075 aluminum alloys, *Corrosion science*, 87, 150–155 (2014).

[39] L. Tomcsanyi, K. Varga, I. Bartik, H. Horányi and E. Maleczki, Electrochemical study of the pitting corrosion of aluminium and its alloys-II. study of the interaction of chloride ions with a passive film on aluminium and initiation of pitting corrosion, *Electrochimica Acta*, 34(6), 855–859 (1989).

[40] A. Pardo, M. Merino, A. E. Coy, R. Arrabal, F. Viejo and E. Matykina, Corrosion behaviour of magnesium/aluminium alloys in 3.5 wt.% nacl, *Corrosion Science*, 50(3), 823–834 (2008).

[41] M. F. Ashby and D. R. H. Jones, *Engineering materials 1: an introduction to properties, applications and design*, vol. 1, Elsevier (2012).

[42] I. Muller and J. Galvele, Pitting potential of high purity binary aluminium alloys-I. Al-Cu alloys. pitting and intergranular corrosion, *Corrosion Science*, 17(3), 179–193 (1977).

[43] M. Yasuda, F. Weinberg and D. Tromans, Pitting corrosion of Al and Al-Cu single crystals, *Journal of the Electrochemical Society*, 137(12), 3708–3715 (1990).

[44] Z. Szklarska-Smialowska, Pitting corrosion of aluminum, *Corrosion Science*, 41(9), 1743–1767 (1999).

[45] T. Chaturvedi et al., An overview of the corrosion aspect of dental implants (titanium and its alloys), *Indian Journal of Dental Research*, 20(1), 91 (2009).

[46] G. Svenningsen, http://www.sintef.no/static/mt/norlight/seminars/norlight2003/Postere/Gaute Svenningsen.pdf (2003).

[47] C.-M. Liao and R. P. Wei, Galvanic coupling of model alloys to aluminum—a foundation for understanding particle-induced pitting in aluminum alloys, *Electrochimica Acta*, 45(6), 881–888 (1999).

[48] M. Guérin, J. Alexis, E. Andrieu, L. Laffont, W. Lefebvre, G. Odemer and C. Blanc, Identification of the metallurgical parameters explaining the corrosion susceptibility in a 2050 aluminium alloy, *Corrosion Science*, 102, 291–300 (2016).

[49] R. Buchheit, L. Montes, M. Martinez, J. Michael and P. Hlava, The electrochemical characteristics of bulk-synthesized Al_2CuMg, *Journal of the Electrochemical Society*, 146(12), 4424–4428 (1999).

[50] Y. Ma, X. Zhou, Y. Liao, Y. Yi, H. Wu, Z. Wang and W. Huang, Localised corrosion in AA2099-T83 aluminium-lithium alloy: the role of grain orientation, *Corrosion Science*, 107, 41–48 (2016).

[51] J. V. de Sousa Araujo, U. Donatus, F. M. Queiroz, M. Terada, M. X. Milagre, M. C. de Alencar and I. Costa, On the severe localized corrosion susceptibility of the AA2198-T851 alloy, *Corrosion Science*, 133, 132–140 (2018).

[52] R. Buchheit Jr, J. Moran and G. Stoner, Localized corrosion behavior of alloy 2090—the role of microstructural heterogeneity, *Corrosion*, 46(8), 610–617 (1990).

[53] V. Proton, J. Alexis, E. Andrieu, J. Delfosse, A. Deschamps, F. De Geuser, M.-C. Lafont and C. Blanc, The influence of artificial ageing on the corrosion behaviour of a 2050 aluminium–copper–lithium alloy, *Corrosion Science*, 80, 494–502 (2014).

[54] J. Li, C. Li, Z. Peng, W. Chen and Z. Zheng, Corrosion mechanism associated with T1 and T2 precipitates of Al-Cu-Li alloys in NaCl solution, *Journal of Alloys and Compounds*, 460(1-2), 688–693 (2008).

[55] J. Li, Z. Zheng, S. Li, W. Chen, W. Ren and X. Zhao, Simulation study on function mechanism of some precipitates in localized corrosion of Al alloys, *Corrosion Science*, 49(6), 2436–2449 (2007).

[56] M. Guérin, J. Alexis, E. Andrieu, C. Blanc and G. Odemer, Corrosion-fatigue lifetime of aluminium–copper–lithium alloy 2050 in chloride solution, *Materials & Design*, 87, 681–692 (2015).

[57] M. Guérin, E. Andrieu, G. Odemer, J. Alexis and C. Blanc, Effect of varying conditions of exposure to an aggressive medium on the corrosion behavior of the 2050 Al–Cu–Li alloy, *Corrosion science*, 85, 455–470 (2014).

[58] N. Birbilis, M. Cavanaugh and R. Buchheit, Electrochemical behavior and localized corrosion associated with Al_7Cu_2Fe particles in aluminum alloy 7075-T651, *Corrosion Science*, 48(12), 4202–4215 (2006).

[59] A. Boag, A. Hughes, A. Glenn, T. Muster and D. McCulloch, Corrosion of AA2024-T3 Part I: Localised corrosion of isolated IM particles, *Corrosion Science*, 53(1), 17–26 (2011).

[60] X. Zhou, C. Luo, T. Hashimoto, A. Hughes and G. Thompson, Study of localized corrosion in AA2024 aluminium alloy using electron tomography, *Corrosion Science*, 58, 299–306 (2012).

[61] C. M. MacRae, A. E. Hughes, J. S. Laird, A. Glenn, N. C. Wilson, A. Torpy, M. A. Gibson, X. Zhou, N. Birbilis and G. E. Thompson, An examination of the composition and microstructure of coarse intermetallic particles in AA2099-T8, including Li detection, *Microscopy and Microanalysis*, 24(4), 325–341 (2018).

[62] Y. Ma, X. Zhou, W. Huang, G. Thompson, X. Zhang, C. Luo and Z. Sun, Localized corrosion in AA2099-T83 aluminum-lithium alloy: The role of intermetallic particles, *Materials Chemistry and Physics*, 161, 201–210 (2015).

[63] G. Critchlow and D. Brewis, Review of surface pretreatments for aluminium alloys, *International Journal of Adhesion and Adhesives*, 16(4), 255–275 (1996).

[64] S. Y. Park, W. J. Choi, H. S. Choi, H. Kwon and S. H. Kim, Recent trends in surface treatment technologies for airframe adhesive bonding processing: a review (1995–2008), *The Journal of Adhesion*, 86(2), 192–221 (2010).

[65] C. Rangel, T. Paiva and P. Da Luz, Conversion coating growth on 2024-T3 Al alloy. the effect of pre-treatments, *Surface and Coatings Technology*, 202(14), 3396–3402 (2008).

[66] W. Pinc, S. Geng, M. O'keefe, W. Fahrenholtz and T. O'keefe, Effects of acid and alkaline based surface preparations on spray deposited cerium based conversion coatings on al 2024-t3, *Applied Surface Science*, 255(7), 4061–4065 (2009).

[67] L. Fedrizzi, A. Bianchi, F. Deflorian, S. Rossi and P. Bonora, Effect of chemical cleaning on the corrosion behaviour of painted aluminium alloys, *Electrochimica acta*, 47(13-14), 2159–2168 (2002).

[68] J. Zhao, G. Frankel and R. L. McCreery, Corrosion protection of untreated aa-2024-t3 in chloride solution by a chromate conversion coating monitored with raman spectroscopy, *Journal of the Electrochemical Society*, 145(7), 2258 (1998).

[69] A. Hughes, R. Taylor and B. Hinton, Chromate conversion coatings on 2024 al alloy, *Surface and Interface Analysis: An International Journal devoted to the development and application of techniques for the analysis of surfaces, interfaces and thin films*, 25(4), 223–234 (1997).

[70] G. Ilevbare, J. Scully, J. Yuan and R. Kelly, Inhibition of pitting corrosion on aluminum alloy 2024-t3: effect of soluble chromate additions vs chromate conversion coating, *Corrosion*, 56(3), 227–242 (2000).

[71] O. Lunder, J. Walmsley, P. Mack and K. Nisancioglu, Formation and characterisation of a chromate conversion coating on aa6060 aluminium, *Corrosion science*, 47(7), 1604–1624 (2005).

[72] M. Costa, Toxicity and carcinogenicity of cr (vi) in animal models and humans, *Critical reviews in toxicology*, 27(5), 431–442 (1997).

[73] M. Costa and C. B. Klein, Toxicity and carcinogenicity of chromium compounds in humans, *Critical reviews in toxicology*, 36(2), 155–163 (2006).

[74] E. Directive et al., Restriction of the use of certain hazardous substances in electrical and electronic equipment (RoHS), *Off. J. Eur. Communities*, 46, 19–23 (2013).

[75] CEC, Regulation (ec) no. 1907/2006 of the european parliament and of the council of 18 december 2006 concerning the registration, evaluation, authorisation and restriction of chemicals (reach) (2006).

[76] S. Pommiers, J. Frayret, A. Castetbon and M. Potin-Gautier, Alternative conversion coatings to chromate for the protection of magnesium alloys, *Corrosion Science*, 84, 135–146 (2014).

[77] M. Kendig and R. Buchheit, Corrosion inhibition of aluminum and aluminum alloys by soluble chromates, chromate coatings, and chromate-free coatings, *Corrosion*, 59(5), 379–400 (2003).

[78] F. Pearistein and V. Agarwala, Trivalent chromium solutions for applying chemical conversion coatings to aluminium alloys or for sealing anodied aluminium, *Plat. Surf. Finish*, 81, 50–55 (1994).

[79] O. Safety, H. Administration et al., Occupational exposure to hexavalent chromium. final rule., *Federal register*, 71(39), 10099 (2006).

[80] R. Twite and G. P. Bierwagen, Review of alternatives to chromate for corrosion protection of aluminum aerospace alloys, *Progress in organic coatings*, 33(2), 91–100 (1998).

[81] J. R. Davis, *Corrosion of aluminum and aluminum alloys*, Asm International (1999).

[82] G. Trägårdh and D. Johansson, Purification of alkaline cleaning solutions from the dairy industry using membrane separation technology, *Desalination*, 119(1-3), 21–29 (1998).

[83] S. Joshi, W. G. Fahrenholtz and M. J. O'Keefe, Effect of alkaline cleaning and activation on aluminum alloy 7075-T6, *Applied Surface Science*, 257(6), 1859–1863 (2011).

[84] C. Moffitt, D. Wieliczka and H. Yasuda, An XPS study of the elemental enrichment on aluminum alloy surfaces from chemical cleaning, *Surface and Coatings Technology*, 137(2-3), 188–196 (2001).

[85] U. Tiringer, J. Kovač and I. Milošev, Effects of mechanical and chemical pre-treatments on the morphology and composition of surfaces of aluminium alloys 7075-T6 and 2024-T3, *Corrosion Science*, 119, 46–59 (2017).

[86] E. Koroleva, G. Thompson, G. Hollrigl and M. Bloeck, Surface morphological changes of aluminium alloys in alkaline solution:: effect of second phase material, *Corrosion Science*, 41(8), 1475–1495 (1999).

[87] A. Hughes, G. Theodossiou, S. Elliott, T. Harvey, P. Miller, J. Gorman and P. Paterson, Study of deoxidation of 2024-T3 with various acids, *Materials science and technology*, 17(12), 1642–1652 (2001).

[88] https://henk0008.home.xs4all.nl/turco, https://henk0008.home.xs4all.nl/turco.

[89] C. A. Matzdorf, J. L. Green III and M. J. Kane, Pretreatment for aluminum and aluminum alloys (2003), US Patent 6,521,029.

[90] J. J. Alba-Galvín, L. González-Rovira, M. Bethencourt, F. J. Botana and J. M. Sánchez-Amaya, Influence of aerospace standard surface pretreatment on the intermetallic phases and CeCC of 2024-T3 Al-Cu alloy, *Metals*, 9(3), 320 (2019).

[91] T. P. Savas and J. C. Earthman, Surface characterization of 7075-T73 aluminum exposed to anodizing pretreatment solutions, *Journal of materials engineering and performance*, 17(5), 674–681 (2008).

[92] S. Toh, A. Hughes, D. McCulloch, J. DuPlessis and A. Stonham, Characterization of non-Cr-based deoxidizers on Al alloy 7475-T7651, *Surface and Interface Analysis: An International Journal devoted to the development and application of techniques for the analysis of surfaces, interfaces and thin films*, 36(12), 1523–1532 (2004).

[93] A. Hughes, T. Harvey, T. Nikpour, T. Muster and S. Hardin, Non-chromate deoxidation of AA2024-T3 using Fe (III)–HF–HNO3, *Surface and interface analysis*, 37(1), 15–23 (2005).

[94] Y. Liu, M. Arenas, A. De Frutos, J. De Damborenea, A. Conde, P. Skeldon, G. Thompson, P. Bailey and T. Noakes, Influence of nitric acid pre-treatment on Al–Cu alloys, *Electrochimica acta*, 53(13), 4454–4460 (2008).

[95] P. Campestrini, E. Van Westing, A. Hovestad and J. De Wit, Investigation of the chromate conversion coating on Alclad 2024 aluminium alloy: effect of the pH of the chromate bath, *Electrochimica acta*, 47(7), 1097–1113 (2002).

[96] S. Kulinich, A. Akhtar, D. Susac, P. Wong, K. Wong and K. Mitchell, On the growth of conversion chromate coatings on 2024-Al alloy, *Applied surface science*, 253(6), 3144–3153 (2007).

[97] J. Nordlien, J. Walmsley, H. Østerberg and K. Nisancioglu, Formation of a zirconium-titanium based conversion layer on AA 6060 aluminium, *Surface and Coatings Technology*, 153(1), 72–78 (2002).

[98] M. Oki, Studies on chromium-free conversion coatings on aluminum, *Journal of Applied Sciences and Environmental Management*, 11(2) (2007).

[99] O. Lunder, C. Simensen, Y. Yu and K. Nisancioglu, Formation and characterisation of Ti–Zr based conversion layers on AA6060 aluminium, *Surface and Coatings Technology*, 184(2-3), 278–290 (2004).

[100] S. Dong, F. Xingguo, S. Mingren, M. Xinxin and T. Guangze, Composition and corrosion resistance of cerium conversion films on 2195al-li alloy, *Journal of Rare Earths*, 30(4), 383–387 (2012).

[101] A. Conde, M. Arenas, A. De Frutos and J. De Damborenea, Effective corrosion protection of 8090 alloy by cerium conversion coatings, *Electrochimica Acta*, 53(26), 7760–7768 (2008).

[102] M. Dabalà, L. Armelao, A. Buchberger and I. Calliari, Cerium-based conversion layers on aluminum alloys, *Applied Surface Science*, 172(3-4), 312–322 (2001).

[103] Y. Guo and G. Frankel, Characterization of trivalent chromium process coating on AA2024-T3, *Surface and Coatings Technology*, 206(19-20), 3895–3902 (2012).

[104] X. Dong, P. Wang, S. Argekar and D. W. Schaefer, Structure and composition of trivalent chromium process (TCP) films on al alloy, *Langmuir*, 26(13), 10833–10841 (2010).

[105] C. A. Munson and G. M. Swain, Structure and chemical composition of different variants of a commercial trivalent chromium process (TCP) coating on aluminum alloy 7075-T6, *Surface and Coatings Technology*, 315, 150–162 (2017).

[106] X. Verdalet-Guardiola, B. Fori, J.-P. Bonino, S. Duluard and C. Blanc, Nucleation and growth mechanisms of trivalent chromium conversion coatings on 2024-T3 aluminium alloy, *Corrosion Science*, 155, 109–120 (2019).

[107] J. Qi and G. E. Thompson, Comparative studies of thin film growth on aluminium by AFM, TEM and GDOES characterization, *Applied Surface Science*, 377, 109–120 (2016).

[108] L. Li, G. P. Swain, A. Howell, D. Woodbury and G. M. Swain, The formation, structure, electrochemical properties and stability of trivalent chrome process (tcp) coatings on aa2024, *Journal of The Electrochemical Society*, 158(9), C274–C283 (2011).

[109] J. D. Andrade, X-ray photoelectron spectroscopy (XPS), in *Surface and interfacial aspects of biomedical polymers*, pp. 105–195, Springer (1985).

[110] K. Przibram, E. Schrödinger, A. Einstein, H. A. Lorentz and M. Planck, *Letters on wave mechanics*, Vision (1967).

[111] ThermoScientific, https://xpssimplified.com/whatisxps-photoemission.php.

[112] N. Fairley, http://www.casaxps.com.

[113] D. Chadwick and M. Karolewski, Calibration of xps core-level binding energies: Influence of the surface chemical shift, *Journal of Electron Spectroscopy and Related Phenomena*, 24(2), 181–187 (1981).

[114] M. Liu, S. Zanna, H. Ardelean, I. Frateur, P. Schmutz, G. Song, A. Atrens and P. Marcus, A first quantitative XPS study of the surface films formed, by exposure to water, on Mg and on the Mg–Al intermetallics: Al_3Mg_2 and $Mg_{17}Al_{12}$, *Corrosion Science*, 51(5), 1115–1127 (2009).

[115] M. Liu, P. Schmutz, S. Zanna, A. Seyeux, H. Ardelean, G. Song, A. Atrens and P. Marcus, Electrochemical reactivity, surface composition and corrosion mechanisms of the complex metallic alloy Al_3Mg_2, *Corrosion science*, 52(2), 562–578 (2010).

[116] V. Smentkowski and S. Ostrowski, Applications of tof-sims in a research and development laboratory, *Microscopy and Microanalysis*, 12(S02), 1226–1227 (2006).

[117] e2s uppa, https://e2s-uppa.eu/en/research/instrumentation/marss/tof-sims-time-of-flight-secondary-ion-mass-spectrometry.html.

[118] D. Eppink and W. Kuebler, Tirem/sem handbook., Tech. rep., ELECTROMAGNETIC COMPATIBILITY ANALYSIS CENTER ANNAPOLIS MD (1994).

[119] J. Davis et al., Asm specialty handbook, *Aluminum and aluminum alloys*, pp. 207–216 (1993).

[120] Constellium, https://softalloys.constellium.com, *France*.

[121] R. Buchheit, J. Moran and G. Stoner, Electrochemical behavior of the T1 (Al2CuLi) intermetallic compound and its role in localized corrosion of Al-2% Li-3% Cu alloys, *Corrosion*, 50(2), 120–130 (1994).

[122] C. Kumai, J. Kusinski, G. Thomas and T. Devine, Influence of aging at 200 °C on the corrosion resistance of Al-Li and Al-Li-Cu alloys, *Corrosion*, 45(4), 294–302 (1989).

[123] J. Jabra, M. Romios, J. Lai, E. Lee, M. Setiawan, J. Ogren, R. Clark, T. Oppenheim, O. Es-Said, E. Lee et al., The effect of thermal exposure on the mechanical properties of 2099-T6 die forgings, 2099-T83 extrusions, 7075-T7651 plate, 7085-T7452 die forgings, 7085-T7651 plate, and 2397-T87 plate aluminum alloys, *Journal of Materials Engineering and Performance*, 15(5), 601–607 (2006).

[124] D. Ortiz, J. Brown, M. Abdelshehid, P. DeLeon, R. Dalton, L. Mendez, J. Soltero, M. Pereira, M. Hahn, E. Lee et al., The effects of prolonged thermal exposure on the mechanical properties and fracture toughness of C458 aluminum-lithium alloy, *Engineering Failure Analysis*, 13(1), 170–180 (2006).

[125] S. Ahmadi, H. Arabi and A. Shokuhfar, Effects of multiple strengthening treatments on mechanical properties and stability of nanoscale precipitated phases in an aluminum-copper-lithium alloy, *Journal of Materials Science & Technology*, 26(12), 1078–1082 (2010).

[126] B. Jiang, F. Cao, H. Wang, D. Yi, Y. Jiang, F. Shen, B. Wang and H. Liu, Effect of aging time on the microstructure evolution and mechanical property in an Al-Cu-Li alloy sheet, *Materials Science and Engineering: A*, 740, 157–164 (2019).

[127] B. Chen, M.-F. Guo, J.-X. Zheng, K.-Y. Zhang, Y. Fan, L.-Y. Zhou, X.-L. Li and C. Lu, The effect of thermal exposure on the microstructures and mechanical properties of 2198 Al-Li alloy, *Advanced Engineering Materials*, 18(7), 1225–1233 (2016).

[128] A. Higgins, Adhesive bonding of aircraft structures, *International Journal of Adhesion and Adhesives*, 20(5), 367–376 (2000).

[129] J. Venables, D. McNamara, J. Chen, T. Sun and R. Hopping, Oxide morphologies on aluminum prepared for adhesive bonding, *Applications of Surface Science*, 3(1), 88–98 (1979).

[130] B. B. Bouiadjra, H. Fekirini, M. Belhouari, B. Boutabout and B. Serier, Fracture energy for repaired cracks with bonded composite patch having two adhesive bands in aircraft structures, *Computational Materials Science*, 40(1), 20–26 (2007).

[131] J. D. Venables, M. E. Tadros and B. M. Ditchek, Durability of adhesively bonded aluminum structures and method for inhibiting the conversion of aluminum oxide to aluminum hydroxide (1981), US Patent 4,308,079.

[132] P. Marcus, C. Hinnen and I. Olefjord, Determination of attenuation lengths of photoelectrons in aluminium and aluminium oxide by angle-dependent x-ray photoelectron spectroscopy, *Surface and interface analysis*, 20(11), 923–929 (1993).

[133] R. Viroulaud, J. Światowska, A. Seyeux, S. Zanna, J. Tardelli and P. Marcus, Influence of surface pretreatments on the quality of trivalent chromium process coatings on aluminum alloy, *Applied Surface Science*, 423, 927–938 (2017).

[134] S. Mirhashemihaghighi, J. Światowska, V. Maurice, A. Seyeux, S. Zanna, E. Salmi, M. Ritala and P. Marcus, Corrosion protection of aluminium by ultra-thin atomic layer deposited alumina coatings, *Corrosion Science*, 106, 16–24 (2016).

[135] B. Š. Batič and M. Jenko, Orientation-dependent ion beam sputtering at normal incidence conditions in fesial alloy, *Journal of Vacuum Science & Technology A: Vacuum, Surfaces, and Films*, 28(4), 741–744 (2010).

[136] G. Ran, S. Wu, X. Liu, J. Wu, N. Li, X. Zu and L. Wang, The effect of crystal orientation on the behavior of a polycrystalline tungsten surface under focused ga+ ion bombardment, *Nuclear Instruments and Methods in Physics Research Section B: Beam Interactions with Materials and Atoms*, 289, 39–42 (2012).

[137] D. Manova, M. Schreck, S. Mändl, B. Stritzker and B. Rauschenbach, Orientation dependent sputter yield of aluminium, *Surface and Coatings Technology*, 151, 72–75 (2002).

[138] D. Paine, G. Weatherly and K. Aust, A stem study of grain-boundary segregation in al-6.5 wt% mg alloy, *Journal of materials science*, 21(12), 4257–4261 (1986).

[139] R. Ricker and D. Duquette, The role of hydrogen in corrosion fatigue of high purity al-zn-mg exposed to water vapor, *Metallurgical Transactions A*, 19(7), 1775–1783 (1988).

[140] E. Hondros and M. Seah, Segregation to interfaces, *International Metals Reviews*, 22(1), 262–301 (1977).

[141] M. Seah and C. Lea, Surface segregation and its relation to grain boundary segregation, *The Philosophical Magazine: A Journal of Theoretical Experimental and Applied Physics*, 31(3), 627–645 (1975).

[142] M. Ahmad, Thermal oxidation behavior of an Al-Li-Cu-Mg-Zr alloy, *Metallurgical and Materials Transactions A*, 18(4), 681–689 (1987).

[143] H. Saleh, T. Weling, J. Seidel, M. Schmidtchen, R. Kawalla, F. Mertens and H.-P. Vogt, An XPS study of native oxide and isothermal oxidation kinetics at 300 °C of AZ31 twin roll cast magnesium alloy, *Oxidation of Metals*, 81(5-6), 529–548 (2014).

[144] J.-J. Jang and J.-H. Ahn, Effect of oxygen-affinity additives on the superconducting properties of magnesium diboride, *Physics Procedia*, 45, 97–100 (2013).

[145] H. Grabke, Surface and interface segregation in the oxidation of metals, *Surface and Interface Analysis: An International Journal devoted to the development and application of techniques for the analysis of surfaces, interfaces and thin films*, 30(1), 112–119 (2000).

[146] G. K. Johnson, R. T. Grow and W. N. Hubbard, The enthalpy of formation of lithium oxide (Li_2O), *The Journal of Chemical Thermodynamics*, 7(8), 781–786 (1975).

[147] F. Czerwinski, The reactive element effect on high-temperature oxidation of magnesium, *International Materials Reviews*, 60(5), 264–296 (2015).

[148] Wikipedia, https://en.wikipedia.org/wiki/Standard_enthalpy_of_formation.

[149] X. Zhou, Z. Hu and D. Yi, Enhancing the oxidation resistance and electrical conductivity of alumina reinforced copper-based composites via introducing Ag and annealing treatment, *Journal of Alloys and Compounds*, 787, 786–793 (2019).

[150] R. Gupta, N. Nayan, G. Nagasireesha and S. Sharma, Development and characterization of Al-Li alloys, *Materials Science and Engineering: A*, 420(1-2), 228–234 (2006).

[151] T. Warner, Recently-developed aluminium solutions for aerospace applications, in *Materials Science Forum*, vol. 519, pp. 1271–1278, Trans Tech Publ (2006).

[152] A. K. Vasudevan and R. D. Doherty, *Aluminum Alloys-Contemporary Research and Applications: Contemporary Research and Applications*, vol. 31, Elsevier (2012).

[153] A. Smith, Aluminium–lithium alloys in helicopter airframes, *Acta materialia*, 38 (2001).

[154] A. Daniélou, J. Ronxin, C. Nardin and J. Ehrström, Fatigue resistance of Al-Cu-Li and comparison with 7xxx aerospace alloys, in *ICAA13 Pittsburgh*, pp. 511–516, Springer (2012).

[155] J.-F. Li, Z.-Q. Zheng, W.-D. Ren, W.-J. Chen, X.-S. Zhao and S.-C. Li, Simulation on function mechanism of T1 ((Al_2CuLi) precipitate in localized corrosion of Al-Cu-Li alloys, *Transactions of Nonferrous Metals Society of China*, 16(6), 1268–1273 (2006).

[156] V. Proton, J. Alexis, E. Andrieu, C. Blanc, J. Delfosse, L. Lacroix and G. Odemer, Influence of post-welding heat treatment on the corrosion behavior of a 2050-T3 aluminum-copper-lithium alloy friction stir welding joint, *Journal of The Electrochemical Society*, 158(5), C139–C147 (2011).

[157] E. Romhanji and M. Popovic, Problems and prospect of Al-Mg alloys application in marine constructions, *Journal of Metallurgy*, 12(4), 297–307 (2006).

[158] A. Glenn, T. Muster, C. Luo, X. Zhou, G. Thompson, A. Boag and A. Hughes, Corrosion of AA2024-T3 Part III: propagation, *Corrosion Science*, 53(1), 40–50 (2011).

[159] J. Moreto, C. Marino, W. Bose Filho, L. Rocha and J. Fernandes, SVET, SKP and EIS study of the corrosion behaviour of high strength Al and Al-Li alloys used in aircraft fabrication, *Corrosion Science*, 84, 30–41 (2014).

[160] E. Ghanbari, A. Saatchi, X. Lei and D. D. Macdonald, Studies on pitting corrosion of Al-Cu-Li alloys Part II: Breakdown potential and pit initiation, *Materials*, 12(11), 1786 (2019).

[161] X. Lei, A. Saatchi, E. Ghanbari, R. Dang, W. Li, N. Wang and D. D. Macdonald, Studies on pitting corrosion of Al-Cu-Li alloys Part I: Effect of Li addition by microstructural, electrochemical, in-situ, and pit depth analysis, *Materials*, 12(10), 1600 (2019).

[162] J.-L. Huang, J.-F. Li, D.-Y. Liu, R.-F. Zhang, Y.-L. Chen, X.-H. Zhang, P.-C. Ma, R. K. Gupta and N. Birbilis, Correlation of intergranular corrosion behaviour with microstructure in al-cu-li alloy, *Corrosion Science*, 139, 215–226 (2018).

[163] Y. Liu and Y. Cheng, Role of second phase particles in pitting corrosion of 3003 al alloy in nacl solution, *Materials and corrosion*, 61(3), 211–217 (2010).

[164] M. Li, F. Wiame, A. Seyeux, P. Marcus and J. Światowska, Effect of thermal oxidation on surface chemistry and elemental segregation of Al-Cu-Li alloy, *Applied Surface Science*, p. 147633 (2020).

[165] R. Buchheit, A compilation of corrosion potentials reported for intermetallic phases in aluminum alloys, *Journal of the Electrochemical Society*, 142(11), 3994–3996 (1995).

[166] R. Buchheit, R. Boger, M. Carroll, R. Leard, C. Paglia and J. Searles, The electrochemistry of intermetallic particles and localized corrosion in Al alloys, *The Journal of the Minerals*, 53(7), 29–33 (2001).

[167] Y. Zhu, K. Sun and G. Frankel, Intermetallic phases in aluminum alloys and their roles in localized corrosion, *Journal of The Electrochemical Society*, 165(11), C807–C820 (2018).

[168] D. S. Kharitonov, C. Örnek, P. M. Claesson, J. Sommertune, I. M. Zharskii, I. I. Kurilo and J. Pan, Corrosion inhibition of aluminum alloy AA6063-T5 by vanadates: microstructure characterization and corrosion analysis, *Journal of The Electrochemical Society*, 165(3), C116 (2018).

[169] G. Ilevbare, O. Schneider, R. Kelly and J. Scully, In situ confocal laser scanning microscopy of AA2024-T3 corrosion metrology I. localized corrosion of particles, *Journal of The Electrochemical Society*, 151(8), B453–B464 (2004).

[170] M. Büchler, T. Watari and W. H. Smyrl, Investigation of the initiation of localized corrosion on aluminum alloys by using fluorescence microscopy, *Corrosion Science*, 42(9), 1661–1668 (2000).

[171] M. Büchler, J. Kerimo, F. Guillaume and W. H. Smyrl, Fluorescence and near-field scanning optical microscopy for investigating initiation of localized corrosion of Al 2024, *Journal of the Electrochemical Society*, 147(10), 3691–3699 (2000).

[172] R. Grilli, M. A. Baker, J. E. Castle, B. Dunn and J. F. Watts, Localized corrosion of a 2219 aluminium alloy exposed to a 3.5% nacl solution, *Corrosion Science*, 52(9), 2855–2866 (2010).

[173] J. Park, C. Paik, Y. Huang and R. C. Alkire, Influence of Fe-rich intermetallic inclusions on pit initiation on aluminum alloys in aerated NaCl, *Journal of the electrochemical society*, 146(2), 517–523 (1999).

[174] R. Ambat, A. J. Davenport, G. M. Scamans and A. Afseth, Effect of iron-containing intermetallic particles on the corrosion behaviour of aluminium, *Corrosion Science*, 48(11), 3455–3471 (2006).

[175] K. Nis et al., Electrochemical behavior of aluminum-base intermetallics containing iron, *Journal of the Electrochemical Society*, 137(1), 69–77 (1990).

[176] G. Chen, M. Gao and R. Wei, Microconstituent-induced pitting corrosion in aluminum alloy 2024-T3, *corrosion*, 52(1), 8–15 (1996).

[177] N. Dimitrov, J. Mann and K. Sieradzki, Copper redistribution during corrosion of aluminum alloys, *Journal of the Electrochemical Society*, 146(1), 98–102 (1999).

[178] J. Gui and T. Devine, Influence of lithium on the corrosion of aluminum, *Scr. Metall.;(United States)*, 21(6) (1987).

[179] K. S. Rao and K. P. Rao, Pitting corrosion of heat-treatable aluminium alloys and welds: a review, *Trans. Indian Inst. Met*, 57(6), 593–610 (2004).

[180] M. Elboujdaini and R. Revie, Metallurgical factors in stress corrosion cracking (scc) and hydrogen-induced cracking (hic), *Journal of solid state electrochemistry*, 13(7), 1091–1099 (2009).

[181] W.-T. Tsai and M.-S. Chen, Stress corrosion cracking behavior of 2205 duplex stainless steel in concentrated nacl solution, *Corrosion science*, 42(3), 545–559 (2000).

[182] G. Chen, K.-C. Wan, M. Gao, R. Wei and T. Flournoy, Transition from pitting to fatigue crack growth—modeling of corrosion fatigue crack nucleation in a 2024-T3 aluminum alloy, *Materials Science and Engineering: A*, 219(1-2), 126–132 (1996).

[183] K. Sankaran, R. Perez and K. Jata, Effects of pitting corrosion on the fatigue behavior of aluminum alloy 7075-T6: modeling and experimental studies, *Materials Science and Engineering: A*, 297(1-2), 223–229 (2001).

[184] U. Trdan and J. Grum, SEM/EDS characterization of laser shock peening effect on localized corrosion of Al alloy in a near natural chloride environment, *Corrosion Science*, 82, 328–338 (2014).

[185] A. Chemin, D. Marques, L. Bisanha, A. de Jesus Motheo, W. W. Bose Filho and C. O. F. Ruchert, Influence of Al_7Cu_2Fe intermetallic particles on the localized corrosion of high strength aluminum alloys, *Materials & Design*, 53, 118–123 (2014).

[186] D. A., P. J., L. C. and N. S., Integrated AFM and SECM for in situ studies of localized corrosion of Al alloys, *Electrochimica Acta*, 52, 7697–7705 (2007).

[187] R. Grilli, M. A. Baker, J. E. Castle, B. Dunn and J. F. Watts, Localized corrosion of a 2219 aluminium alloy exposed to a 3.5% NaCl solution, *Corrosion Science*, 52, 2855–2866 (2010).

[188] A. Davoodi, J. Pan, C. Leygraf and S. Norgren, The role of intermetallic particles in localized corrosion of an aluminum alloy studied by SKPFM and integrated AFM/SECM, *Journal of The Electrochemical Society*, 155(5), C211–C218 (2008).

[189] M. Li, A. Seyeux, F. Wiame, P. Marcus and J. Światowska, Insights on the al-cu-fe-mn intermetallic particles induced pitting corrosion of al-cu-li alloy, *Corrosion Science*, p. 109040 (2020).

[190] P. Cornette, S. Zanna, A. Seyeux, D. Costa and P. Marcus, The native oxide film on a model aluminium-copper alloy studied by xps and tof-sims, *Corrosion Science*, 174, 108837 (2020).

[191] A. Seyeux, G. Frankel, N. Missert, K. Unocic, L. Klein, A. Galtayries and P. Marcus, Tof-sims imaging study of the early stages of corrosion in al-cu thin films, *Journal of the Electrochemical Society*, 158(6), C165 (2011).

[192] D. S. Lidke and K. A. Lidke, Advances in high-resolution imaging–techniques for three-dimensional imaging of cellular structures, *Journal of cell science*, 125(11), 2571–2580 (2012).

[193] A. J. Bushby, K. M. P'ng, R. D. Young, C. Pinali, C. Knupp and A. J. Quantock, Imaging three-dimensional tissue architectures by focused ion beam scanning electron microscopy, *Nature protocols*, 6(6), 845 (2011).

[194] C. Egan, S. Jacques, M. Wilson, M. Veale, P. Seller, A. Beale, R. Pattrick, P. Withers and R. Cernik, 3d chemical imaging in the laboratory by hyperspectral x-ray computed tomography, *Scientific reports*, 5, 15979 (2015).

[195] R. D. Hanna and R. A. Ketcham, X-ray computed tomography of planetary materials: A primer and review of recent studies, *Geochemistry*, 77(4), 547–572 (2017).

[196] T. Hashimoto, X. Zhang, X. Zhou, P. Skeldon, S. Haigh and G. Thompson, Investigation of dealloying of s phase (Al_2CuMg) in AA2024-T3 aluminium alloy using high resolution 2D and 3D electron imaging, *Corrosion Science*, 103, 157–164 (2016).

[197] B. Mingo, R. Arrabal, A. Pardo, E. Matykina and P. Skeldon, 3D study of intermetallics and their effect on the corrosion morphology of rheocast aluminium alloy, *Materials Characterization*, 112, 122–128 (2016).

[198] M. Laleh, A. E. Hughes, S. Yang, J. Li, W. Xu, I. Gibson and M. Y. Tan, Two and three-dimensional characterisation of localised corrosion affected by lack-of-fusion pores in 316L stainless steel produced by selective laser melting, *Corrosion Science*, 165, 108394 (2020).

[199] B. Chen, M. Guizar-Sicairos, G. Xiong, L. Shemilt, A. Diaz, J. Nutter, N. Burdet, S. Huo, J. Mancuso, A. Monteith et al., Three-dimensional structure analysis and percolation properties of a barrier marine coating, *Scientific reports*, 3, 1177 (2013).

[200] P. Bleuet, P. Gergaud, L. Lemelle, R. Tucoulou, P. Cloetens, J. Susini, G. Delette and A. Simionovici, 3d chemical imaging based on a third-generation synchrotron source, *TrAC Trends in Analytical Chemistry*, 29(6), 518–527 (2010).

[201] R. Vallabhaneni, T. J. Stannard, C. S. Kaira and N. Chawla, 3D X-ray microtomography and mechanical characterization of corrosion-induced damage in 7075 aluminium (Al) alloys, *Corrosion Science*, 139, 97–113 (2018).

[202] S. Jung, M. Foston, U. C. Kalluri, G. A. Tuskan and A. J. Ragauskas, 3D chemical image using ToF-SIMS revealing the biopolymer component spatial and lateral distributions in biomass, *Angewandte Chemie International Edition*, 51(48), 12005–12008 (2012).

[203] J. S. Fletcher, Latest applications of 3d tof-sims bio-imaging, *Biointerphases*, 10(1), 018902 (2015).

[204] L. Zheng, A. Wucher and N. Winograd, Chemically alternating langmuir-blodgett thin films as a model for molecular depth profiling by mass spectrometry, *Journal of the American Society for Mass Spectrometry*, 19(1), 96–102 (2011).

[205] S. Vaidyanathan, J. S. Fletcher, R. Goodacre, N. P. Lockyer, J. Micklefield and J. C. Vickerman, Subsurface biomolecular imaging of streptomyces coelicolor using secondary ion mass spectrometry, *Analytical chemistry*, 80(6), 1942–1951 (2008).

[206] J. S. Fletcher, S. Rabbani, A. Henderson, N. P. Lockyer and J. C. Vickerman, Three-dimensional mass spectral imaging of hela-m cells–sample preparation, data interpretation and visualisation, *Rapid Communications in Mass Spectrometry*, 25(7), 925–932 (2011).

[207] M. A. Robinson, D. J. Graham and D. G. Castner, ToF-SIMS depth profiling of cells: z-correction, 3D imaging, and sputter rate of individual NIH/3T3 fibroblasts, *Analytical chemistry*, 84(11), 4880–4885 (2012).

[208] E. Niehuis, R. Moellers, F. Kollmer, H. Arlinghaus, L. Bernard, H. J. Hug, S. Vranjkovic, R. Dianoux and A. Scheidemann, In-situ tof-sims and sfm measurements providing true 3d chemical characterization of inorganic and organic nanostructures, *Microscopy and Microanalysis*, 20(S3), 2086–2087 (2014).

[209] D. Mercier, J. Światowska, S. Zanna, A. Seyeux and P. Marcus, Role of segregated iron at grain boundaries on Mg corrosion, *Journal of The Electrochemical Society*, 165(2), C42–C49 (2018).

[210] M. Esmaily, P. Malmberg, M. Shahabi-Navid, J. Svensson and L. Johansson, A ToF-SIMS investigation of the corrosion behavior of Mg alloy AM50 in atmospheric environments, *Applied Surface Science*, 360, 98–106 (2016).

[211] A.-I. Stoica, J. Światowska, A. Romaine, F. Di Franco, J. Qi, D. Mercier, A. Seyeux, S. Zanna and P. Marcus, Influence of post-treatment time of trivalent chromium protection coating on aluminium alloy 2024-T3 on improved corrosion resistance, *Surface and Coatings Technology*, 369, 186–197 (2019).

[212] R. N. Sodhi, Time-of-flight secondary ion mass spectrometry (ToF-SIMS):—versatility in chemical and imaging surface analysis, *Analyst*, 129(6), 483–487 (2004).

[213] D. W. Heard, J. Boselli, R. Rioja, E. A. Marquis, R. Gauvin and M. Brochu, Interfacial morphology development and solute trapping behavior during rapid solidification of an Al–Li–Cu alloy, *Acta materialia*, 61(5), 1571–1580 (2013).

[214] J.-T. Li, J. Światowska, A. Seyeux, L. Huang, V. Maurice, S.-G. Sun and P. Marcus, XPS and ToF-SIMS study of Sn–Co alloy thin films as anode for lithium ion battery, *Journal of Power Sources*, 195(24), 8251–8257 (2010).

[215] D. Golodnitsky, M. Nathan, V. Yufit, E. Strauss, K. Freedman, L. Burstein, A. Gladkich and

E. Peled, Progress in three-dimensional (3D) li-ion microbatteries, *Solid State Ionics*, 177(26-32), 2811–2819 (2006).

[216] A. Davoodi, J. Pan, C. Leygraf, R. Parvizi and S. Norgren, An insight into the influence of morphological and compositional heterogeneity of an individual intermetallic particle on aluminium alloy corrosion initiation, *Materials and corrosion*, 64(3), 195–198 (2013).

[217] A. Boag, A. Hughes, N. Wilson, A. Torpy, C. MacRae, A. Glenn and T. Muster, How complex is the microstructure of aa2024-t3?, *Corrosion Science*, 51(8), 1565–1568 (2009).

[218] F. Viejo, A. Coy, F. García-García, M. Merino, Z. Liu, P. Skeldon and G. Thompson, Enhanced performance of the AA2050-T8 aluminium alloy following excimer laser surface melting and anodising processes, *Thin Solid Films*, 518, 2722–2731 (2010).

[219] S. Ghosh, *Effect of stress on initiation and propagation of localized corrosion in alumninium alloys*, Ph.D. thesis, University of Birmingham (2008).

[220] T. Boettcher, M. Rother, S. Liedtke, M. Ullrich, M. Bollmann, A. Pinkernelle, D. Gruber, H.-J. Funke, M. Kaiser, K. Lee et al., On the intermetallic corrosion of Cu-Al wire bonds, in *2010 12th Electronics Packaging Technology Conference*, pp. 585–590, IEEE (2010).

[221] T. J. Leclère and R. C. Newman, Self-regulation of the cathodic reaction kinetics during corrosion of AlCu alloys, *Journal of The Electrochemical Society*, 149(2), B52–B56 (2002).

[222] X. Zhou, G. Thompson, H. Habazaki, K. Shimizu, P. Skeldon and G. Wood, Copper enrichment in Al-Cu alloys due to electropolishing and anodic oxidation, *Thin Solid Films*, 293(1-2), 327–332 (1997).

[223] Y. Zhu and G. Frankel, Effect of major intermetallic particles on localized corrosion of aa2060-t8, *Corrosion*, 75(1), 29–41 (2019).

[224] L. Lacroix, L. Ressier, C. Blanc and G. Mankowski, Combination of afm, skpfm, and sims to study the corrosion behavior of s-phase particles in aa2024-t351, *Journal of the Electrochemical Society*, 155(4), C131 (2008).

[225] D. Costa, T. Ribeiro, F. Mercuri, G. Pacchioni and P. Marcus, Atomistic modeling of corrosion resistance: a first principles study of o2 reduction on the al (111) surface covered with a thin hydroxylated alumina film, *Advanced Materials Interfaces*, 1(3), 1300072 (2014).

[226] A. Hughes, R. Taylor, K. Nelson, B. Hinton and L. Wilson, Characterisation of surface preparation of 2024 aluminium alloy for conversion coating, *Materials science and technology*, 12(11), 928–936 (1996).

[227] O. Lunder and K. Nisancioglu, The effect of alkaline-etch pretreatment on the pitting corrosion of wrought aluminum, *Corrosion*, 44(7), 414–422 (1988).

[228] L. Li and G. M. Swain, Formation and structure of trivalent chromium process coatings on aluminum alloys 6061 and 7075, *Corrosion*, 69(12), 1205–1216 (2013).

[229] J.-T. Qi, T. Hashimoto, J. Walton, X. Zhou, P. Skeldon and G. Thompson, Trivalent chromium conversion coating formation on aluminium, *Surface and Coatings Technology*, 280, 317–329 (2015).

[230] J. Qi, A. Němcová, J. Walton, X. Zhou, P. Skeldon and G. Thompson, Influence of pre-and post-treatments on formation of a trivalent chromium conversion coating on AA2024 alloy, *Thin Solid Films*, 616, 270–278 (2016).

[231] J. Qi, L. Gao, Y. Li, Z. Wang, G. Thompson and P. Skeldon, An optimized trivalent chromium conversion coating process for AA2024-T351 alloy, *Journal of The Electrochemical Society*, 164(7), C390 (2017).

[232] M. Ely, J. Światowska, A. Seyeux, S. Zanna and P. Marcus, Role of post-treatment in improved corrosion behavior of trivalent chromium protection (TCP) coating deposited on aluminum alloy 2024-T3, *Journal of The Electrochemical Society*, 164(6), C276–C284 (2017).

[233] F. George, P. Skeldon and G. Thompson, Formation of zirconium-based conversion coatings on aluminium and Al–Cu alloys, *Corrosion science*, 65, 231–237 (2012).

[234] J. Cerezo, I. Vandendael, R. Posner, K. Lill, J. De Wit, J. Mol and H. Terryn, Initiation and

growth of modified Zr-based conversion coatings on multi-metal surfaces, *Surface and Coatings Technology*, 236, 284–289 (2013).

[235] J. Qi, Y. Miao, Z. Wang, Y. Li, X. Zhang, P. Skeldon and G. Thompson, Influence of copper on trivalent chromium conversion coating formation on aluminum, *Journal of The Electrochemical Society*, 164(12), C611 (2017).

[236] A. Sarfraz, R. Posner, M. M. Lange, K. Lill and A. Erbe, Role of intermetallics and copper in the deposition of ZrO_2 conversion coatings on AA6014, *Journal of The Electrochemical Society*, 161(12), C509–C516 (2014).

[237] I. Häusler, C. Schwarze, M. U. Bilal, D. V. Ramirez, W. Hetaba, R. D. Kamachali and B. Skrotzki, Precipitation of T1 and θ' phase in Al-4Cu-1Li-0.25Mn during age hardening: microstructural investigation and phase-field simulation, *Materials*, 10(2), 117 (2017).

[238] C. T. Rueden, J. Schindelin, M. C. Hiner, B. E. DeZonia, A. E. Walter, E. T. Arena and K. W. Eliceiri, Imagej2: Imagej for the next generation of scientific image data, *BMC bioinformatics*, 18(1), 529 (2017).

Appendix A

Intermetallic particles and corrosion behaviour of Al-Cu-Li alloys

Preliminary information about intermetallic particles induced pitting corrosion is presented in this appendix: intermetallic particles in AA2050-T8 Al-Cu-Li alloy and pitting corrosion behaviour in aggressive NaCl electrolyte. The Intermetallic particles in AA2050-T8 was studied by microscopic techniques such as SEM, TEM and optical microscopy. Then, the corrosion behaviour of sample in 0.1 M NaCl was studied. The amount of pits and pitting area was measured by optical microscopy and calculated by image manipulation software

A.1 Intermetallic particles in AA2050-T8 Al-Cu-Li alloy

IMPs are divided into two groups based on the size. One corresponds to large IMPs of diameter over 1 µm and the other corresponds to small IMPs which are of nanometre size.

Large intermetallic particles in AA2050

In order to study the large IMPs of AA2050, SEM is performed on a randomly selected region of AA2050-T8 Al-Cu-Li alloy as shown in Fig. A.1. Then EDX mapping was performed in the framed region of Fig. A.1. The chemical analysis is presented in Fig. A.2.

According to the SEM and EDX mapping of AA2050-T8, only one kind of larger IMPs can be

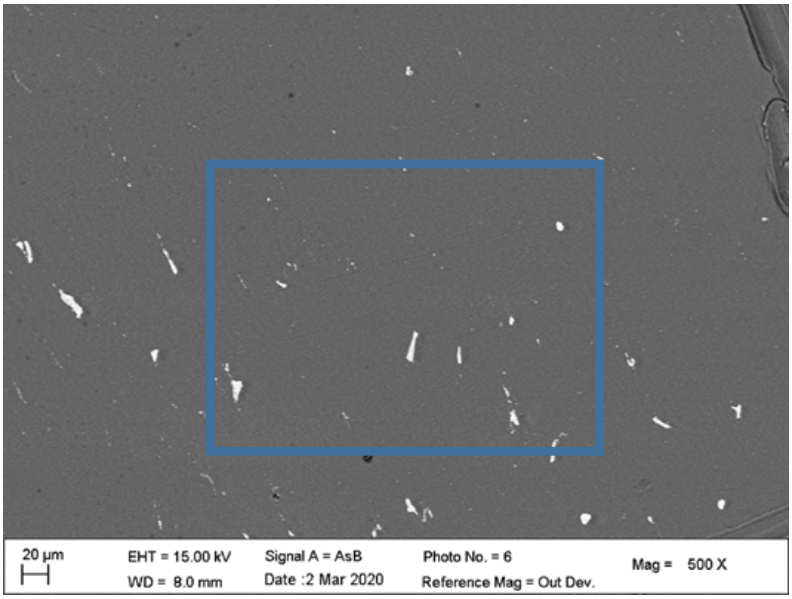

Figure A.1: Scanning electron microscopy of AA2050-T8

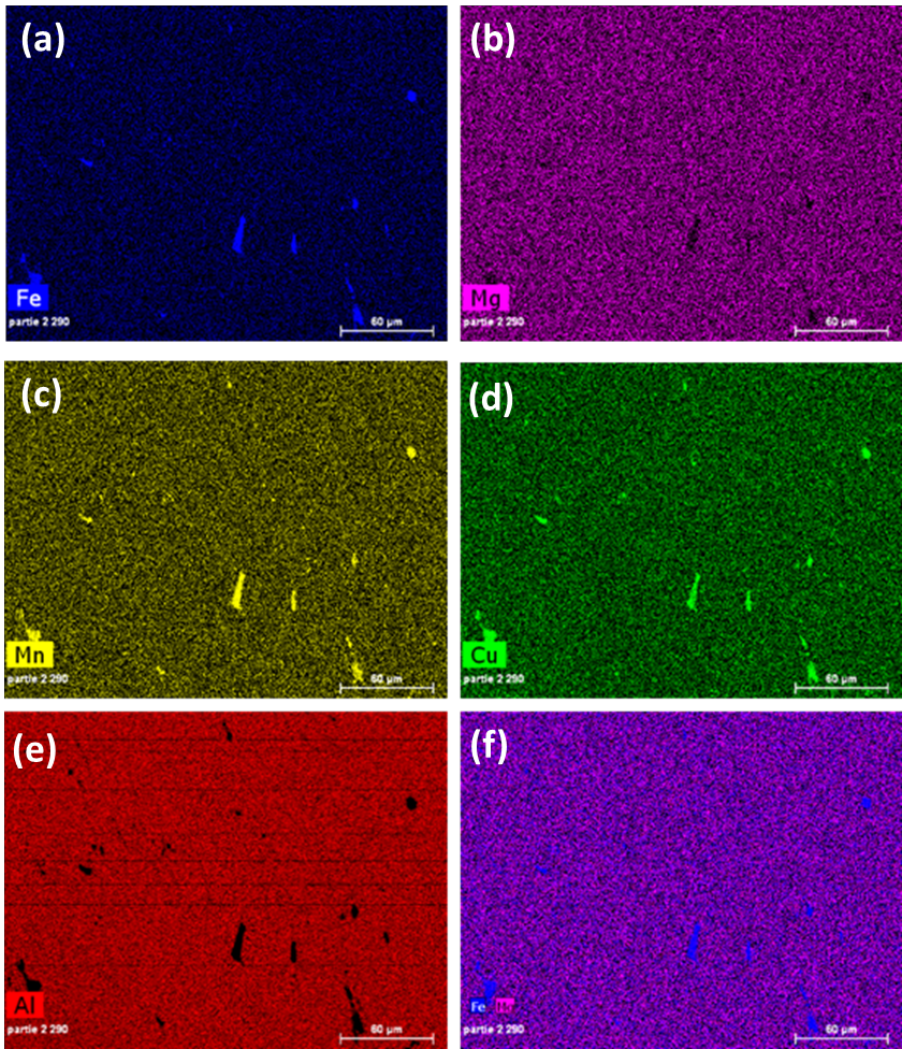

Figure A.2: EDX mapping of AA2050-T8 of (a) Fe, (b) Mg, (c) Mn, (d) Cu, (e) Al and (f) overlay of Fe and Mg

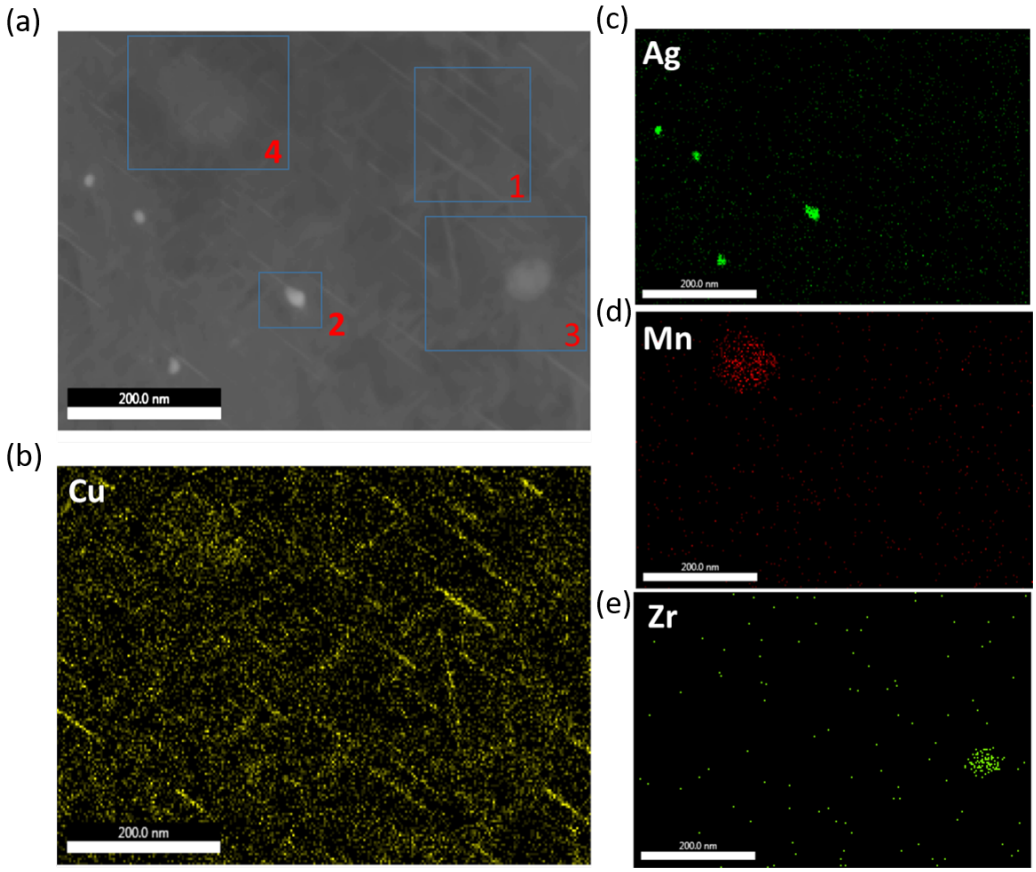

Figure A.3: TEM (a) and EDX elemental mapping images (b) Cu, (c) Ag, (d) Mn, (e) Zr of small IMPs in AA2050

evidenced, which is Al-Cu-Fe-Mn IMPs. To estimate the amount of Al-Cu-Fe-Mn IMPs in AA2050-T8, the area ratio of IMPs of four randomly selected regions (Fig. B.4 in Appendix B), including the corresponding region of Fig. A.1, are calculated. The average value of large IMPs area ratio are 0.56 $\pm$ 0.15 % and the average size of the larger IMPs is 4.5 $\pm$ 2.5 μm^2. All dataa are presented in appendix B.

Small intermetallic particles in AA2050

As previously introduced, the smaller IMPs in Al-Cu-Li alloys such as T1 phase are of nanometre size and the resolution of SEM is not sufficient to evidence this small IMPs. Therefore, TEM is used for analysing the smaller IMPs in AA2050. Different types of small IMPs are evidenced based on the TEM analysis such as T1 phase (Al_2CuLi) or θ' phase (Al_2Cu with a needle shape, Ag cluster, Zr-containing dispersoid and smaller Al-Cu-Fe-Mn IMPs. The TEM/EDX images of each kind of IMPs are presented in Fig. A.3. Four kinds of small IMPs with different shape and chemical

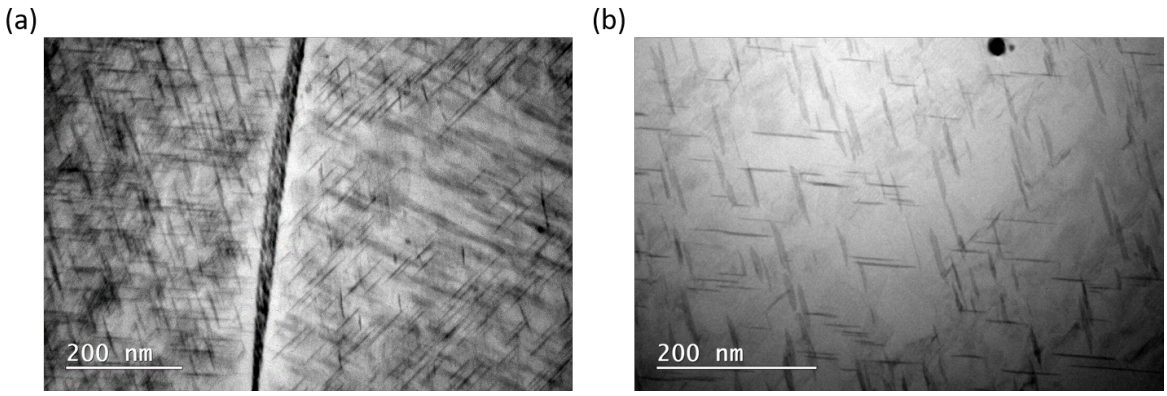

Figure A.4: TEM images of T1 phase in AA2050-T8 (a) along grain boundary, (b) inside the grain

composition are highlighted as 1 to 4 in the first image. IMPs with Cu-enrichment and typical needle shape are evidenced in Fig. A.3 (b). Although Li is impossible to evidence by EDX in this case, the typical shape and size of IMPs suggests that this kind of IMPs is supposed to be T1 or θ' phase. According to the Cu image in Fig. A.3 (b), the amount and density of these needle-shape IMPs is high with a homogeneous distribution in the Al matrix. This is confirmed by the TEM images presented in Fig. A.4. The length and thickness of these IMPs is about 50–100 nm and 2–10 nm, respectively, which is similar to the description of T1 and θ' phases in literature [19, 237].

The second kind of IMPs presented in Fig. A.3(e) are 50 nm IMPs with Zr enrichment. As previously introduced, Zr can combine with Al and form nano-size dispersoid with effect on anti-recrystallization and promote the precipitates to be uniform. The third kind of IMPs corresponds to Ag-rich clusters (Fig. A.3(c)) of approximately 10 nm in size and have similar effects than Zr-containing IMPs [7, 10, 11]. The forth kind of IMP are enriched with Cu and Mn. A cluster of Al-Cu-Mn IMPs with size from 50–500 nm is presented in Fig. A.6. The shape of Al-Cu-Mn IMPs likes rod or round (maybe influenced by the observation direction) and the size of them is around 100–500 nm. A similar small IMP is also observed as presented in Fig. A.6, which are nano-sized Al-Cu-Fe-Mn IMPs. The size of them is around 50 nm and 150 nm with irregular shape. As previously introduced, most literature only mentioned or investigated the large Al-Cu-Fe-Mn IMPs in micro scale. Therefore, it is surprising to find nano-size Al-Cu-Fe-Mn IMPs in Al-Cu-Li alloy.

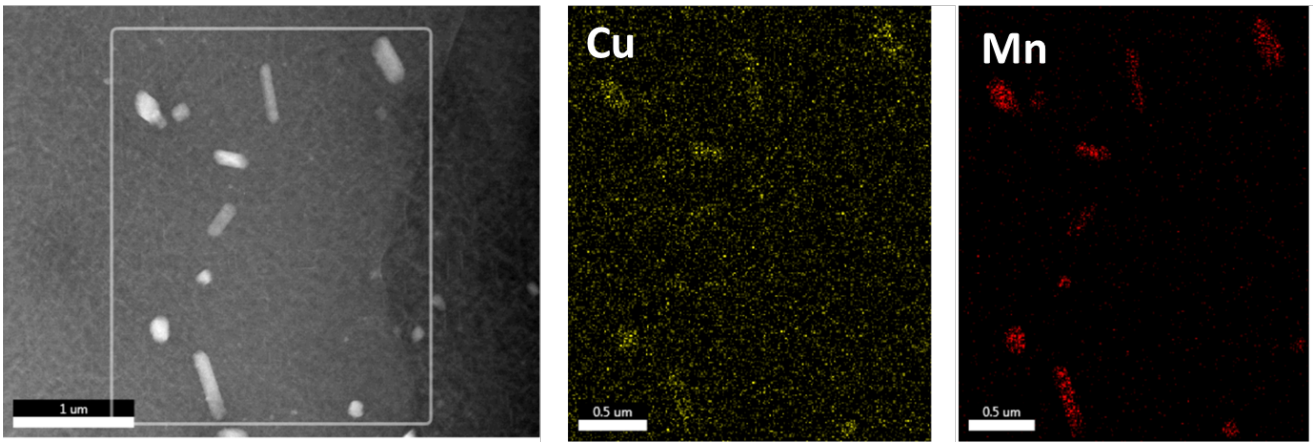

Figure A.5: TEM and EDX elemental mapping images of small Al-Cu-Mn IMPs (100-500 nm) in AA2050

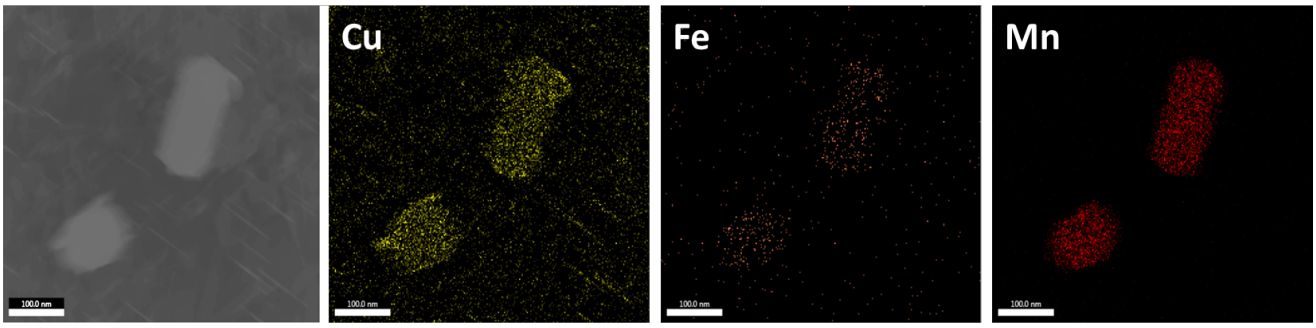

Figure A.6: TEM and EDX elemental mapping images of smaller Al-Cu-Fe-Mn IMPs (100-200 nm) in AA2050

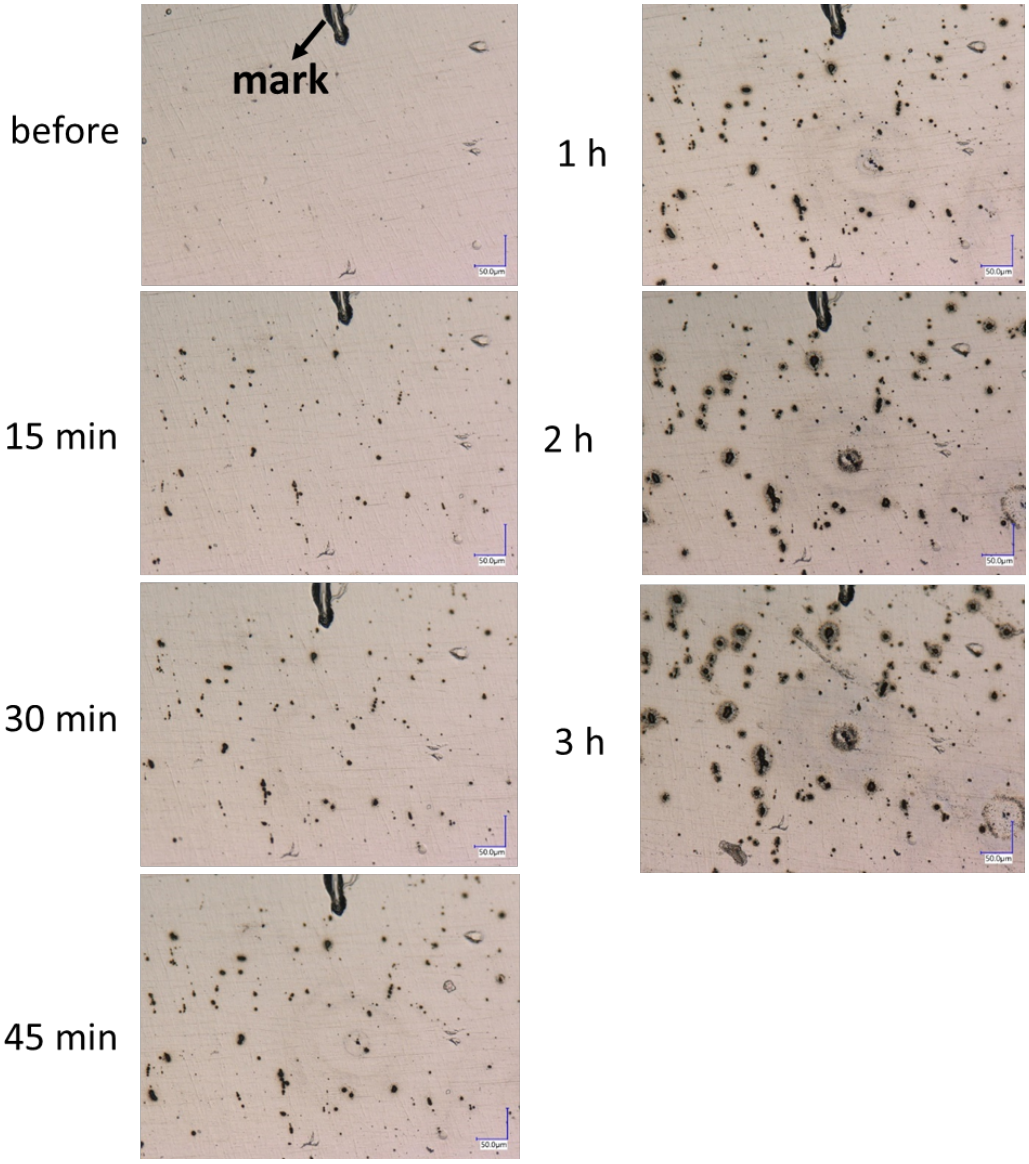

Figure A.7: Optical microscopy image of evolution of pitting corrosion of AA2050 as a function of immersion time in 0.1 M NaCl

A.2 Corrosion behaviour in aggressive NaCl electrolyte

In this thesis, the initial corrosion of AA2050 was investigated in 0.1 M NaCl electrolyte and the pitting corrosion behaviour at different immersion time was characterized by SEM and optical microscope. The polished (0.3 µm) surface is marked by a sharp needle and placed into the 0.1 M NaCl electrolyte for different time then analysed by optical microscope. Fig. A.7 shows the evolution of corrosion morphology of marked area as a function of immersion time in 0.1 M NaCl.

According to Fig. A.7, few small pits are formed when surface is immersed in 0.1 M NaCl for 15 min and the corresponding size and amount keep increasing during immersion. After 3 h

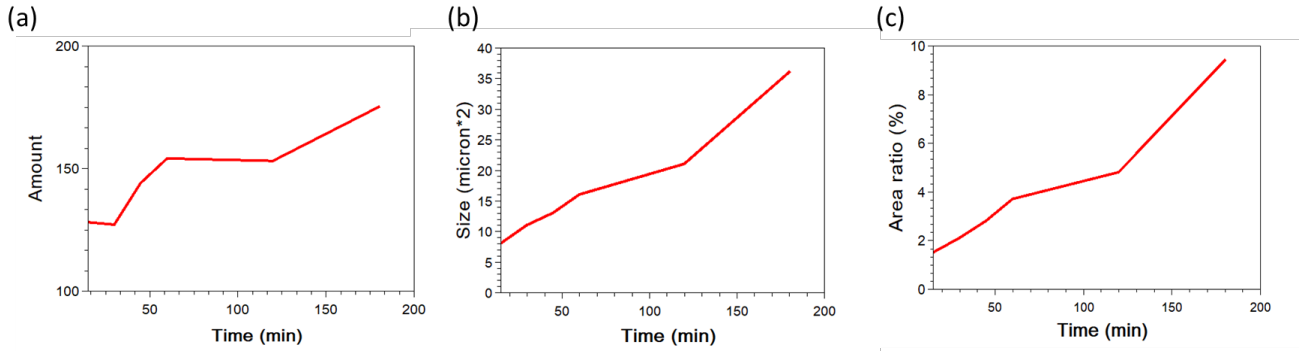

Figure A.8: Evolution of pits of corroded AA2050 as a function of immersion time in 0.1 M NaCl (a) evolution of amount of pits, (b) evolution of average size of pits, (c) evolution of area ration of pits

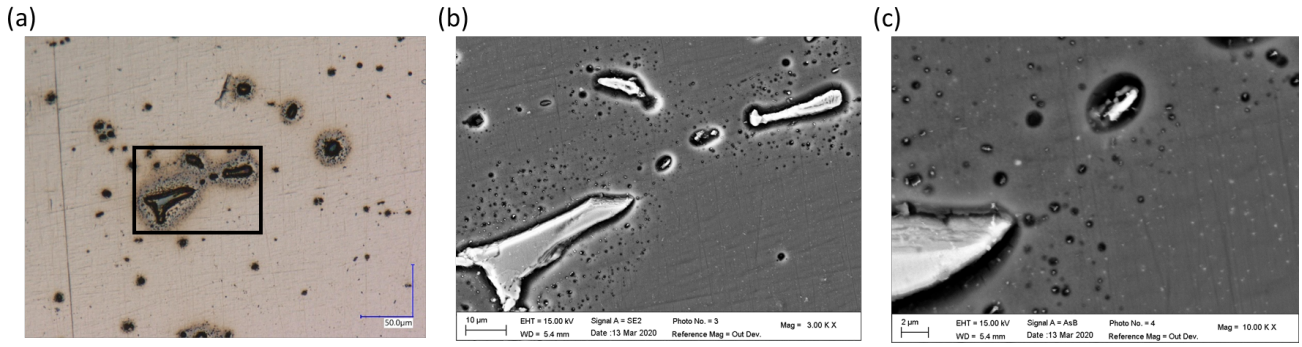

Figure A.9: Corrosion morphology of AA2050 after 3 h immersion in 0.1 M NaCl (a) optical microscopy (b) SEM of the marked region in (a), a zoom in of (b) at the boundary of IMP and matrix

immersion, severe pitting corrosion is observed on the surface. The pitting area is simulated and quantified by the “ImageJ” software [238]. The evolution of size and area ratio as a function of immersion time is indicated in the following figures.

Fig. A.8 (a) shows the amount evolution of pits. The amount of pits keeps stable in the first 30 min and start to increase while the average size of pits keeps increasing during immersion and increases faster after 2 h of immersion as shown in Fig. A.8 (b). As shown in Fig. A.8 (c), the evolution of area ratio of pits is similar with the evolution of average size and a significant increase of pitting area observed after 2 h immersion. This significant increase of pitting area and average size of pits is supposed to be induced form the “shadow” around the IMPs as shown in Fig. A.7, which is presented after 2 h immersion and became significant after the third hour. In order to better evidence this shadow, SEM and optical microscopy images were performed after immersion in the 0.1 M NaCl for 3 h (Fig. A.9).

Fig. A.9 (a) shows a pitting area selected on the optical image of the surface where Al-Cu-Fe-Mn IMPs are observed. As described previously, shadow is observed around the IMPs (pits). Fig.

A.9 (b) is the SEM of the marked region in Fig. A.9 (a). Many small pits can be observed around the large Al-Cu-Fe-Mn IMPs. These pits are of nanometre size. As shown in Fig. A.9 (c), there are still small IMPs that can be observed in some of the small pits. Moreover, the trace of the small IMPs can be evidenced on the non-corroded region also. It indicates that, the small pits are located over and around the IMPs and lager Al-Cu-Fe-Mn IMPs promote this pitting behaviour. As introduced in previous section, there are several kinds of small nano-size IMPs, it is therefore difficult to figure out which kinds of IMPs induced this small pits. However, it seems clear that the larger Al-Cu-Fe-Mn IMPs play an important role in the corrosion behaviour of AA2050 Al-Cu-Li alloy on the corrosion initiation. Since most of the pits is located at large Al-Cu-Fe-Mn IMPs, therefore, a detailed study of Al-Cu-Fe-Mn IMPs during corrosion initiation is essential. ToF-SIMS depth profiles, ToF-SIMS 2D and 3D chemical mappings were used to study the corrosion behaviour and the corresponding surface modifications of the Al-Cu-Fe-Mn IMPs during the initial steps of corrosion. The results and discussion is presented in the chapter4, which are transcription of published or submitted scientific articles.

Appendix B

Supplementary results

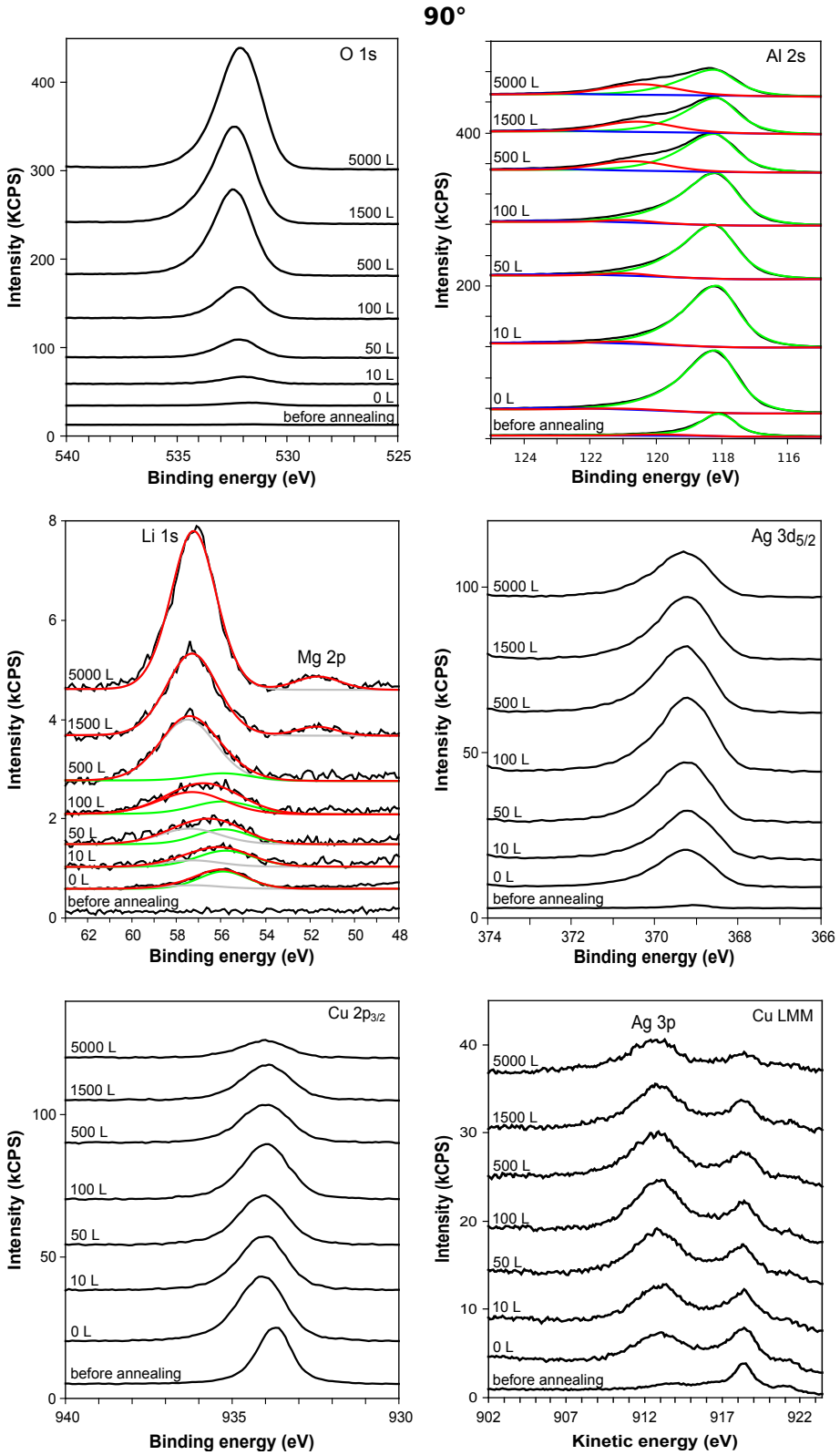

Figure B.1: XPS spectrum at 90° take-off angle

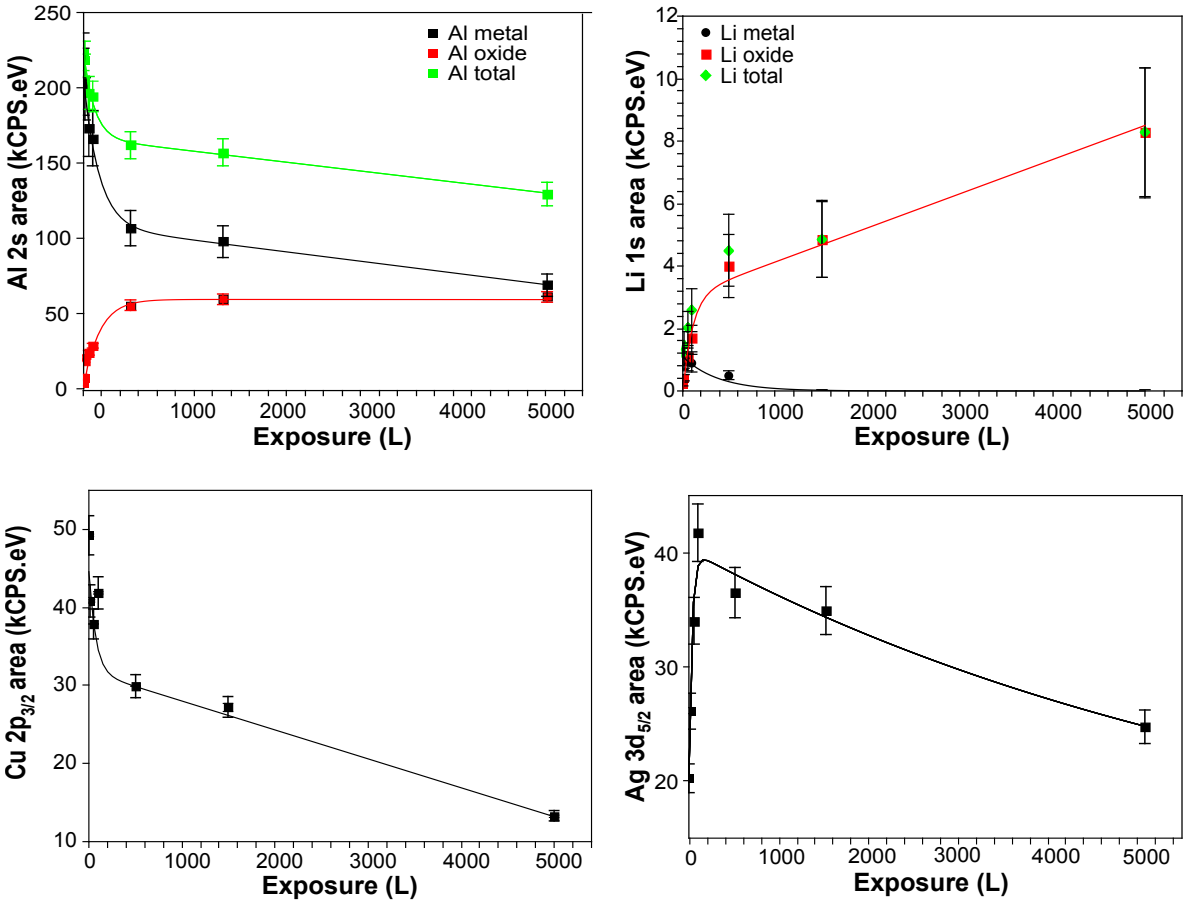

Figure B.2: Intensity of XPS components at 90° take-off angle

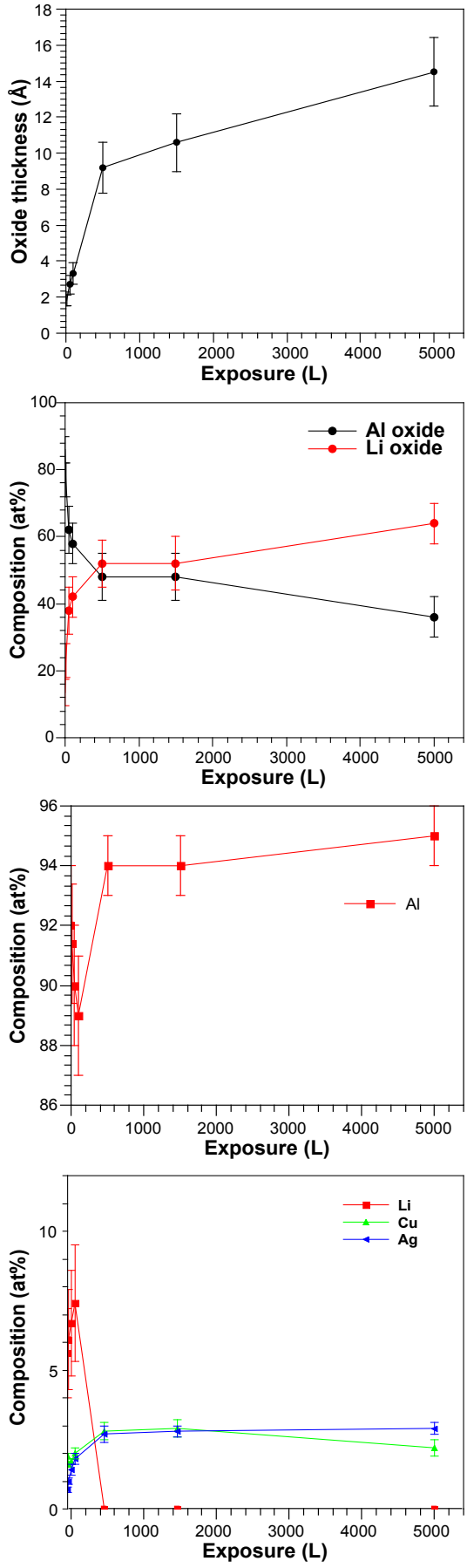

Figure B.3: Composition of oxide layer

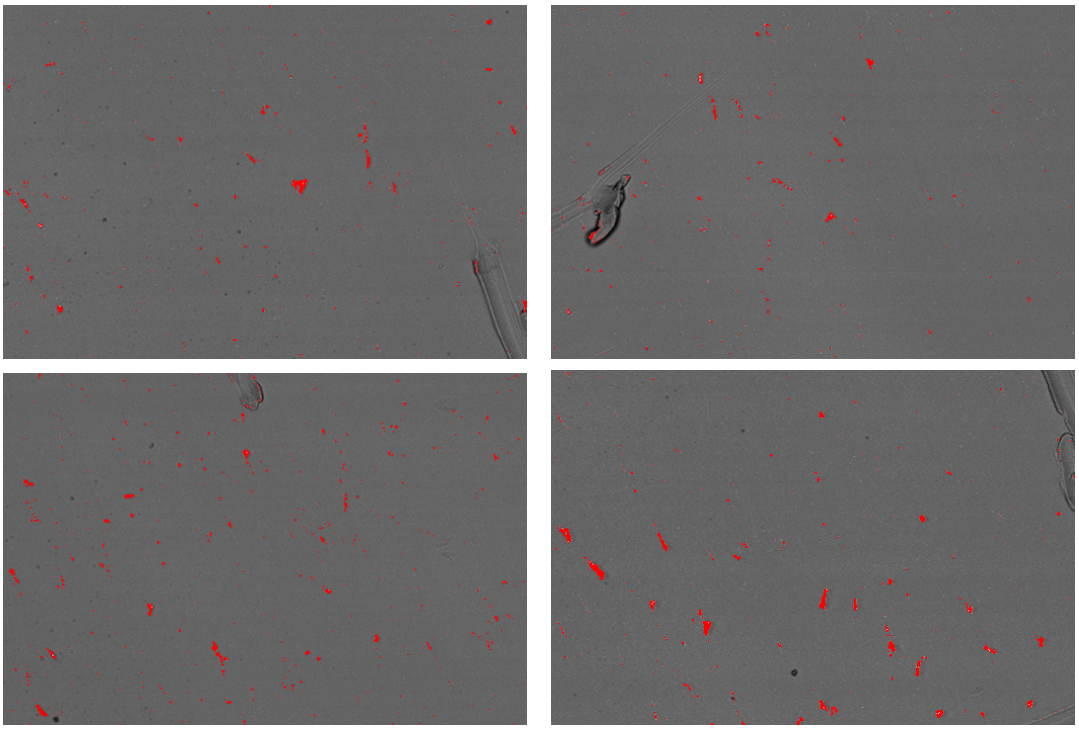

Figure B.4: SEM images of randomly selected area of AA2050-T8 for the calculation of amount and area ratio of larger intermetallic particles

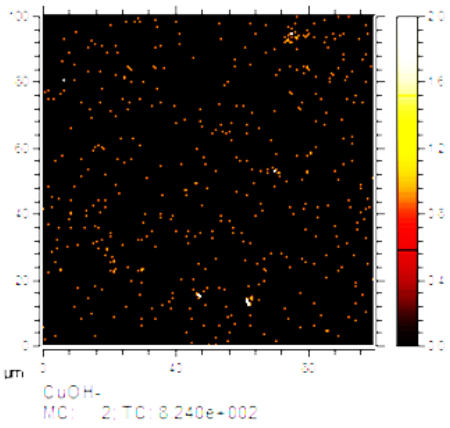

Figure B.5: ToF-SIMS image chemical mapping (100 µm × 100 µm) of $CuOH^-$ obtained for AA2050-T8 after immersion in 0.1M NaCl for 45 min at the metal/oxide interface (sputtered to 150 s)

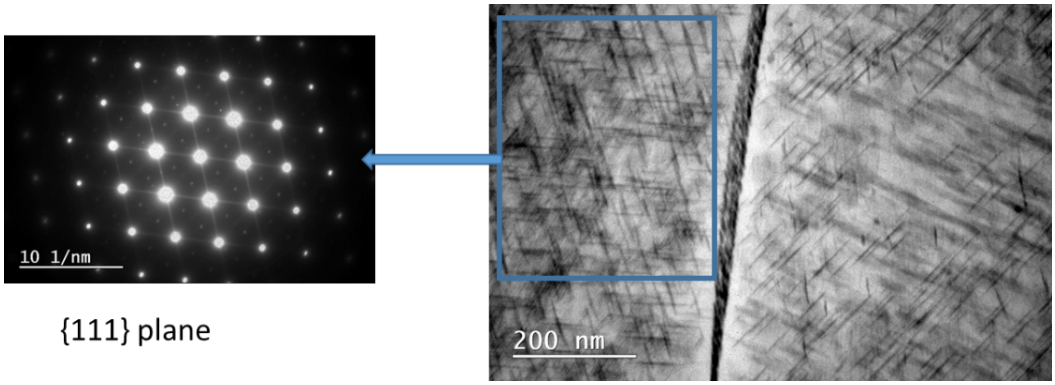

Figure B.6: Transmission electron microscopy of AA2080-T8 in 111 plane: needle-shape T1 phase homogeneously distributes in the Al matrix

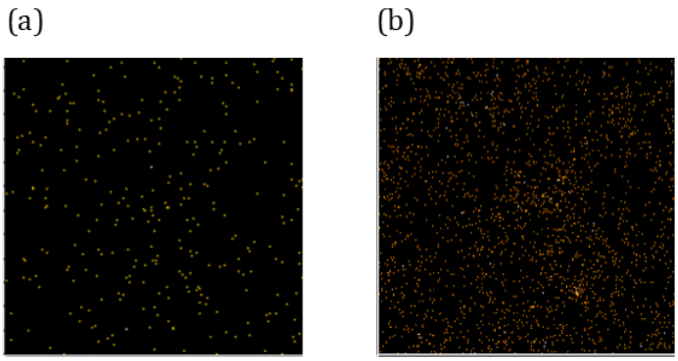

Figure B.7: ToF-SIMS image chemical mapping (100 µm × 100 µm) of $CuOH^-$ in the region of interest comprising a selected Al-Fe-Cu-Mn IMP after immersion in 0.1M NaCl for 45 min (a) in the oxide (sputtered to 65 s) and (b) at the metal / oxide interface (sputtered to 150 s)

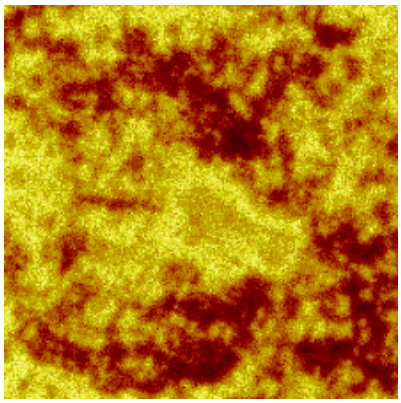

Figure B.8: Re-treated ToF-SIMS chemical mapping (100 µm × 100 µm) of AA2050-T8 in the region of interest for O^- signal in the oxide (sputtered to 65 s)

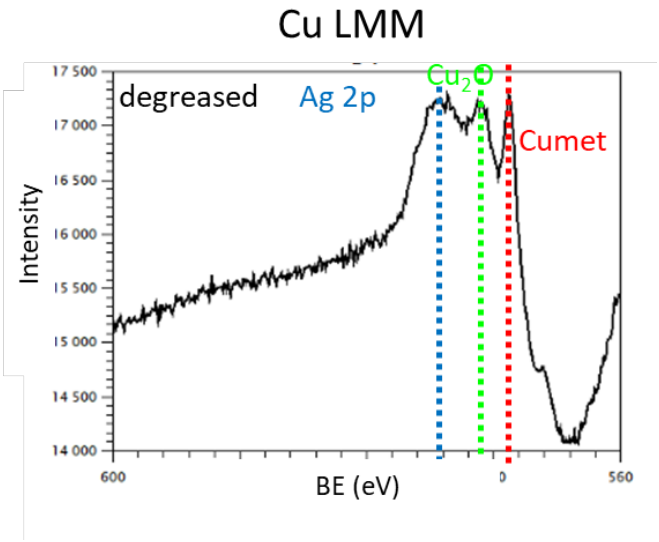

Figure B.9: Cu LMM spectrum of degreased surface

Annexe : résumé étendu de thèse

Chapitre 1 : état de l'art et objectifs

L'aluminium est l'un des métaux les plus couramment utilisés au monde. Pour répondre aux exigences de chaque application, des éléments d'alliage tels que Cu, Mg, Mn ou Zn sont souvent ajoutés à la matrice d'Al afin de modifier et d'améliorer les propriétés spécifiques telles que la résistance, la dureté ou la soudabilité. Les alliages Al-Cu-Li (tel que AA2050) sont considérés comme des matériaux qui pourraient à terme avantageusement remplacer les alliages Al-Cu conventionnels (AA2024) dans l'industrie aérospatiale. Pour chaque pourcent de Li ajouté, le module élastique peut augmenter jusqu'à 6 % avec une réduction de 3 % de la densité. Cependant, la teneur en Li de la plupart des alliages Al-Cu-Li aérospatiaux est limitée à moins de 1,4 % pour garantir que la phase T1 (Al_2CuLi), qui a un meilleur effet de renforcement et une meilleure stabilité thermique, constitue le principal type de particules intermétallique (IMP) de renforcement. La microstructure des précipités et les propriétés mécaniques correspondantes des alliages Al-Cu-Li peuvent être améliorées sous traitement thermique en optimisant la distribution, la densité et la taille des IMP de renforcement. Par exemple, dans le cas de AA2050-T3, seules quelques phases T1 s'accumulent aux joints de grains. Mais si l'AA2050 est recuit à l'état T8, il se forme une phase T1 beaucoup plus dense, répartie de manière homogène à la fois aux joints de grains et à l'intérieur des grains et la résistance correspondante est supérieure à celle de l'AA2050-T3.

En ce qui concerne la durée de vie des aéronefs, on essaie d'éviter à la fois la corrosion et l'oxydation car elles peuvent entraîner de graves détériorations ou même la destruction des matériaux.

La corrosion est un problème aux conséquences graves en terme de coût et de sécurité dans

de très nombreux domaines industriels. Deux comportements typiques de la corrosion localisée des alliages Al-Cu-Li sont observés : l'un correspond à la dissolution de la phase anodique T1, l'autre est induit par le couplage galvanique local entre la matrice et les IMP cathodiques Al-Cu-Fe-Mn. Étant donné que la phase T1 est plus anodique par rapport à la matrice Al, une sévère corrosion intragranulaire (IGC) et une corrosion transgranulaire (TGC) ont été observées dans les alliages Al-Cu-Li et dépendent en grande partie de la dissolution du Li présent principalement dans la phase nanométrique T1 (Al_2CuLi). La présence de Li dans la phase T1 la rend plus anodique que la matrice et favorise sa dissolution lors de la corrosion. Les IMP de type Al-Cu-Fe-Mn sont très courants dans la plupart des alliages industriels d'Al. Ils sont formés pendant le processus de coulée et sont répartis de manière aléatoire dans les alliages d'Al. Ils induisent la corrosion par piqûres en créant un couplage galvanique avec la matrice. La distribution du Li dans les IMP de type Al-Fe-Cu-Mn et son effet sur la corrosion par piqûres ne sont pas encore clairement établis. Peu d'études ont tenté de mettre en évidence la distribution du Li dans les IMP. Elles ont révélé que les particules à faible teneur en cuivre contiennent beaucoup moins de lithium que les particules à forte teneur en cuivre. Elles ont également révélé que les particules à haute teneur en cuivre étaient plus réactives en raison de la teneur élevée en Li.

Pour améliorer la résistance à la corrosion et les propriétés mécaniques de surface, un traitement de surface est nécessaire dans l'industrie aérospatiale avant la mise en service. Le traitement de surface peut être conçu pour améliorer l'adhérence entre deux phases dans un matériau composite ou pour une meilleure résistance à la corrosion. Dans l'industrie aérospatiale, le traitement de surface initial consiste en une immersion dans un bain de dégraissage alcalin suivi d'un décapage acide puis d'un revêtement d'anodisation ou de conversion. Normalement, le dégraissage alcalin et le décapage acide sont considérés comme le prétraitement. Le nettoyage alcalin consiste à éliminer l'épaisse couche d'oxyde natif et la contamination organique laissée après la fabrication, également appelée **"dégraissage"** et deuxièmement, le nettoyage à l'acide, également appelé **"décapage"**, pour éliminer la couche d'oxyde formée pendant l'étape de dégraissage, les IMP en surface et diminuer la sensibilité à la corrosion. L'objectif du prétraitement (dégraissage et décapage) est d'optimiser l'état de surface par une plus grande homogénéité chimique et une adaptabilité plus élevée pour les traitements de surface chimiques/électrochimiques successifs.

Ce sont des processus importants pour le traitement de surface et ils jouent un rôle essentiel dans le succès ou l'échec de la suite de la procédure. Le procédé chrome trivalent (TCP) est reconnu comme un processus de conversion prometteur pour le remplacement des espèces de chrome hexavalent en raison de son avantage écologique. Le bain utilisé pour le TCP contient généralement des constituants ZrF_6^{2-} et Cr^{3+} dans une solution aqueuse avec un pH de 3,8 à 4,0 à 40 °C. C'est un processus de dépôt contrôlé par le pH créé par Zr^{VI} et Cr^{III}. Au début du procédé TCP, l'oxyde natif se dissout par l'activation d'ions fluorure et du fluoroaluminate est formé à la surface du substrat. En raison de la consommation de protons, le pH local augmente sur la surface et conduit au dépôt d'espèces Cr et Zr en formant une couche de conversion. Par conséquent, une structure à deux couches se forme au cours du processus TCP. Normalement, l'épaisseur de la couche TCP est d'environ 40 nm à 120 nm en fonction du temps de dépôt avec une résistance à la corrosion comparable à celle des autres traitements de conversion des chromates. Seules quelques études se sont concentrées sur le comportement des alliages Al-Cu-Li lors du traitement de surface. Il a été mis en évidence une dissolution significative du Li et de l'Al et un enrichissement en Cu en surface lors du nettoyage alcalin. Ensuite, une dissolution préférentielle de Cu, Fe, Mn et Mg sur les surfaces nettoyées par une solution alcaline est observée dans l'acide nitrique avec une vitesse de dissolution plus lente pour Li. À notre connaissance, aucune étude n'a porté sur la couche TCP formée sur les alliages Al-Cu-Li. Il est donc nécessaire de tester l'adaptabilité de ce (pré)traitement de surface pour les alliages Al-Cu-Li en vue de permettre le développement ultérieur du matériau et des traitements de surface.

Outre la corrosion, l'oxydation (en particulier l'oxydation thermique) est un autre facteur important en ce qui concerne la dégradation des matériaux utilisés en aviation. La ségrégation se produit pendant l'oxydation thermique. Un cas typique est la ségrégation de surface du Li sur la surface recuite d'alliages Al-Cu-Li qui induit une accélération du processus d'oxydation et un ramollissement de la surface. Le magnésium, un élément d'alliage actif dans les alliages Al-Cu-Li, a un comportement de ségrégation similaire à haute température, en particulier aux joints de grains. Ce phénomène a un effet important sur l'IGC, la fissuration par corrosion sous contrainte (SCC) et la fragilisation par l'hydrogène (HE). Les éléments d'alliage nobles tels que l'Ag dans les alliages Al-Cu-Li ségrègent également vers la surface libre au cours des traitements thermiques. Cependant,

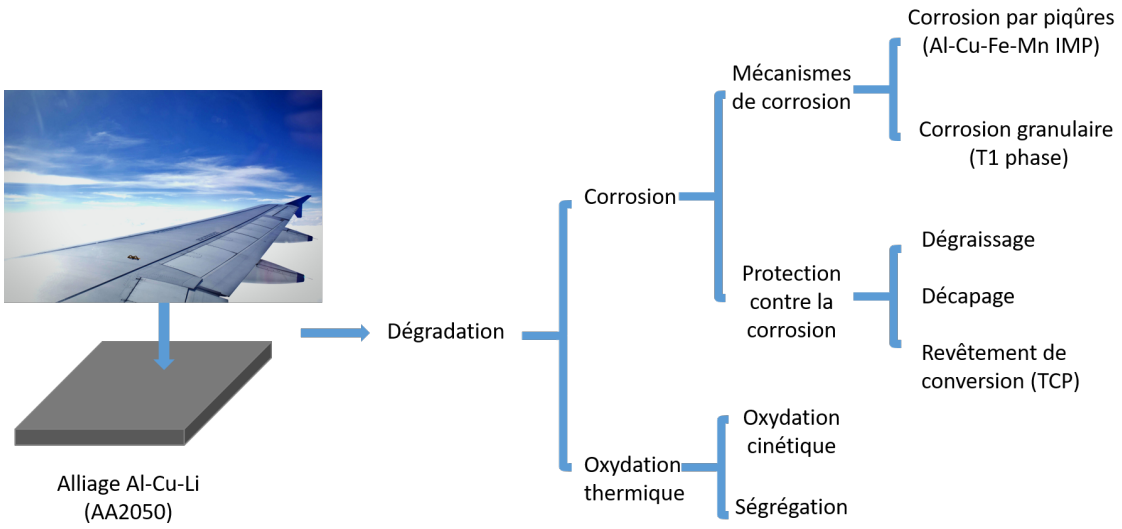

FIGURE R.1 : Description schématique des différents aspects de la dégradation de l'alliage Al-Cu-Li abordés dans cette thèse

le comportement de ségrégation de surface de l'Ag dans les alliages industriels d'Al est moins étudié et son influence sur les propriétés telles que la dureté ou la résistance à la corrosion n'est pas claire.

La surface étant considérée comme la région la plus impactée par l'environnement extérieur et l'un des premiers sites de la dégradation, l'évolution de la structure chimique de la surface est particulièrement importante.

Chapitre 2 : techniques et préparation d'échantillon

Les expériences ont été conçues pour étudier la topographie, la microstructure, la structure chimique de surface et le comportement électrochimique du matériau. Différentes techniques ont été utilisées pour réaliser ces expériences.

Pour étudier la topographie et la microstructure du matériau, nous avons utilisé la microscopie électronique à balayage (SEM), la microscopie électronique à transmission (TEM) et la microscopie optique. La résolution spatiale du SEM peut atteindre 100 à 50 nm mais reste insuffisante pour observer la phase nanométrique T1 dans Al-Cu-Li. Par conséquent, le MET est utilisé pour observer la nanostructure du matériau.

La structure chimique de la surface a été étudiée par des techniques sensibles à la surface

telles que la spectrométrie de masse d'ions secondaires à temps de vol (ToF-SIMS) et la spectrométrie de photoélectrons induits par rayons X. Le ToF-SIMS possède une très haute sensibilité (plage de détection d'un pour un milliard pour la plupart des éléments). Il s'agit d'une technique d'analyse de surface avec une sélectivité chimique élevée ($M/\Delta M \geq 10\ 000$). Elle est basée la combinaison de la spectrométrie de masse des ions secondaires et analyse de masse en temps de vol. Tout d'abord, un faisceau d'ions primaires focalisé (typiquement Bi^+) est pulsé sur une surface de matériau avec une énergie cinétique de l'ordre de grandeur de quelques keV résultant en une cascade de collision à l'intérieur du matériau et l'émission de diverses particules secondaires, telles que des électrons, des espèces neutres, des atomes et des molécules présents à la surface. Les ions secondaires analysés en ToF-SIMS sont issus des 2 à 3 premières monocouches et sont caractéristiques de la composition de la surface. La résolution latérale du ToF-SIMS peut atteindre une valeur inférieure à 100 nm. Il est également possible d'obtenir des profils en profondeur des matériaux organiques, inorganiques et métalliques, ce qui permet d'explorer la variabilité chimique dans la direction perpendiculaire à la surface.

L'analyse chimique par XPS est à la fois qualitative et quantitative. L'analyse quantitative des données XPS est basée sur des spectres et un modèle de surface théorique. Un modèle de film d'oxyde en couches peut être postulé afin de calculer l'épaisseur et la composition du film d'oxyde ainsi que la composition du substrat métallique. L'ajustement des pics expérimentaux à l'aide de composantes simulées symétriques pour les espèces oxyde, et asymétriques pour les composants métalliques a permis de quantifier les proportions relatives de chaque espèce. La distribution d'Al et des autres éléments d'alliage dans l'oxyde et le substrat métallique peuvent également être calculées à partir de leur rapport d'intensité ($I_{\mathrm{M}}^{\mathrm{M_{ox}}} / I_{\mathrm{M}}^{\mathrm{M_{met}}}$).

Les mesures électrochimiques ont été réalisées dans une cellule électrochimique classique à 3 électrodes avec un fil de platine comme contre-électrode et une électrode au calomel saturé (SCE) comme électrode de référence. Le potentiel en circuit ouvert (OCP) et les balayages anodiques et cathodiques (LSV) ont été enregistrés pour étudier le comportement à la corrosion des matériaux.

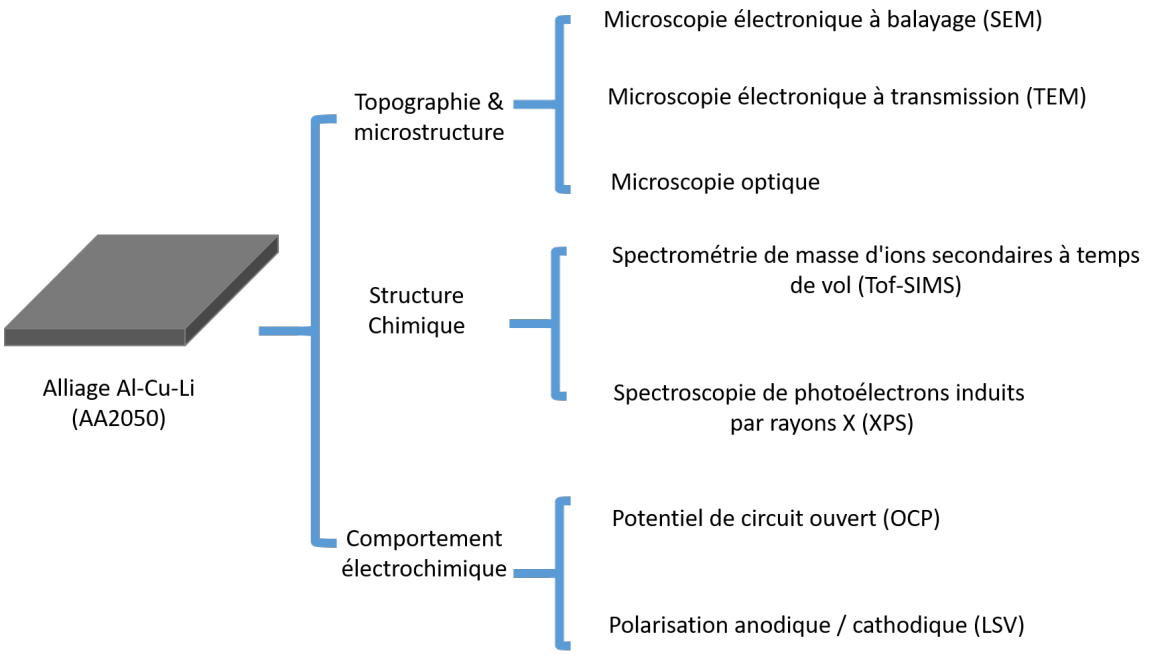

FIGURE R.2 : Techniques de caractérisation de surface utilisées dans cette thèse

Chapitre 3 : effet de l'oxydation thermique sur la chimie de surface et la ségrégation sur Al-Cu-Li

La stabilité thermique des alliages Al-Cu-Li est critique dans les conditions de travail extrêmes rencontrées dans l'industrie aéronautique. Dans ce chapitre, les étapes initiales de l'oxydation thermique d'un alliage industriel AA 2050-T8 Al-Cu-Li ont été étudiées par XPS *in situ* et ToF-SIMS.

Le recuit de l'échantillon à 200 °C avant oxydation conduit à un enrichissement de surface en Li et Ag métalliques. Lorsqu'il est exposé à de l'oxygène à basse pression ($P_{O_2} \leq 10^{-6}$ mbar), une couche d'oxyde mixte Li-Al est formée. Les intensités de photoémission enregistrées à des angles d'émission de 45 ° et 90 ° par rapport à la surface sont compatibles avec la formation d'une couche continue d'oxyde pour une exposition à l'oxygène de 0 à 5000 langmuirs. En supposant une composition homogène de la couche d'oxyde, une épaisseur de 9 $\pm$ 1 Å à 5000 langmuirs a été calculée. La teneur relative en Li et Al dans la couche d'oxyde évolue d'une valeur initiale de 50 % pour se stabiliser à 70 % de Li au-delà de 100 langmuirs d'exposition à l'oxygène. Dans le même temps, la teneur en Li à la surface du substrat métallique est réduite de 10 % à 0 %.

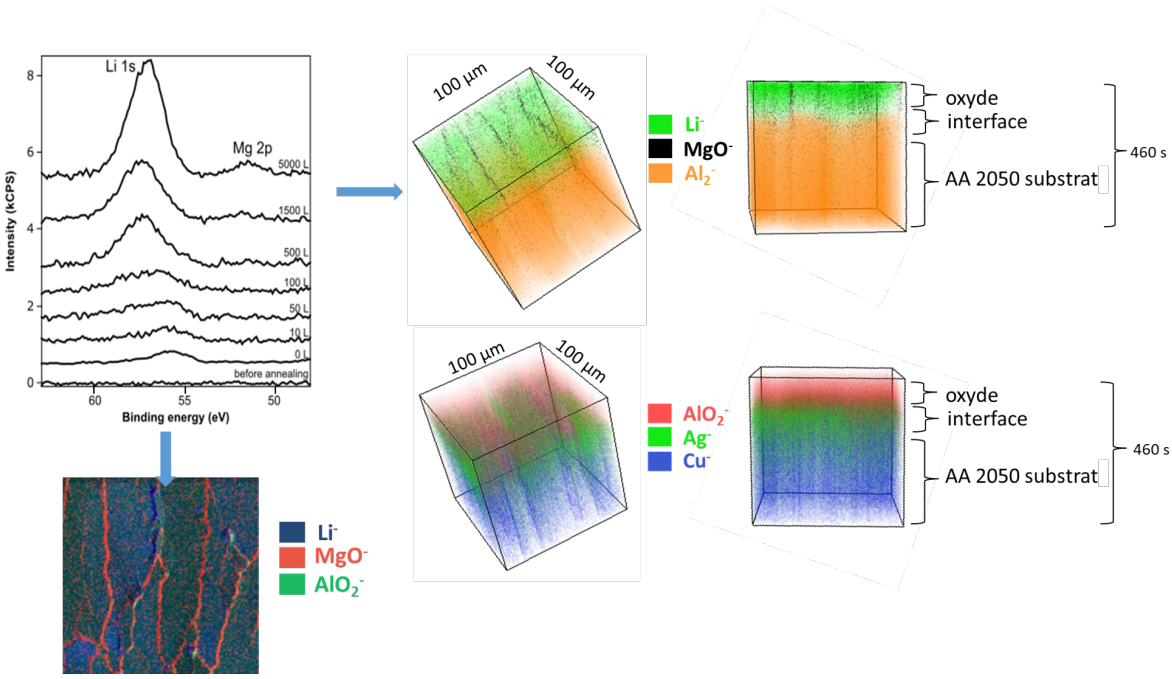

FIGURE R.3 : Spectres XPS in situ et cartographie ToF-SIMS 3D de la surface oxydée thermiquement

De plus, des sites de ségrégation spécifiques sont mis en évidence par la cartographie chimique tridimensionnelle ToF-SIMS. Pour Li, une distribution homogène en surface, tandis que pour Mg l'accumulation aux joints de grains ont été observés. La ségrégation d'Ag induite par le traitement thermique à l'interface oxyde/alliage a été confirmée par ToF-SIMS.

Chapitre 4 : corrosion des alliages Al-Cu-Li

Dans ce chapitre, le comportement vis-à-vis de la corrosion de l'alliage Al-Cu-Li AA2050-T8 dans les électrolytes agressifs est présenté. Des mesures TEM ont révélé la nanostructure du matériau et les différentes IMP observées dans l'alliage Al-Cu-Li sont explicitées.

Les mesures TEM montrent une phase T1 en forme d'aiguille hautement concentrée qui est le précipité majoritaire, distribué de manière homogène dans les grains. La longueur et l'épaisseur de ce type d'IMP sont respectivement d'environ 50 à 100 nm et 2 à 10 nm. Outre la phase T1, des dispersoïdes de taille nanométrique enrichies en Zr, Ag ou Cu et Mn sont observés par TEM. Les grandes IMPs Al-Cu-Fe-Mn dont le diamètre est supérieur à 1 µm constituent un autre type d'IMP principal de l'échantillon et sont considérés comme les sites initiaux de la corrosion par piqûres.

L'étude de la cinétique de corrosion et de la morphologie de la corrosion des IMP Al-Cu-Fe-Mn dans AA2050-T8 immergé dans l'électrolyte NaCl 0,1 M. Les profils ToF-SIMS en profondeur, l'imagerie 2D, et l'imagerie 3D ainsi que les mesures XPS ont été réalisés sur la surface corrodée afin d'étudier de manière générale et locale la modification de surface lors de la corrosion.

Deux IMPs Al-Cu-Fe-Mn ont été mesurées avant et après corrosion par cartographie chimique ToF-SIMS 2D et 3D. Des sites préférentiels d'initiation de la corrosion ont été mis en évidence dans la matrice de l'alliage à proximité ou au-dessus des IMP Al-Fe-Cu-Mn. La présence de chlorures et d'hydroxydes a été mise en évidence au niveau des piqûres enrichies en Cu et Fe et l'hydroxyde de Cu s'est avéré être l'un des produits de corrosion présent dans la zone de la piqûration. La formation d'une couche d'oxyde-hydroxyde avec une composition différente et/ou une épaisseur plus élevée sur l'IMP que la matrice d'alliage a été mise en évidence. La distribution de Li sur la surface corrodée a été révélée par la cartographie 3D ToF-SIMS. Un peu de Li a été détecté dans la matrice de l'alliage, tandis qu'aucun Li n'était présent dans la zone de l'IMP où la corrosion par piqûres s'est produite. Le lithium métallique était toujours présent dans la matrice.

La cartographie chimique 2D et 3D ToF-SIMS a donné une version 2D/3D de la topographie de corrosion par piqûres de la surface. Les performances du ToF-SIMS pour la détection 3D de la corrosion par piqûres sont illustrées en particulier en ce qui concerne la sensibilité élevée aux espèces de faible masse atomique comme le Li. Les cartographie ToF-SIMS 3D peuvent également être récupérées sous forme de projection 2D et de profils en profondeur séparés pour un meilleur examen de l'observation latérale et approfondie. De plus, des traces de Li ont été clairement détectées sur les cartographie 3D après corrosion. Aucun Li n'a été observé sur l'oxyde formé sur les IMPs alors qu'une trace de Li a été détectée dans l'oxyde formé sur la matrice indiquant que le Li se distribue dans l'oxyde dissous après corrosion par piqûres.

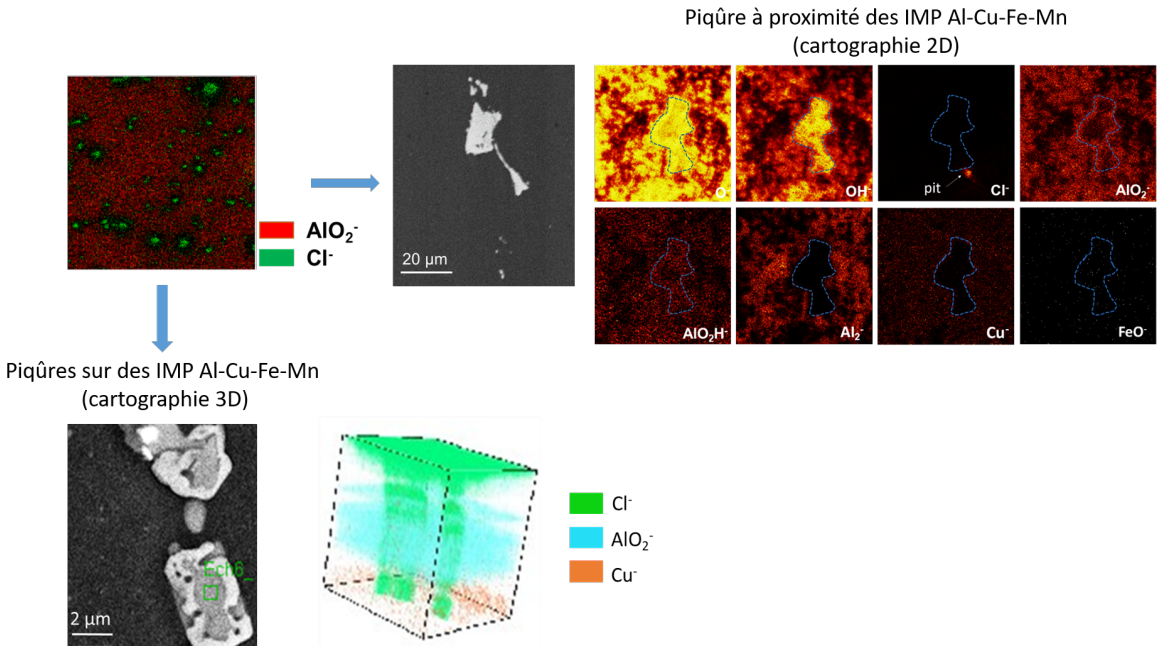

FIGURE R.4 : Cartographie chimique 2D et 3D de la piqûration de surface induite par les IMP

Chapitre 5 : modifications de surface induites par les pré-traitements et effets sur la structure chimique des dépôts de conversions sur Al-Cu-Li alloy (AA2050)

Le procédé chrome trivalent (TCP) a été développé en tant que processus de conversion prometteur visant à améliorer les propriétés de corrosion et l'adhérence des alliages d'aluminium. Un ensemble de prétraitements de surface tels que la gravure alcaline et le décapage acide est généralement appliqué sur l'alliage d'aluminium avant le dépôt TCP afin d'optimiser ses propriétés.

Dans notre étude, les modifications de surface d'un alliage Al-Cu-Li (AA2050) à différentes étapes de prétraitement (dégraissage alcalin et décapage acide) et suivant le procédé chrome trivalent sont étudiées par spectroscopie de photoélectrons induits par rayons X (XPS), spectrométrie de masse d'ions secondaires à temps de vol (ToF-SIMS) et microscopie électronique à balayage (SEM). Une influence significative du prétraitement sur le traitement TCP ultérieur est mise en évidence en comparant les couches TCP formées sur des échantillons polis et prétraités.

La dissolution préférentielle des IMP et des joints de grains pendant le prétraitement a été mise en évidence. De plus, le prétraitement conduit à la formation d'une couche d'oxyde d'alumi-

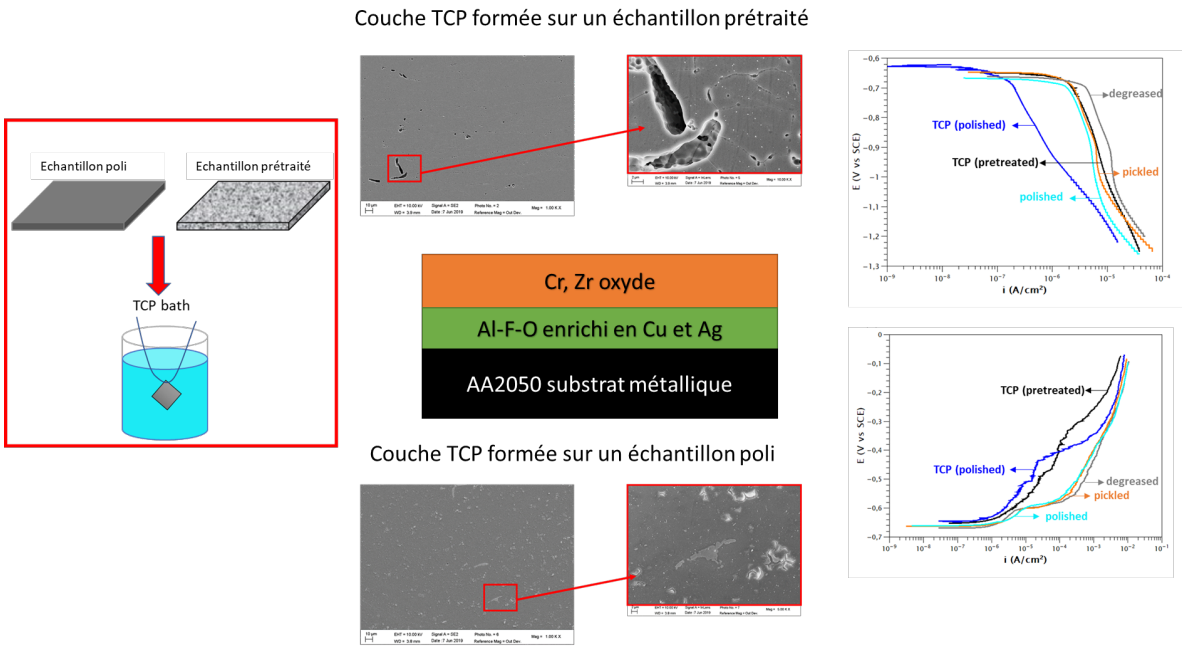

FIGURE R.5 : Morphologie de surface et comportement électrochimique des couches TCP formées sur substrats poli ou prétraité

nium plus épaisse avec un enrichissement important en Cu et Ag en surface. Le revêtement TCP formé sur un échantillon poli ou prétraité présente une structure multicouche avec une couche externe d'oxyde de Zr et Cr et une couche interne d'Al-O-F contenant Li et Ag. Un revêtement de conversion TCP plus épais (oxyde externe) avec moins de fissures est formé sur la surface prétraitée par rapport à la surface polie. De plus, un enrichissement en Cu est mis en évidence sur la couche TCP de l'échantillon prétraité. Le comportement de l'enrichissement en Cu sur la surface prétraitée lors du dépôt TCP est interprété sur la base des résultats des mesures XPS, ToF-SIMS et électrochimiques. Premièrement, le Cu dans l'oxyde d'aluminium passif est dissous au début du dépôt TCP, puis avec la consommation de protons, l'augmentation du pH conduit au dépôt d'espèces Zr et Cr accompagnées des espèces Cu qui avaient tendance à se dissoudre à partir d'une surface prétraitée. Le dépôt de Cu ainsi que le Cu métallique accumulé à la surface du substrat augmentent la réactivité cathodique de la surface et favorisent la croissance du revêtement TCP. La voltampérométrie linéaire à balayage indique que le revêtement TCP joue un rôle critique sur la résistance à la corrosion et que l'enrichissement de Cu dans les couches TCP augmente efficacement le courant cathodique.

Conclusions and perspectives

L'alliage Al-Cu-Li (AA2050-T8) est un alliage particulièrement adapté pour remplacer les alliages d'aluminium aérospatiaux classiques tels que l'alliage Al-Cu-Mg (AA2024) ou l'alliage Al-Cu-Zn (AA7050). La teneur supplémentaire en Li dans l'alliage AA2050 joue un rôle essentiel dans l'amélioration de ses propriétés mécaniques. Cependant, en raison de la nature active du Li, son comportement sous diverses environnements est difficile à déterminer.

En tant que matériau d'application pour l'aérospatial, les propriétés des alliages Al-Cu-Li doivent être complètement étudiées et évaluées dans diverses circonstances pour assurer la sécurité et la durée de vie des aéronefs. Par conséquent, notre objectif lors de cette thèse fut de mener une étude complète de la physico-chimie de surface des alliages Al-Cu-Li en ce qui concerne le comportement à la corrosion, le traitement de surface industriel et l'oxydation thermique.

La première partie de la thèse a consisté à étudier le comportement à la corrosion de la surface polie dans les électrolytes agressifs (à base de chlorure) afin d'étudier le mécanisme de corrosion de l'alliage Al-Cu-Li et le rôle du Li. Tout d'abord, une attaque relativement forte se produit autour et au-dessus des IMP. La cartographie chimique des piqûres par ToF-SIMS a révélé un enrichissement en Cu, Fe, Cl. Des piqûres et des tranchées sont observées à la frontière entre les IMP et la matrice. L'intensité élevée de OH^- observée sur les IMP indiquent une surface hautement hydratée sur les IMP. Cette hydratation est induite par la nature cathodique des IMP. Un couplage galvanique est créé entre les IMP et la matrice dans l'électrolyte et la réaction cathodique (réduction de l'oxygène) se produit sur les IMP produisant des OH^-. Ceux-ci réagissent avec les espèces Al dissoutes et se déposent sur les IMP. Le comportement du Li est également détecté par les profils ToF-SIMS en profondeur. Avant la corrosion, l'existence de Li est clairement observée dans la couche d'oxyde mais après corrosion, de Li de la couche oxydée a nettement diminué indiquant une dissolution de Li pendant le processus de corrosion.

Pour améliorer le comportement à la corrosion et les propriétés de surface telle que l'adhérence, un traitement de surface est réalisé dans l'industrie. Pendant le traitement de surface, les IMP qui sont les sites préférentiels de corrosion sont éliminés et une couche d'oxyde plus épaisse est formée avec une résistance à la corrosion plus élevée. Dans cette thèse, le traitement de surface complet appliqué dans l'industrie est réalisé, y compris le dégraissage alcalin, le décapage acide

et le revêtement de conversion TCP. Le dégraissage alcalin et le décapage acide sont considérés comme un prétraitement de surface pour le procédé TCP. Outre l'élimination des IMP, les résultats XPS et ToF-SIMS ont révélé une couche d'oxyde plus épaisse avec enrichissement en Cu et en Ag après traitement de surface. De plus, certains travaux indiquent que le prétraitement de surface influence la couche de TCP en ce qui concerne à la fois la morphologie et la structure chimique. La couche TCP formée sur la surface prétraitée est plus épaisse et présente moins de fissures que celle formée sur la surface polie. En outre, un enrichissement en Cu est observé sur la couche TCP de l'échantillon prétraité. Le LSV anodique et le LSV cathodique ont été réalisés sur les deux couches de TCP mettant en évidence leur rôle critique sur la résistance à la corrosion. Le courant anodique des deux couches TCP est beaucoup plus faible que celui de la surface polie ou prétraitée. Cependant, pendant la polarisation cathodique, la couche TCP de l'échantillon prétraité a le courant le plus élevé. Cette activité cathodique élevée est attribuée à l'enrichissement en Cu. Le Cu enrichi en surface augmente la propriété cathodique de surface et favorise la réaction cathodique. Le Li dans les alliages Al-Cu-Li ne joue pas un rôle critique sur le processus TCP et les propriétés de la couche TCP.

L'oxydation et la corrosion peuvent se produire dans un environnement atmosphérique ayant la capacité d'accélérer la dégradation de la structure du matériau. Par conséquent, l'oxydation est considérée comme un autre phénomène inévitable lors de l'utilisation de l'alliage. L'oxydation à haute température améliore la variabilité de la surface. Dans cette thèse, les étapes initiales de l'oxydation thermique à 200 °C de l'alliage Al-Cu-Li ont été étudiées par XPS in-situ et cartographie 3D ToF-SIMS. La formation d'une couche continue d'oxyde Al-Li mixte est révélée et modélisée par un mode couche homogène. Une épaisseur d'oxyde de 9 ± 1 Å est calculée après une exposition de 5000 L à l'oxygène. Outre l'épaisseur de l'oxyde, la composition chimique de la couche d'oxyde et du substrat métallique est également déterminée. Tout d'abord, un comportement de ségrégation du Li et de l'Ag est observé lors du recuit avant oxydation. Lors de l'exposition à l'oxygène, le Li s'oxyde rapidement tandis que l'Ag reste à l'état métallique et s'enrichit à l'interface oxyde/métal. La composition chimique de la couche d'oxyde après chaque étape d'exposition (jusqu'à 5000 L) a été bien révélée. Une couche d'oxyde riche en Li se forme sur l'échantillon

lorsqu'il est exposé à l'oxygène. L'Ag ségrège à l'interface oxyde/métal à l'état métallique. De plus, une ségrégation de Mg est observée aux joints de grains.

Perspectives

Dans cette thèse, les alliages Al-Cu-Li ont été étudiés en ce qui concerne le comportement à la corrosion et le comportement à l'oxydation qui sont deux facteurs déterminants pour la dégrégation de la structure métallique.

Oxydation thermique

Dans cette thèse, nous nous sommes concentrés sur les étapes initiales de l'oxydation thermique des alliages Al-Cu-Li, qui nous paraissent essentielles pour comprendre les mécanismes qui apparaîtront dans des conditions plus réalistes. Nous sommes convaincus que l'exposition de l'échantillon à la pression ambiante soulèvera des points très intéressants qui bénéficieront de ce travail effectué à plus basse pression. Dans l'environnement à pression ambiante, le comportement d'oxydation de l'Al-Cu-Li sera une référence plus réaliste à l'estimation de la dégradation. De plus, la modification de la couche TCP sous haute température est intéressante à étudier.

Chaque aspects est intéressant à poursuivre. La corrosion et l'oxydation sont deux aspects critiques pour la dégradation de la structure métallique et donc essentiels lors de la mise en service des alliages.

Corrosion

Le comportement de corrosion initial lié aux IMP Al-Cu-Fe-Mn est révélé. Cependant, après 2 heures d'immersion dans l'électrolyte NaCl 0,1 M, de petites piqûres autour des plus grands IMP sont observées et augmentent considérablement la surface de piqûration. Ce comportement n'est pas observé dans les alliages Al-Cu-Mg AA2024. Par conséquent, il pourrait être intéressant de l'étudier. De plus, le comportement de passivation de l'alliage Al-Cu-Li dans l'électrolyte doux est également un nouvel aspect à notre connaissance. On observe un enrichissement en Li dans la couche passivée. Certaines études ont révélé le comportement similaire du Li pendant la polarisation anodique. Le comportement du Li lors de la passivation est intéressant à étudier.

Traitements de surface (anti-Corrosion)

La modification de surface au cours de chaque étape du prétraitement et du processus TCP est mise en évidence. L'effet du prétraitement de surface est révélé. On suppose que le Cu sur la surface prétraitée a un rôle critique sur le processus TCP et modifie également la propriété électrochimique de la couche TCP. Il serait intéressant de continuer à explorer l'effet du Cu sur le processus TCP. De plus, le post-traitement est une procédure avancée dans l'industrie aérospatiale. L'effet du post-traitement sur les alliages Al-Cu-Li n'a pas encore été étudié. Cela pourrait être le sujet d'une étude plus approfondie.

RÉSUMÉ

Les alliages Al-Cu-Li sont considérés comme des matériaux de pointe dans le domaine de l'aéronautique en raison de leurs excellentes propriétés mécaniques et de leur faible poids. Cependant, ces alliages, comme d'autres alliages à base d'aluminium, sont sensibles à la corrosion en raison de la présence de particules intermétalliques (IMP) telles que les particules Al-Cu-Fe-Mn, constituant la phase T1 (Al_2CuLi). Ces particules intermétalliques peuvent conduire à des modifications de surface pendant le traitement de l'alliage et lors de l'exposition à diverses conditions de travail. L'objectif de cette thèse de doctorat est de comprendre les modifications de surface induites par les traitements thermiques, le comportement de l'alliage nu Al-Cu-Li (AA2050) vis-à-vis de la corrosion et l'efficacité de la protection contre la corrosion après traitements chimiques (dégraissage, décapage et dépôt TCP). Cette thèse de doctorat est composée de trois parties. Dans la première partie, la composition de surface de l'AA2050-T8 tel que reçu et les modifications de surface de l'alliage induites par l'oxydation thermique à 190°C, ont été étudiées *in situ* à l'aide de la spectroscopie de photoémission induites par rayons X (XPS). La formation d'une couche mixte d'oxyde d'Al-Li a été démontrée après exposition de l'échantillon à de l'oxygène à basse pression. L'analyse de la cartographie chimique 3D *post mortem* par spectrométrie de masse d'ions secondaires en temps de vol (ToF-SIMS) a révélé la ségrégation de Mg aux joints de grains et l'enrichissement en Ag à l'interface oxyde/métal. Dans la deuxième partie, la corrosion de l'alliage AA2050-T8 exposé à des électrolytes agressifs à base de chlorure a été étudiée en détail par ToF-SIMS 2D et 3D et microscopie électronique à balayage (MEB). Une couche d'oxyde-hydroxyde de composition différente et d'épaisseur plus élevée a été démontré au-dessus des IMPs par rapport à celle formée sur la matrice de l'alliage. En outre, le comportement de Li dans l'oxyde a également été discuté. Dans la troisième partie, les traitements chimiques de surface, y compris le dégraissage, le décapage et le revêtement de conversion (TCP) et les modifications chimiques de surface associées, ont été étudiés à l'aide des techniques XPS, ToF-SIMS et MEB. L'amélioration du comportement de corrosion sur l'alliage traité TCP a été révélée. Une forte influence de l'enrichissement en cuivre sur la qualité, la composition et les performances vis-à-vis de la corrosion du traitement TCP a été démontrée.

MOTS CLÉS

alliage Al-Cu-Li, oxydation thermique, corrosion, prétraitement, couche de conversion chimique, analyse de surface

ABSTRACT

Al-Cu-Li alloys are considered as advanced materials for the aircraft manufacturing due to their high mechanical properties and low weight. However, Al-Cu-Li alloys, similarly to other Al alloys, are susceptible to corrosion due to the presence of intermetallic particles (IMP) such as Al-Cu-Fe-Mn particles, T1 phase (Al_2CuLi). These IMPs can lead to different surface modifications of the alloy during the alloy treatment and/or exposure to various working conditions. The objective of this PhD thesis was to understand the surface modifications induced by thermal treatments, the corrosion behaviour of bare Al-Cu-Li alloy (AA2050) and the corrosion protection efficiency of the alloy after chemical treatments (degreasing, pickling and TCP deposition). This PhD thesis is composed of three parts. In the first part, the surface composition of the as received AA2050-T8 and the alloy surface modifications induced by thermal oxidation at 190°C, using *in situ* X-ray photoelectron spectroscopy (XPS), were performed. The formation of a mixed Al-Li oxide layer was demonstrated after sample exposure to oxygen at low pressure. *Post mortem* time-of-flight secondary ion mass spectrometry (ToF-SIMS) 3D chemical mapping and ion depth profile analyses showed Mg segregation at the grain boundaries and Ag enrichment at the oxide/metal interface. In the second part, the pitting corrosion of the AA2050-T8 alloy exposed to the aggressive chloride-based electrolytes was studied in details by ToF-SIMS 2D and 3D chemical mapping and scanning electron microscopy (SEM). The formation of an oxide-hydroxide layer with different composition and higher thickness was evidenced over the IMPs than over the alloy matrix. Moreover, the behaviour of Li in the oxide was also discussed. In the third part, the surface chemical treatments including degreasing, pickling and conversion coating (TCP) and related surface chemical modifications were studied using XPS, ToF-SIMS and SEM. An improved corrosion behaviour on TCP coated alloy was revealed. A strong influence of copper enrichment on the quality, composition and corrosion performance of the TCP was demonstrated.

KEYWORDS

Al-Cu-Li alloy, thermal oxidation, corrosion, pretreatment, chemical conversion layer, surface analysis